



# Università degli Studi di Ferrara

DOTTORATO DI RICERCA IN  
SCIENZE CHIMICHE

CICLO XXVI


COORDINATORE Prof. Carlo Alberto Bignozzi

***Chemical and Physical Characterization of  
Electrocatalysts based on Iridium Oxide and  
prepared by Sol-Gel and Physical Vapor Deposition***

Settore Scientifico Disciplinare CHIM/02

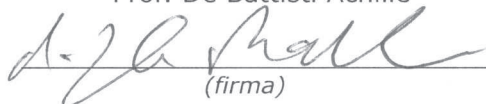
**Dottorando**

Dott. Rosestolato Davide

  
\_\_\_\_\_  
(firma)

**I Tutore**

Prof. De Battisti Achille

  
\_\_\_\_\_  
(firma)

**II Tutore**

Dr. Ferre Sergio

  
\_\_\_\_\_  
(firma)

Anni 2011/2013

*“Science never solves  
a problem without  
creating ten more”*

**George Bernard Shaw**

*“Nihil enim tantam vim habet ad animi magnitudinem gignendam, quam  
posse singula, quae in vita occurrunt, via ac ratione explorare eaque  
semper sic intueri, ut simul tecum reputes...”*

**Marcus Aurelius**

*This work of thesis is dedicated to my Family, who supports me in both good and bad  
times of my life.*

*With love, Davide*

# Index

1. Scope	1
Bibliography	4
2. Introduction and Purposes: DSA anodes <sup>®</sup> for chlorine and oxygen evolution reactions	5
3. Application of DSA anodes <sup>®</sup>	9
3.1.Applications that involve the Oxygen Evolution Reaction	9
3.1.1. Electroplating and Electrogalvanizing	9
3.1.2. Electrowinning	10
3.1.3. Cathodic protection using impressed currents	10
3.1.4. Incineration of contaminants	11
3.2.Applications that involve the Chlorine Evolution Reaction	12
3.2.1. Chlor-alkali industry: Chlorine production	12
3.2.2. Chlorine cell technologies	14
3.2.2.1. Mercury cells	14
3.2.2.2. Diaphragm cells	15
3.2.2.3. Membrane cells	16
3.2.3. Water disinfection	19
3.2.4. Treatments for agriculture and food industry	19
3.2.5. Sterilization of water used for medical purposes	20
Bibliography	21
4. Preparation Methods used for Metal Oxide coated electrodes	23
4.1.Sol-Gel method	23
4.1.1. Historical notions on Sol-Gel method	24
4.1.2. Importance of precursors: Hydroxo-Chloro Aceto complexes	25
4.2.Physical Vapor Deposition	28
4.2.1. Sputter deposition	29
4.2.2. Alloys	31
4.2.3. Physical Basic Phenomena	32

4.2.4. Plasma Sputtering	35
4.2.5. DC Sputtering	38
4.2.6. RF Plasma Sputtering	39
4.2.7. Magnetron Sputtering	41
4.2.8. Reactive Sputtering for compound thin films	42
<b>Bibliography</b>	44
<b>5. Nuclear Spectrometry: Backscattering Spectrometry and Elastic Recoil Detection</b>	45
5.1.Introduction	45
5.2.The kinematic factor and mass resolution	47
5.3.Elastic scattering cross sections	48
5.4.Experimental geometry	50
5.5.Effects of energy loss of ions in solids	51
5.5.1. Definitions	51
5.5.2. Depth scale and Depth resolution	52
5.6.Experimental apparatus	54
5.7.Numerical calculations of spectra: Areal density calculations and computer simulation	55
5.8.Elastic Recoil Detection (ERD)	55
<b>6. Electrode preparation: Experimental details about the samples deposition</b>	58
6.1.Sputtered samples prepared on titanium supports	58
6.2.Sol Gel samples prepared on titanium supports	59
6.3.Sol-gel Samples prepared on amorphous silica supports	59
6.4.Sol-gel Samples prepared on doped silicon wafer supports	60
<b>7. Experimental Details: Microstructural, Surface and Electrochemical Analysis</b>	60
<b>Bibliography</b>	64
<b>8. Ex-Situ and On-Site Characterizations</b>	65
8.1.Systematic study of the Iridium and Titanium oxide solid mixture by Wide Angle X-ray Scattering (WAXS)	65
8.2.Calcination process investigated through synchrotron light	78
8.3.WAXS analysis of coatings deposited on Ti supports	82

8.4.RBS analysis of electrode materials	84
8.5.AFM analysis: roughness index evaluation	86
8.6.Cyclic Voltammetry experiments for the estimation of the number of electroactive sites	91
8.7.ERD Analysis: evaluation of the amount of protons involved in the charging/dischargin process of iridium sites	101
<b>Bibliography</b>	<b>106</b>
9. Electrochemical characterization: investigation on the Chlorine Evolution Reaction	108
9.1.About the Chlorine Evolution Reaction: chronicle of mechanisms proposed	108
9.2.Polarization curves: Tafel slopes and Reaction Orders evaluation	117
9.3.Preliminary tests for checking the electrochemical apparatus of measure	122
9.4.Polarization Curves collected at 25 °C	124
9.5.Effect of the temperature	131
9.6.Effect of the coverage on Tafel slopes and Reaction Orders	139
9.7.Impedance spectroscopy analysis on ChIER	145
<b>Bibliography</b>	<b>156</b>
10. Effects of chlorine evolution on materials	160
10.1. XRD investigation - evaluation of phases modifications	160
10.2. RBS and XPS experiments: findings from the ChIER	161
10.3. Service life evaluation: accelerated tests on electrode devices	165
11. Summary on Discussions, and Conclusions	169
<b>Bibliography</b>	<b>175</b>
<b>Acknowledgments</b>	<b>177</b>

## **Keywords**

Iridium Oxide

Film

Dimensionally Stable Anode

Physical Vapor Deposition

Sputtering

Sol-Gel

Chlorine evolution

## Abstract (Ita)

La richiesta di materiali elettrodici che soddisfino alle caratteristiche di elevata attività catalitica e soddisfacente stabilità sotto particolari condizioni di potenziale e densità di corrente applicati, ha orientato la ricerca verso la sintesi di nuovi dispositivi sempre più efficienti. Fra questi, gli elettrodi a base di RuO<sub>2</sub> e IrO<sub>2</sub> hanno trovato utilizzo nella preparativa dei DSA (*Anodi Dimensionalmente Stabili*), grazie alle loro buone performance elettrocatalitiche e la loro resistenza a corrosione. Un significativo incremento della stabilità di questi materiali può essere ottenuta aggiungendo ossidi dei cosiddetti metalli “valvola” (TiO<sub>2</sub>, SnO<sub>2</sub>, ecc.), che hanno la duplice funzione di aumentare la stabilità del *device*, diluendo l’ossido elettrocatalizzatore per ridurre i costi di produzione.

Come descritto nei **Capitoli 1 & 2**, la presente ricerca mira al miglioramento di elettrodi a base di ossido di iridio, da utilizzare per le reazioni di sviluppo di cloro e di ossigeno; gli obiettivi principali consistono nella riduzione dei costi di produzione e nell’incremento dell’attività catalitica e della stabilità dei dispositivi elettrodici. Il principale utilizzo dei DSAs riguarda l’industria del cloro-soda, ove vengono sfruttati come anodi per la produzione di cloro, e diversi processi legati all’elettro-metallurgia in soluzione acquosa, dove il processo anodico è rappresentato dalla evoluzione di ossigeno. Una breve *review* sulle applicazioni di questi dispositivi è presentato nel **Capitolo 3**. E’ stata oggetto di studio una preparativa non convenzionale: lo *sputtering reattivo*, che appartiene alla famiglia delle *Physical Vapor Depositions* (PVDs). La preparativa industriale dei DSAs sfrutta comunemente la tecnica sol-gel, per ragioni legate ai costi e alla semplicità operativa, tuttavia, la sintesi via sputtering può offrire diversi vantaggi in termini di attività e reattività del dispositivo finale. Entrambi i metodi di preparazione sono stati approfonditamente discussi nel **Capitolo 4**.

Il **Capitolo 5** tratta i dettagli teorici su cui si basano le tecniche nucleari; dato l’utilizzo poco diffuso per la caratterizzazione di questo tipo di materiali, è stato fatto un riassunto delle nozioni principali sulle tecniche RBS e ERDA.

Questo lavoro di tesi è stato focalizzata su film costituiti da ossidi misti di iridio e titanio, preparati mediante i due metodi sopracitati (sol-gel e sputtering reattivo), a 350 e 450 °C. I dettagli sulle preparative sono stati raccolti nel **Capitolo 6**.

Le analisi strutturali e morfologiche (AFM, RBS, ERDA, XRD, SEM-EDX, XPS) sono state accoppiate a studi elettrochimici (CV, PC, EIS), al fine di ottenere una descrizione approfondita dei materiali studiati. Le informazioni relative ai dettagli sperimentali sono incluse nel **Capitolo 7**. La correlazione tra le proprietà strutturali e catalitiche di un materiale, rappresenta uno step

fondamentale nello sviluppo di un nuovo catalizzatore. Le informazioni disponibili in letteratura sono spesso poco chiare o contraddittorie, come nel caso del meccanismo di reazione proposto per l'evoluzione elettrochimica di cloro.

Le caratterizzazioni *ex-situ* e *on site* tramite XRD, RBS, AFM, CV e ERDA sono discusse nel **Capitolo 8**. Studi preliminari sul comportamento della miscela, effettuato tramite XRD, hanno dimostrato che per quantitativi superiori al 20 % in moli iridio, la cristallizzazione dei due componenti avviene in forma rutilo (con riferimento particolare al TiO<sub>2</sub>, l'accrescimento di questa fase non è cineticamente favorita in queste condizioni sperimentali) con formazione parziale di una soluzione solida, e la crescita segue preferenzialmente specifiche direzioni cristallografiche (ad esempio, la (110)). Le analisi RBS, AFM, ERDA e CV, effettuate su campioni preparati attraverso sputtering, hanno evidenziato che i film sono più compatti rispetto a quelli ottenuti via sol-gel, e costituiti da strutture colonnari che paiono essere la fonte di un " meso/nano" porosità estesa a tutto il coating; quest'ultima caratteristica può influenzare fortemente il trasporto di massa dei reagenti nelle porzioni più interne dell'elettrodo. I campioni sol-gel, al contrario, sono caratterizzati da una superficie fortemente rugosa, che porta ad un aumento della reale area attiva di ben due ordini di grandezza. La diversa struttura dei materiali può influenzare notevolmente la stabilità dei dispositivi: una delle cause di disattivazione dei DSAs<sup>®</sup> consiste nella passivazione del supporto di titanio metallico per contatto con l'elettrolita che può permeare attraverso il film: il fenomeno è plausibilmente più probabile quando il materiale presenta fessure e macropori, che consentono la permeazione della soluzione elettrolitica, portando alla disattivazione del dispositivo. Inoltre, una compattezza del deposito può anche aumentare la resistenza alla dissoluzione del materiale elettrocatalitico, prolungando notevolmente la vita utile.

Il meccanismo della reazione di evoluzione di cloro (ChlER), è stato indagato a fondo, e la discussione dettagliata si può trovare nel **Capitolo 9**. L'indagine ha richiesto un'attenta analisi utilizzando la spettroscopia di impedenza e l'applicazione di un modello matematico proposto da Conway nei primi anni '90. Questo approccio ha portato ad identificare una sequenza di stadi in accordo con il cosiddetto meccanismo di Volmer-Heyrovsky. L'intero quadro dei dati sperimentali diventa interpretabile ipotizzando il coinvolgimento di una elevata copertura di intermedi di reazione, attraverso cui si giustificano le anomalie verificatesi in termini di pendenze di Tafel e ordini di reazione. L'analisi di spettroscopia di impedenza ha rilevato un contributo importante associato alla porosità per i campioni preparati a 350 °C. Gli esperimenti di polarizzazione effettuati a diverse temperature, hanno consentito di ottenere informazioni sulla reattività del sito attivo e su come questa sia relata al metodo di preparazione e alla temperatura di calcinazione. Gli elevati valori di copertura coinvolti nel processo (circa 0.7-0.8) sono stati confermati da misurazioni *ex situ*



effettuate su campioni sintetizzati *ad hoc* dopo pesanti trattamenti di polarizzazione in condizioni di sviluppo di cloro: RBS e XPS hanno confermato la presenza di cloro (anione e radicale) sulle superfici dei campioni (Capitolo 10), e, nel caso dei film preparati a temperatura più bassa, anche nel bulk. Inoltre, il **Capitolo 10** include prove XRD sui campioni sottoposti a forti polarizzazioni in evoluzione di cloro, e prove accelerate di Service Life. Infine, il **Capitolo 11** raccoglie le conclusioni tratte sulla base di tutto il quadro dei risultati sperimentali raccolti.

## Abstract

The request for electrode materials that exhibit satisfactory catalytic activity and high stability under particular conditions of potential and current density, has stimulated the synthesis of new devices, characterized by improved performances. Among these, electrodes based on RuO<sub>2</sub> and IrO<sub>2</sub> have found wide application in the field of DSA anodes<sup>®</sup> (*Dimensionally Stable Anodes*), thanks to their features of good electrocatalytic activity and high resistance to corrosion. An increase of the stability of materials can be obtained through the utilization of mixtures of oxides: along with the electrocatalytic oxide, other ones (TiO<sub>2</sub>, SnO<sub>2</sub>, *etc.*) are added, which have the double purpose of increasing the corrosion resistance of the electrode, while diluting the main oxide to minimize the production costs of the device.

As described in **Chapters 1 & 2**, the present research aims to the improvement of iridium-based electrodes, to be used for chlorine and oxygen evolution reactions, and to the development of “better” materials, which should be characterized by reduced costs of production and/or higher catalytic activity and stability. Their main uses concerns the chlor-alkali industry, where they are exploited as anodes for the chlorine production, and several electro-metallurgy processes, where the anodic process is represented by the oxygen evolution; a short review on these and others uses has been presented in **Chapter 3**. A not conventional preparative was chosen: the reactive sputtering, which belongs to the family of Physical Vapor Depositions (PVDs). The industrial preparative of DSA anodes<sup>®</sup> typically exploits the most common sol-gel technique, for reasons related to costs and operational simplicity; however, the sputtering synthesis may offer advantages, in terms of activity and reactivity of the final device, and, therefore, a specific investigation has been planned. Both preparation methods have been deeply discussed in **Chapter 4**.

**Chapter 5** deals with the theoretical details on which nuclear techniques are based, because of the fact that their utilization for the characterization of this kind of materials is uncommon; a quite detailed review of theoretical notions about RBS and ERDA has been reported.

This work of thesis has been focused on films constituted by mixed oxides of iridium and titanium, prepared through the two different methods mentioned above (sol-gel and reactive sputtering), at 350 and 450 °C. Details on the preparation have been resumed in **Chapter 6**.

Structural and morphological analyses (AFM, RBS, ERDA, XRD, SEM-EDX, XPS) have been coupled to electrochemical studies (CV, PC, EIS), aiming to obtain a thorough description of the studied materials. All experimental details are included in **Chapter 7**. The

relationship between the structural and catalytic properties represents a key-step in the development of a new catalyst, and the information available in the literature is often unclear or contradictory, as in the case of the reaction mechanisms proposed for the chlorine evolution at noble-metal-oxide-based materials.

The *ex-situ* and *on-site* characterizations via XRD, RBS, AFM, CV and ERDA are discussed in **Chapter 8**. Preliminary studies on the behavior of the mixture, carried out via XRD, showed that for quantities exceeding 20 %mol in iridium, the crystallization of both components occurs in the rutile form (with reference to TiO<sub>2</sub>, this phase is not kinetically favored under these experimental conditions) with partial formation of a solid solution, and the growth preferentially follows specific crystallographic directions (*e.g.*, the (110)). RBS, AFM, ERDA and CV analyses, carried out on samples prepared by sputtering, evidenced that films are more compact than those obtained by sol-gel, and constituted by columnar structures that are the source of a “meso/nano”-porosity; the latter can strongly affect the mass transport of reagents in the innermost portions of the electrode. Samples prepared by sol-gel, conversely, are characterized by a strongly wrinkled surface, which leads to an increase of the real active area of two orders of magnitude. The different structure of the materials greatly influences the stability of the devices: one of the causes of deactivation of DSA electrodes<sup>®</sup> consists on the passivation of the titanium metal at the interlayer: this event is plausibly more probable when the material exhibits cracks and macro-pores, which allow the permeation of the electrolyte solution, leading to device decommissioning. Moreover, a compactness of the deposit can also increase the resistance to dissolution of the electrocatalytic material, prolonging greatly the service life.

The mechanism of chlorine evolution reaction (ChIER) has been also investigated, and a detailed discussion can be found in **Chapter 9**. The investigation required a careful analysis using impedance spectroscopy and also the application of a mathematical model proposed by Conway in the early 90s. This approach has led to identify a sequence of stages in agreement with the so-called Volmer-Heyrovsky mechanism. The whole picture of experimental data becomes interpretable by assuming the involvement of a rather high coverage by reaction intermediates, which allows explaining the abnormalities occurred in terms of Tafel slopes and reaction orders. The impedance spectroscopy analysis pointed out an important contribution associated to the porosity for the samples prepared at 350 °C. Polarization experiments carried out at different temperatures provided information on the reactivity of the active site and on how this reactivity depends on both temperature and method of preparation. The high values of coverage involved in the process (around 0.7 - 0.8) have been confirmed by *ex-situ* measurements carried out on *ad hoc* samples, after heavy treatments of polarization

under ChLER conditions: RBS and XPS confirmed the presence of chlorine (radical anion) on sample surfaces (Chapter 10), and even in the bulk in the case of films fired at the lowest temperature. Moreover, **Chapter 10** included XRD tests on sample after strong polarizations under chlorine evolution and accelerated service life tests. Finally, **Chapter 11** collects the conclusions drawn on the basis of the whole picture of experimental results collected.

# 1. Scope

Since the introduction of the Dimensionally Stable Anodes (hereafter DSA) [1] in chlor-alkali processes already almost half a century ago, the number of fields where these devices have found application has been continuously increasing together with the need for improvement of their performance in chlorine synthesis itself.

The constant applicative demand has prompted active research on the different features of the DSA performance, aiming at:

- Increase of the catalytic activity, associated to a good selectivity toward the electrochemical reaction of interest. This feature is fundamental in the chlorine electrosynthesis process.
- Increase of the electrode “service life”, of great interest in chlor-alkali industry, but also in aqueous electrometallurgy, where the anode works under severe oxygen evolution conditions.
- minimization of the amount of noble-metal components (typically Ru, Ir, Pt, Pd) in the active coating of the industrial electrode, without losses of electrode performance.

As discussed later, the application fields vary from the synthesis of chlorine to a large number of processes where the anodic evolution of oxygen represents the counter-part of a cathodic reaction of interest, such as a reduction of metal ions (*electrowinning, electroforming, electroplating, electrogalvanizing, etc.*) [2]. In this complex context, this thesis work has been focused on the first of the three above points, *i.e.* the study of the catalytic properties of a DSA-type coating toward the chlorine evolution reaction, and its dependence on the preparation method. In fact, reading and analyzing the large amount of papers produced on this topic (see, for example, refs. [3-10]), a direct correlation between the structural and morphological features and the electrocatalytic properties of materials based on ruthenium oxide or iridium oxide does not seem to have been found or discussed in a satisfactory way; very often, the preparation of high performance materials is carried out after the definition of synthetic pathways optimized through the experience and a great number of trials. This is justified by the difficulties associated with the comprehension of the chemistry of the sol-gel method, which is the most diffuse method used for the preparation of DSA anodes<sup>®</sup> at an industrial scale. Focusing on materials based only on iridium oxide and titanium oxide, the objective is the construction of a wide experimental context that could permit to do a precise prediction of properties in relation with the deposition operative parameters. Moreover, the synthesis based on reactive sputtering (belonging to the family of

the physical vapor depositions) was studied and compared with the conventional sol-gel technique, because of the advantages that it can offer, such as a better control on the composition and on the lateral homogeneity of samples. The reactive sputtering is used for the preparation of materials of interest in the field of semi-conductors, but it has not been used yet for the synthesis of noble-metal oxide materials at an industrial scale, for which the operative conditions have to be accurately searched.

The Chlorine Evolution Reaction (ChLER) was taken as a model reaction within this thesis work, also in consideration of the fact that, in spite of the large amount of papers published on the subject, yet no satisfactory univocal mechanistic interpretation of the reaction mechanism can be found in the literature, especially when the process was investigated at ceramic conductor metal oxides. Our purpose was to propose a satisfactory mechanism; in fact, the development of materials with a high selectivity towards the ChLER cannot be attempted without a deep knowledge of the interactions of chloride ions with the electrode film. Moreover, the choice of studying the ChLER is also justified in the light of the good performances that materials based essentially on IrO<sub>2</sub>-TiO<sub>2</sub> mixtures show in chlor-alkali cells [11].

The experimental work has been purposely centered, throughout the thesis, on aspects associated with the electrocatalytic activity, especially investigating structure and surface reactivity features. Particular attention has been given to the study of the ChLER kinetics, and on the properties of iridium electroactive sites. Specifically, the roles of the method and of the temperature of preparation have been considered, focusing on a close to Ir-Ti 35-65 % mol relative molar concentration of oxides. On the contrary, the aspects related to service-life have been considered and studied only partially, within the framework of this thesis, since they were judged to be beyond the primary objectives. However, it is worth mentioning that a detailed analysis of service-life is currently in progress, with the aim of shedding light on the preparative variables (*i.e.*, deposition technique and temperature) and on how they affect the electrode service-life.

Because of the different cultures required for solving this ambitious purpose, the work has been carried out not only within the group of electrochemistry of the University of Ferrara (headed by Prof. De Battisti), but also with the research groups of Prof. Battaglin (Dipartimento di Scienze Molecolari e Nanosistemi, Università Ca' Foscari di Venezia), for the sputtering deposition and the different nuclear analyses, Prof. Benedetti and Prof. Riello (Dipartimento di Scienze Molecolari e Nanosistemi, Università Ca' Foscari di Venezia), for the XRD analysis, and Prof. Lasia (Département de Chimie - Université de Sherbrooke, CN), for the studies using the Electrochemical Impedance Spectroscopy (EIS).

I believe that the synergic contribution of different cultures, different approaches and point of views, is the key to maintain a correct vision of the topics of research, and the unique way for reaching good results.

## Bibliography

1. H.B. Beer, *J. Electrochem. Soc.* **127**, 303C (1980).
2. P. Duby, *JoM* **45**(3), 41 (1993).
3. S. Trasatti, G. Lodi, *In Electrodes of conductive metallic oxides, Part B*, Edited by S. Trasatti, Elsevier, Amsterdam, 301 (1981).
4. S. Trasatti, G. Lodi, *In Electrodes of conductive metallic oxides, Part B*, Edited by S. Trasatti, Elsevier, Amsterdam, 521 (1981).
5. D.M. Novak, B.V. Tilak, B.E. Conway, *In Modern aspects of electrochemistry*, Vol. 14, Edited by B. E. Conway, J. O'M. Bockris, Plenum. Press, New York, 195 (1982).
6. Ch. Comninellis, G.P. Vercesi, *J. of Appl. Electrochem.* **21**, 335 (1991).
7. P.C.S. Hayfield, *Platinum Metals Rev.* **42**(1), 27 (1998).
8. P.C.S. Hayfield, *Platinum Metals Rev.* **42**(2), 46 (1998).
9. P.C.S. Hayfield, *Platinum Metals Rev.* **42**(3), 116 (1998).
10. S. Trasatti, *Electrochim. Acta* **45**, 2377 (2000).
11. D.M. Novak, B.V. Tilak, B.E. Conway, *In Modern aspects of electrochemistry*, Vol. 14, Edited by B. E. Conway, J. O'M. Bockris, Plenum. Press, New York, 195 (1982).



## 2. Introduction and Purposes: DSA anodes<sup>®</sup> for Chlorine and Evolution reactions

Electrocatalysis is expressed when the electrochemical rate constant of an electrode process depends on (i) the chemical nature of the electrode material, (ii) the physical state of the surface, (iii) the crystal orientation of single-crystal surfaces or alloying effects [1]. An electrode is considered more electroactive than another when, at constant overpotentials ( $\eta$ ), a given reaction takes place with a faster kinetic. This evaluation can be also attained in terms of overpotentials at constant apparent current density,  $j$ . The exchange current density,  $j_0$  (the equilibrium reaction rate at  $\eta=0$ ) is frequently use to classify different electrocatalysts [2]. One of the most important application of oxide based catalysts, treated in this work of thesis, is related to a gas evolution reaction, because the oxygen evolution is practically unknown at “bare” metal electrodes and chlorine evolution from aqueous solutions takes place on a more or less oxidized surface [2].

Dimensionally Stable anodes (DSAs), which consist of a thin layer of a stable electrocatalytic and conductive coating deposited on a base metal, have been widely employed for oxygen and chlorine evolution reactions in the electrochemical industry [3,4,50]. The main objective is the minimization of the potential difference,  $\Delta V$ , between experimental potential at which the reaction takes place and the thermodynamic value. In order to have an efficient electrochemical process, the anodic ( $\eta_a$ ) and cathodic ( $\eta_c$ ) overpotentials should to be significantly reduced, thus allowing the system to converge towards a reversible condition, featured by great kinetic constants. Hence, the utmost role of electrocatalysis is to minimize  $\eta$ , thus increasing  $j_0$  [4]. Electrode materials of technological interest should possess several qualities as high surface area and high electrical conduction [5].

The metal-oxides of the film are composed of active electrocatalytic component (usually RuO<sub>2</sub> or IrO<sub>2</sub>, owing to their activity toward chlorine and oxygen evolution reactions) and one or more valve-metal oxides which dilute the catalysts, hence reducing the costs, and stabilize the device, thus guaranteeing mechanic solidity and a better adhesion on the support. It has also been demonstrated that the nature of the secondary component influence the selectivity of the catalytic material toward different processes [6].

In the past decades, iridium oxide has significantly drawn the researchers' attention toward Oxygen evolution reaction [7]. This was mainly due to the high corrosion resistance

properties exhibited by IrO<sub>2</sub> based materials under oxygen evolution reaction in sulphuric media [8,9,10]. Different electrodes have been developed in the last decades towards OER and ChIER such as IrO<sub>2</sub>+TiO<sub>2</sub> [11], IrO<sub>2</sub>+ZrO<sub>2</sub> [12] and IrO<sub>2</sub>+Nb<sub>2</sub>O<sub>5</sub> [13]. Among these, it has been reported that the 70% IrO<sub>2</sub> and 30% Ta<sub>2</sub>O<sub>5</sub> combination (percentage mole fraction) represent the best compromise between electrocatalytic activity and service life in acidic media [14,15].

In comparison with chlorine evolution reaction, the oxygen evolution reaction occurs at higher potentials and during the ongoing of the process the pH is usually observed to decrease; therefore, under OER most materials experience severe damage, due to their dissolution. Considering the noble metals commonly used for the production of electrocatalysts, their activity can be classified as follows: Ru > Ir > Pd > Rh > Pt > Au [16]. Based on the good results obtained with RuO<sub>2</sub>-TiO<sub>2</sub> and RuO<sub>2</sub>-Ta<sub>2</sub>O<sub>5</sub> based-materials in the chlor-alkali industry, these anodes were extensively studied to optimize their activity toward oxygen evolution reaction. Several compositions of electrocatalysts and based metals have been studied, thus highlighting different overpotentials with respect to the OER, which often reflect the chemical and physical properties of the material itself, *i.e.*, conductivity, multivalence states, etc.. Tab.2.1 lists the standard redox potentials of different oxide couples.

<b>Higher/lower oxide couple</b>	<b>Standard electrode potential at 25 °C (V vs. SHE)</b>
<b>IrO<sub>2</sub>/Ir<sub>2</sub>O<sub>3</sub></b>	0.93
<b>RuO<sub>2</sub>/Ru<sub>2</sub>O<sub>3</sub></b>	0.94
<b>OsO<sub>2</sub>/OsO<sub>4</sub></b>	1.00
<b>NiO<sub>2</sub>/Ni<sub>2</sub>O<sub>3</sub></b>	1.43
<b>CoO<sub>2</sub>/Co<sub>2</sub>O<sub>3</sub></b>	1.45
<b>RhO<sub>2</sub>/Rh<sub>2</sub>O<sub>3</sub></b>	1.73
<b>PtO<sub>3</sub>/PtO<sub>2</sub></b>	2.00
<b>PdO<sub>3</sub>/PdO<sub>2</sub></b>	2.03

Tab.2.1. Standard potentials of few oxide couples

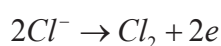
Despite the excellent electrocatalytic activity of ruthenium oxide, it's readily oxidized at 1.39 V/SHE to give off the volatile ruthenium tetroxide (RuO<sub>4</sub>) [17,18,19]. Osmium was excluded from the application because of the toxicity associated with the volatility of osmium tetroxide, while nickel and cobalt oxides exhibit low electrical conductivity. Therefore,

iridium oxide is the most stable and active electrocatalyst coating, especially when it is prepared from chloride precursors such as  $\text{H}_2\text{IrCl}_6$ ,  $\text{IrCl}_4$ , *etc.*.

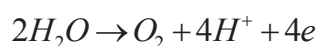
Other studies carried out by Industrie De Nora [20] demonstrated the importance of valve metal oxides. Oxides belonging to this category are usually spinels (*e.g.*,  $\text{Co}_3\text{O}_4$ ,  $\text{NiCo}_2\text{O}_4$ , *etc.*), which are less expensive, but are less active, than iridium and ruthenium oxides [21,22].

In this work, the attention was given to mixtures of iridium- and titanium-based oxides, *i.e.*, 1:2 mol (the composition normally adopted in the industry) focusing on two different deposition temperatures (350 and 450 °C) and on two different preparation methods: Sol Gel method and a particular technique belonging to the family of PVD (Physical Vapor Deposition) procedures, the Rf-magnetron sputtering. In the current state of art, the latter approach is not widely diffused and used nowadays. However, it is interesting to study its possible usage, since it allows the chemical composition, the thickness, and the lateral homogeneity to be finely controlled. The objective is to correlate the structural properties to the electrocatalytic characteristics of the differently prepared materials, seeking for an exhaustive and interpretative model that justifies each experimental observation. The reaction of chlorine evolution has been taken into consideration as a “reaction-model” for our reasoning, due to its significant involvement in the industrial sector and for its simplicity. As will be discussed later, the mechanism of chlorine evolution reaction is still not well understood, and this study also aims to rationalize a mechanism compatible with determined electrochemical parameters. The utilization of iridium instead of ruthenium oxide (the main target studied in literature) allows the advantage of a better experimental response owing to its stability under anodic polarization; because of the similarity between the cited compounds, information related to the kinetic of the process can be also easily extended to the ruthenium oxide case and comparing results to the overall proposed in the literature.

As already mentioned, one of the most important applications of  $\text{IrO}_2$  is in the chlor-alkali industry as anode, and it is not surprising that is one of the most studied reactions in electrochemistry. The standard electrode potential for the ChLER at 25°C is 1.36 V (vs. SHE) in acidic media, calculated from the Gibbs energy of formation of  $\text{Cl}^-$ .



The electrolytic process is generally run over a small range of acidic pH, since the oxygen evolution reaction is thermodynamically favored over the chlorine reaction ( $E^\circ=1.23$  V Vs. SHE). The ChLER has a high reversibility and therefore the chlorine evolution can occur at considerable rates.



Moreover, the oxygen evolution reaction leads to the acidification of the Nernst diffusion solution and thus increasing the equilibrium reaction potential. In a sense, O<sub>2</sub> evolution from chloride solutions can be seen as a “self-retarding” process [23] (see Fig.2.1).

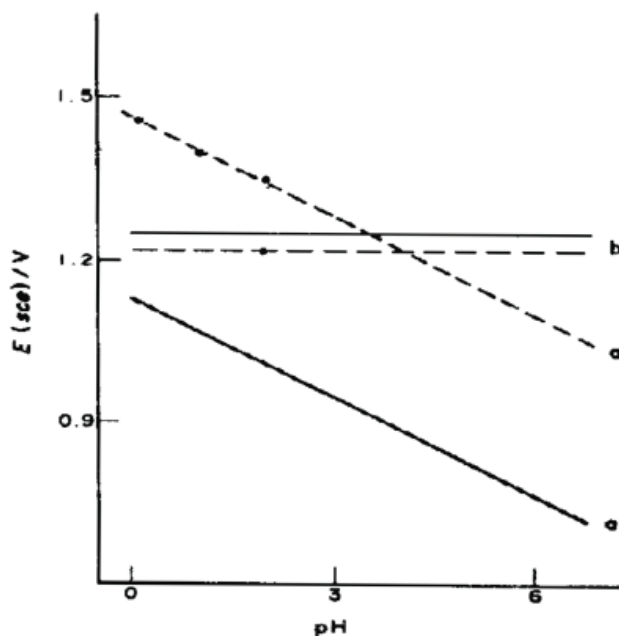
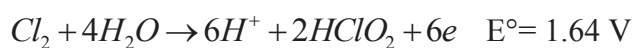
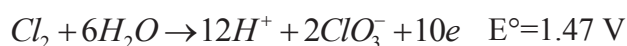
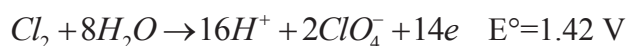


Fig.2.1. (a) Oxygen evolution reaction: thermodynamic potential with respect to pH (continuous line); kinetic potential trend respect to pH (dashed line). (b) Chlorine evolution reaction: thermodynamic potential respect to pH (continuous line); kinetic potential trend respect to pH (dashed line) Reproduced from *Electrochimica Acta*, Vol.32, No.3, pp. 369-382, 1987, Copyright 1987, Elsevier [23].

Chlorine presents a solubility in water which is dependent on the solution pH. In addition to solvated chloride molecules, different chlorinated species are likely to be present in the solution as a result of several chemical reactions [24].



(Standard potential are expressed Vs. SHE).

The existence and the stability of these species depend also on the pH of the solution, as can be noted in the Pourbaix diagrams, well known in literature [24].

## 3. Application of DSA anodes

### 3.1. Applications that involve the Oxygen Evolution Reaction

DSA<sup>®</sup> are widely diffused in applications that involve oxygen evolution reaction as the main process or as anodic reaction for a cathodic one of interest. For example, in metallurgy it should be mentioned electroplating, electrogalvanizing, electrowinning and methods of cathodic protection which exploit the utilization of impressed currents [25]. In these areas, DSA anodes can be involved in different applications including also the electrochemical incineration.

#### 3.1.1. Electroplating and Electrogalvanizing

Electrochemical techniques for depositing thin layers of metals are preferable to others thermic pathways because of the possibility to produce a more homogeneous deposit using very simple apparatus and without modifying the nature of the treated support.

Electrodeposition is the process of producing a coating, usually metallic, on a surface by the action of electric current. The deposition of a metallic coating onto an object is achieved by putting a negative charge on the object to be coated and immersing it into a solution which contains a salt of the metal to be deposited (in other words, the object to be plated is made the cathode of an electrolytic cell). The metallic ions of the salt carry a positive charge and are thus attracted to the object. When they reach the negatively charged object (that is to be electroplated), it provides electrons to reduce the positively charged ions to metallic form.

The electrodeposited layers have can have the role of:

- Ensuring a sufficient protection against aggressive environmental agents eventually present where the material is used (*Electrogalvanizing*).
- Representing a decoration for the metallic (or not) surface treated (*Electroplating*).

The galvanic deposit should have different qualities as good adhesion, absence of porosity, low roughness, good mechanic characteristics. This situation can be realized choosing the operative conditions (current densities, electrochemical bath) properly.

### **3.1.2. Electrowinning**

Electrowinning is one of the most important processes in the industrial electrochemistry. Electrowinning is a process used to remove metal ions from liquid solutions such as rinse water, plating baths, and used process solutions. Most often used to recover precious metals, it relies on an electronic current to plate the metal ions onto a cathode. Recovered metals can then be sold for scrap (if the recovered metal species is not sufficiently pure) or processed for use in plating. The solution can also be recycled with less stress on water treatment systems.

An electrowinning unit consists of a large tank known as a reaction chamber. This chamber houses at least one set of cathodes, which are negatively charged electrodes, and anodes, which are positively charged electrodes. When the unit is turned on, direct current (DC) flows from the cathode to the anode through the liquid solution. The flow of electricity causes metals in the solution to plate onto the cathode in a process similar to electroplating or electrogalvanizing.

The efficiency of the electrowinning process depends on the concentration of metal in the solution. It becomes progressively less efficient as more metal is removed. The surface area of the cathode also affects efficiency. The greater the surface area, the greater the efficiency, which is why electrowinning units have been designed that use large rectangular plates or mesh grids as cathodes. The final variable that affects efficiency is the type of metal being recovered. Metals most commonly recovered by electrowinning include copper, silver, and gold. Cadmium, zinc, and even nickel can also be recovered using this process. Nickel is least common because the solution must be carefully pH-controlled throughout the process in order for it to be effective. Although electrowinning is a useful process, it does have some drawbacks. It becomes very inefficient if the solution has less than 1000 mg of metal ions per liter. Also, it can be used in solutions that contain chlorides, such as hydrochloric acid, but it is less common because electrolysis of chlorine ions can result in chlorine gas, which is extremely hazardous.

### **3.1.3. Cathodic protection using impressed currents**

The cathodic protection can be used to preserve a metal structure by corrosion when it is immersed in an electrolytic solution (sea water, wastewater, soft water, etc.) or in contact with a humid solid matrix (soils, concrete, insulations, etc.). The metal can be covered with protective coatings or not. The protection is realized through an imposed current under

cathodic polarization; an anode is linked with the metal structure of interest through a DC power supply (Fig.3.1).

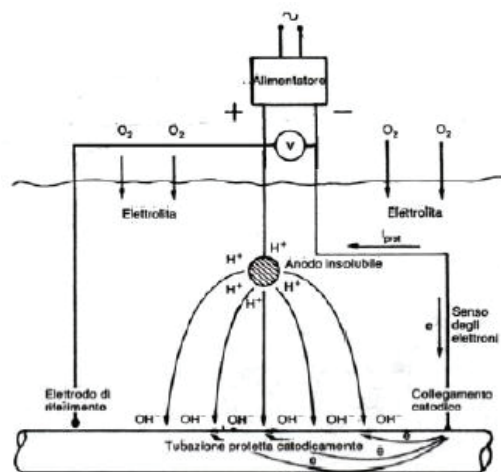


Fig.3.1. Scheme of a cathodic protection plant using impressed currents.

The anode is immersed in the corrosive media (water or soil) few centimeters far from the cathode or tens meters far (remote anode). Commonly used anodes were made of graphite, granular carbon or lead (especially for seawater), but, because of their good stability, the utilization of DSAs<sup>®</sup> has widely increased its diffusion.

### 3.1.4. Incineration of contaminants

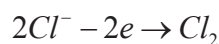
The environmental normative has become extremely rigid in the recent years, this is why this kind of application of DSAs<sup>®</sup> treating organic compounds in soils (electro-remediation) and waters (deuration and sterilization of drinking water) has developed in relative short times. These kind of materials have been proposed for the destructive oxidation of contaminants in industrial effluents [26,27,28,29,30]; it has been show that the oxidation of organics can occur under conditions of simultaneous O<sub>2</sub> evolution [31,32,33], but the incineration is possible also indirectly, exploiting the synthesis of active chlorine via chlorides reduction (undirected method) [34,35,36,37] as discussed in the Par. 3.2.3.

## 3.2. Applications that involve the Chlorine Evolution Reaction

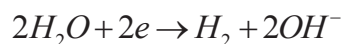
### 3.2.1. Chlor-Alkali industry: Chlorine production [38]

The electrolysis of aqueous sodium chloride, normally brine obtained directly from natural salt deposits, to yield chlorine, sodium hydroxide and hydrogen is the largest of the electrolytic industries. In fact, chlorine is considered as a commodity and it is involved in several processes as reagent for manufacturing products from polymers to drugs. In 2009, 62.8 million metric tons of chlorine was the amount produced all over the world [49], while, in 2011, European chlorine production was nearly 10 million tons. Germany is Europe's largest chlorine producer (43.8%), followed by Belgium/The Netherlands (15.0%), and France (11.0%); these top three regions together accounted for nearly 70% of total European chlorine manufacture in 2011.

The main electrode reaction at the anode is:



And, at the cathode:



Both chlorine and sodium hydroxide (produced at the cathode as consequence of the hydrogen evolution) must be considered to be main products and which is in greater demand varies with time; their utilization is resumed in Tab.3.1. Hydrogen can be used as a chemical (*e.g.* for the hydrogenation of fats), otherwise as a fuel for the power station of the plant.

The chlor-alkali industry is of particular interest for the electrochemical engineering because of three different types of electrolytic processes based on mercury, diaphragm and membrane cells exist side by side and each must be taken into account for evaluating costs, environmental impact, etc.. The first cells were introduced in the 1890s, the last 40 years have seen extensive and notable advances in the technology for minimizing the risks related to mercury (in mercury cells), and for reducing costs associated to power consumption and maintenance.



<p><u>Chlorine</u></p> <ul style="list-style-type: none"> <li>• Manufacture of polyvinylchloride.</li> <li>• Manufacture of polycarbonates and polyurethanes from phosgene.</li> <li>• Preparation of chlorinated organic solvents (methylene chloride, chloroform, carbon tetrachloride, per- and trichloroethylene, 1,1,1-trichloroethane).</li> <li>• Synthesis of other organic compounds (chlorobenzenes, alkyl chlorides, herbicides).</li> <li>• Preparation of fluorocarbons.</li> <li>• Pulp and paper manufacture.</li> <li>• Preparation of inorganic compounds (sodium hypochlorite, titanium tetrachloride, iodine chlorides).</li> <li>• Water treatment.</li> <li>• Army purposes.</li> </ul>
<p><u>Caustic soda</u></p> <ul style="list-style-type: none"> <li>• Synthesis of many organic compounds.</li> <li>• Manufacture of textiles and rayon.</li> <li>• Soap and detergent production.</li> <li>• Oil refining.</li> <li>• Paper and pulp manufacture.</li> <li>• Aluminum extraction.</li> <li>• Manufacture of inorganic compounds (sodium cyanide, sodium salts).</li> </ul>

Tab.3.1. Major uses of chlorine and caustic soda [38].

Some critical aspects are interesting for the process development:

- Robust and cost effective cell design.
- High current densities to minimize capital investment in plant.
- Cell components which are reliable, readily available and have long lifetime.
- Good current efficiency and material yields for both the anode and the cathode reactions. Parasitic reaction contributions should be minimized.
- Minimize the power consumption. In fact, the cell voltage:

Chloride ion is always oxidized in slightly acid solution (about 2) to prevent hydrolysis of chlorine to hypochlorite while the pH at the cathode will be at least 14 (except for the mercury cell).

The reaction kinetic plays a primary role in the energetic balance of the process; not only it is desirable for the overpotentials for the required anode and cathode reactions,  $\eta_A$  and

$\eta_c$ , to be low but it is also necessary for parasitic reactions to be suppressed (the oxygen evolution reaction at the cathode). The stability, the surface area and the exchange current are all fundamental parameters to evaluate performances of an electrocatalyst.

Historically, the anodic material used in chlor-alkali industry has been graphite or some related form of carbon. The overpotential for chlorine evolution was high as 500 mV and the wear rate 5-7 lb per ton of chlorine. There was, during years, some attempt to replace these by a dispersed form of a precious metal, e.g. Pt or Pt/Ir on a titanium base, with a reduction in the overpotential to 100 mV. These anodes were expensive and not sufficiently stable. So, the development in the early 1960s of materials known as dimensionally stable anodes completely undermined carbon electrodes. These materials are titanium-based with a coating of ruthenium or iridium dioxide containing other transition metal oxides, e.g.  $\text{Co}_3\text{O}_4$ ,  $\text{SnO}_2$ ,  $\text{TiO}_2$ , etc. They are both excellent catalysts (5-40 mV for ChlER) and extremely inert, their service life can be of several years. Other companies have developed anodes based on  $\text{PdO}_2$  or  $\text{M}_x\text{Co}_{3-x}\text{O}_4$ . The replacement of carbon by DSA<sup>®</sup> is almost complete and it has reduced the energy requirement of 8-15% (with a decreasing of cell voltage from 2.5-5 V to 0.45 V). Regarding the cathode, in diaphragm cells has been steel where the hydrogen overpotential is about 400 mV, while, in the case of membrane cells it is usually made of nickel or coated titanium. Coatings of Ni alloys present an overpotential around 150-200 mV, and the expectation is to reduce it to 20-50 mV.

Also the geometry of electrodes assumes a primary role because of the gas evolution: some different shape-variants exists for allowing a rapid and facilitated separation of the gas from the surface, minimizing the important ohmic contribution derived from them. The utilization of carbon based devices doesn't permit an easy modification of electrodes because of the mechanic characteristic of the material, and also under these terms, the introduction of DSAs<sup>®</sup> represented an important step forward in this field.

## **3.2.2. Chlorine cell technologies**

### **3.2.2.1. Mercury plants**

In a mercury cell the cathodic electrode reaction, which represents the counter process of the chlorine evolution reaction is:



And the amalgam is then electrolyzed in order to recovery mercury and chemicals of interest ( $H_2$  and  $NaOH$ ):



A typical mercury cell is shown in Fig.3.2. It consists of a large plant of about 15x2x1 m where the about 300 anodes are far about few millimeters from the mercury cathode.

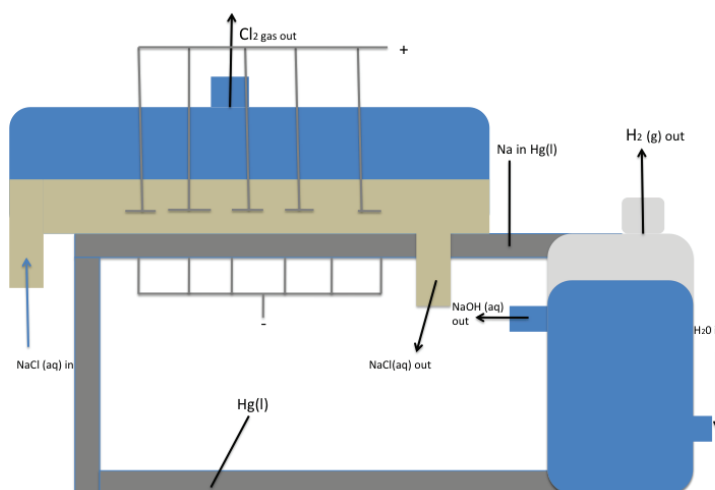


Fig.3.2. Schematic of a typical mercury cell.

The brine concentration used is 35% and the work temperature is  $60^{\circ}C$ ; the brine exits from the cell with a concentration in salt of about 17%, and it is recycled after have reported its concentration to the saturation limit.

The voltage of work is near 4.5 V.

The chlorine gas leaves the cell at the top while the sodium amalgam leaves at the base, and it is conveyed through two washing weirs for removing all sodium chloride and entering into the denuder. The denuder consists of a cylindrical vessel packet with graphite balls impregnated with Fe or Ni, which have the function of catalyze the amalgam decomposition.

### 3.2.2.2. Diaphragm cells

This kind of cell uses a separator between anodes and cathodes based on asbestos mixed with polymers for improving mechanical properties; electrode reactions generate chlorine and sodium chloride directly. Fig.3.3 reports the principle of a diaphragm cell.

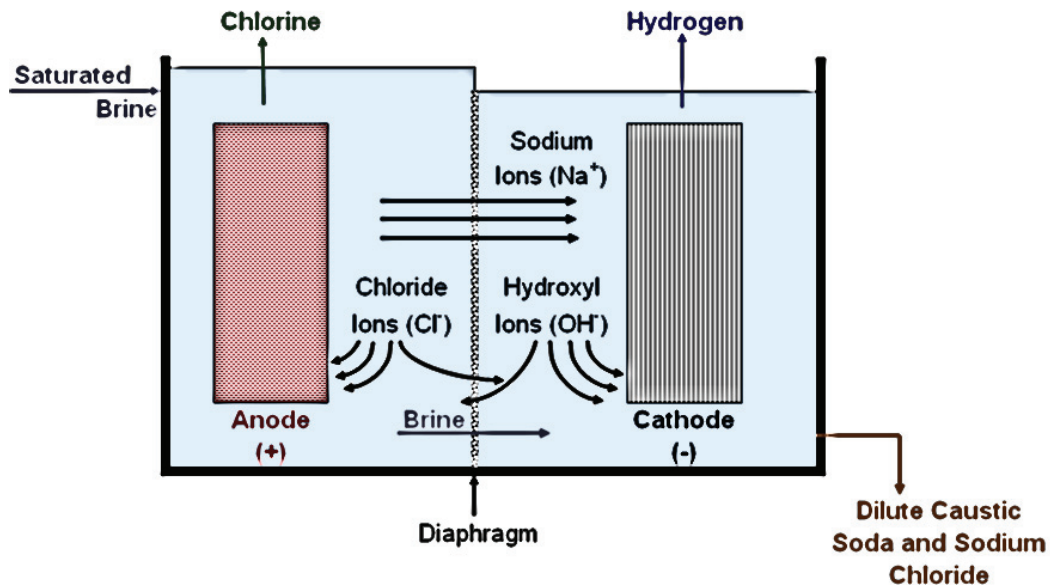


Fig.3.3. Diaphragm cell.

The asbestos is deposited directly on a steel gauze that acts as the cathode; the anode is located close to the diaphragm and the 30-35% brine flows through the cell. Products are collected in the two separate tank. The steel gauze cathode is often covered with a dispersion of a metal catalyst for minimize the energy consumption due to cathodic overpotential. But, the utilization of asbestos diaphragm is affected by several problems:

1. It is a purely a physical barrier and all ions can be subjected to diffusion when a concentration gradient is established. If the production of sodium hydroxide exceeds 10%, diffusion (and migration) of  $\text{OH}^-$  can lead to loss of chlorine by hydrolysis to hypochlorite and to the parasitic reaction of oxygen evolution.
2. The IR drop associated to diaphragm is quite high (about 1.0-1.6 V). Moreover it increases with time because of the deposition of calcium and magnesium hydroxides in the pores; if these cations are contained in the brine.
3. Diaphragm has to be substituted every few months. Various co-polymers can added for increasing its longevity.

### 3.2.2.3. Membrane cells

The approach and the processes involved are the same of the ones described in Par. 3.2.2.2, but the asbestos diaphragm is substituted with a ion-exchange conductive membrane. Membrane cell has represented the most widespread approach since 2007 for producing chlorine, and nowadays it is the most common cell used in chlor-alkali plants.

These kind of plants can work with higher current densities because the low ohmic drop contribution of the membrane (500 mA/cm<sup>2</sup>, respect to 150-300 mA/cm<sup>2</sup> of diaphragm cells), and can produce pure 50% of NaOH because of the selectivity between anions and cations of the electrode separator. Membrane cells are generally made from a series of frames in a filter press arrangement. The scheme of a module is reported in Fig.3.4.

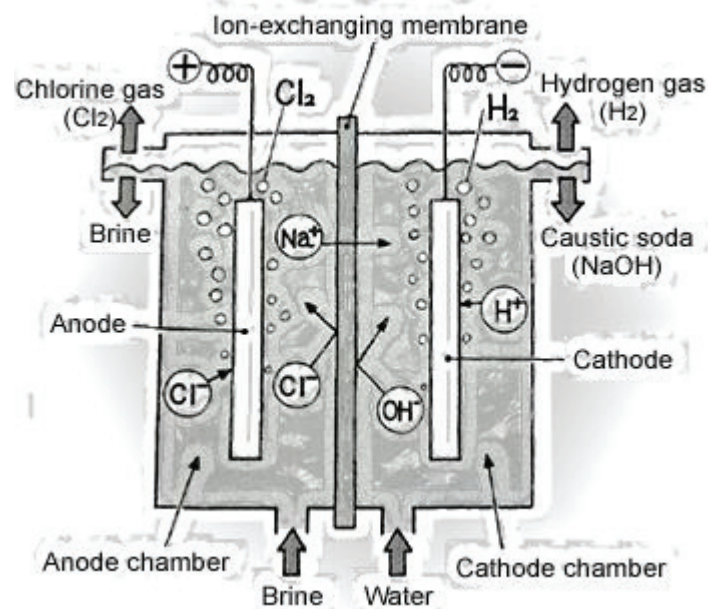


Fig.3.4. Membrane cell. The research on membranes is going on actively and worldwide for improving their performances in terms of chemical and thermal stability and conductivity. Most common membranes used including the family of Nafion<sup>®</sup> and Flemion<sup>®</sup>.

The electrodes are vertical and placed nearby the membrane. Also they are constructed with slits or louvres or from expanded metal in such a way a “gas lift” system is originated that doesn’t permit an accumulation of gas between electrodes.

The plate-and-frame construction is preferred because it is well suited for bipolar electrical connection; the cell current can reach 10 000 A with a required total voltage around 300 V. The energy consumption in a modern membrane cell is about 2400 kWh per produced ton of chlorine; this power consumption can be further reduced to 1600-1700 kWh per ton of Cl<sub>2</sub>, if the cathode is replaced by an oxygen-depolarized cathode in which oxygen is reduced to water in a kind of internal fuel cell [39].

Tab.3.2 reports the most important parameters for recent chlor-alkali plants for each kind of cell.

	Mercury cell	Diaphragm cell	Membrane cell
Cell Voltage / V	-4.4	-3.45	-2.95
Current density / A cm <sup>-2</sup>	1.0	0.2	0.4
Current efficiency for Cl <sub>2</sub> / %	97	96	98.5
Energy consumption / kWh per ton of NaOH			
(a) Electrolysis only	3150	2550	2400
(b) Electrolysis + evaporation to 50% NaOH	3150	3260	2520
Purity Cl <sub>2</sub> / %	99.2	98	99.3
Purity H <sub>2</sub> / %	99.9	99.9	99.9
O <sub>2</sub> in Cl <sub>2</sub> / %	0.1	1-2	0.3
Cl <sup>-</sup> in 50% NaOH / %	0.003	1-1.2	0.005
Sodium hydroxide concentration prior to evaporation / %	50	12	35
Mercury pollution considerations	Yes	No	No
Requirement for brine purification	Some	More stringent	Very extensive
Production rate per single cell / tons NaOH per year	5000	1000	100
Land area for plant of 10 <sup>5</sup> tons NaOH per year/m <sup>2</sup>	3000	5300	2700

Tab.3.2. General data for Chlor-alkali plants [38].

In recent years, current densities of about 6.0 A m<sup>-2</sup> have been reached in membrane electrolyzers.

Membrane cells may well meet all the requirements of the market, and the mercury cells have fallen into obsolescence for reasons of environmental hazards and power consumption costs. The past forty years has seen continuous changes and improvements in the chlor-alkali industry based on achievements in developing low-overpotential anodes and cathodes, membranes and new control strategies, but the membrane cells appears the most convenient approach in chlor-alkali plants.

### **3.2.3. Water disinfection**

For water treatment, particularly for water disinfection purposes, a process called anodic oxidation, electrochemical disinfection or electrochemical treatment is frequently used; it is believed that the main disinfecting agent in this process is the hypochlorite ion and hypochlorous acid produced from the naturally occurring chloride ions in the processed water [40,41,42]. The chloride content in naturally derived water and drinking water can vary significantly between values as low as about 10 ppm to 250 ppm or more. The process of electrochemical disinfection has several advantages over other more common processes of water disinfection; compared to the processes such as chlorination by the use of gaseous chlorine or concentrated hypochlorite solution, no addition of chemicals is necessary (and the hazard correlated to these substances is avoided). Ozonization and especially ultraviolet irradiation can be very effective at the point of use but provide no residual disinfection capacity. The devices used for this application can be divided in two categories: direct electrolyzers and generator of oxidant mixtures. The first type of device is directly interfaced with the contaminated water, while the second kind is used for producing a high concentration solution of oxidant (anolyte) from a concentrated chloride solution that is used as disinfectant, producing strong oxidants as  $\text{ClO}^-/\text{HClO}$ ,  $\text{H}_2\text{O}_2$  and other “short living” species.

### **3.2.4. Treatments for agriculture and food industry**

Every food product must satisfy strict regulations imposed by local governments in order to protect the consumer. Among the characteristics that have to be monitored there are toxicity, nutritional details, the use of preservatives, the presence and the amount of microorganisms, treatments of sterilization or disinfection used, etc.. Some of the critical points are the preservation and the disinfection of foods, aspects that are particularly important in the case of fresh foods such as meat, fruits and vegetables [43,44,45,46]. Disinfection is equally important in the treated products, but once this phase is successful, the most serious problem is to choose the conservation process to keep the food microbiologically wholesome.

A well-known technique for the elimination of pathogens is the pasteurization, which is usually applied to liquid foods such as milk and fruit juices; another solution involves the reduction of water activity, which can be obtained by the addition of significant quantities of sugar or salt in foods. Even the dehydration of fruits and vegetables is a drastic method for

decreasing water activity; further way involves the addition of chemicals such as chlorine, chlorine derivatives and antibiotics.

The chlorine and its derivatives are used for the food disinfection; sodium hypochlorite is used for the sterilization of fruits and vegetables, but also the seeds, treatment of the latter with sodium hypochlorite reduces the losses caused by pathogens during the germination process that has no side effects, the only problem is that the products are susceptible to reinfection. Hypochlorite solutions are also used as extra treatment for the elimination of infections due to fungi and mycotoxins, this type of infection takes place on water-rich foods, such as bread and cereals. To avoid internal infections due to fungi, is usually used a disinfectant that removes the mycoflora from the surface; studies carried out on naturally infected cereals and fruits rich in water have shown that the contact between the food and a hypochlorite solution, having a concentration comprised between 0.4 and 2% for 2 minutes, is sufficient to ensure disinfection of the treated surfaces. Recently, this technology has also been extended to the disinfection of seeds, meat, trees and containers (bottles) for drinks. In Brief Summaries of Papers and Reports of the Second International Symposium on Electrochemical Activation in Medicine, Agriculture and Industry (Moscow 1999) it is possible to find examples regarding the utilization of innovative devices for production of active anolytes and catholytes. The devices for disinfection of food produce oxidizing solutions (anolytes) that contain hypochlorite, hypochlorous acid, chlorine dioxide and, in some cases, ozone.

### **3.2.5. Sterilization of water used for medical purposes**

The quality and the characteristics of water utilized for medical purposes must be optimal obviously.

The conventional method is based on the heating of the water at high temperatures, in order to kill harmful microorganisms. Unfortunately, this treatment is not able to eliminate spores and fungi, and, for this reason, alternative solutions must be taken in consideration. Moreover, the electrochemical methods have been proposed both for disinfection and for direct and indirect approaches; the indirect treatment is the most used, and it consists of the use of anolyte. Commercially, there are different types of devices, which operate on the same principle; the solutions of chlorine based oxidants are able to eliminate all harmful organisms. The solutions show efficiency already at concentrations of 20-50 mg/l.

The anolyte is used for the prevention and treatment of diseases [47,48].



## Bibliography

1. B.E. Conway, B.V. Tilak, in: D.D. Eley, H. Pines, P.B. Weisz (Eds.), *Advances in Catalysis*, Academic Press, San Diego CA **38**, 3 (1992).
2. S. Trasatti (Ed.), *Electrodes of Conductive Metallic oxides*, part B, Elsevier, Amsterdam (1981).
3. H.B. Beer US Patent *US549194*, 1966; *US710551*, 1968.
4. M.D. Spasojevic, N.V. Krstajic, M.M. Jaksic, *J. Res. Inst. Catalysis* **31**, 77 (1983).
5. S. Trasatti, *Electrochim. Acta* **29**, 369 (1984).
6. A. De Battisti, G. Lodi, M. Cappadonia, G. Battaglin, R. Kotz, *J. Electrochem. Soc.* **136**, 2596 (1989).
7. S. Ardizzone, A. Carugati, S. Trasatti, *Jour. of Electroanal. Chem.* **126**, 287 (1981).
8. M.P.C. Wijnen, A.A.H. Drinkenburg (Eds.), *Precision Process Technology*, Kluwer, Netherlands, 681-688 (1993).
9. G.N. Martelli, R. Omelas, G. Faita, *Electrochem. Acta* **39**, 1551 (1994).
10. O. De Nora, A. Nidola, G. Trisoglio, G. Bianchi, British Patent I 399576 (1976).
11. J. Kristof, J. Mink, *Electrochim. Acta* **39**, 1531 (1994).
12. A. Benedetti, P. Riello, G. Battaglin, A. Barbieri, *J. of Electroanal. Chem.* **376**, 195 (1994).
13. A.J. Terezo, E.C. Pereira, *Electrochim. Acta* **45**, 4351 (2000).
14. G.P. Vercesi, J.Y. Salamin, C. Comninellis, *Electrochim. Acta* **36**, 991 (1991).
15. C. Comninellis, G.P. Vercesi, *Journ. of Appl. Electrochem.* **21**, 335 (1991).
16. H.B. Beer, *J. electrochem. Soc.* **127**, 303 (1980).
17. F. Hine, M. Yasuda, T. Noda, T. Yoshida, J. Okuda, *J. electrochem. Soc.* **126**(9), 1439 (1979).
18. R. Manoharan, J.B. Goodenough, *Electrochim. Acta* **36**, 19 (1991).
19. R.S. Yeo, J. Orehtsky, W. Visscher, S. Srinivasan, *J. Electrochem. Soc.* **128**(9), 1900 (1981).
20. O. De Nora, G. Bianchi, A. Nidola, G. Trisoglio, Patent US 3 878 083 (1975).
21. V.V. Shalaginov, d.M. Shub, N.V. Kozlova, V.M. Lomova, *Elektrokhimiya* **19**, 537 (1983).
22. E.A. Kalinovskii, E.M. Shembel, V.V. Stender, *Elektrokhimiya* **8**, 819 (1972).
23. S. Trasatti, *Electrochim. Acta* **32**, 369 (1987).
24. M. Pourbaix, N. de Zoubov, J. Van Muylder, *Atlas d'équilibres électrochimiques*, Gauthier-Villars & C<sup>ie</sup> Ed., cap. 4, 590 (1963).

25. D. Pletcher, *Industrial Electrochemistry*, Chapman & Hall, pp.114-127 (1982); D. Pletcher, *Industrial Electrochemistry*, Chapman & Hall, pag.172 (1982).
26. C. Comninellis, C. Pulgarin, *Journ. of Appl. Electrochem.* **23**, 108 (1993).
27. C. Comninellis, *Electrochim. Acta* **39**, 1857 (1994).
28. C. Comninellis, A. De Battisti, *J. Chim. Phys.* **93**, 673 (1996).
29. C. Comninellis, E. Plattner, C. Seigne, C. Pulgarin, P. Péringier, *Swiss Chem.* **14**, 25 (1992).
30. C. Comninellis, A. Nerini, *Journ. of Appl. Electrochem.* **25**, 23 (1995).
31. O. Simond, C. Comninellis, *Electrochim. Acta* **42**, 2013 (1997).
32. O. Simond, V. Schaller, C. Comninellis, *Electrochim. Acta* **42**, 2009 (1997).
33. G. Fòti, D. Gandini, C. Comninellis, *Cur. Top. Electrochem.* **5**, 71 (1997).
34. F. Bonfatti, A. De Battisti, S. Ferro, G. Lodi, S. Osti, *Electrochim. Acta* **46**, 305 (2000).
35. F. Bonfatti, S. Ferro, F. Lavezzo, M. Malacarne, G. Lodi, A. De Battisti, *Journ. of the Electrochem. Society* **147**, 592 (2000).
36. C.M. Martinez-Huitle, S. Ferro, A. De Battisti, *Electrochem. and Solid State Lett.* **8**, D35 (2005).
37. C.A. Martínez-Huitle, S. Ferro, S. Reyna, M. Cerro-López, A. De Battisti, M.A. Quiroz, *J. Braz. Chem. Soc.* **19**, 150 (2008).
38. D. Pletcher, *Industrial Electrochemistry*, Chapman & Hall, pp. 88-113 (1982).
39. F. Gestermann, A. Ottaviani, *Modern Alkali Technology* **8**, 49 (2001).
40. G.E. Stoner, G.L. Cahen Jr., M. Sachyani, E. Gileadi, *Bioelectroche. Bioenerg.*, **9**, 229-243 (1982).
41. G. Paternarakis, E. Foutoukidis, *Wat. Res.* **24**, 1491-1496 (1990).
42. M. Borneff, *Gwf-wasser/abwasser* **122**, 141-146 (1981).
43. Anon, *Food Eng.* **42** (1), 115 (1970).
44. Bartz J.A., Lill R.E., *Plant Dis.* **12** (1), 9 (1988).
45. Endemann G. E. F., *S. Afr. Citrus. J.* **422** (21), 23 (1969).
46. Goodin P.L., *Agri. Res.* **26** (4), 8 (1977).
47. Melnikova V. M., Belikov G. P., Loktionova N. V., Bakhir V. M., Sukhova O. I., *Bulletin of Vinnitsa State Medical University* **2**, 327 (2000).
48. Kavruk L. S., Ziborova Y. A., *Veterinarnyi Konsultant* **23**, 6 (2002).
49. Chemical Week, May 25, 2009.2.
50. S. Trasatti, *Electrochim. Acta* **45**, 2377 (2000).

## 4. Preparation Methods used for Metal Oxide coated electrodes

With the research progress achieved on metal oxide based materials in the last 40 years, several new standard procedures have been developed to improve the deposition and the characteristics of the coated electrode [1,2,3,4,5], hence minimizing costs and synthesis time. The most conventional methods, which are based on the pyrolysis of salty precursors, will be reviewed and discussed in next Section Par.4.1.

Furthermore, new and innovative synthesis processes, such as sputtering technique which belongs to the group of the Physical Vapor Depositions (PVD) [6], will be also highlighted in Section 4.2. Particularly, PVD methods offer several advantages with respect to the pyrolysis-based treatments, in terms of composition and morphological control. Therefore, a systematic study on PVD synthesis will allow for a better understanding of the electrode characteristics and performance.

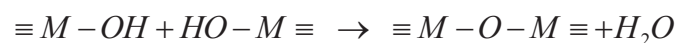
### 4.1. Sol-Gel method

The Sol-Gel process can be defined as the conversion of a precursor solution into an inorganic solid compound through a chemical reaction. The starting compound is often an inorganic metal salt (acetate, nitrate, chloride, sulfate, etc.) or an organic specie as metal alkoxide. Metal alkoxides are probably the most diffused precursors in aqueous Sol-Gel method and their chemistry is well known. Fig.4.1 reports the steps of the process: in the first step, the metal alkoxide is transformed into a sol (dispersion of colloidal particles in a liquid), which reacts further to a gel, an interconnected, rigid and porous inorganic network enclosing a continuous liquid phase. The conversion involves two main process: hydrolysis and condensation.

#### Hydrolysis



#### Condensation:



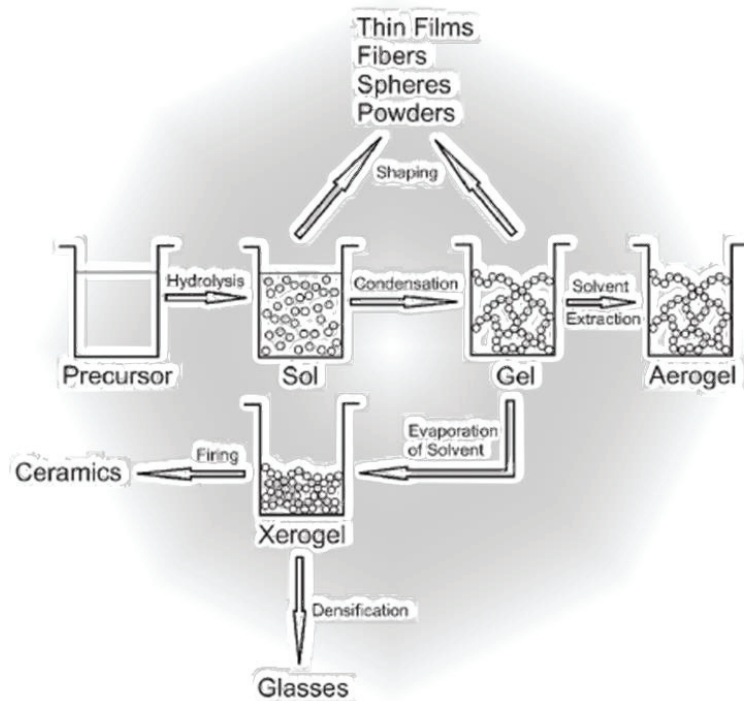


Fig.4.1. Schematic of Sol-Gel process for obtaining a ceramic or a glassy material.

During the hydrolysis, the alkoxide groups (-RO) are replaced through the attack of a nucleophilic oxygen atom of water molecule under the release of an alcohol and the formation of the metal hydroxide. Condensation reaction between two hydroxylated species leads to a M-O-M bond, whereas the reaction between a hydroxide and an alkoxide leads to the same species but under release of an alcohol. The aqueous Sol-Gel process is studied from several years and the illustrated reactions that can occur may produce several kind of different compounds, with the result that this technique is not easily controllable. One of the advantage of this approach, in addition to be easy to apply and quite cheap, is the fact that sol or gel can be shaped in the desired form (monoliths, films, fibers, monosized powders) before the heating treatment that leads to a ceramic substance [7].

#### 4.1.1. Historical notions on Sol-Gel method

The first metal precursor was synthesized by Ebelmen starting from  $\text{SiCl}_4$  [8]. He noted that a gelation process occurs if it was maintained in contact with air for long times. Geffcken [9] in 1930s recognized that alkoxides could be used for preparing oxide films. This process was then studied and optimized from the Schott glass company in Germany [10] because of its interest in the applicative field. Several and, in some cases, contradictory theories on gel structure regarded the gel as a coagulated sol with each of the particles

surrounded by a layer of bound water, or as an emulsion. The network structure of silica was accepted in 1930s largely through work of Hurd [11], who evidenced the existence of a solid structure where empty spaces are filled with a continuum liquid phase. The process to obtain Aerogel using a supercritical extraction was developed from Kistler [12] in 1932, who further demonstrated the existence of a solid skeleton. Later the process became interesting also for mineralogist in order to study the phase-equilibria. The ceramic industry became interested in gels only in the late '60s; controlled hydrolysis and condensation of alkoxide compounds were depth investigated by Levine, Thomas and Dislich [13,14].

As usual, the technology on Sol-Gel have preceded the science, and the publications about the method started to increase around '80-'90 and some critic doubts and question marks exists in this branch.

#### 4.1.2. Importance of precursors: Hydroxo-Chloro Aceto complexes

Reviewing the literature on the dimensionally stable anodes preparative, it is possible to find a large quantity of different kinds of precursors used dependently on the oxide that has to be deposited. They consist usually in salts such as chlorides, nitrates, sulphates, etc. dissolved in aqueous or non-aqueous solutions (alcohols in particular). The Tab.4.1 below summarized the most widely used.

<i>Oxide</i>	<i>Precursors</i>
RuO <sub>2</sub>	RuCl <sub>3</sub> ·xH <sub>2</sub> O, Ru(NO)(NO <sub>3</sub> ) <sub>3</sub>
IrO <sub>2</sub>	IrCl <sub>3</sub> ·xH <sub>2</sub> O, H <sub>2</sub> IrCl <sub>6</sub> ·6H <sub>2</sub> O
MnO <sub>2</sub>	Mn(NO <sub>3</sub> ) <sub>2</sub> ·4H <sub>2</sub> O
Co <sub>3</sub> O <sub>4</sub>	Co(NO <sub>3</sub> ) <sub>2</sub> ·6H <sub>2</sub> O, CoCO <sub>3</sub> ·xH <sub>2</sub> O
NiO	Ni(NO <sub>3</sub> ) <sub>2</sub> ·6H <sub>2</sub> O
TiO <sub>2</sub>	TiCl <sub>3</sub> , TiCl <sub>4</sub> , Ti(OR) <sub>4</sub>
SnO <sub>2</sub>	SnCl <sub>2</sub> ·2H <sub>2</sub> O, SnCl <sub>4</sub>
PdO <sub>x</sub>	PdCl <sub>2</sub>
PtO <sub>x</sub>	H <sub>2</sub> PtCl <sub>6</sub> ·xH <sub>2</sub> O
RhO <sub>x</sub>	RhCl <sub>3</sub> ·xH <sub>2</sub> O
ZrO <sub>2</sub>	ZrCl <sub>4</sub> , ZrOCl <sub>2</sub> , ZrO(NO <sub>3</sub> ) <sub>2</sub>

Tab.4.1. Summary table for the common precursors used in the thermal synthesis of metal oxide based materials.

Morozov, De Battisti and Ferro in collaboration with Industrie De Nora S.p.A. [15] patented in 2010 an aqueous tin-based precursor for Sol-Gel deposition, which led to significant tin-enrichment of the Sol-Gel sample, by reducing the volatility of the precursors. The precursor consisted of a chloro-hydroxo-aceto complex (M-HAC) which detailed stoichiometry is still not well defined:



Where M represents the metal atom. Furthermore, this procedure offered further advantages, such as:

- The matrix is an aqueous solution (health safety, etc.).
- It consists of a suspension of a solid in a liquid and the concentration of the system can be increased up to 1-2 mol/l.
  - Less paint layers are necessary to reach a high thickness of the film deposited.
  - More control in reproducibility and homogeneity in the samples prepared.
  - Minimization of costs related to the time consumption for the manufacture of a device.

In relation to the advantages proposed, precursors of the same nature based on iridium and titanium were prepared and used in this thesis work. RBS analyses provided information to gain insights of the thickness of the deposited samples. At first, several depositions were done on polished titanium supports that have been analyzed in cross section using SEM (an example is reported in Fig.7). This procedure was carried out in order to estimate the thickness of the coating deposited respect to the paint layers applied on supports. We attested that working with solutions 0.755 M in Ir-HAC and 2 M in Ti-HAC, a deposit of 2 micrometers of thickness can be produced using 6 paints layer and, obviously, 3 paint layers are sufficient for reaching about 1 micrometer. The minimal standard deviation associated with this kind of preparation cannot be limited below 0.5 micrometers.

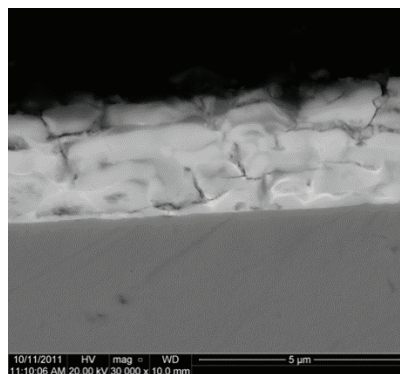


Fig.4.2. Cross section SEM image of a IrO<sub>2</sub>-TiO<sub>2</sub> 1:2 mol (fired at 350 °C) film deposited on a titanium support obtained with six paint layers of precursor. Average thickness of deposits: 2.59 ± 0.55 μm.

For few kind of analysis (such as few RBS and ERDA experiments described in the following parts of this work), less thick films were required. To obtain deposits of hundreds of nanometers, a dilution of the starting precursor solution was done. To ensure that the nature of the hydroxo-chloro-complexes does not change with a dilution of the solution provoking phenomena of strange hydrolysis of salts, few UV-Vis spectra were collected for IrHAC and TiHAC applying strong dilution ratio using a 10% solution of acetic acid (Fig.4.3).

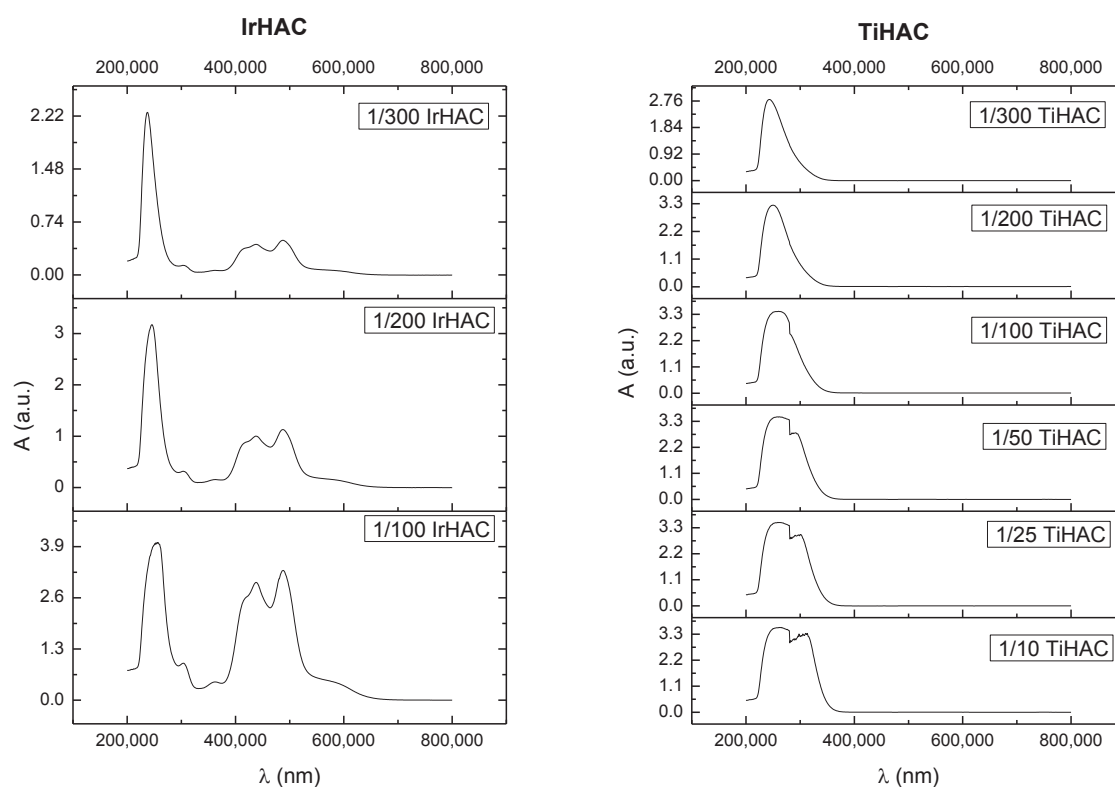


Fig.4.3. UV-Vis spectra collected for IrHAC (on the left) and TiHAC (on the right) diluted in different ratios (from 1/10 to 1/300 in one case, and from 1/10 to 1/300 in the other one) with a 10% solution of  $\text{CH}_3\text{COOH}$ .

Is easy to see that the characteristic spectra for both compounds do not change their after the dilution except for the intensity of peaks, ensuring the preservation of the nature of the compounds.

SEM image on Sol-Gel samples shows, in general, “cracked-mud” patterns (Fig.4.4).

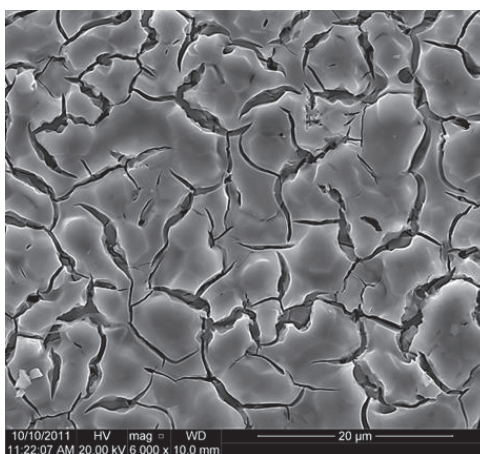


Fig.4.4. Typical “cracked-mud” surface of a Sol-Gel sample well visible through SEM.

De Battisti and coworkers [16] demonstrated that the formation and decomposition of various types of surface species during the film growth, can have a significant effect on the morphology (specific surface area, porosity, roughness) of the samples, thereby influencing the electrocatalytic performances. In addition to the main reaction (formation of oxide phases) via the conversion of the chloride precursors, is accompanied by side reactions (formation and decomposition of surface complexes), which can favor the formation of cracks along the surface.

## 4.2. Physical Vapor Deposition [17]

Physical Vapor Deposition (PVD) includes a variety of vacuum deposition and it is a general term used to describe any of a multiplicity of purely physical methods used to deposit thin films by the condensation of a vaporized form of the material onto various surfaces.

All deposition processes, and specifically for PVD, consist of three major steps:

- Generation of the deposition species (from an appropriate source).
- Transport of the species from the source to substrate where various flow regimes can apply.
- Film growth on the substrate.

Among the many variants of PVD the most used are:

**Evaporative deposition** – A thermal evaporator uses an electric resistance heater to melt the material and raise its vapor pressure to a useful range. The process is carried out in vacuum conditions in order to maximize the efficiency of the deposition, and to reduce accumulation



of impurities derived from residual gas in the chamber. The limitation is represented by the fact that only materials with a much higher vapor pressure than heating element can be deposited without contamination on the film.

**Electron beam physical vapor deposition** – An electron beam evaporator produces a high-energy beam from an electron gun to evaporate a small spot of material; since the heating is not uniform, lower vapor pressure materials can be deposited. Typical deposition rates for electron beam evaporation range from 1 to 10 nanometers per second.

**Sputter deposition** – A plasma (usually a noble gas, such as Argon) is generated and utilized for knocking a “target” in order to catch off few atoms at a time. The target can be kept at a relatively low temperature, since the process is not an evaporation, making this one of the most flexible deposition techniques. It is especially useful for compounds or mixtures, where different components would otherwise tend to evaporate at different rates. Note, sputtering step coverage is more or less conformal. In reactive sputtering, amounts of gas as oxygen and nitrogen are mixed with the plasma-forming gas. After the material is sputtered from the target, it reacts with this gas, so that the deposited film is of different nature.

**Cathodic Arc deposition** – It belongs to the family of ion beam depositions where an electrical arc is created that blasts ions from the cathode. The arc has extremely high power density resulting in a high level of ionization (30-100%), multiply charged ions, neutral particles, clusters and macro-particles (droplets). Compound film can be deposited through the utilization of reactive gas introduced during the preparation procedure.

**Pulsed laser deposition** – A focused laser light vaporizes the surface of the target material and convert it to plasma; plasma usually reverts to a gas before it reaches the substrate. The technique has the advantages of good control and reproducibility. It is an excellent tool for high-value-added structures and research purposes, but it is not widely used for industrial coatings due to high cost and low average deposition rates.

#### **4.2.1. Sputter deposition**

If an energetic particle strikes a surface (the target), atoms of material can be released, and, then, they deposit onto a “substrate”, *e.g.*, a silicon wafer or a metallic support. This

effect is known as “sputtering”. The source of the ions might either be a local plasma (diode or planar magnetron sputtering) or a separate ion beam source (ion beam deposition). The ejected particles are characterized by a wide range of energy distribution and only about 1% of them is ionized (Fig.4.5). The entire range from high-energy ballistic impact to low-energy thermalized motion is accessible by changing the background gas pressure. The sputtering gas is often an inert gas such as argon. Many parameters can be varied for controlling the sputtering deposition for obtaining a better control of growth and microstructure of films.

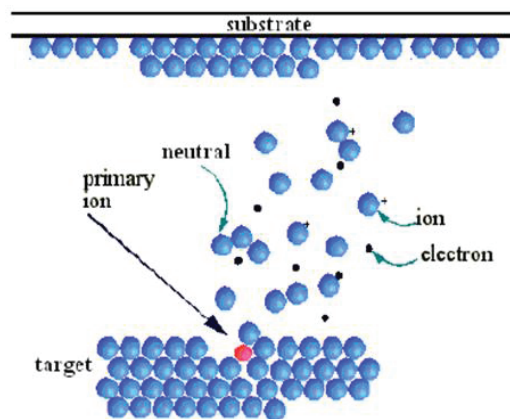


Fig.4.5. Scheme of Sputtering phenomena.

Sputtering is used extensively in the semiconductor industry to deposit thin films of various materials in integrated circuit processing. Thin antireflection coatings on glass for optical applications are also deposited by sputtering. Because of the low substrate temperatures used, sputtering is a good method to deposit contact metals for thin-film transistors. Sputtering is also used as the process to deposit the metal (Aluminum) layer during the fabrication of CD and DVD discs. Hard disks surfaces use sputtered  $\text{CrO}_x$  and other sputtered materials. Efficient photovoltaic solar cell fabrication utilizes sputtering. Sputtering is one of the main processes for manufacturing optical waveguides. One of the most important feature of this technique concerns the independence of sputtering process to the melting point of targets; so, also high-boiling materials can be handle without particular problems.

## 4.2.2. Alloys

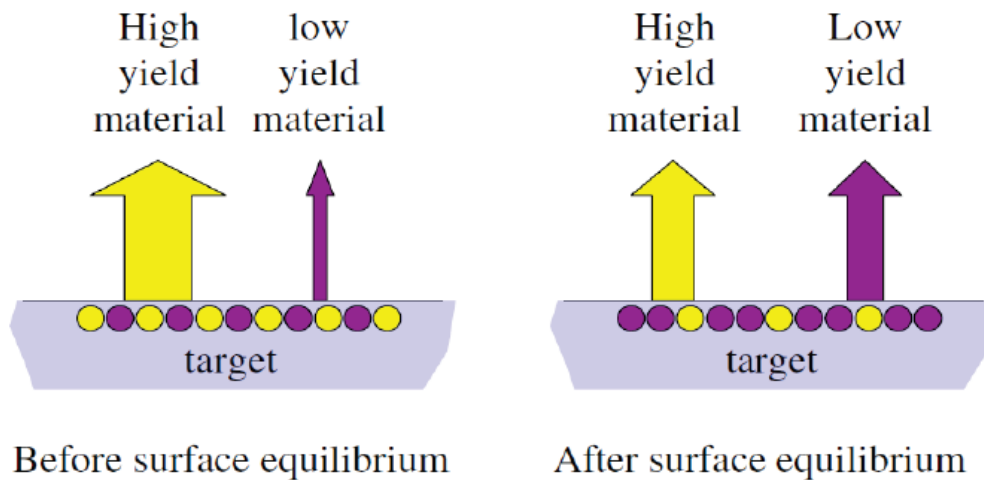


Fig.4.6. Sputtering phenomena on an alloy.

The different sputtering yield of different atoms is dependent on different mass of target atoms. In general there are no problem of adhesion on the substrate.

Sputtering sources contain no hot parts (to avoid heating they are typically water cooled) and are compatible with reactive gases such as oxygen. Sputtering sources are usually magnetrons that utilize strong electric and magnetic fields to trap electrons close to the surface of the magnetron, which is known as the target. The electrons follow helical paths around the surface than would otherwise occur. The extra ions created as a result of these collisions leads to a higher deposition rate. It also means that the plasma can be sustained at a lower pressure. The sputtered atoms are neutrally charged and so are unaffected by the magnetic trap. Charge build-up on insulating targets can be avoided with the use of RF sputtering works well to produce highly insulating oxide films but only with the added expense of RF power supplies and impedance matching networks.

The technique used in this work of thesis for manufacturing oxide based coatings is called reactive sputtering. In this case, the film is generated by reactions among target species in plasma and the support gas (usually  $O_2$ ,  $N_2$ ,  $NH_3$ , *etc.*) introduced in the vacuum chamber besides Ar.

The composition of the film can be controlled by varying the relative pressures of the inert and reactive gases. Also a control in film stoichiometry can be obtained and, of course, it can open the possibility to apply the technique for several preparations.

### 4.2.3. Physical Basic Phenomena

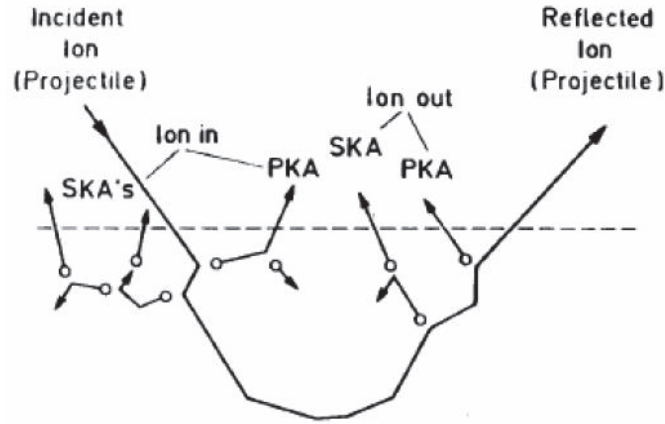


Fig.4.7. Distinction of four different processes leading to sputtering. PKA: primary knock-on atom; SKA: secondary knock-on atom. “Ion in” means the projectile is moving into the solid at the collision; “Ion out” means that the projectile has been backscattered in the solid and is moving back towards the surface.

The sputtering yield can be calculated using the following semi-empirical formula [18].

$$Y(E) = 0.042 \frac{Q\alpha^* (M_2 / M_1)}{U_s} \frac{S_n(E)}{1 + \Gamma k_e \varepsilon^{0.3}} \left[ 1 - \sqrt{\frac{E_{th}}{E}} \right]$$

Where:

$$\Gamma = \frac{W}{1 + (M_1 / 7)^3}$$

$$k_e = 0.079 \frac{(M_1 + M_2)^{3/2}}{M_1^{3/2} M_2^{1/2}} \frac{Z_1^{2/3} Z_2^{1/2}}{(Z_1^{2/3} + Z_2^{2/3})^{3/4}}$$

$$\alpha^* = \begin{cases} 0.0249(M_2 / M_1)^{0.56} + 0.0035(M_2 / M_1)^{1.5} & \text{for } M_1 \leq M_2 \\ 0.0875(M_2 / M_1)^{-0.15} + 0.165(M_2 / M_1) & \text{for } M_1 > M_2 \end{cases}$$

The threshold energy is calculated as:

$$\frac{E_{th}}{U_s} = \begin{cases} \frac{6.7}{\gamma} & \text{for } M_1 \geq M_2 \\ \frac{1 + 5.7(M_1 / M_2)}{\gamma} & \text{for } M_1 < M_2 \end{cases}$$

$U_s$ = surface binding energy= heat of sublimation;  $E_{th}$ = sputtering threshold energy;  $M_1$  and  $M_2$ = masses of incident and target particles, respectively;  $Z_1$  and  $Z_2$ = atomic numbers of incident and target particles, respectively;  $\gamma = 4M_1M_2/(M_1+M_2)^2$  is the energy transferred in a zero impact parameter collision.

The energy dependent nuclear stopping cross section,  $S_n(E)$ , can be calculated with the analytical function developed by Lindhard.

$$S_n(E) = 84.78 \frac{Z_1 Z_2}{(Z_1^{2/3} Z_2^{2/3})^{1/2}} \left( \frac{M_1}{M_1 + M_2} \right) s_n(\varepsilon)$$

Calculating the nuclear stopping cross section requires calculation of the reduced elastic cross section, which is a function of the reduced energy. The reduced energy,  $\varepsilon$  is given by:

$$\varepsilon = \frac{0.03255}{Z_1 Z_2 (Z_1^{2/3} Z_2^{2/3})^{1/2}} \left( \frac{M_1}{M_1 + M_2} \right) E$$

The reduced elastic cross section can be calculated with the analytical expression:

$$s_n(\varepsilon) = \frac{3.441 \sqrt{\varepsilon} \ln(\varepsilon + 2.718)}{1 + 6.355 \sqrt{\varepsilon} + \varepsilon(-1.708 + 6.882 \sqrt{\varepsilon})}$$

The fit parameters, Q, W and s are function of  $Z_2$  and are tabulated in Yamamura and Tawara's table reported below (Tab.4.2).

target	Z	$U_e$ (eV)	Q	W	s
Be	4	3.32	1.66	2.32	2.5
B	5	5.77	2.62	4.39	2.5
C	6	7.37	1.70	1.84	2.5
Al	13	3.39	1.0	2.17	2.5
Si	14	4.63	0.66	2.32	2.5
Ti	22	4.85	0.54	2.57	2.5
V	23	5.31	0.72	2.39	2.5
Cr	24	4.10	0.93	1.44	2.5
Mn	25	2.92	0.95	0.88	2.5
Fe	26	4.28	0.75	1.20	2.5
Co	27	4.39	1.02	1.54	2.5
Ni	28	4.44	0.94	1.33	2.5
Cu	29	3.49	1.0	0.73	2.5
Ge	32	3.85	0.59	2.08	2.5
Zr	40	6.25	0.54	2.50	2.8
Nb	41	7.57	0.93	2.65	2.8
Mo	42	6.82	0.85	2.39	2.8
Ru	44	6.74	1.31	2.36	2.5
Rh	45	5.75	1.14	2.59	2.5
Pd	46	3.89	0.85	1.36	2.5
Ag	47	2.95	1.08	1.03	2.8
Sn	50	3.14	0.47	0.88	2.5
Tb	65	4.05	0.90	1.42	2.5
Tm	69	2.42	0.65	0.85	2.5
Hf	72	6.44	0.65	2.25	2.5
Ta	73	8.1	0.56	2.84	2.8
W	74	8.9	0.72	2.14	2.8
Re	75	8.03	1.03	2.81	2.5
Os	76	8.17	1.11	2.86	2.5
Ir	77	6.94	0.96	2.43	2.5
Pt	78	5.84	1.03	3.21	2.5
Au	79	3.81	1.08	1.64	2.8
Th	90	6.2	0.63	2.79	2.5
U	93	5.55	0.66	2.78	2.5

Tab.4.2. Yamamura and Tawara's table for each target.

Fig.4.8 underlines the dependence of the sputter deposition yield from the projectile, from the target considered, from the angle of the ion beam and, obviously, from the energy that is impressed to the projectile.

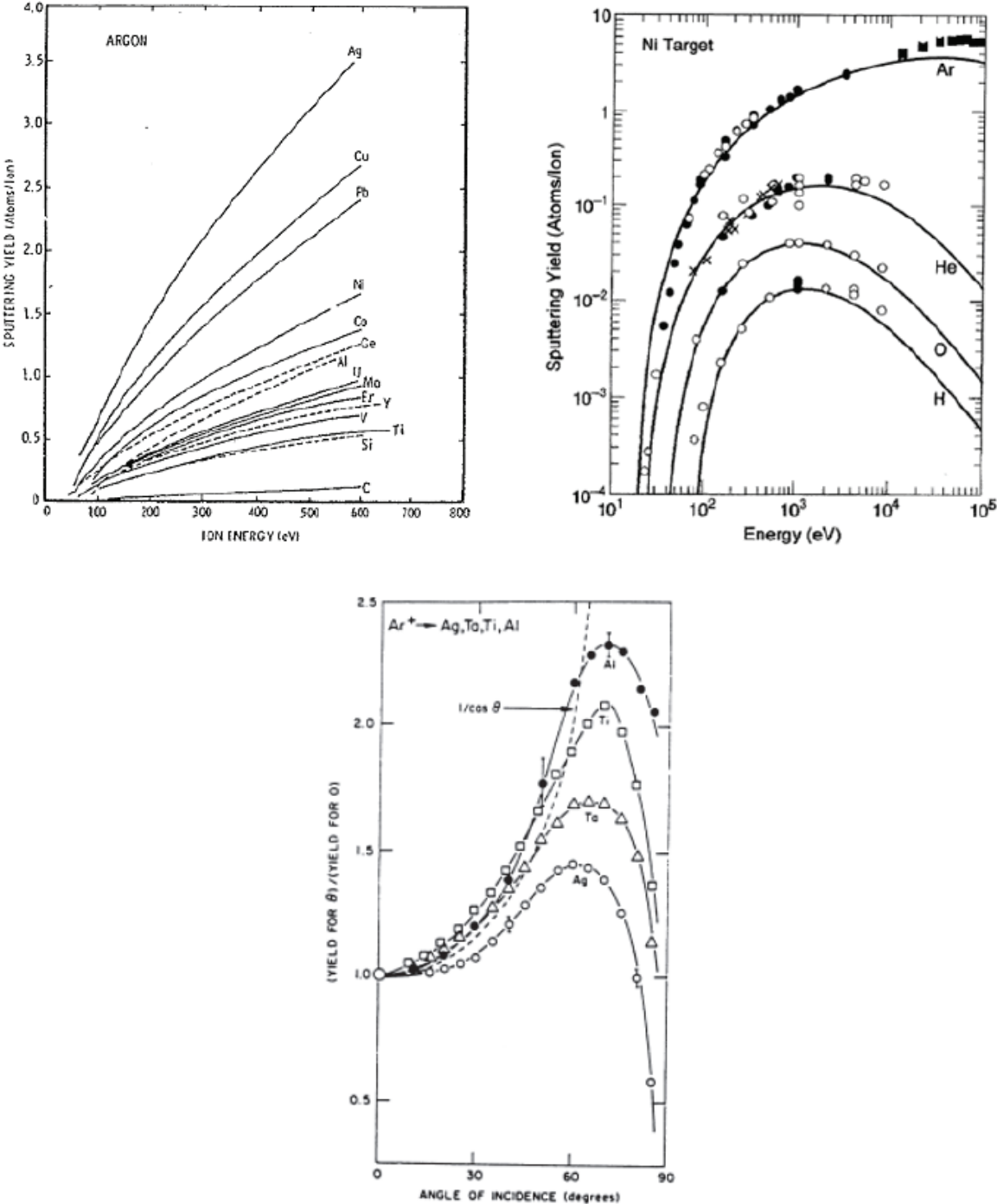


Fig.4.8. Dependence of the sputtering yield Vs. Ion Energy for different target (up-left, the ion beam is constituted of Ar) and for different Ion beam (up-right) Sputtering yield in function of the angle of incidence of the ion beam using different projectile (down).

The mean energy of the ion beam is of the order of tens of eV's: much higher than that of evaporated atoms, with implications on adhesion and density of sputtered films.

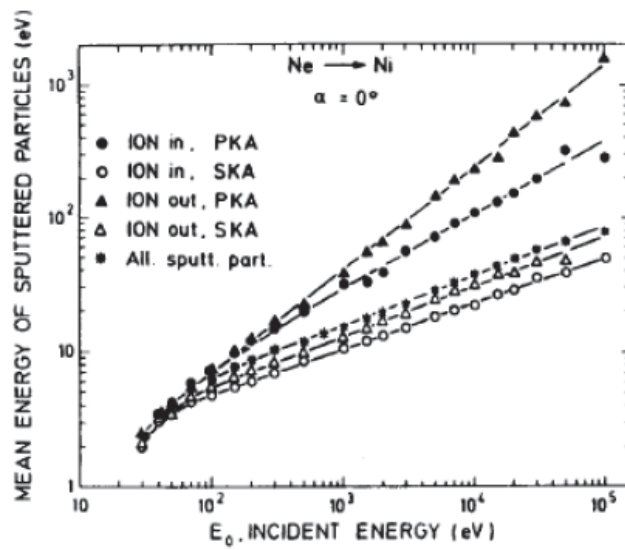


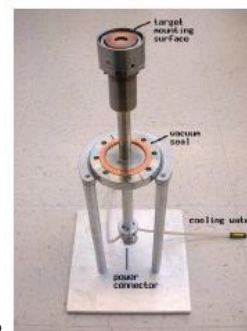
Fig.4.9. Bombardment of Ni by Ne at normal incidence,  $\alpha=0^\circ$ . The dependence of the mean energy of all sputtered atoms and of atoms sputtered due to the four different types of processes Vs. the projectile energy  $E_0$ .

#### 4.2.4. Plasma Sputtering

The Plasma Sputtering Equipment is reported in Fig.4.10.



A



B

Fig.4.10. Plasma Sputtering Equipment. Off-axis rotating system to improve the film thickness uniformity (A). Magnetron sputter gun (B).

## Collision Processes

The most probable pathways active after a collision are:

- Ionization:  $e + \text{Ar} \rightarrow 2e + \text{Ar}^+$

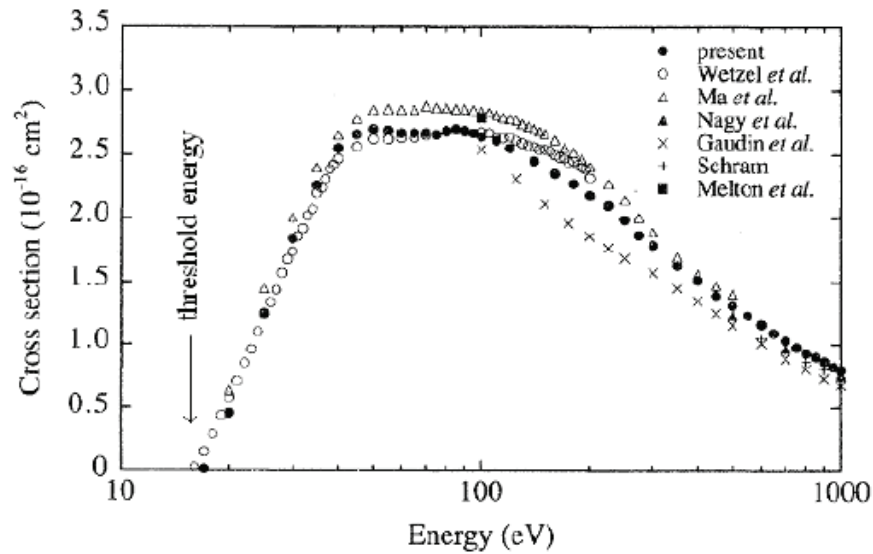


Fig.4.11. Total cross sections for electron-impact ionization of Ar.

The two electrons produced by this process can be accelerated by an electric field until they, too, can produce ionization, and this process sustains the plasma.

- Excitation:  $e + \text{Ar} \rightarrow e + \text{Ar}^*$

Transfer of energy allows Ar to jump to a higher energy level.

- Relaxation:  $\text{Ar}^* \rightarrow \text{Ar} + h\nu$

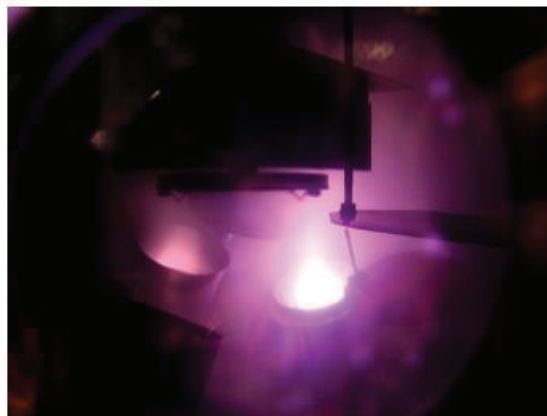


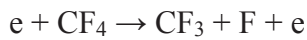
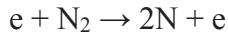
Fig.4.12. Nitrogen plasma.

As the excited ion falls back to its original energy level, it must release energy. In this case a photon is released. The color of the glow is characteristic of the gas:  $h\nu = \Delta E$ ; oxygen plasmas



are blue, nitrogen purple, etc.. The picture shows the plasma light emission for Rf-magnetron sputtering in air (roughly: 80% N<sub>2</sub> – 20% O<sub>2</sub>).

- Dissociation (source of interesting chemistry in plasmas).



To maintain a discharge, in-flight collisions are needed, hence the electrode distance must be smaller than:

$$\lambda = \frac{kT}{\sqrt{2}\pi\sigma^2} \approx \frac{5 \cdot 10^{-5}}{P(\text{torr})} m$$

The relation between the minimal electrode distance  $d$ , the ignition voltage  $U$  and the gas pressure  $p$  to ignite gas discharge is given by the Paschen-law (Fig.4.13):

$$U = \frac{B \cdot p \cdot d}{\ln \left[ \frac{A \cdot p \cdot d}{\ln(1/\gamma)} \right]}$$

**A, B:** empirical constants, depending on the gas  
 **$\gamma$ :** Secondary electron emission coefficient

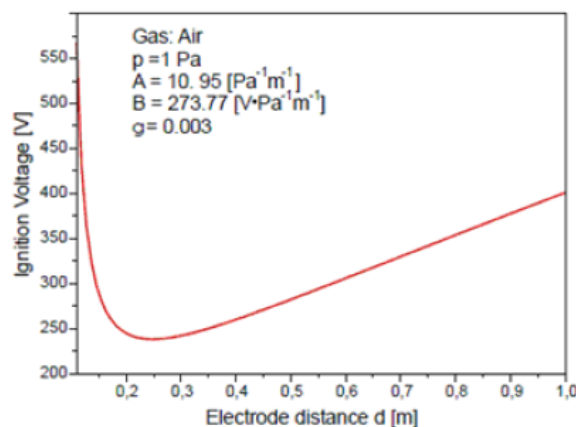


Fig.4.13. Paschen law.

Consider a neutral plasma, consisting of a gas of positively charged ions and negatively charged electrons. If one displaces by a tiny amount all of the electrons with respect to the ions, the Coulomb force pulls back, acting as a restoring force. If the electrons are cold, it is possible to show that the charge density oscillates at the *plasma frequency* ( $\omega_{pe}$ ):

$$\omega_{pe} = \sqrt{\frac{n_e e^2}{m\epsilon_0}}$$

Where  $n_e$  is the density of electrons,  $e$  is the electric charge,  $m$  is the mass of the electron, and  $\epsilon_0$  is the permittivity of free space. Note that the above formula is derived under the approximation that the ion mass is infinite. This is generally a good approximation, as the electrons are so much lighter than ions.

The plasma period is  $\tau_p = 1/\omega_p$ , and the distance  $\langle vT \rangle \tau_p$  traveled by a typical plasma particle during a plasma period defines, from the practical point of view, the *Debye length*, which has the form:

$$\lambda_D = \sqrt{\frac{\epsilon_0 k_B T}{ne^2}}$$

Note the  $\lambda_D$  is independent of mass, and therefore generally comparable for different species.

#### 4.2.5. DC Sputtering

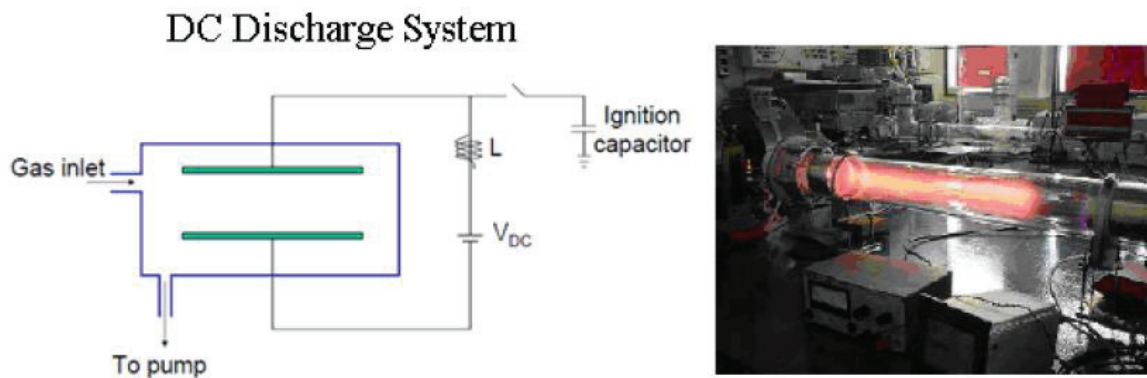


Fig.4.14. Schematization of a DC-Sputtering system.

As described before, plasma is formed essentially by Ar ions and electrons; because of the high mobility of the last, it is a good conductor.

Under a strong electric field, electrons can easily escape and collected to the anode. The resulting charge unbalance gives origin to a Coulomb force which hinders a further electrons escape. Moreover, ions impinging the cathode cause the emission of secondary electrons which are accelerated by the electric field and, hitting neutral gas molecules, are the main source of ionization. At (dynamic) equilibrium the body of the plasma is neutral (no internal electric field, no net charge, hence  $n_{ions} = n_{electrons} = 10^8 - 10^{12} /cm^3$ ), and is surrounded by a layer of positive charges (Ar ions). As a result, the plasma potential,  $V_p$ , is higher than the potential of any surface that faces the plasma (in electric contact with the plasma) and the electric field is constrained in the regions of positive space charge close to the electrodes (plasma sheaths). The Debye length tells us how rapidly the potential perturbation is attenuated in the plasma: over a distance  $\lambda_D$ , the perturbation is attenuated by 0.37 (1/e) of its initial value. For the plasma considered above,  $\lambda_D = 15\mu m$ . Qualitatively, the potential distribution in a dc sputtering discharge is reported in Fig.4.15.

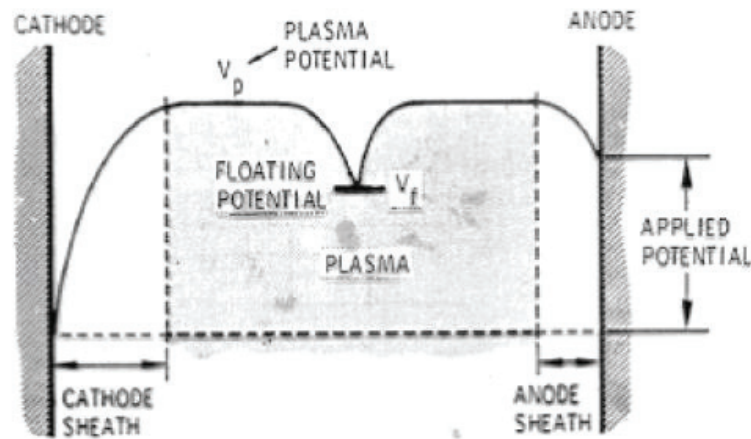


Fig.4.15. Potential distribution during a dc sputtering deposition.

The floating potential,  $V_f$ , is the potential of an isolated substrate. Consider a suspended isolated substrate in a plasma: since the flux of electrons is much higher than the flux of ions, the surface starts charging negatively. This repels electrons and attracts positive ions until the electron flux is equals the ion flux.

#### 4.2.6. RF Plasma Sputtering

The use of rf (radio frequency, 13.56 MHz) power doesn't allow the insulated electrode surface to reach equilibrium since the alternating potential polarity affects the electrons, sending them into an oscillatory path.

A matching network is necessary to couple the impedance of the generator to that of the discharge (Fig.4.16). In this case, the power transfer from the generator to the discharge is at peak efficiency and the reflected rf power is minimized. Usually, the rf power supply is capacitively coupled to the target while the chamber walls function as the opposing electrode and are grounded.

## RF Plasma System

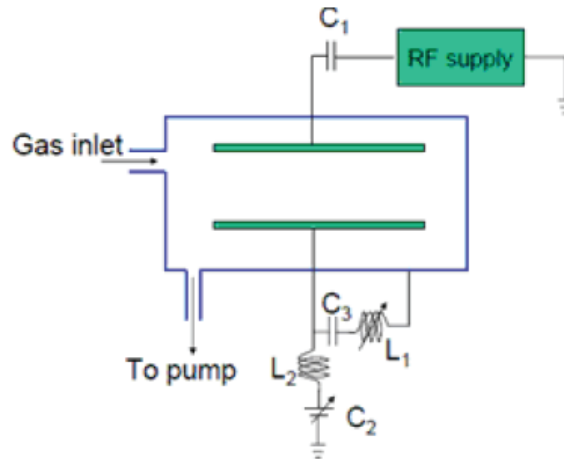


Fig.4.16. RF Plasma Sputtering system.

As the target is powered, on the first positive half-cycle it will rapidly collect electrons, while the other, more negative electrode will collect ions, but at much slower rate. The collection of the large number of electrons will charge the capacitor, leading to an added negative dc bias. In the second, negative, half-cycle an ion current is collected. However, this current is much smaller than the electron current and does not balance the collected electron charge.

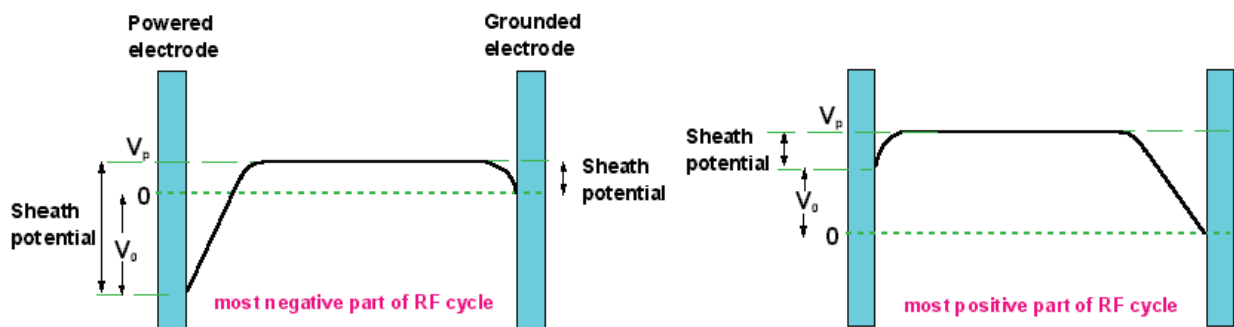


Fig.4.17. Potential between electrodes during the two half-cycle of the process.

Continuing through a number of cycles, the average dc bias on the electrode gradually drops until it reaches a sufficiently negative voltage than when the positive peak of the applied voltage exceed 0 V, enough electrons are collected to balance the number of slower ions collected on the remainder of the cycle. The target is called the cathode electrode, even though for short times during the cycle it functions as the anode. The cathode surface area must be smaller than the anode in order for most of the voltage drop to occur at the target.

## 4.2.7. Magnetron Sputtering

The above reported picture of the plasma features shows that it behaves like a diode. The “diode sputtering” has proven to be a useful technique in the deposition of thin films when the cathode is covered with source material (“sputtering target”). Diode sputtering, however, has two major problems: the deposition rate is slow and the electron bombardment of the substrate is extensive and can cause overheating and structural damage. The development of magnetron sputtering deals with both of these issues simultaneously.

In the presence of a magnetic field, the Lorentz force causes a circular motion of the electrons (usually the effect on ions is negligible) with the cyclotron frequency (Fig.4.18).

$$\omega_c = eB/m_e$$

Where  $e$ ,  $m_e$ , denote the charge and masses of the electrons, and  $B$  refers to the magnetic field.

The radius of this motion is given by

$$r_c = m_e v / eB$$

Where  $v$  is the velocity component perpendicular to  $B$ .

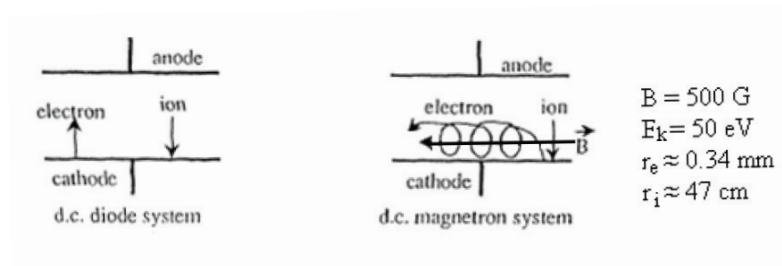


Fig.4.18. dc diode system Vs. dc magnetron system.

By using magnets behind the cathode to trap the free electrons in a magnetic field directly above the target surface, these electrons are not free to bombard the substrate to the same extent as with diode sputtering. At the same time the extensive, circuitous path carved by these same electrons when trapped in the magnetic field, enhances their probability of ionizing a neutral gas molecule by several orders of magnitude. This increase in available ions significantly increases the rate at which target material is eroded and subsequently deposited onto the substrate.

## 4.2.8. Reactive Sputtering for compound thin films

As mentioned before, the utilization of a reactive gas (such as oxygen or nitrogen) can lead to the preparation of a compound film. Because of the nature of the process and of involved species, it is common that parasitic events occur with a consequent decreasing of efficiency of film preparation.

One of the most important undesirable event is called “target poisoning”, and it can complicate reactive sputtering with a reduction in the thin film growth rate.

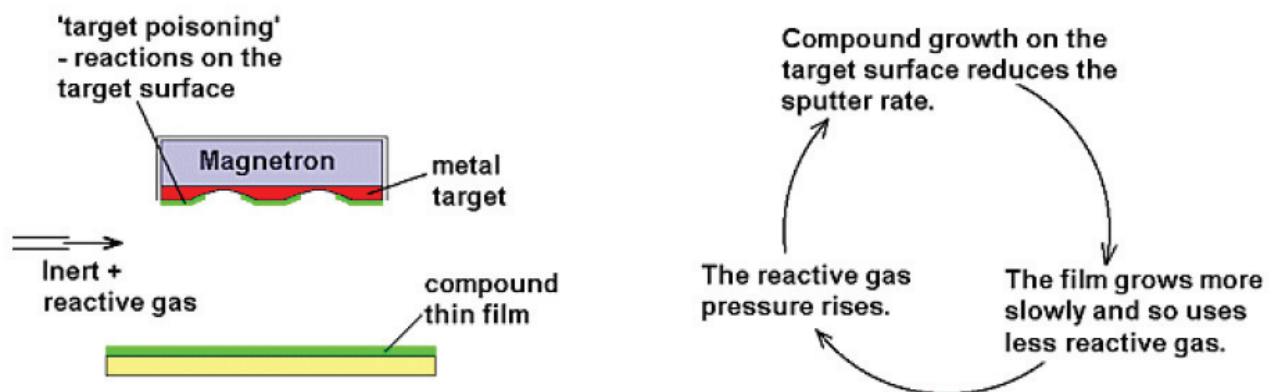


Fig.4.19. Cycle of target poisoning and its consequences on the sputter yield/rate.

Two key points exist in this reactive sputtering process:

- Part of the reactive gas is going down the pumps, the rest is going into the growing thin film.
- Compounds tend to sputter more slowly than metals.

So a sort of positive feedback loop can start, and it is seen as “target hysteresis” (Fig.4.20): variations in the thin film deposition rate, target voltage or reactive gas partial pressure. Of course, in order to maximize the efficiency of preparation of a compound by reactive sputtering, this phenomenon must be avoided. Best performance is achieved by careful design of the system furniture, the pumping system, the magnetron and the gas delivery. The target hysteresis can be completely eliminated by the use of a feedback system controlling the reactive gas flow, the control signal can come from emission lines from the plasma, reactive gas pressure measurements or target voltage.

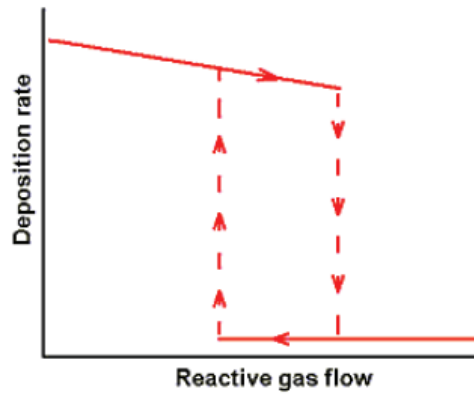


Fig.4.20. Target Hysteresis.

## Bibliography

1. D. Profeti, T.A.F. Lassali, P.Olivi, *Journ. of Applied Electrochem.* **36**, 883 (2006).
2. A.E. Gash, T.M. Tillotson, J.H. Satcher Jr., L.W. Hrubesh, R.L. Simpson, *Journ. of Non-Crystalline Solids* **285**, 22 (2001).
3. R.R.L. Pelegrino, L.C. Vicentin, A.R. De Andrade, R. Bertazzoli, *Electrochem. Comm.* **4**, 139 (2002).
4. V. Trieu, B. Schley, H. Natter, J. Kintrup, A. Bulan, R. Hempelmann, *Electrochim. Acta* **78**, 188 (2012).
5. C. Hummerlgard, J. Gustavsson, A. Cornell, H. Olin, J. Bäckström, *Thin Solid Films* **536**, 74 (2013).
6. S.S. Kim, S.D. Kim, *Thin Solid Films* **516**, 3673 (2008).
7. C. J. Brinker, G. W. Scherer, *Sol-gel Science: The Physics and Chemistry of Sol-gel Processing*, pp. 2-10 (1990).
8. J.J. Ebelmen, *Ann.* **57**, 331 (1864).
9. W. Geffcken, E. Berger, German Patent 736411 (1939).
10. H. Schroeder, *Phys. Thin films* **5**, 87 (1969).
11. C.B. Hurd, *Chem. Rev.* **22**, 403 (1938).
12. S.S. Kistler, *J. Phys. Chem.* **36**, 52 (1932).
13. L. Levene, I.M. Thomas, U.S. Patent 3640093 (1972).
14. H. Dislich, *Angewandte Chemie* **10** (6), 363 (1971).
15. A. Morozov, A. De Battisti, S. Ferro, G.N. Martelli US 2010/0126851 A1 (2010).
16. L. Vázquez-Gómez, E. Horváth, J. Kristóf, A. Rèdey, A. De Battisti, *Applied Surface Science* **253**, 1178 (2006).
17. G. Battaglin, *Lecture Notes on "Physical Vapor Deposition"*.
18. Y. Yamamura, H. Tawara, *Atomica Data and Nuclear Tables*, **62** (1996), 149.



In this chapter, notions of Backscattering spectrometry and Elastic Recoil Detection analysis are presented, owing to the fact that they are *unconventional* techniques, used for the characterization of DSAs. The measurements carried out in the frame of this thesis work have produced quite interesting results, which help in understanding of the composition profile of the materials, along the thickness, and in the evaluation of surface properties, an aspect that is strongly related with the electrochemical properties of samples.

## 5. Backscattering Spectrometry [1]

### 5.1. Introduction

Backscattering spectrometry represents one of the most important surface (and near surface region) techniques for determining stoichiometry of materials, impurity distribution and, in general, concentration profiles of atoms. It exploits ion beams in the energy range of the MeV that are backscattered after the collision with sample atoms, and through different atomic masses, the distribution of target elements can be determined by the measurement of the number and energy distribution of backscattered particles.

During the analysis, ions scatter elastically from sample with a particular energy that depends on the mass of struck particle; moreover, if a fraction of the ion beam penetrates inside the target's bulk, a loss in energy can occur. The intensity/counts of backscattered particles is usually plotted against the channel number: as a rule, it is linearly related to the backscattered ion energy,  $E_I$ .

What appears in the spectrum is a nearly flat-topped "peak" for each element present in the film; the peak widths are caused by the energy loss of analyzed ions in the film material.

The film elements may be identified by insertion of measured energies ( $E_I^i$ ) of the high-energy sides of the peaks into

$$K_i \equiv \frac{E_I^i}{E_0} \quad \text{Eq.5.1}$$

for calculating the kinematic factor  $K$  for the  $i$ -th element.  $E_0$  is the incident ion kinetic energy. In turn, the kinematic factor,  $K$ , is given by

$$K = \frac{E_I}{E_0} = \left[ \frac{\left( M_2^2 - M_1^2 \sin^2 \vartheta \right)^{1/2} + M_1 \cos \vartheta}{M_1 + M_2} \right]^2 \quad \text{Eq.5.2}$$

where  $\vartheta$  is the angle through which the incident ion is scattered, while  $M_1$  and  $M_2$  are the masses of the incident and target particles, respectively. Since the parameters  $M_1$ ,  $E_0$  and  $\vartheta$  are usually known,  $M_2$  can be determined and the target element is thus identified. The areal density  $(Nt)_i$  in atoms per unit area, may be determined for the  $i$ -th element once the detector solid angle,  $\Omega$ , the integrated peak count  $A_i$  for  $Q$  incident ions, and the measured or calculated cross section  $\sigma_i(E, \vartheta)$  are known:

$$(Nt)_i = \frac{A_i \cos \vartheta_i}{Q\Omega\sigma_i(E, \vartheta)} \quad \text{Eq.5.3}$$

$N_i$  is the atomic density (atoms per unit volume) of the  $i$ -th element and  $t$  represents the physical film thickness. If the scattering follows a Rutherford behavior (pure Coulomb scattering), then  $\sigma_i(E, \vartheta)$  may be calculated:

$$\sigma_E(E, \vartheta) = \left(\frac{Z_1 Z_2 e^2}{4E}\right)^2 \times \frac{4 \left[ \left( M_2^2 - M_1^2 \sin^2 \vartheta \right)^{1/2} + M_2 \cos \vartheta \right]^2}{M_2 \sin^4 \vartheta \left( M_2^2 - M_1^2 \sin^2 \vartheta \right)^{1/2}} \quad \text{Eq.5.4}$$

where  $Z_1$  and  $Z_2$  are the atomic numbers of the incident and target ions, respectively. This equation is given in *cgs* units. For very thin films,  $E$ , the analysis ion energy immediately before scattering, may be taken as  $E_0$ ; for thicker films, the mean energy of analyzed ions in the film should be used for  $E$ . The average stoichiometric ratio for the compound film ( $A_m B_n$ ) may be calculated from Eq.5.3 for both elements:

$$\frac{n}{m} = \frac{N_B}{N_A} = \frac{A_B}{A_A} \times \frac{\sigma_A(E, \vartheta)}{\sigma_B(E, \vartheta)} \quad \text{Eq.5.5}$$

For obtaining the physical thickness  $t$ , a conversion of areal densities  $Nt$  is necessary, and it requires the knowledge of the density  $\rho_{AB}$ .

$$N_A^{AB} = \frac{m\rho_{AB}N_0}{M_{AB}}; N_B^{AB} = \frac{n\rho_{AB}N_0}{M_{AB}} \quad \text{Eq.5.6}$$

Then, Eq.5.7 can be used to calculate  $t$ :

$$t = \frac{(Nt)_A}{N_A^{AB}} = \frac{(Nt)_B}{N_B^{AB}} \quad \text{Eq.5.7}$$

Here,  $N_0$  is the Avogadro number, while  $M_{AB} = mM_A + nM_B$  represents the molecular weight of the compound  $A_mB_n$ .

Uncertainties in the results are around  $\pm 3\%$  for areal densities, and of about 10% for the average stoichiometric ratios.

The major part of analyses are carried out using  $^4\text{He}$  ions with energies of 1.2 MeV, because of reasons associated to sources and detectors (based on silicon) resolution, and for

increasing the backscattering cross section, which is larger for helium if those values of energies are involved. If the source energy is decreased to the level of keV, the competitive yield of etching/sputtering phenomenon is amplified.

The main advantages of Rutherford backscattering (RBS) with  $^4\text{He}$  ions are the following:

- it is an absolute approach, that does not require the use of standards;
- it is a quite fast analytical tool;
- it is a non-destructive technique;
- it may be used for depth profiling (with a depth resolution of 10-30 nm).

Its sensitivity is not so bad (about  $10^{-4}$ ) for the detection of heavy elements in or on light matrices, but it's quite poor (about  $10^{-1}$ ) in the case of light elements in or on heavy matrices.

Higher energy sources, obtained with heavier atoms ( $^{16}\text{O}$ ,  $^{35}\text{Cl}$ ), can be used to improve the mass resolution of light elements; moreover, recent developments on detectors (time of flight, TOF, and electrostatic analyzers) have permitted the utilization of lower-energy ions, allowing particular applications and analysis.

## 5.2. The kinematic factor and mass resolution

Equation 5.2 (the expression for the kinematic factor  $K$ ) is the result of the application of energy and momentum conservation to a two-bodies collision between isolated particles of masses  $M_1$  and  $M_2$ . The incident beam of particles 1 (with a kinetic energy  $E_0$ ) is scattered, with a final kinetic energy  $E_1$  and through a laboratory angle  $\vartheta$ , by target particle 2 (initially at rest); the binding energy of particle 2 in the target is neglected. Tables of kinematic factors can be found in literature; in addition, the kinematic factors for other ions can be calculated using Eq.5.2. Average kinematic factors are also listed. The average mass for natural isotopic abundance has been used in the calculation of average kinematic factors.

For a fixed  $\vartheta$ , the energy separation,  $\Delta E_1$ , for beam particles scattered by target particles of mass difference  $\Delta M_2$  is (from Eq.5.1):

$$\Delta E_1 = E_0 \left( \frac{dK}{dM_2} \right) \Delta M_2 \quad \text{Eq.5.8}$$

If  $\Delta E_1$  is set equal to  $\delta E$ , the minimum energy separation that can be experimentally resolved, then  $\delta M_2$ , the mass resolution of the system can be estimated as follows:

$$\delta M_2 = \frac{\delta E}{E_0 \left( \frac{dK}{dM_2} \right)} \quad \text{Eq.5.9}$$

### 5.3. Elastic scattering cross sections

#### Definition of differential cross section

The average differential cross section,  $\sigma(\vartheta, E)$ , for the scattering of beam particles of incident energy  $E$ , by target particles in a thin film, is defined as:

$$\sigma(\vartheta, E) = \left( \frac{1}{Nt} \right) \frac{dQ(E)}{Q} \frac{1}{\Omega(\vartheta)} \quad \text{Eq.5.10}$$

where  $Nt$  is the number of target atoms per unit area (perpendicular to the beam), and  $[dQ(E)]/Q$  is the fraction of incident particles scattered within the small solid angle  $\Omega(\vartheta)$ , centered at a deflection angle  $\vartheta$ .

#### Rutherford cross section

Considering the interaction between an incident nucleus ( $M_1, Z_1, e, E$ ) and a target one ( $M_2, Z_2$ , initially at rest) as a Coulomb-type force,  $\vec{F}_{12} = (Z_1 Z_2 e^2 / r^2) \hat{r}$ , the Rutherford cross section in the laboratory system can be readily estimated by using Eq.5.4.

An accurate approximation for large backscattering angles and  $(M_1/M_2) \ll 1$  was proposed by Chu *et al.* (1978):

$$\sigma_R(E, \vartheta) \approx 0.02073 \left( \frac{Z_1 Z_2}{4E} \right)^2 \left[ \sin^{-4} \left( \frac{\vartheta}{2} \right) - 2 \left( \frac{M_1}{M_2} \right)^2 \right] \quad \text{Eq.5.11}$$

#### Non-Rutherford cross sections

During a real experiment, deviations from the Rutherford conditions are verified at both, high and low energies, for target-projectile pairs. One of the main causes for this behavior has to be found in the partial shielding of nuclear charges by shell electrons surrounding the nuclei.

After several investigations, it was proved that the corrections proposed by L'Ecuyer *et al.* (1979) and Wenzel and Whaling (1952), reported below in Eqs.5.12 and 5.13, are adequate.

$$\sigma / \sigma_R = 1 - \frac{0.049 Z_1 Z_2^{4/3}}{E_{CM}} \quad \text{Eq.5.12}$$

$$\sigma / \sigma_R = 1 - \frac{0.0326 Z_1 Z_2^{7/2}}{E_{CM}} \quad \text{Eq.5.13}$$

The high energy deviations of the cross section from Rutherford behavior are caused by short-range nuclear forces, and measurements carried out in 1990-91 by Bozoian *et al.* and Hubbard *et al.* have partially solved this problem. Fig.5.1 reports data pertaining to  $^1\text{H}$ ,  $^4\text{He}$ , and  $^7\text{Li}$  beams.

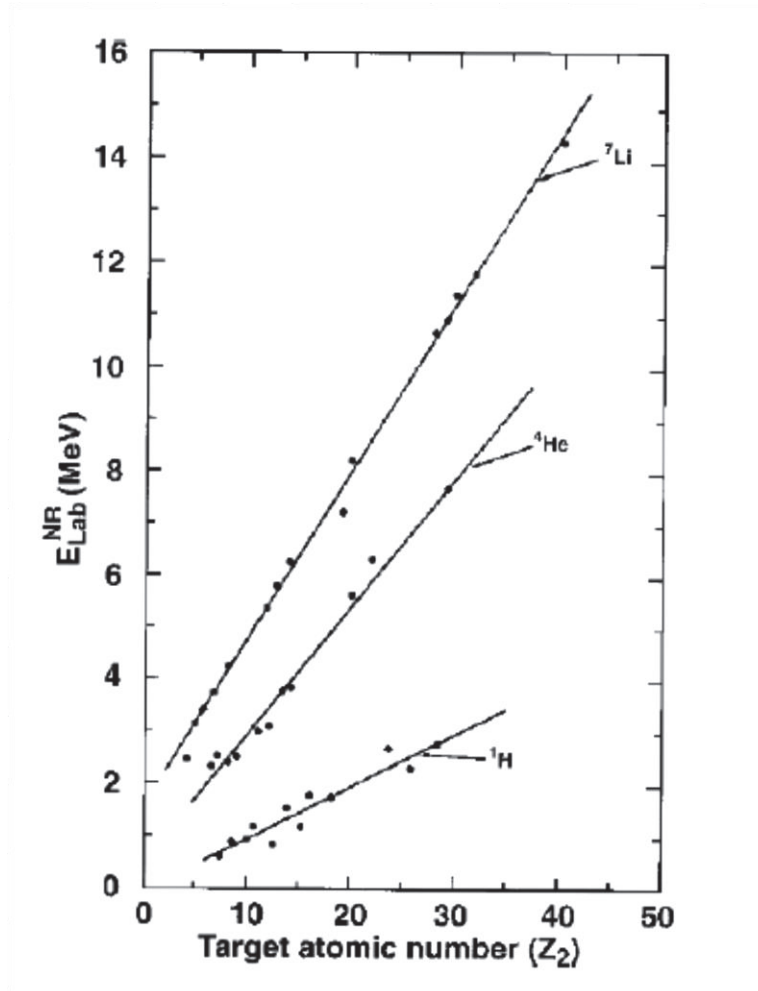


Fig.5.1. Laboratory projectile energies,  $E_{\text{Lab}}^{\text{NR}}$ , at which backscattering cross sections (for  $160^\circ < \vartheta_{\text{Lab}}$ ) deviate from Rutherford by 4% vs. target atomic number  $Z_2$ , for  $^1\text{H}$ ,  $^4\text{He}$  and  $^7\text{Li}$  projectiles. The  $^1\text{H}$  and  $^4\text{He}$  points are experimental, while  $^7\text{Li}$  were obtained from optical model calculations. Image extracted from [1].

The straight lines on Fig.5.1 represent rough boundaries, separating a region of Rutherford behavior (below the line) from a region of non-Rutherford behavior (above the line). Equations resulting from a least-squares fits to the points in Fig.5.1 are the following (Eqs.5.14):

$$\text{For } ^1\text{H: } E_{\text{Lab}}^{\text{NR}} \approx (0.12 \pm 0.01)Z_2 - (0.5 \pm 0.1) \quad \text{Eq.5.14 (a)}$$

$$\text{For } ^4\text{He: } E_{Lab}^{NR} \simeq (0.25 \pm 0.01)Z_2 - (0.4 \pm 0.2) \quad \text{Eq.5.14 (b)}$$

$$\text{For } ^7\text{Li: } E_{Lab}^{NR} \simeq (0.330 \pm 0.005)Z_2 - (1.4 \pm 0.1) \quad \text{Eq.5.14 (c)}$$

where  $E_{Lab}^{NR}$  is the laboratory projectile kinetic energy (in MeV) at which the backscattering cross section (if  $\vartheta_{Lab} > 160^\circ$ ) deviates from Rutherford by 4%, for a target atom of atomic number  $Z_2$ . Note that cross sections for backscattering of  $^1\text{H}$  at 1 MeV are non-Rutherford for  $Z_2 < 15$ , while cross sections for  $^4\text{He}$  at 2 MeV are Rutherford for  $Z_2 > 6$ . At present, no practical method exists for a rapid and accurate calculation of these high-energy non-Rutherford cross sections: they must be measured. Advantages associated with the use of non-Rutherford cross sections, such as improved accuracy in determination of stoichiometric ratios and increased sensitivity for detection of light elements in heavy-element matrices, frequently justify the additional work required to make the above measurements.

For solving stoichiometric problems, it should be noted that the average stoichiometric ratio for two elements depend both on the integrated peak counts and the relative cross sections. Frequently, a deconvolution/simulation process is required for analyzing experimental data, which inevitably limits the accuracy of the procedure; the problem is quite common, especially in the cases of non-uniform film composition.

The utilization of ions with a high energy can help for reducing peaks overlap and, because of this reason, it should be chosen always as high as possible, taking care of the cross sections characteristics for elements analyzed.

## 5.4. Experimental geometry

The most used experimental geometries are referred to IBM and Cornell specifications. For both, the projectile beam is horizontal and the sample surface is vertical. For the IBM geometry, scattered beam, incident one and sample (normal) are placed in the same plane, while for the Cornell one, the detector is located below the incident beam, and projectile and scattered beams are in a vertical plane.

In both geometries, the normal and the scattered beam is  $\vartheta_2$ . The “tilt” axis is vertical through the beam spot on the sample surface, so the “tilt” angle is  $\vartheta_1$  in both cases. The relation between the scattering angle  $\vartheta$ ,  $\vartheta_1$  and  $\vartheta_2$  is  $\vartheta = \pi - |\vartheta_1 \pm \vartheta_2|$  for the IBM geometry and  $\cos \vartheta_2 = \cos(\pi - \vartheta) \cos \vartheta_1$  for the Cornell geometry. In the IBM geometry, for a given tilt angle  $\vartheta_1$ , the angle  $\vartheta_2$  depends on the direction of  $\vartheta_1$ , *i.e.*, whether the sample is rotated toward or away from the direction of the scattered beam. The relation between the inward and

outward path lengths and the perpendicular distance  $x$ , below the sample surface, at which a backscattering event has occurred is given by:

$$d_{in} = \frac{x}{\cos \vartheta_1} ; d_{out} = \frac{x}{\cos \vartheta_2} \quad (\text{IBM}) \quad \text{Eq.5.15 (a)}$$

$$d_{in} = \frac{x}{\cos \vartheta_1} ; d_{out} = \frac{x}{\cos \vartheta_1 \cos \vartheta_2} \quad (\text{Cornell}) \quad \text{Eq.5.15 (b)}$$

## 5.5. Effects of energy loss of ions in solids

### 5.5.1. Definitions

A lot of information that is possible to extract by RBS are determined by the energy loss of the ion beam that penetrates in deeper layers of analyzed material. The stopping power of a material, for a particular ion, is usually defined as the energy loss per distance travelled in the material, and denoted as  $dE/dx$ . This quantity depends on the nature and energy of the ion, as well as on the nature of the crossed material. Usual units for the stopping power are eV/Å or eV/nm.

Another quantity, the stopping cross section  $\varepsilon$ , is defined as the energy loss per areal density (atom/cm<sup>2</sup>) of crossed material; this quantity is independent of the volume density of the material. Usual units are 10<sup>-15</sup> eV cm<sup>2</sup>. The relation between the above two quantities is given by

$$\frac{dE}{dx} = N\varepsilon \quad \text{Eq.5.16}$$

where  $N$  is the atomic density (atoms/cm<sup>3</sup>). Values of ion stopping cross sections in all elements were made available by an extensive study based on semi-empirical fitting of experimental data (Ziegler *et al.*, 1985).

To simplify the treatment, a parameterization of proton stopping cross section involving eight parameters per element is given, together with scaling rules for extension to any analysis ion. The calculation associated to this problematic is quite complicated but several approximations exists. One of them, the Bragg rule (Bragg and Kleeman, 1905), is commonly used to calculate stopping cross sections of ions in compounds or mixtures of different elements. This approximation simply assumes that each target atom acts independently, in the energy loss process, and ignores any effects of chemical bonding in the material. For a compound  $A_m B_n$ , this rule can be expressed as follows:

$$\varepsilon^{A_m B_n} = m\varepsilon^A + n\varepsilon^B \quad \text{Eq.5.17}$$

Where the compound stopping cross section is given in terms of energy loss per molecule per cm<sup>2</sup> crossed. The related stopping power is given by:

$$\left(\frac{dE}{dx}\right)^{AB} = N^{AB} \varepsilon^{AB} = N_A^{AB} \varepsilon^A + N_B^{AB} \varepsilon^B \quad \text{Eq.5.18}$$

where  $N^{AB}$  represents the molecular density (molecules/cm<sup>3</sup>), while  $N_A^{AB}$  and  $N_B^{AB}$  are the atomic densities of A and B in the compound (the  $m$  and  $n$  subscripts on A and B are suppressed in this notation).

The estimation of the energy loss,  $\Delta E$ , of ions crossing a solid involves the integration of the stopping power:

$$\Delta E = \int \frac{dE}{dx} dx \quad \text{Eq.5.19}$$

If thin targets are considered, the stopping power can be taken as a constant, and quantities of analyzed atoms can be estimated referring to the incident energy (surface energy approximation) or to the mean energy of the beam in the target (mean energy approximation).

### 5.5.2. Depth scale and Depth resolution

By correlating the energy of scattering particles to the depth of the target, a depth-profiling information can be deduced. If the orientation of the sample and positions of both source and detector are maintained fixed, and the kinematic factor of the considered element is known, the procedure is quite easy to be carried out.

Let's indicate as  $\Delta E$  the difference in energy, at the detector, of a particle scattered at the surface and of a particle scattered at a depth  $x$ , measured perpendicularly to the sample surface. This quantity is given, as a function of  $x$ , by:

$$\Delta E = [S]x \quad \text{Eq.5.20}$$

where  $[S]$  is known as the energy loss factor, and is defined by:

$$[S] = \left[ K \left( \frac{dE}{dx} \right)_{in} \frac{1}{\cos \vartheta_1} + \left( \frac{dE}{dx} \right)_{out} \frac{1}{\cos \vartheta_2} \right] \quad \text{Eq.5.21}$$

The corresponding relation, introducing the areal density and stopping cross sections, is given by Eq.5.22:

$$\Delta E = [\varepsilon]Nx \quad \text{Eq.5.22}$$

For a single element sample, the quantity  $[\varepsilon]$  is known as the stopping cross section factor, and is defined by:



$$[\varepsilon] = \left[ K \varepsilon_{in} \frac{1}{\cos \vartheta_1} + \varepsilon_{out} \frac{1}{\cos \vartheta_2} \right] \quad \text{Eq.5.23}$$

Eq.5.23 represents the most important equation for solving the depth-profiling problem.

The equation can be extended to a multi-element sample: in the case of a compound  $A_m B_n$ ,  $N$  becomes  $N^{AB}$ , the molecular density expressed in molecules per  $\text{cm}^3$ , while corresponding values are considered for  $K$  and  $\varepsilon_{out}$ . The relations for the element  $A$  are given by Eq.5.24 and 5.25.

$$\Delta E_A = [\varepsilon]_A^{AB} N^{AB} x \quad \text{Eq.5.24}$$

$$[\varepsilon]_A^{AB} = \left[ K_A \varepsilon_{in}^{AB} \frac{1}{\cos \vartheta_1} + \varepsilon_{out,A}^{AB} \frac{1}{\cos \vartheta_2} \right] \quad \text{Eq.5.25}$$

Analogous relations can be written for the element B. The lower index refers to the scattering element and the upper index refers to the stopping material. A surface energy approximation is often used for stopping cross section factors.

By using Eq.5.20, it is possible to see that the minimum detectable depth difference,  $\delta x$ , is related to the minimum detectable scattered particle energy difference,  $\delta E$ :

$$\delta x = \frac{\delta E}{[S]} \quad \text{Eq.5.26}$$

Sources of energy spread include detector resolution, energy spread in the ion beam, straggling and kinematic effects. Since energy straggling increases as the ion beam crosses the sample, the depth resolution degrades with depth in the sample.

The depth resolution can be improved by increasing  $[S]$ : this is usually done by tilting the sample normal relative to the incoming beam (*i.e.*, increasing  $\vartheta_1$  and/or  $\vartheta_2$ ). In general, using an ion beam of  $^4\text{He}$  with energy of 2 MeV, a depth of 40-50 nm can be examined with a resolution, at the maximum depth, of about 500 nm.

## 5.6. Experimental apparatus

The RBS apparatus is presented in Fig.5.2.

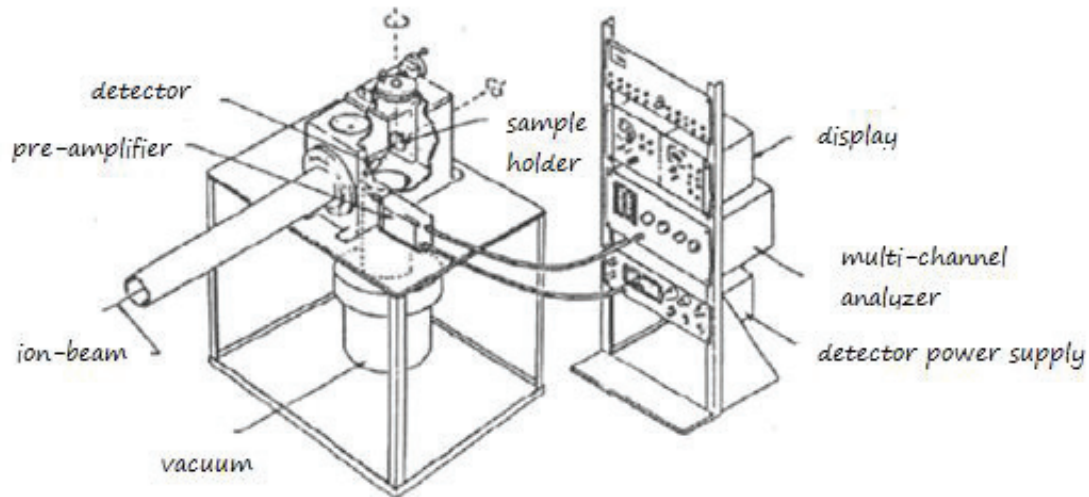


Fig.5.2. Complete apparatus for RBS analysis.

The particles accelerator can generate a collimated ion beam characterized by an energy in the order of magnitude of MeV. Fig. 30 shows more in detail the geometry of instrumentation used.

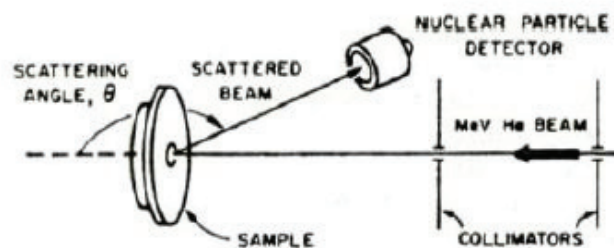


Fig.5.3. A collimated beam of alpha particles collides on a planar sample; the backscattered particles are measured by a detector placed at an angle  $\theta$ . The system is under vacuum.

A semiconductor is used as detector: an output voltage that is proportional to the backscattered particles energy collected is generated, and variables are correlated. A big number of these detectors are based on inversely polarized silicon; when  $\alpha$  particles hit the

depletion zone, they generate electron-hole couples in surplus, with respect to those naturally present in the material, allowing for the origin of an electric current.

The signal generated by the detector is pulsed, the height of pulses is proportional to the energy of backscattered particles. The analyzer collects pulses with different height in different voltage channels, and it is properly calibrated: thanks to this expedient, a direct correlation between energy and channel number exists.

## **5.7. Numerical calculations of spectra: Areal density calculations and computer simulation**

Different approaches exist, but one of the most used (also exploited in this thesis work) consists of analyzing the spectra by computer simulation, with calculation of the energy spectrum of backscattered particles, specifying the target and the experimental conditions.

Because of the nature of the samples investigated in this thesis work, the above approach was used to characterize films composed of oxides of iridium and titanium. The procedure requires to alter the guess composition until the calculated and the measured energy spectra are closely matched. This can be done by manually changing the sample composition for each iteration or using a least-squares fitting procedure to find the target composition that best fits with the experimental spectrum. A well-known RBS analysis program is RUMP, which was developed at Cornell University [5]; it was used in the present case and it will be further explained in what follows.

## **5.8. Elastic Recoil Detection (ERD) [3]**

This technique was first introduced in 1976 by L'Ecuyer *et al.*; before its introduction, Nuclear Reaction Analysis (NRA) was the predominant ion-beam technique for obtaining depth profiles of light elements, but the simplicity of ERD has led to an extensive use of the latter. However, in many cases ERD shows sensitivity and depth resolution that are poorer than those of NRA. ERD uses heavy-ion beams with high energy (MeV) to detect target atoms characterized by a low atomic number ( $1 < Z < 9$ ). However, the heavy-ion projectile only needs to have a mass greater to that of the target atom, and in fact alpha particles are commonly used to obtain recoil spectra for hydrogen and its isotopes (this form of ERD is called Forward Recoil Spectrometry, FRES). ERD has become the technique of choice for analyzing many light elements, owing to:

- Simplicity
- Possibility of simultaneous multi-element profilings
- Reasonable sensitivity
- Good depth resolution

The physical concepts and the equations governing ERD and RBS are the same (Fig.5.4), and through the use of dedicated software, ERD spectra are easily manipulated to obtain full quantitative analyses. Much like RBS, ERD only depends on four physical concepts:

1. The kinematic factor describes the energy transfer from a projectile to a target nucleus in an elastic collision.
2. The differential scattering cross section gives the probability for the scattering event to occur.
3. The stopping powers give the average energy loss of the projectile and of the recoiled target atom as they cross the sample.
4. The energy straggling gives the statistical fluctuation in energy loss, and indirectly represents inhomogeneities of the analyzed surface.

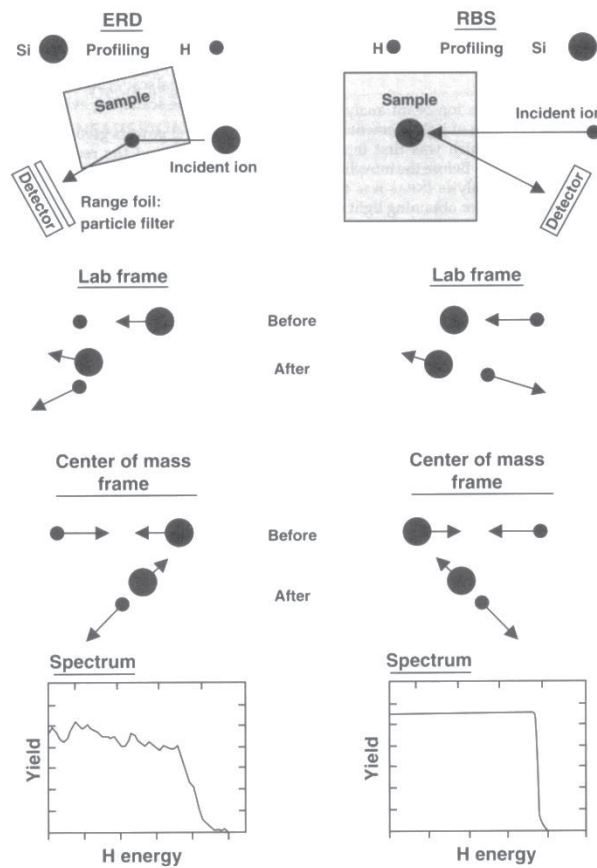


Fig.5.4. A schematic comparison of elastic recoil detection (ERD) and Rutherford backscattering spectrometry (RBS) scattering geometries, in the lab and center-of-mass frames of reference. The Si atom is presented by the larger filled circles, while the H atom is represented by the smaller circles; the situations after and before the collision are presented. Obtained spectra (ERD and RBS) appear qualitatively similar. From [3].

The yield, for a given element, can be related to the atomic concentration of that element. For samples with a limited depth resolution, a measure of the integrated peak area, which represents the areal density (number of atoms/cm<sup>2</sup> along the layer thickness), is the better analytical approach.

In the present work, ERD has been used to determine the amount of deuterium (Fig.5.5) entrapped in the oxide-based films after a given cathodic polarization in 1M D<sub>2</sub>SO<sub>4</sub> in D<sub>2</sub>O. Because of the characteristics of investigated films, the oxidative and reductive processes that involve the electroactive sites are accompanied by the injection/dejection of protons, if the environment allows this phenomenon. Protons can move inside and outside the film, jumping between the water molecules of the solvent (“pseudo-Grotthuss” mechanism), with the result of a hydration of the film that changes its structure until the reaching of a stable structure. During this complex process, which involves several layers of material, hydrogen atoms can remain encaged inside the catalyst. Hydrogen is largely present in Sol-Gel films because of the by-products of combustion of salt precursors, during calcination, and the recourse to deuterated solvents permits to distinguish which atoms are really involved in the injection/dejection process. The ERD measures can supply indications about the thickness of the material involved in the redox catalytic action.

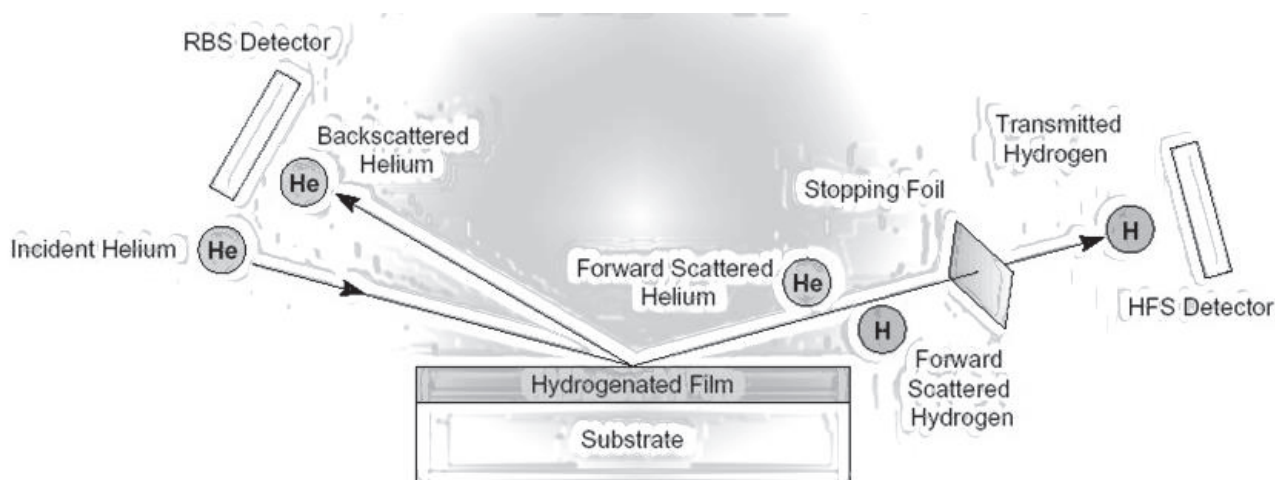


Fig.5.5. H and D contents in a thin film are determined with a detection limit <0.01 at.%. Because of the relatively small energy loss of H in solids, the depth resolution of this method is typically ~300-600Å

## 6. Electrode preparation: Experimental details about samples deposition

### 6.1. Sputtered samples prepared on titanium supports

Titanium supports with a geometric surface area of 4 cm<sup>2</sup> were purchased from Titanium Consulting & Trading (Italy) and preliminary electro-polished, following the teachings reported in ref. [9]. Oxide films were grown at two different temperatures (350 and 450 °C) on the aforementioned titanium supports, as well as on fused silica sheets and crystalline (100) doped silicon wafers. Depositions were done in a custom-built rf-magnetron sputtering system (13.56 MHz), equipped with 3 independent 2” sources and a rf-biased sample holder. The magnetron sputtering sources were positioned at a ~30° inclination with respect to the substrate normal, and at a target-to-substrate (center to center) distance of 12 cm. The sample holder, on the ceiling of the vacuum chamber, was rotated at 5 rpm in order to assure a deposition uniformity better than 5%. The base pressure of the chamber was about 2×10<sup>-10</sup> bar. Targets materials were 2” diameter Ir (99.9 %) and Ti (99.995 %) metallic disks. Before starting the depositions, sources were conditioned for 15 minutes at the operating conditions. Pure (99.9995 %) Ar and a 20% mixture of O<sub>2</sub> in Ar gases were used at a working pressure of 5×10<sup>-6</sup> bar. Prior to the deposition, the substrates were sputter-cleaned at 20 W for 20 minutes in pure Ar, in order to remove any residual surface contamination.

The deposition conditions were preliminary studied by checking the amount of deposited oxides as a function of the power applied to the sources, building calibration curves that have permitted to predict the better conditions for the synthesis of expected samples.

At first, a 200 nm thick Ti layer was deposited (in pure Ar) onto the bare substrates, in order to provide a reproducible substrate and to guarantee a better adhesion of the subsequent oxide film.

Ir-Ti oxide layers were grown in a 20% O<sub>2</sub>-Ar mixture, to obtain a high sputtering rate and a complete oxidation of deposited layers [10]. Powers to the sources were adjusted as to attain layers of the chosen composition with a thickness of about 0.75 μm in a deposition time of 30 minutes. Under these conditions, preparation of devices does not exceed 1 hour of time. Powers in the range of 35-38 W were chosen for the Ir source, and close to 300 W for the Ti, allowing a molar ratio Ir-Ti of 1:2. Titanium sputtering cross section is extremely lower than

iridium one, and a high value of power supply is necessary for reaching the desired concentration in the film within a reasonable time.

## **6.2. Sol-gel samples prepared on titanium supports**

IrO<sub>2</sub>-TiO<sub>2</sub> sol-gel samples were prepared by pyrolysis of Ti-supported deposits consisting of mixtures of iridium(III) and titanium(IV) chloro-hydroxo-aceto complexes in aqueous solution 0.755 M and 2 M, respectively. Vehicle solutions contained the required molar ratios of cations, and they were prepared by mixing convenient volumes of the original solutions. Deposits were prepared by painting the 4×4 cm<sup>2</sup> electropolished Ti-supports, with aqueous solutions; after the solvent evaporation, carried out at 100 °C for 5 minutes per layer, each deposit was pyrolyzed in air at 350 or 450 °C for 15 minutes, and the procedure was repeated until an oxide film thickness of about 1 μm was reached: about three layers are necessary for reaching the desired thickness, as tested with several samples, verifying the thickness of oxide material by a cross section SEM analysis.

## **6.3. Sol-gel samples prepared on amorphous silica supports**

The same approach described in Par. 6.2 was used for the preparation of films on amorphous silica supports; these specimens have been subsequently investigated for carrying out a detailed, non-electrochemical characterization of the oxide mixtures. Films were prepared with a thickness of 2 μm. The nature of the support does not interfere with the XRD analysis (this was also experimentally verified). The silica supports were brushed, before the deposition, in order to guarantee a good wettability and so a decent adhesion of deposits. In this case, a wide range of concentrations for the mixture and of preparation temperatures were explored, aiming to gain information about the formation of crystalline phases and, in case, of a substitutional solid solution. The investigated compositions (expressed as molar percentages of iridium and titanium, respectively) were the following: 5:95, 10:90, 20:80, 50:50, 80:20 and 90:10 %mol; each composition was prepared at four different pyrolysis temperatures: 250, 350, 450 and 550 °C.

## 6.4. Sol-gel Samples prepared on doped silicon wafer supports

Eventually, two samples of IrO<sub>2</sub>-TiO<sub>2</sub> 1:2 mol, calcined at 350 and 450°C, were prepared on doped silicon wafers; a lower thickness was chosen for these specimens: about 0.2 μm (instead of 1 μm). The silicon supports are monocrystalline and oriented along the <100> direction, with a heavily n-doped layer having a thickness of 525±25 μm: the resistivity is of about 0.001-0.005 Ω cm; because of this high conductivity, there is no risk to work with an insulating support not even when applying an anodic polarization. *n*-doping was achieved by ion bombardment with arsenic.

These samples, characterized by an extremely smooth surface and a low amount of deposit, were prepared in order to perform analyses with RBS and ERD, which are of interest because of the possibility to detect chlorides and deuterium atoms (tests will be discussed in detail later). For the preparation of devices, the precursor solution was diluted 1:5 using a 10% CH<sub>3</sub>COOH solution, in order to guarantee the stability of the chloro-hydroxo-aceto complexes suspension, and four layers were painted on the supports. Because of the hydrophobic nature of silicon, a drop of a surfactant (Triton X-100 – Fig. 6.1) was added for ensuring the adhesion of the deposit to the support.

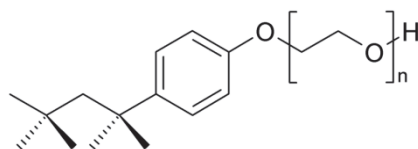


Fig. 6.1. Triton X-100 (C<sub>14</sub>H<sub>22</sub>O(C<sub>2</sub>H<sub>4</sub>O)<sub>n</sub>) is a nonionic surfactant, which has a hydrophilic polyethylene oxide chain (on average it has 9.5 ethylene oxide units) and an aromatic hydrocarbon lipophilic or hydrophobic group. TRITON X-100 is soluble at 25°C in water, toluene, xylene, trichloroethylene, ethylene glycol, ethyl ether, ethyl alcohol, and isopropyl alcohol.

Before starting the deposition of the oxide films, supports were cleaned in a 10% HF solution in order to minimize the thickness of the SiO<sub>2</sub> layer that spontaneously forms on the surface.

## 7. Experimental Details: Microstructural, Surface and Electrochemical Analysis

Several physical and chemical techniques were used for the characterization of samples; they can be divided in two main branches: one related to the structural and



morphological “ex-situ” characterization, and the second related to electrochemical investigations. The ex-situ investigations, used within this thesis, offer advantages, with respect to in-situ analyses for monitoring the anodes properties, that are essentially attributable to their non-destructive nature.

The elemental composition of films was measured by Rutherford Backscattering Spectroscopy [4] by using a 2 MeV  $^4\text{He}^+$  beam at Laboratori Nazionali INFN of Legnaro (Padova, Italy). Depth concentration profiles were determined by fitting the experimental spectra and using the RUMP computer code [5]. Elastic Recoil Detection analyses, on films deposited on doped silicon, were also carried out in the INFN center of Legnaro, maintaining the same particle beam (2 MeV  $^4\text{He}^+$ ) but changing the angles (15 degrees) between the incident and recoiled particles and the sample. Just before the detector, a 9  $\mu\text{m}$ -thick aluminized mylar sheet was placed to block the diffused helium ions. If such a prudence is not used, scattered He particles may represent a source of anomalous background current that can hinder the detection of signals of interest.

X-Ray Diffraction (XRD) analyses were carried out using a Bruker D8 Advanced Powder diffractometer; the Cu  $K\alpha$  radiation, a graphite monochromator, and a proportional counter with a pulse height discriminator were used; the profile intensities were measured step by step, with a definition of  $0.02^\circ$  in  $\vartheta$ . The residence time for each step was fixed to 2 seconds but, for certain tests, it was increased to 10 seconds, thus improving the signal-to-noise (S/N) ratio in the case of samples with a low degree of cristallinity.

A part of the structural investigation was carried out in Trieste, in the research center *Elettra*, using the new furnace designed for powder diffraction measurements at high temperature and the synchrotron light. A detailed description of the system (MCX line, Material Characterization by X-Rays [12]) is reported in a paper of Riello *et al.* [6]; the oven can accommodate either capillary or small flat samples. The diffraction patterns were collected on a curved imaging plate that can be exposed to a range of  $2\vartheta$  of about  $130^\circ$ . The temperature of the oven, the heating ramp, the atmosphere and the data collection conditions are all programmable according to parameters specified by the user. The specimens to be analyzed were prepared within quartz capillaries of 0.3 mm diameter starting from liquid precursors, dried at 130-150  $^\circ\text{C}$  and then calcined. Different mixtures were studied, varying the relative composition of oxides (from a Ir-Ti ratio of 10:90 to a 90:10 %mol) and working between 100 and 600 or 1000  $^\circ\text{C}$ , using a temperature ramp of about 0.17  $^\circ\text{C}/\text{second}$ . After the dehydration treatment, about 1 ml/min of air was insufflated inside the capillary continuously in order to simulate the real condition of film formation. In a few cases, a pyrolysis in absence of oxygen was carried out for evaluating the effects on growth of oxide

phases. A source beam of 10 keV (1.24 Å) was chosen, basing on the adsorption intensity of analyzed samples. During measurements, the sample capillaries were rotated by  $\pm 90^\circ$  in order to avoid possible effects of preferred orientation.

XRD peaks were treated using a fitting algorithm that exploits the minimizing iterations of the Levenberg-Marquardt method, approximating the experimental signals with pseudo-Voigt functions.

Scanning Electron Microscopy (SEM) investigations were collected with a FEI Quanta 400 equipped with EDX probe for microstructural analysis.

Atomic Force Microscopy (AFM) was used to obtain information about the roughness of samples; actually, one of the fundamental parameters in the science of heterogeneous catalysis is represented by the real surface area, which may differ greatly from the geometric area. The instrumentation, located at the microscopy laboratory of Venezia Nano-Tech in Mestre (Venice), consists of a NT-MDT microscope equipped with a NSG10 golden silicon tip. AFM imaging was obtained working in semi-contact modality, to avoid possible damages caused by a tap-mode procedure.

The frequency varied between 0.8 and 0.9 Hz, depending on the sample, and it was adjusted before each test to optimize the image resolution. Relatively large area portions (from  $50 \times 50 \mu\text{m}$  to  $10 \times 10 \mu\text{m}$ ) were inspected, in order to obtain accurate values.

Depending on the purposes, the different tests were carried out on samples prepared with different thicknesses and on different supports (titanium, amorphous silica or doped silicon). A detailed description of experimental conditions will be given in the paragraphs related to data discussion.

As regards the electrochemical part, a limited surface area ( $1 \text{ cm}^2$ ) of each sample was used for testing; the remaining electrode surface was protected by wrapping it with a Teflon tape. Cyclic voltammetric measurements were performed with an Autolab PGSTAT 20 digital apparatus equipped with a SCANGEN module; measurements were carried out in a three-electrode cell equipped with a Luggin capillary. A double-junction saturated calomel electrode (SCE), and a large-area Pt mesh were used as reference and counter electrodes, respectively.

To investigate the chlorine evolution reaction (ChIER), different chloride solutions, saturated with  $\text{Cl}_2$  at pH  $< 2$ , were employed; the low pH was chosen to suppress the parasitic OER (Oxygen Evolution Reaction) [7]; gaseous chlorine was electrochemically synthesized in a secondary cell, and bubbled into the working cell by means of a silicone pipe connected to a glass frit. A triple-body measuring cell was adopted, where the working and counter electrode

(WE and CE, respectively) compartments were divided by a Nafion membrane. The reference electrode (RE) was placed in another compartment, connected to the WE through a Luggin capillary and a liquid junction bridge (for increasing the impedance of the reference circuit). To attain further information about the mechanism of the ChLER, Electrochemical Impedance Spectrometry (EIS) data were recorded, under different conditions, using a Solartron SI 1287 electrochemical interface coupled with a Solartron SI 1260 impedance/gain-phase analyzer. For improving the data quality, the electrochemical cell was modified by removing the liquid junction between WE and RE, in order to minimize the impedance between them: to avoid the introduction of artifacts, the latter should be less than 1 k $\Omega$  [8]. A quasi-reference electrode was used, which was constituted by an Ag wire covered with a thin layer of AgCl, directly immersed in the chloride-containing WE electrolyte; its potential was evaluated before each test by using a commercial double junction calomel electrode.

The thickness of analyzed films was obtained by RBS, and further confirmed by SEM analyses, carried out on cross sections, as well as using a capacitive  $\alpha$ -profilometer (these investigations were carried out on a limited number of samples, especially prepared for this verification).

Finally, the service-life of electrode devices was evaluated through accelerated tests: galvanostatic polarizations were carried out, under oxygen evolution conditions, in a 15% H<sub>2</sub>SO<sub>4</sub> solution at 55-60 °C, following a protocol suggested by Industrie De Nora [11]. Frequent conditions used for these experiments contemplate a galvanostatic polarization at 30 kA/m<sup>2</sup>, but such a polarization is not advisable in the case of electrodes prepared without any particular treatment of the metal support and without the insertion of a resistant interlayer, so the current density was reduced to 10 kA/m<sup>2</sup>. Tests were carried out in a single-body cell, with a two-electrode system in which WE is the sample to be examined (with a surface of 1 cm<sup>2</sup>), while CE is a Zr plate with a surface of about 4 cm<sup>2</sup>. The deactivation time is typically defined as the period necessary for obtaining an increase in the WE potential of 1 V. The WE is placed in horizontal position for facilitating the detachment of bubbles from the surface; owing to the high current density applied, the production of oxygen is very energetic and the above “trick” appears indispensable.

## Bibliography

1. J.A. Leavitt, L.C. McIntyre Jr., M.R. Weller, *Backscattering Spectrometry, Handbook of Ion beam materials analysis*, **4**, pag. 39-81.
2. L.R. Doolittle, *Nucl. Instr. And Meth.* **B9**, 344 (1985); L.R. Doolittle, *Nucl. Instr. And Meth.* **B15**, 227 (1986).
3. J.C. Barbour, B.L. Doyle, *Elastic Recoil Detection: ERD, Handbook of Ion beam materials analysis*, **5**, p. 83-138.
4. G. Battaglin, A. Carnera, P. Mazzoldi, G. Lodi, P. Bonora, A. Daggetti, S. Trasatti, *J. Electroanal. Chem.* **135**, 313 (1982).
5. L.R. Doolittle, *Nucl. Instr. Meth. Phys. Res.* **B9**, 344 (1985).
6. P. Riello, A. Lausi, J. Macleod, J.R. Plaisier, G. Zeraushek, P. Fornasiero, *J. of Synchrotron Radiation* **20**, 194 (2013).
7. S. Trasatti, G. Lodi, In *Electrodes of Conductive Metallic Oxides, Part B*, Elsevier, 535 (1981); S. Trasatti, *Electrochem. Acta* **36**, 225 (1981).
8. A. Lasia, *Electrochemical Impedance Spectroscopy and its Applications*, Springer, XI, 367 (2014).
9. P. Barricelli, M. Boccardo, G. Maranelli, IT PD 2008 0104 (2008).
10. R.H. Horng, D.S. Wu, L.H. Wu, M.K. Lee, *Thin Solid Films* **373**, 231 (2000).
11. A. Calderara, F. Sala, F. Timpano, WO 2012 101141 A1 (2012).
12. A. Lausi, E. Busetto, M. Leoni, P. Scardi, *Synchrotron Radiation in Nat. Science* **5**, 100 (2006).

## 8. Ex-Situ and On-Site Characterizations

### 8.1. Systematic study of the Iridium and Titanium oxide solid mixture by Wide Angle X-ray Scattering (WAXS)

Several investigations on ruthenium-based electrodes were made, and can be found in literature; attention has been addressed, in particular, to their electrochemical properties for the chlorine and oxygen evolution reactions, but only a few assessments about the correlation between their electrochemical behavior and their morphological and microstructural features have been tempted. One of the first interesting works has been proposed by Pizzini *et al.* [1], who tried to correlate the conductive properties of films based on ruthenium and titanium oxides, prepared at different temperatures and with different methods, to the content of chloride entrapped in the bulk structure of electrodes obtained by the pyrolysis of salt precursors. Other interesting articles were published by O’Leary and Navin in 1974 [2], by Hine *et al.* in 1977 [3] and by Gerrard and Steel in 1978 [4]: the nature of the mixture was studied, highlighting the importance of the metastable solid solution formed by iridium and titanium. More recently, a very exhaustive work on the properties of binary rutile compounds ( $\text{MO}_2$ , where  $M = \text{Ir, Ru, Sn and Ti}$ ) was carried out by Novell-Leruth *et al.* [5] through computational modeling (DFT, Density Function Theory), for investigating the interactions, solubility and segregation phenomena that occur when different metal oxides are mixed.

An extensive structural characterization of the mixture composed by iridium and titanium oxides has been carried out within this work of thesis, through WAXS analysis on samples prepared “ad hoc” on supports of amorphous silica. The information obtained, and discussed in this paragraph, has been taken into account for explaining the electrochemical properties (as it will be discussed later). As described in the “Experimental details” section (Chapter 7), films of 2  $\mu\text{m}$  thickness were deposited by the Sol-gel technique, changing the operative variables: composition of aqueous precursors solutions and preparation temperature. Because of the nature of the sol-gel preparation, both crystalline and amorphous domains are formed; since, as is well known, iridium and titanium cations partially satisfy the Hume-Rothery rules [6], a solid solution can be formed. In particular, there are two sets of rules: one refers to substitutional solutions, while the other to interstitial ones. In relation with the first family, the following conditions must be respected:

- The atomic radius of solute and solvent atoms cannot differ by more than 15%:

$$\text{difference \%} = \frac{r_{\text{solute}} - r_{\text{solvent}}}{r_{\text{solvent}}} \times 100$$

- The crystal lattices of solute and solvent must match.
- Complete solubility occurs when the solvent and solute have the same valency; a metal will dissolve a metal of higher valency to a greater extent than one of lower valency.
- The species have to have a similar electronegativity. If the electronegativity difference is too large, intermetallic compounds may be formed instead of solid solutions.

The second family of rules is reported here for completeness, but our case does not involve the formation of interstitial solutions, because of the characteristics of the iridium and titanium atoms.

- Solute atoms must be smaller than the interstitial sites present in the solvent lattice.
- Atoms must have similar electronegativity.

Iridium and titanium are characterized from atomic radii of 187 and 140 pm, respectively, and their percentage difference is higher than 30%. However, regarding the other three Hume-Rothery rules, the requirements are verified: the electronegativity is quite similar (1.54 for Ti, and 2.20 for Ir, using the Pauling scale); iridium oxide can crystallize in the rutile form under the examined experimental conditions, while titanium oxide can assume either a rutile or an anatase form, depending on the operative parameters; the latter lattice is favored because of kinetic reasons [7]. A representation of the elementary cell of the cited crystallographic systems is reported in Fig.8.1. The rutile crystal of ruthenium oxide is reported instead of iridium oxide, but it doesn't represent a problem because elementary cells are quite similar.

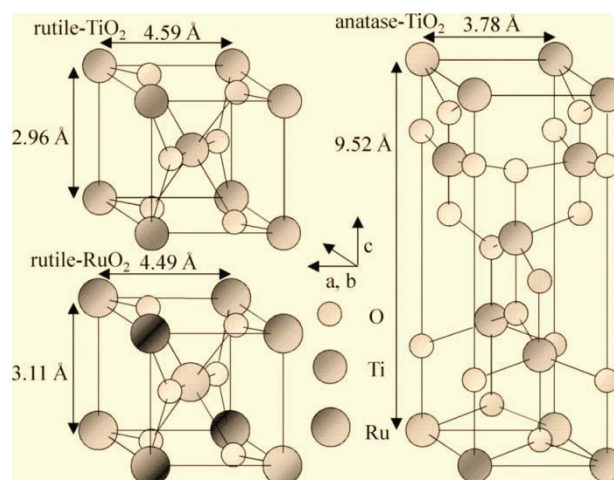


Fig.8.1. Elementary cells for rutile-TiO<sub>2</sub> and RuO<sub>2</sub>, on the left, and for anatase-TiO<sub>2</sub>, on the right. The anatase form is characterized by a larger cell volume, and the packaging of the tetrahedral units in the lattice is less efficient.

Therefore, the considered oxides satisfy the 75% of the conditions for obtaining a solid substitutional solution.

Table 8.1 reports characteristics of the lattices for the different crystallization forms of titanium oxide; the information was extracted from the database of the International Centre for Diffraction Data [8].

	<b>Rutile</b>	<b>Anatase</b>	<b>Brookite</b>
	<b>TiO<sub>2</sub></b>	<b>TiO<sub>2</sub></b>	<b>TiO<sub>2</sub></b>
<i>Form. Wt.</i>	79.890	79.890	79.890
<i>Z</i>	2	4	8
<i>Crystal System</i>	Tetragonal	Tetragonal	Orthorhombic
<i>Point group</i>	4/mmm	4/mmm	mmm
<i>Space group</i>	P4 <sub>2</sub> /mnm	I4 <sub>1</sub> /amd	Pbca
<i>Unit cell</i>			
<i>a (Å)</i>	4.58	3.78	9.18
<i>b (Å)</i>	4.58	3.78	5.45
<i>c (Å)</i>	2.95	9.52	5.15
<i>Volume (Å<sup>3</sup>)</i>	62.07	136.25	257.38
<i>Molar Volume</i>	18.69	20.16	19.38
<i>Density (g/l)</i>	4.2743	3.895	4.123
<i>Thermal</i>			
<i>Expansion(Volumetric)</i>			
<i>alpha (K<sup>-1</sup>)</i>	28.9		
<i>a<sub>0</sub></i>	0.2890		

Tab.8.1. Different crystallographic forms of titanium oxide: features.

Omitting the brookite form (whose formation is possible only by working at high values of pressure and temperature), the rutile form represents the stable structure from a thermodynamic point of view, while anatase is kinetically easier to obtain. Tab.8.2 collects the most important characteristics of rutile IrO<sub>2</sub>, as they appear in the ICDD database.

<b>Rutile</b>	
<b>IrO<sub>2</sub></b>	
<i>Form. Wt.</i>	224.22
<i>Z</i>	2
<i>Crystal System</i>	Tetragonal
<i>Point group</i>	4/mmm
<i>Space group</i>	P4 <sub>2</sub> /mnm
<i>Unit cell</i>	
<i>a (Å)</i>	4.50
<i>b (Å)</i>	4.50
<i>c (Å)</i>	3.15
<i>Volume (Å<sup>3</sup>)</i>	63.83
<i>Molar Volume</i>	
<i>Density (g/l)</i>	11.666
<i>Thermal</i>	
<i>Expansion(Volumetric)</i>	
<i>alpha (K<sup>-1</sup>)</i>	
<i>a<sub>0</sub></i>	

Tab.8.2. Parameters of the rutile form of Iridium oxide (Pattern 00-043-1019 – Calculated).

As anticipated in Par.6.3, specific M-HAC aqueous precursors were used, at different ratios, in order to obtain the following film compositions:

1. IrO<sub>x</sub>-TiO<sub>x</sub> 5:95%mol;
2. IrO<sub>x</sub>-TiO<sub>x</sub> 10:90%mol;
3. IrO<sub>x</sub>-TiO<sub>x</sub> 20:80%mol;
4. IrO<sub>x</sub>-TiO<sub>x</sub> 50:50%mol;
5. IrO<sub>x</sub>-TiO<sub>x</sub> 80:20%mol;
6. IrO<sub>x</sub>-TiO<sub>x</sub> 90:10%mol.

Each mixture was synthesized by firing the precursors at 4 different calcination temperatures: 250, 350, 450 and 550 °C. All X-ray diffractograms were collected by inspecting the interval of 2-θ between 15 to 90°; then, two spectra pertaining to samples calcined at 550 °C (Fig.8.2) have been taken in consideration for signals assignment.



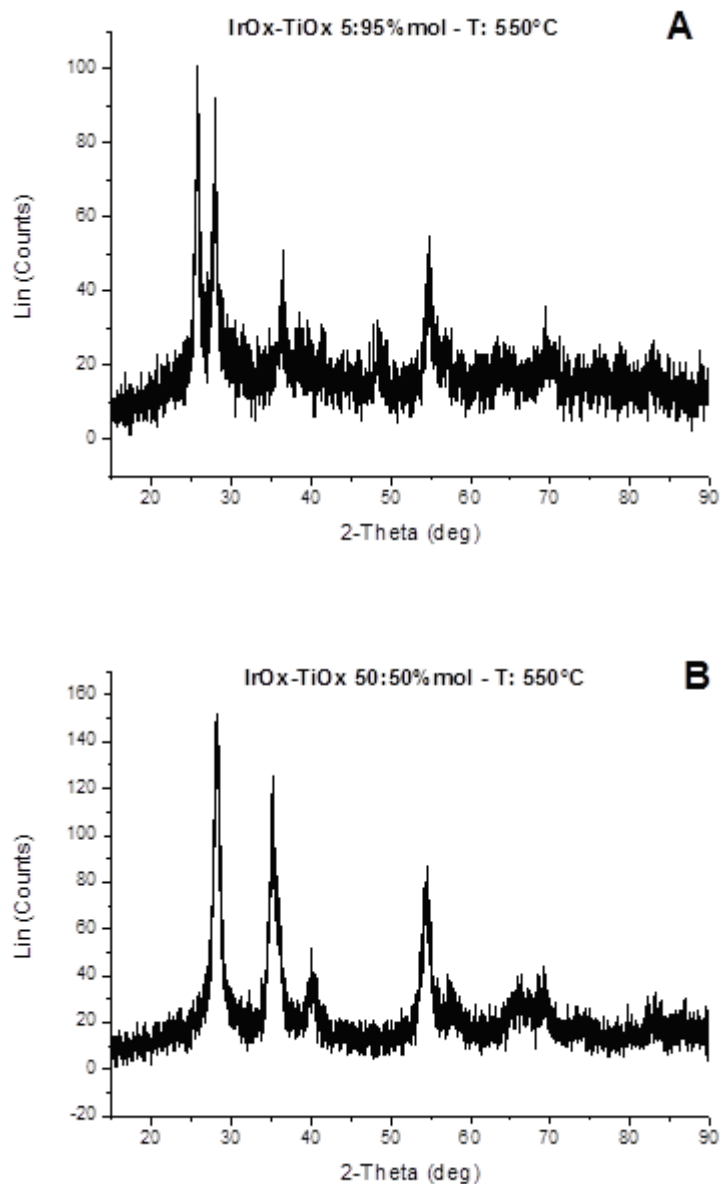


Fig.8.2. X-ray diffraction patterns of IrO<sub>x</sub>-TiO<sub>x</sub> 5:95 %mol (A) and IrO<sub>x</sub>-TiO<sub>x</sub> 50:50 %mol (B), prepared at 550 °C.

The structure of the sample appears quite complex, formed by both (nano)crystalline and amorphous fractions, as well as by different phases. As demonstrated by De Battisti and coworkers, by working on samples prepared via sol-gel, the presence of chemical impurities (carbon and/or hydrogen) in amounts comparable with those of the main components (metal ions, oxygen) [9] causes the formation of crystallites that are separated by large amorphous zones; the organic impurities accumulate in the latter [10]. These impurities derive mainly from an incomplete pyrolysis of precursors and minimally by an “encapsulation” of atmospheric water.

Because of the possible overlap between peaks and of the complexity of the studied system, a proposal of attribution of lattice planes has been tempted, as shown in Tab.8.3.

<b>2-Theta (deg)</b>	<b>Lattice planes</b>	<b>Crystalline phase</b>
25.65	(101)	Anatase
27.00 – 28.00	(110)	Rutile
34.00 – 36.00	(101)	Rutile
40.15	(111)	Rutile
		(IrO <sub>2</sub> : 40.23°; TiO <sub>2</sub> : 41.19°)
48.40	(202)	Anatase
54.85	asymmetric signal, probably due to a convolution of different signals: (211), (105), (211)	TiO <sub>x</sub> -rutile/anatase and IrO <sub>x</sub> -rutile
57.00	(220)	Anatase
65.00 – 69.00	(310), (301)	Rutile

Tab.8.3. Tentative assignment of signals.

At first, the effect of the temperature was examined: an analysis of diffraction patterns of the samples calcined at 250 °C (Fig.8.3) evidences the formation of completely amorphous phases (the broadened peak that falls at around 25° is a characteristic of the substrate made of amorphous silica).

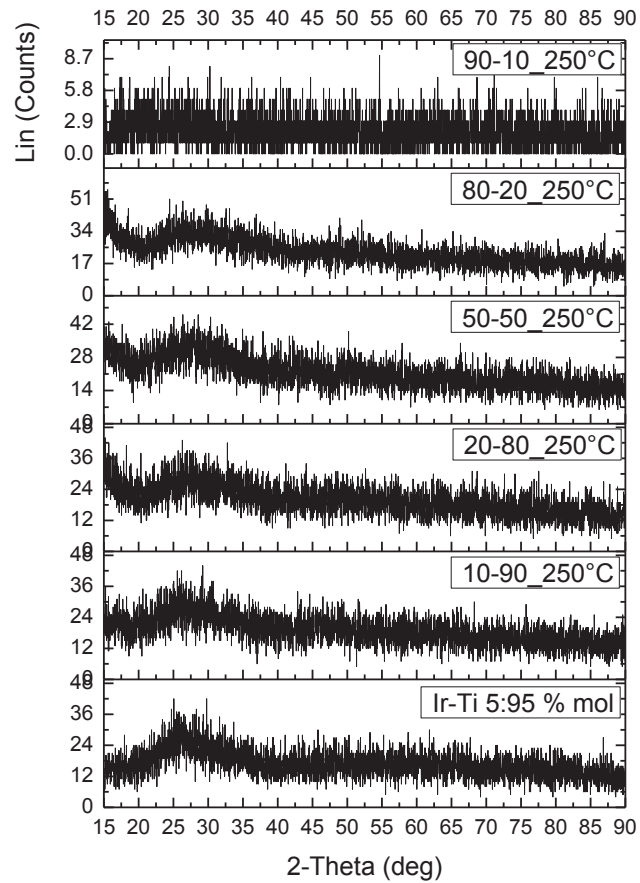


Fig.8.3. Diffractograms of samples prepared at 250 °C; in the figure, Iridium oxide concentration in the mixture decreases from top to the bottom.

The first hints for a peak formation, which are not very intense and the signals are rather broadened, has been assessed at 350 °C, for the highest iridium concentrations (Fig.8.4): this value of temperature seems to represent a sort of critical point to obtain distinguishable crystalline regions.

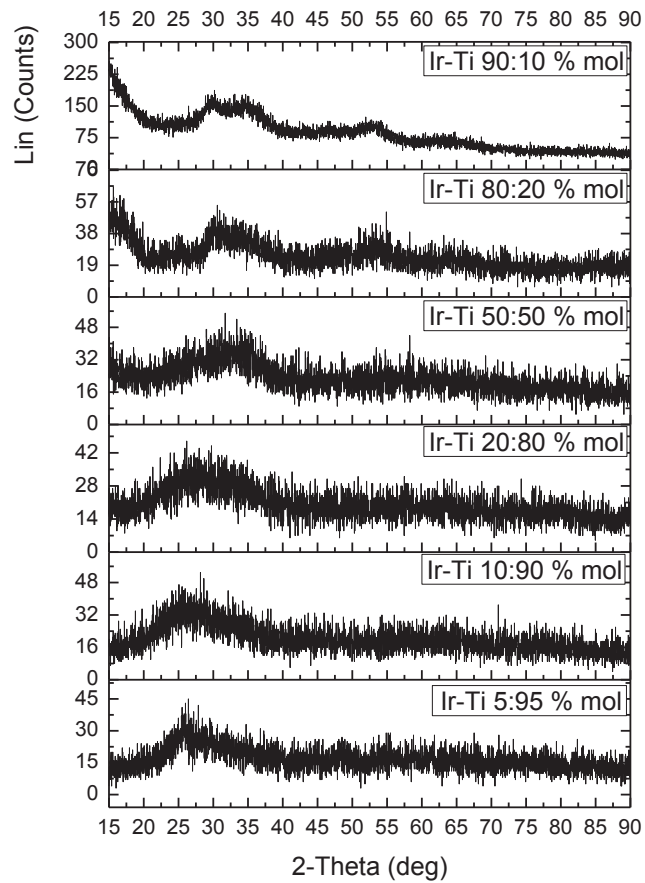


Fig.8.4. Diffractograms of samples prepared at 350 °C; in the figure, Iridium oxide concentration in the mixture decreases from top to the bottom.

Diffractograms of samples prepared at 450 and 550 °C are reported in Fig.8.5 and 8.6, respectively.

The relation proposed by Scherrer [11] was used to determine the average size of crystallites, along a given diffractometric direction (Eq.8.1).

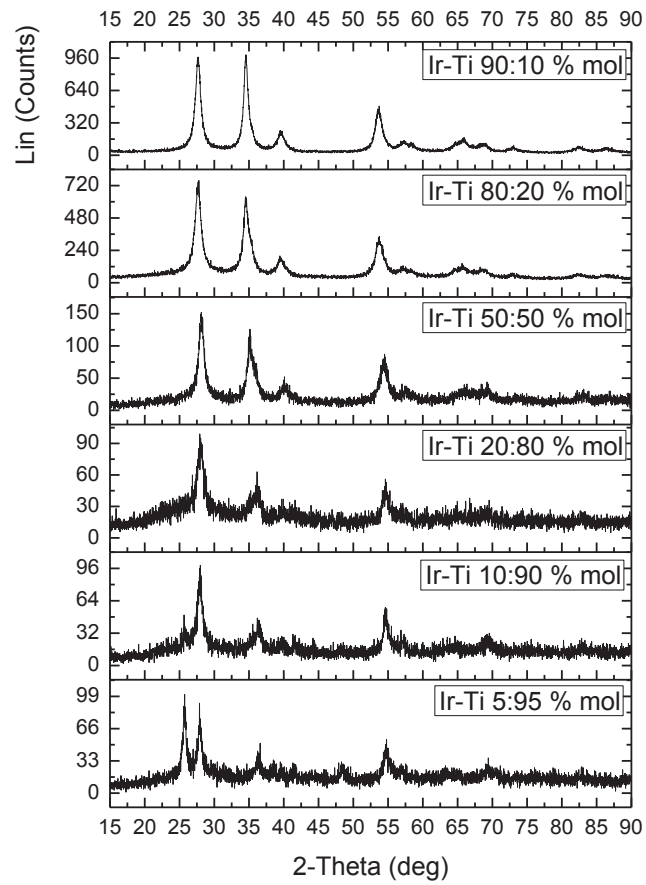


Fig.8.5. Diffractograms of samples prepared at 450 °C; in the figure, Iridium oxide concentration in the mixture decreases from top to the bottom.

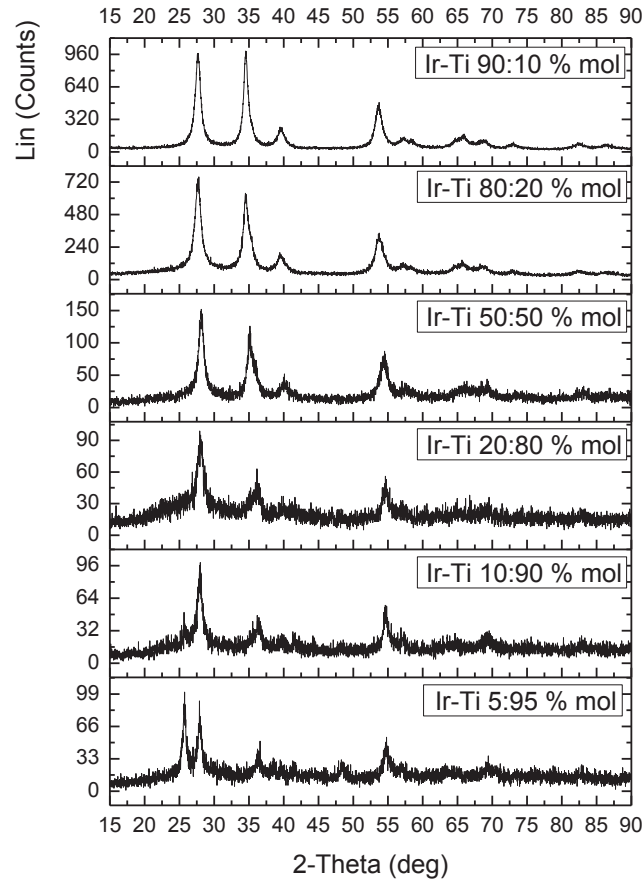


Fig.8.6. Diffractograms of samples prepared at 550 °C. in the figure, Iridium oxide concentration in the mixture decreases from top to the bottom.

$$t = \frac{B\lambda}{FWHM \cos \vartheta} \quad \text{Eq.8.1}$$

In Eq.8.1,  $t$  stands for the average dimension of crystallites along a particular crystallographic direction,  $B$  is a constant parameter that depends on the shape of grains (in our case it was assumed equals to 1, assuming spherical-shaped particles);  $FWHM$  is the acronym of “*Full Width at Half Maximum*”, expressed in radians and, eventually,  $\vartheta$  represents the half of the center of peak maximum on the abscissa axe, expressed in radians too. Calculations were done for samples prepared at 450 and 550 °C considering specific lattice directions, related to more intense and well-defined peaks (Tab.8.4).

<b>IrO<sub>2</sub> –TiO<sub>2</sub> %mol</b>	<b>T(°C)</b>	<b>2-theta(°)</b>	<b>Plane and Phase</b>	<b>t (Å)</b>
5:95	450	27.9683	(110) Rutile	<b>87</b>
	550	27.9035		<b>96</b>
	450	36.4353	(101) Rutile	<b>90</b>
	550	36.3190		<b>82</b>
10:90	450	27.9811	(110) Rutile	<b>88</b>
	550	27.9660		<b>111</b>
	450	36.2214	(101) Rutile	<b>68</b>
	550	36.2803		<b>70</b>
20:80	450	27.9639	(110) Rutile	<b>86</b>
	550	28.0054		<b>83</b>
	450	35.9985	(101) Rutile	<b>54</b>
	550	35.9869		<b>48</b>
50:50	450	28.1110	(110) Rutile	<b>80</b>
	550	28.1422		<b>92</b>
	450	35.5495	(101) Rutile	<b>61</b>
	550	35.3096		<b>60</b>
80:20	450	27.6264	(110) Rutile	<b>79</b>
	550	27.6672		<b>80</b>
	450	34.5110	(101) Rutile	<b>97</b>
	550	34.6415		<b>70</b>
90:10	450	27.6538	(110) Rutile	<b>69</b>
	550	27.6681		<b>89</b>
	450	34.4971	(101) Rutile	<b>88</b>
	550	34.5844		<b>106</b>
5:95	450	37.4229	(101) Rutile	<b>17</b>
	550	36.3190		<b>82</b>
10:90	450	36.2214		<b>68</b>
	550	36.2803		<b>70</b>
20:80	450	35.9985		<b>54</b>
	550	35.9869		<b>48</b>
50:50	450	35.5495		<b>61</b>
	550	35.3096		<b>60</b>
80:20	450	34.5110		<b>97</b>
	550	34.6698		<b>68</b>
90:10	450	34.4971		<b>88</b>
	550	34.5844		<b>106</b>

Tab.8.4. Summary of average crystallite dimensions, estimated using the Scherrer formula.

The error associated to this evaluation can be estimated around 20%; on the basis of data, the following findings can be drawn: as expected, the temperature favors the formation of more extended crystalline domains and, in general, the dimensions of crystallites can vary in different ways, along different lattice planes; in certain cases, the average sizes remain unvaried.

Concerning the effect of the composition, interesting information about the system can be obtained by inspecting Fig.8.7.

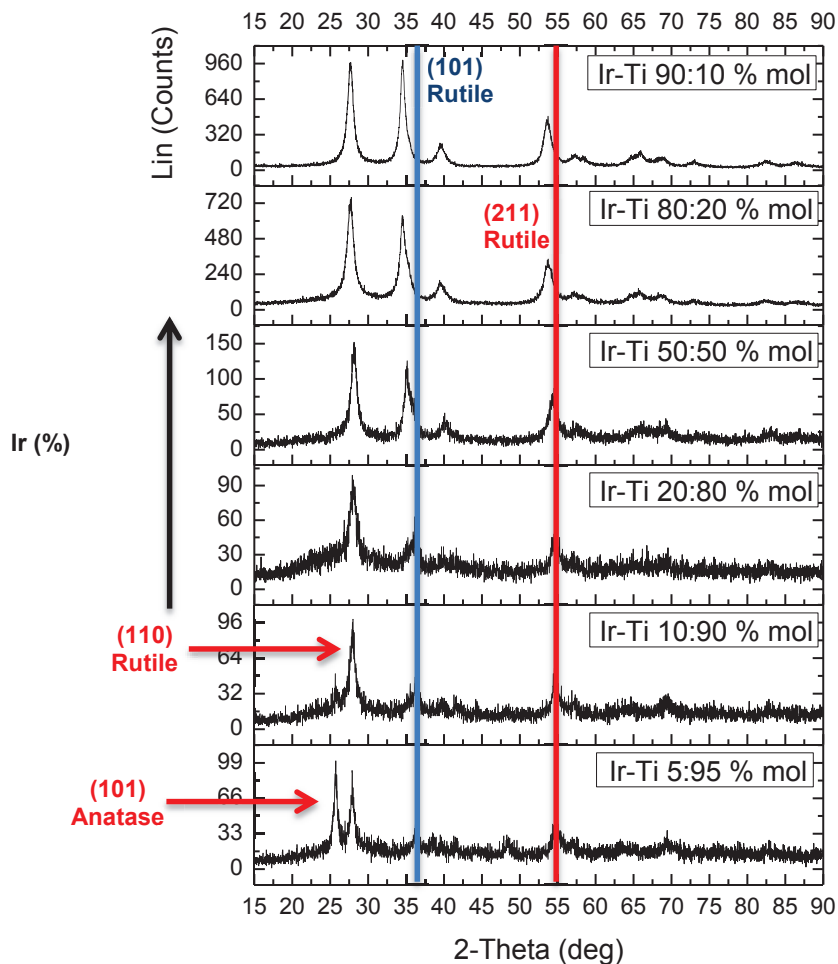


Fig.8.7. Diffractograms of samples with different iridium concentration, prepared at 550 °C.

When titanium oxide is the main component in the mixture, its crystallization occurs preferentially under the form of anatase, because of kinetic reasons [7]: both the temperature (as underlined before) and the relative concentration promote the formation of this metastable structure. By increasing the concentration of iridium oxide, the crystallinity degree of all the system appears increasing, and titanium centers seem to be forced to assemble in a rutile-type cell: in fact, observing for example the peak associated to the (101) family of anatase, it can be noted that it decreases in intensity when moving from the composition Ir-Ti 5:95 %mol to the 10:90 %mol, and that it completely disappears when iridium and titanium have the same molar abundance. The multiphase character of the IrO<sub>2</sub>-TiO<sub>2</sub> coatings is possibly caused by the nature of precursors used: the different degree of hydrolysis of the complexes may lead to



a very heterogeneous organization of metal centers in the structure, as discussed by Roginskaya et al. in relation to chloride precursors of iridium and titanium [12].

Moreover, the partial formation of a substitutional solid solution is manifested through the shift of two of the highest signals (highlighted by the red and blue vertical straight lines in Fig.8.7), i.e., the (101) and (201) family planes of rutile, which were considered for calculating the cell parameters. Because of the symmetry of the tetragonal cell ( $a = b \neq c$ ;  $\alpha = \beta = \gamma = 90^\circ$ ), only two equations are necessary to solve the problem of evaluating the variation of the volume of the cell, in function of the iridium oxide concentration. The equation that relates the inter-planar distances to the Miller indexes for the tetragonal lattice is (Eq.8.2):

$$\frac{1}{d_{hkl}^2} = \frac{h^2 + k^2}{a^2} + \frac{l^2}{c^2} \quad \text{Eq.8.2}$$

Substituting the values of indexes (h, k, l) and of plane distances ( $d_{hkl}$ ) for the considered signals, it is possible to write a two equations system, where the parameters  $a$  and  $c$  can be calculated through its resolution:

$$\begin{cases} \frac{1}{d_{101}^2} = \frac{h^2}{a^2} + \frac{l^2}{c^2} = \frac{1}{a^2} + \frac{1}{c^2} \\ \frac{1}{d_{211}^2} = \frac{h^2 + k^2}{a^2} + \frac{l^2}{c^2} = \frac{5}{a^2} + \frac{1}{c^2} \end{cases} \quad \text{Eq.8.3}$$

The values of  $d_{hkl}$  can be easily determined on the basis of the Bragg's equation (Eq.8.4), assuming a first order of diffraction ( $n=1$ ):

$$d_{hkl} = \frac{\lambda}{2 \sin \vartheta} \quad \text{Eq.8.4}$$

where  $\lambda=1.54 \text{ \AA}$  (wavelength of the Cu  $K\alpha$  radiation used as beam for the analysis), and  $\vartheta$  can be deduced by the position of peaks in the diffractograms.

By carrying out the calculations and correlating the values of cell volume (Tab.8.5) to the concentration of iridium, a good linearity is obtained, in agreement with the Vegard's law (Fig.8.8), which is thus satisfyingly verified along the whole range of explored concentrations.

<b>Data relative to samples prepared at 550 °C</b>			
<b>IrO<sub>2</sub> (%)</b>	<b>a (Å)</b>	<b>c (Å)</b>	<b>V<sub>cell</sub> (Å<sup>3</sup>)</b>
<b>5</b>	4.54	2.95	<b>60.80</b>
<b>10</b>	4.56	2.95	<b>61.34</b>
<b>20</b>	4.54	2.98	<b>61.42</b>
<b>50</b>	4.49	3.11	<b>62.70</b>
<b>80</b>	4.52	3.17	<b>64.76</b>
<b>90</b>	4.53	3.17	<b>65.05</b>

Tab.8.5. Results of calculations done for verifying the Vegard's law.

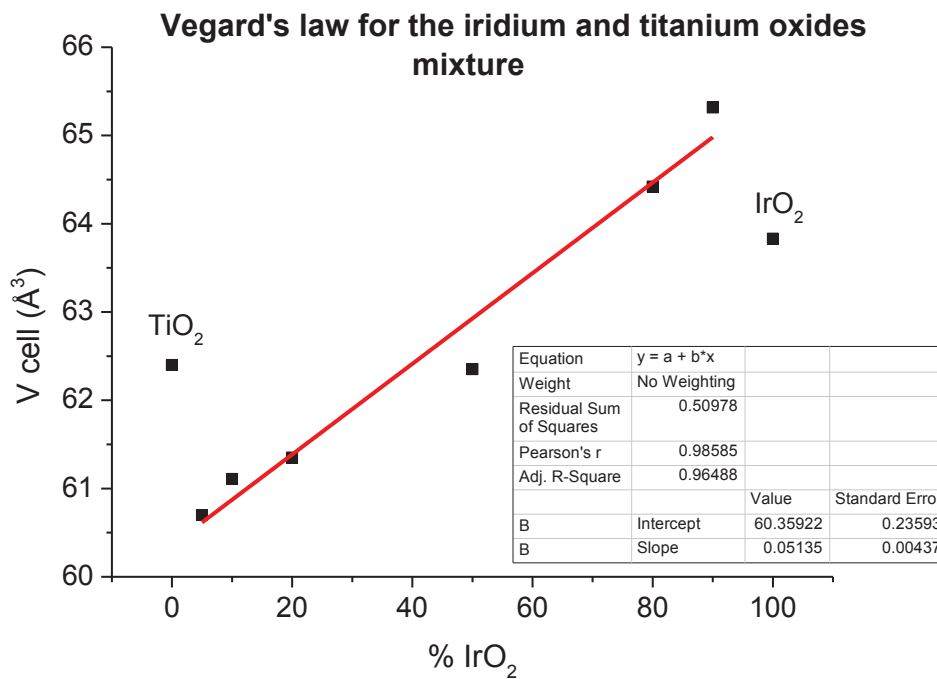


Fig.8.8. Vegard plot for the different mixtures based on iridium and titanium oxides.

The volume of the cell has been plotted, instead of the single lattice parameters, because the analogous plot for  $a = b$  has shown to be difficult to explain: this is quite normal for species that don't completely satisfy the Hume-Rothery's laws, i.e. the cell can grow differently along the three crystallographic directions [13].

## 8.2. Calcination process investigated through synchrotron light

The synchrotron light was used for investigating the behavior of precursor salts during pyrolysis, trying to gain information about the grow of the crystalline phases.

Fig.8.9 reports an example of a series of diffractograms collected between 100 and 1000 °C for the mixture  $\text{IrO}_x\text{-TiO}_x$  33:67 % mol (the composition chosen to synthesized the electrode devices studied in this work of thesis).

Peak identification was carried out by considering the  $s$  parameter, which is defined as follows:

$$s = \frac{2 \sin \vartheta}{\lambda} \quad \text{Eq.8.5}$$

where  $\vartheta$  is the angle at which the peak falls, and  $\lambda$  is the wavelength used as source for generating the pertaining diffraction spectrum. This strategy allows to compare experimental results collected through X-ray radiations having different wavelength.

### $\text{IrO}_2\text{-TiO}_2$ 33:67% mol

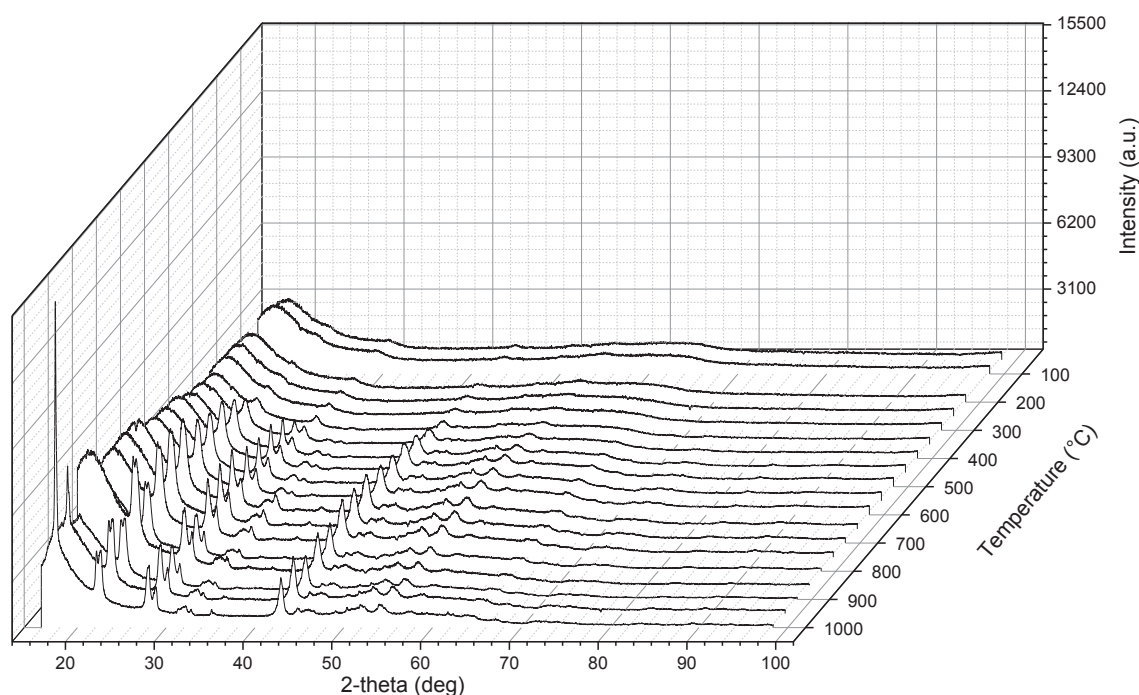


Fig.8.9. Diffractograms of the  $\text{IrO}_x\text{-TiO}_x$  33:67 %mol collected by increasing the calcination temperature in continuum.

The specimen remains substantially amorphous up to 400 °C; then, by increasing further the temperature, a crystallization process starts, and the characteristic rutile-phase peaks can be recognized. A sort of inertia is shown, probably because of the continuously increasing pyrolysis conditions, and the temperature at which the crystallization starts is somewhat retarded with respect to cases presented in Par. 8.1. The crystallites seem to grow preferentially along the (110) direction. Unlike the ruthenium-titanium oxide phases, already reported in literature [4], the phase diagram of the oxides of iridium and titanium seems to be characterized by a higher degree of complexity: the resolution allowed by the synchrotron light highlights the coexistence of at least two phases: in all probability, one is richer in iridium oxide while the other in titanium oxide. It is known that oxides of iridium and titanium partially satisfy the Hume-Rothery's conditions, and the formation of a solid solution between them is thus possible. However, for temperatures higher than 650-700 °C, the oxide phase seems to separate into two distinct tetragonal lattices (well visible by analyzing the (110) peak at about  $2\text{-Theta}$ : 22.4°, Fig.8.10). The intense and thin peak that appears at angles  $< 20^\circ$  and arises at 900 °C is characteristic of the cristobalite structure, caused by the thermal treatment on the silica capillary [14].

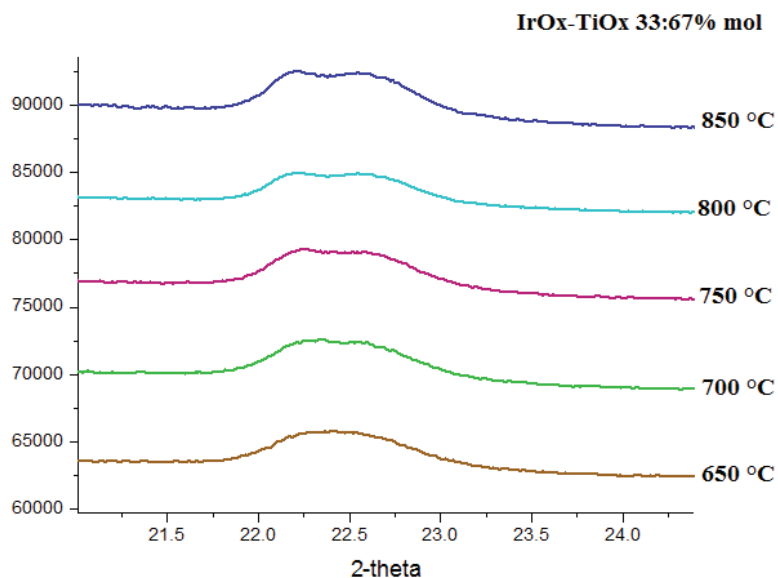


Fig.8.10. Demixing of the phases in the case of IrO<sub>2</sub>-TiO<sub>2</sub> 33:67 %mol, when increasing the temperature to over 700 °C.

The diffractograms collected at 600 °C, by varying the composition of the mixtures, are reported in Fig.8.11; as it can be seen, when the titanium oxide concentration is dominant, the presence of signals related to anatase can be clearly attested. However, when the iridium oxide concentration becomes higher than 30 %mol, the titanium oxide is forced to crystallize in the rutile form. Moreover, the average crystallinity of the system seems to improve by increasing the iridium content.

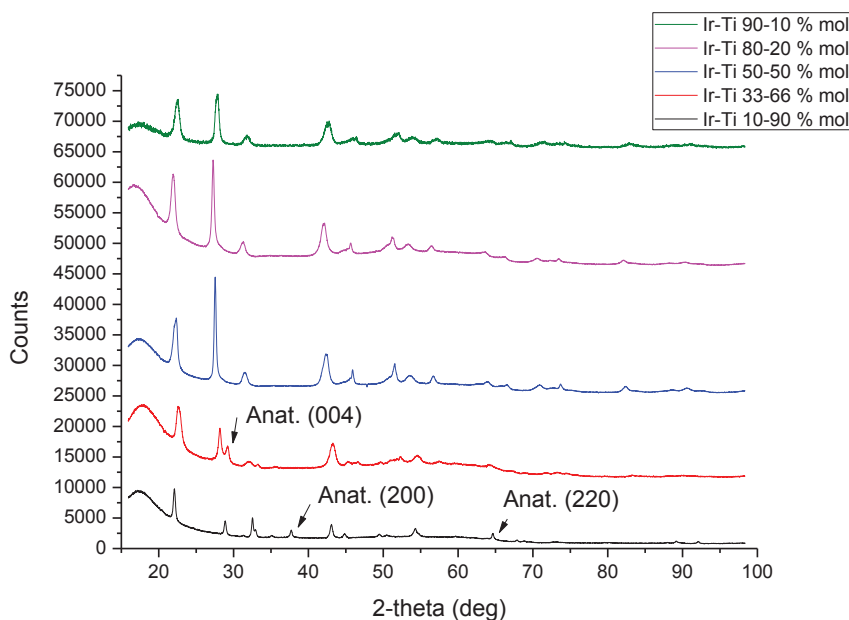


Fig.8.11. Diffractograms collected at 600 °C, by varying the iridium/titanium compositional ratio of the analyzed samples.

Several evidences obtained in this section confirm the experimental picture described in Par.8.1.

In addition, for the pure iridium-based precursor, a pyrolysis in absence of oxygen was also carried out, in order to investigate the behavior of this component that seems to strongly force the thin film evolution. As expected, a crystallization of the system is obtained only for temperatures higher than 550 °C: the absence of oxidative conditions hinders the formation of the oxide lattice; interestingly, the appearance of another phase could be witnessed, as shown in Fig.8.12, which started to be visible at 500 °C.

The signal associated to this phase, that overlaps to the peak of the capillary quartz, is probably associated to  $\text{IrCl}_3$ ; actually, the presence of a low oxidation state, for the electrocatalytic metal centers, may have important consequences in terms of electrochemical properties of the film, when they are subjected to polarization under chlorine and/or oxygen evolution conditions (anodic polarization). A calcination in absence of oxygen can reproduce what happens in the deeper layers of the material, during the assembly of an industrial electrodic device: the presence of sites with a low oxidation state can induce modifications in the neighboring metal sites, thus affecting the catalytic pathway for the processes that may occur at the electrode surface.

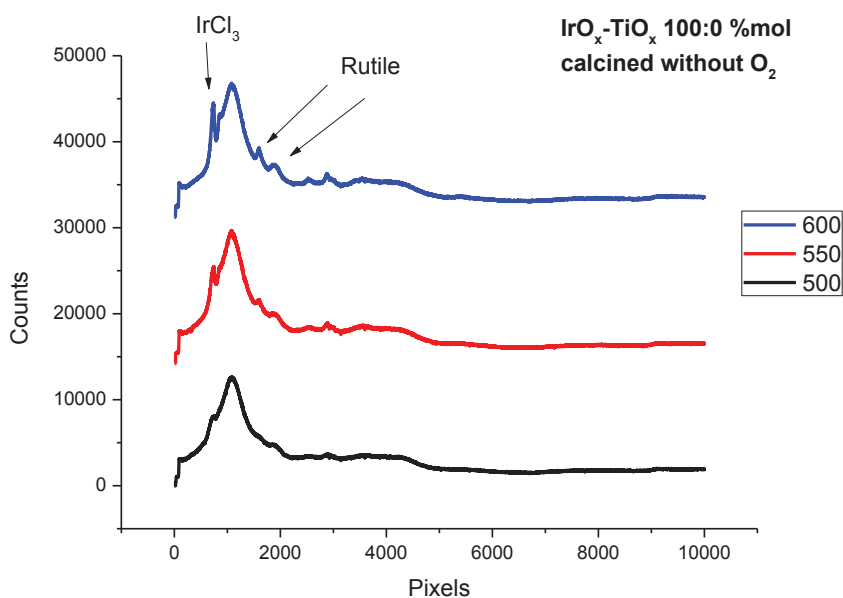


Fig.8.12. Diffractograms collected at 500, 550 and 600 °C for the pure iridium precursor.

Of course, further investigation is necessary to confirm this hypothesis.

### 8.3. WAXS analysis of coatings deposited on Ti-supports

The diffractometric analysis, carried out on coatings deposited on metal supports, appears quite disturbed by contributions related to the latter, which are manifested through intense spikes from  $40^\circ < 2\theta < 70^\circ$ ; anyway, a semi-quantitative treatment can be still done. Fig.8.13 collects some diffractograms, together with the assignment of peaks.

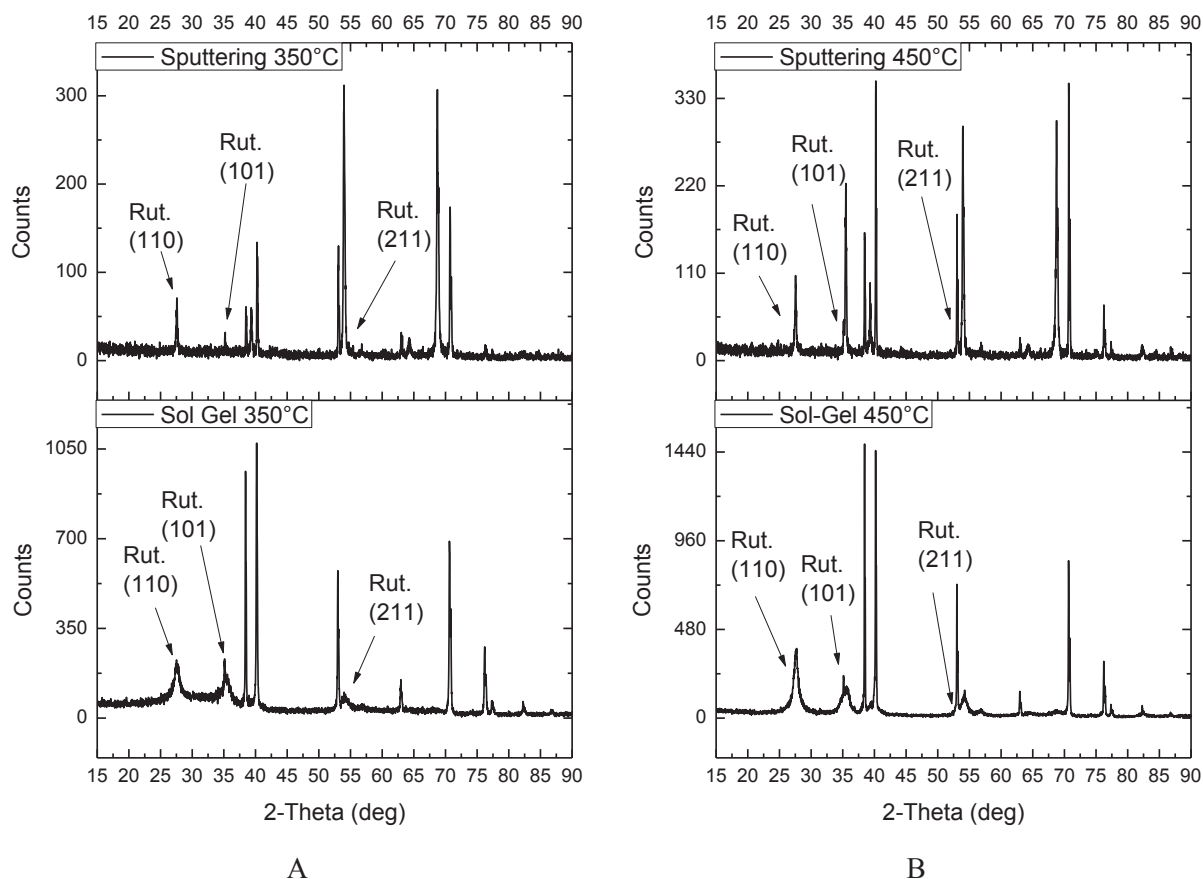


Fig.8.13. X-Ray diffractograms registered for Sol-Gel and sputtered samples, prepared at (A) 350 and (B) 450 °C.

Films comprise both crystalline and amorphous portions and, in general, the sputtered samples are characterized by a lower degree of crystallinity. Only the rutile-type phase appears, which seems to grow preferentially along the (110) direction, probably for kinetic reasons, as already verified for film deposited on amorphous silica. Looking at the diffractograms of Sol-Gel samples, the most important signals, which fall at about  $2\theta = 27^\circ$ ,  $35^\circ$  and  $54^\circ$ , appear asymmetric, thus suggesting the existence of multiple components; at least two phases exist, one probably richer in iridium and the other in titanium oxide. In the

case of sputtered samples, the symmetry of signals is better, and also the FWHM is sensitively lower, indicating a larger average dimension of crystallites.

As anticipated, the average dimension of crystallites is clearly higher for sputtered samples, and this can indicate a greater compactness in the structure.

Some peak signals showed to be difficult to assign, as the one that appears at about 38° (only in the diffractograms of sputtered deposits), between two intense signals related to the Ti support; such kind of not-easily-assignable signals have been attributed to other phases, with different stoichiometry in oxygen. During deposition with both techniques, the deeper layers of material are pyrolyzed in an atmosphere poor of oxygen and can thus crystallize in a structure with a high concentration of oxygen vacancies (this applies especially for titanium oxide) [15].

The volume of the cell was estimated focusing on (110) and (211) peaks, by using equations linked to the tetragonal lattice characteristics of the rutile cell (as proposed in Eq.8.6), as it was explained in the previous paragraph, in relation with samples deposited on amorphous silica.

$$\left\{ \begin{array}{l} \frac{1}{d_{110}^2} = \frac{h^2}{a^2} + \frac{k^2}{a^2} = \frac{2}{a^2} \\ \frac{1}{d_{211}^2} = \frac{h^2 + k^2}{a^2} + \frac{l^2}{c^2} = \frac{5}{a^2} + \frac{1}{c^2} \end{array} \right. \quad \text{Eq.8.6}$$

The values of calculated cell volumes have been summarized in Tab.8.6; all estimated values fall between the values of volumes for IrO<sub>2</sub> and TiO<sub>2</sub> reported in literature (63.83 [16] and 62.40 Å<sup>3</sup> [17], respectively).

<b>Sample</b>	<b>a (Å)</b>	<b>b (Å)</b>	<b>V (Å<sup>3</sup>)</b>
<b>Sol-Gel 350 °C</b>	4.570	3.011	<u>62.90</u>
<b>Sol-Gel 450 °C</b>	4.563	3.023	<u>62.95</u>
<b>Sput. 350 °C</b>	4.569	3.020	<u>63.07</u>
<b>Sput. 450 °C</b>	4.573	3.018	<u>63.13</u>

Tab.8.6. Calculated cell volumes, for the investigated electrode materials.

Both the presence of iridium and the formation of a partial solid solution, represent a stress for the titanium-oxide cell (the main component in the mixture); the temperature of preparation does not seem to influence the lattice, but, conversely, a modification is induced by the method of preparation. Reactive sputtering allows a vertical growth of the coatings,

while, in the case of Sol-Gel coatings, the oxide-based material developed layer by layer without suffering particular stresses; the gel scaffold is heavily conditioned by the water removal, during dehydration, and this is probably the cause of the higher cell volumes obtained in that case.

## 8.4. RBS analysis of electrode materials

A first analysis was carried out by means of RBS on “as prepared” samples (about 1  $\mu\text{m}$  of thickness), in order to evaluate the status of the material (in terms of quality and features) just after its preparation. The analyzed Sol-Gel films were prepared on electro-polished titanium supports and they are the same used for the electrochemical characterization that will be discussed in the following paragraphs; with regard to sputtered specimens, the RBS analyses were performed on films synthesized on silicon supports. In fact, the sputtering deposition allows the simultaneous depositions of films with the same characteristics on different supports, and silicon-supported samples were used for RBS tests in order to avoid the contribution of titanium due to the support.

Sputtered specimens are characterized by well interpretable spectra: peaks appear well defined and resolved (Fig.8.14 A & B); the characteristics of the preparation methods allow to reach a good uniformity and a low roughness on the surface, besides a negligible content of impurities such as carbon, chlorine, etc., which are on the contrary the cause of the noise in data collected from Sol-Gel films (Fig.8.15).

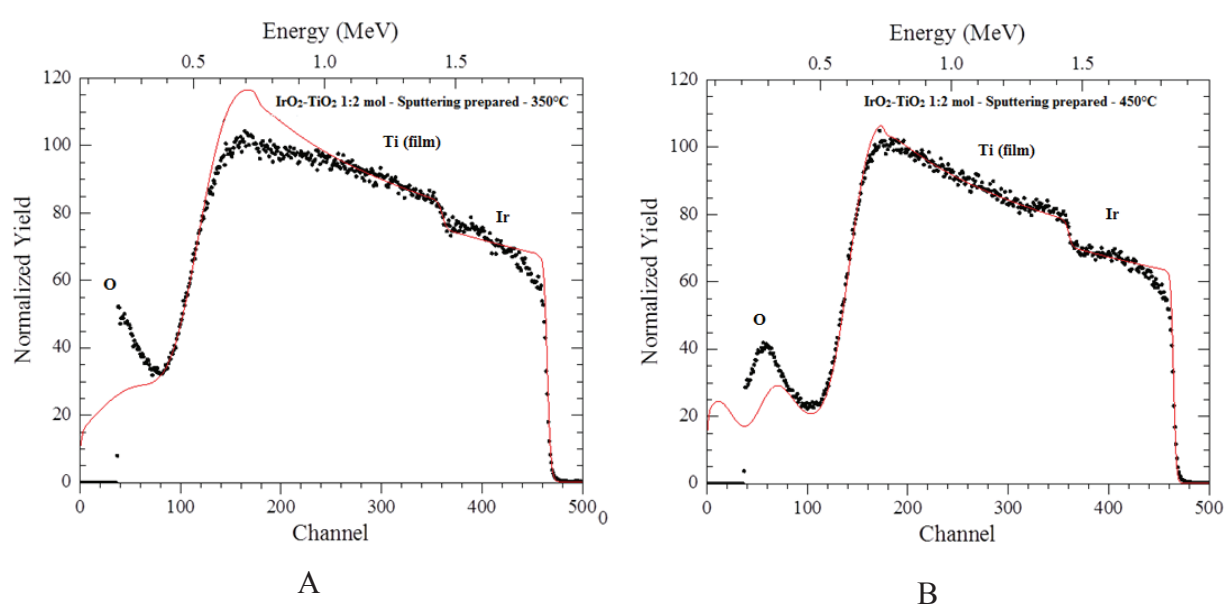


Fig.8.14. RBS spectra for samples of 1 $\mu\text{m}$  thickness, synthesized by sputtering on titanium supports, at (A) 350 and (B) 450  $^{\circ}\text{C}$ .



Analyzing the spectrum in Fig.8.14 A using RUMP data analysis, some interesting information can be deduced, such as the surface density (that amounts to  $3750 \times 10^{15}$  mol/cm<sup>2</sup>), and molar stoichiometry of the sample, which comes out to be Ir: 0.42, Ti: 0.58, O: 2 ( $\pm 0.05$ ). Concerning the spectrum in Fig. 8.14 B, the surface density is of  $3550 \times 10^{15}$  mol/cm<sup>2</sup>, while the stoichiometry is Ir: 0.41, Ti: 0.59, O: 2 ( $\pm 0.05$ ). Both samples are a little bit richer in iridium than expected, and this may be due to the low cross-section sputtering of titanium: these small variations in atomic ratios are normal in these kind of depositions and were considered not relevant for the work purposes. Another interesting value that can be inferred from spectra is the Straggle, i.e. a measure of the entity of the energy dispersion of backscattered particles, which is proportional to the roughness index: for samples prepared at 350°C, its value is close to 20, while it decreases to about 10 in the case of samples synthesized at 450°C. A low preparation temperature is the cause of this phenomenon: the obtained film is less compact and surface dissimilarities are originated.

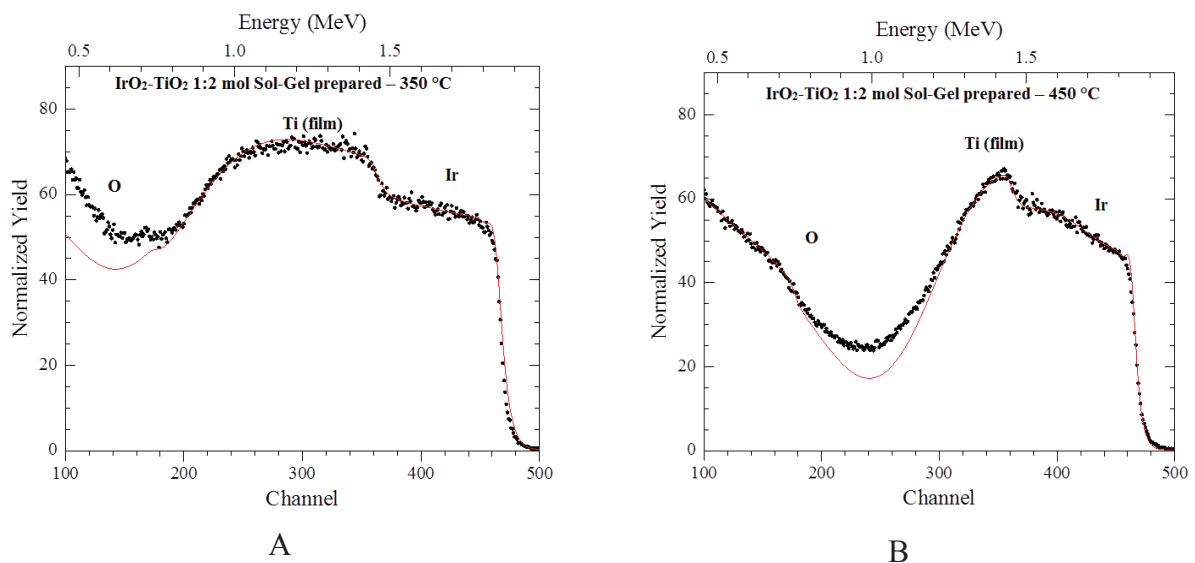


Fig.8.15. RBS spectra for samples of 1 $\mu$ m thickness, prepared on titanium supports using the Sol-Gel approach: (A) 350 °C, (B) 450 °C.

Sol-gel samples, conversely, are not easy to analyze by means of RBS because of the presence of byproducts, both on the surface and in the bulk of material, originated by an incomplete pyrolysis of precursors during the preparation. High percentage amount of carbon, hydrogen and chlorine can be detected. This aspect, together with the roughness of films (higher than that of samples prepared by sputtering), are responsible of the measured complex profiles. The thickness measured is a little bit lower than the expected of 1  $\mu$ m, but included

in the tolerance interval permitted by the preparative. The films prepared at 350 °C have a thickness of about 0.9 μm, while those synthesized at 450 °C are 0.7-0.8 μm thick. The oxygen stoichiometry of prepared oxides is nearly 2.3. One of the most interesting aspects can be assessed by looking at the profile of iridium signal for the Sol-Gel film prepared at 450 °C: in fact, basing on the Rutherford backscattering cross-section trend in function of the energy of the incident beam, it's normal to register an increase of the signal while the energy decreases, with a dependence on Energy<sup>-1/2</sup> (Eq.5.11, Par.5.3); however, in this case, an anomalous increasing in iridium signal intensity was registered. It means that the concentration of iridium atoms is growing in the bulk of the film, and consequently the quantity of titanium needs to decrease in the same way, suggesting a segregation of TiO<sub>2</sub> domains on the surface. This aspect can have important effects on the electrocatalytic activity, which will be discussed in details in following sections. A similar behavior was found also for other samples based on ruthenium, iridium and titanium oxides [18].

## 8.5. AFM analysis: roughness index evaluation

The Atomic Force Microscopy has been chosen as the technique for a direct evaluation of the surface roughness of the electrodes studied. The roughness can be calculated on a profile (line) or on a surface (area); the first value is often indicated with  $R_a$ ,  $R_q$ , etc., while the second with  $S_a$ ,  $S_q$ , etc.; the latter can give more useful and significant information. The definitions of the linear roughness factors are the following [19]:

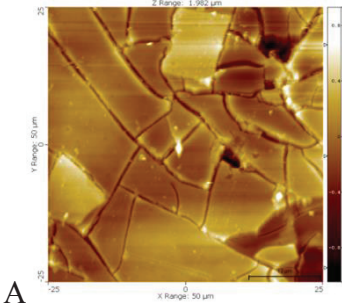
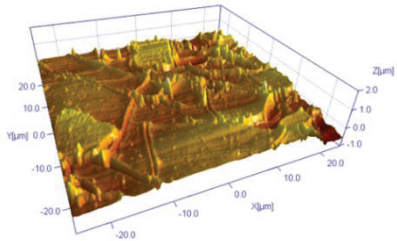
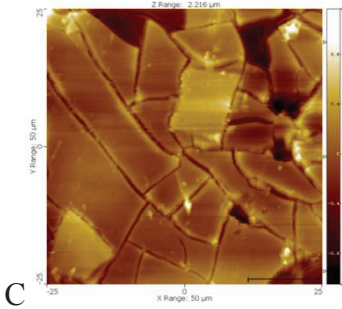
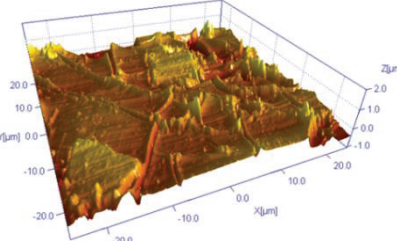
$$R_a = \frac{1}{n} \sum_{i=1}^n |y_i| \quad \text{Eq.8.7}$$

$$R_q = \sqrt{\frac{1}{n} \sum_{i=1}^n y_i^2} \quad \text{Eq.8.8}$$

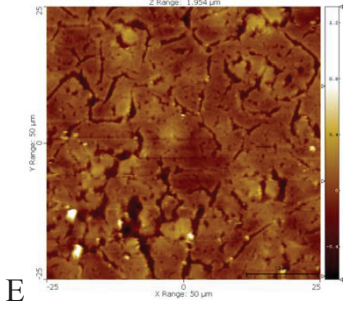
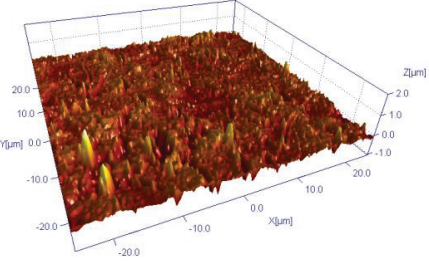
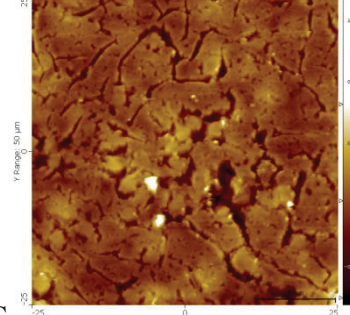
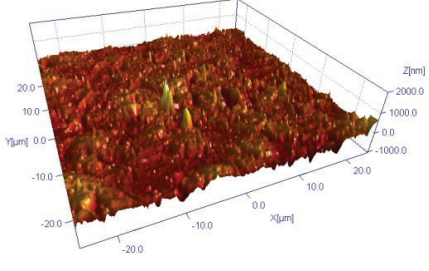
$R_a$  consists of an arithmetic average of absolute  $n$  values of  $y_i$  (height of the  $i$ -th peak along the chosen direction), while  $R_q$  represents the root mean square (RMS) of  $R_a$ . The roughness units are expressed as length units, nanometers in our case. The definitions of  $S_a$  and  $S_q$  are similar of those just reported, but they refer to a surface profile in 2-dimensions. The roughness factor is proportional to the ratio between the real surface area and the geometric surface area and, in these terms, its understanding is fundamental in the science of catalysis.

Because of the lateral inhomogeneity of the studied samples, especially concerning those prepared via Sol-Gel, areal parameters were determined, working on a quite wide surface area (about 2500 μm<sup>2</sup>). For sputtered samples, images at different magnifications

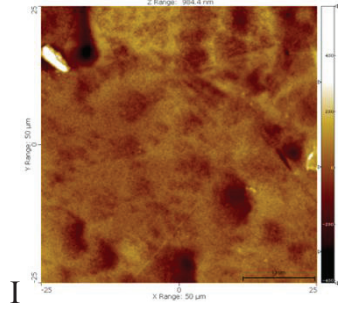
(e.g., by working on a surface of 10×10 μm) were collected to compare the results obtained in different regions of the surface. The most significant parameters have been obtained by analyzing the larger surface portions; because of the presence of diffuse cracks visible on their surface, Sol-Gel samples were monitored in two different zones (Tab.8.8).

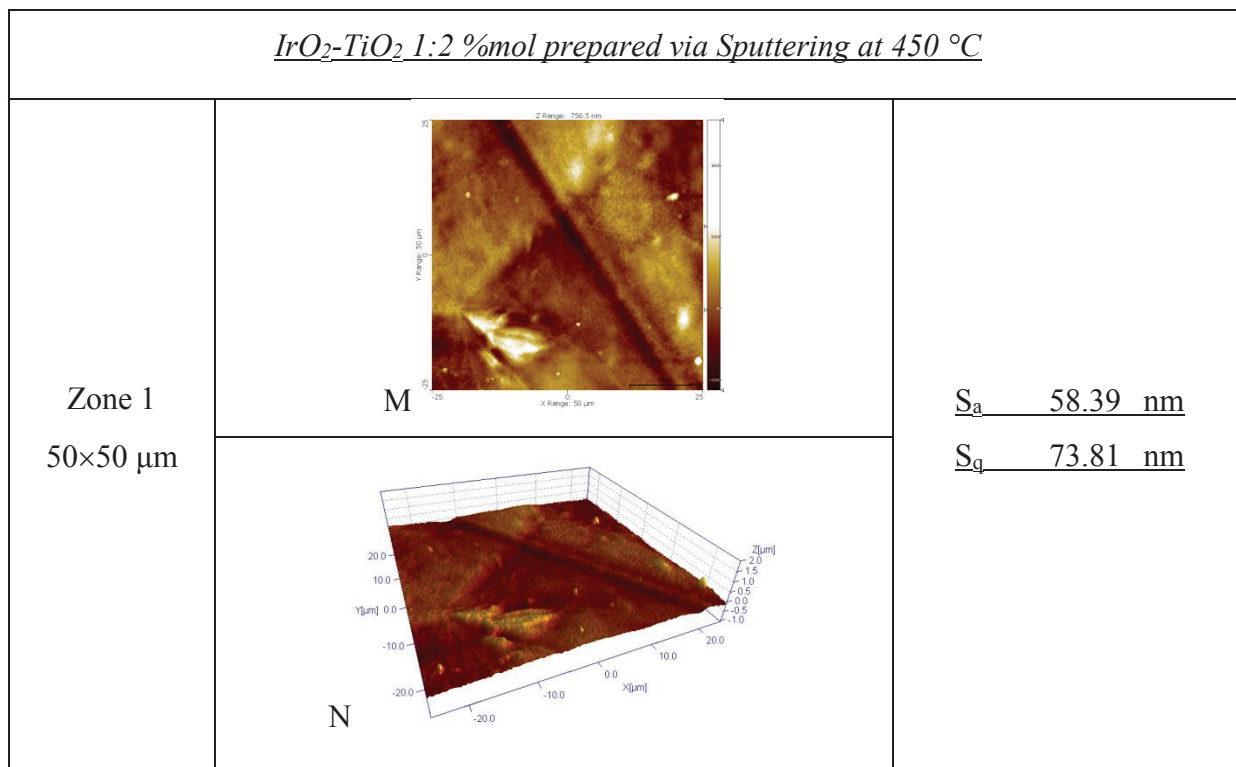
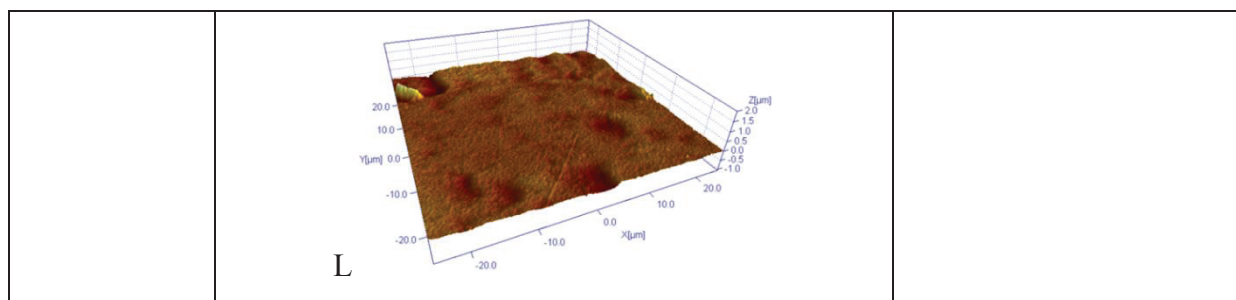
<i>IrO<sub>2</sub>-TiO<sub>2</sub> 1:2 %mol prepared via Sol-Gel at 350 °C</i>		
Zone 1 50×50 μm	 <p>A</p>	<u>S<sub>a</sub></u> 162.51 nm <u>S<sub>q</sub></u> 209.01 nm
	 <p>B</p>	
Zone 2 50×50 μm	 <p>C</p>	<u>S<sub>a</sub></u> 175.91 nm <u>S<sub>q</sub></u> 240.62 nm
	 <p>D</p>	

*IrO<sub>2</sub>-TiO<sub>2</sub> 1:2 %mol prepared via Sol-Gel at 450 °C*

<p align="center">Zone 1 50×50 μm</p>	 <p align="center">E</p>	<p align="center"><u>S<sub>a</sub> 110.49 nm</u></p> <p align="center"><u>S<sub>q</sub> 152.45 nm</u></p>
	 <p align="center">F</p>	
<p align="center">Zone 2 50×50 μm</p>	 <p align="center">G</p>	<p align="center"><u>S<sub>a</sub> 112.88 nm</u></p> <p align="center"><u>S<sub>q</sub> 155.19 nm</u></p>
	 <p align="center">H</p>	

*IrO<sub>2</sub>-TiO<sub>2</sub> 1:2 %mol prepared via Sputtering at 350 °C*

<p align="center">Zone 1 50×50 μm</p>	 <p align="center">I</p>	<p align="center"><u>S<sub>a</sub> 45.27 nm</u></p> <p align="center"><u>S<sub>q</sub> 64.00 nm</u></p>
---	---	---



Tab.8.8. Summary of AFM images collected by working on 2500 μm<sup>2</sup> of surface

In the case of the Sol-Gel samples, the roughness parameters were estimated as the average of the values reported in Tab.8.8; in order to facilitate a comparison between samples, the experimental results are resumed in Tab.8.9.

Sample	S <sub>a</sub> (nm)	S <sub>q</sub> (nm)
Sol-Gel 350°C	169.21	224.82
Sol-Gel 450 °C	111.69	153.82
Sputtering 350 °C	45.27	64.00
Sputtering 450 °C	58.39	73.81

Tab.8.9. Surface average roughness and quadratic mean roughness for all the samples

The differences between Sol-Gel and Sputtering samples are impressive: a difference that amounts to one order of magnitude, in terms of surface extension; the different preparation technique is the main factor leading to this difference. In fact, analyzing the most enlarged images, collected by AFM (Fig.8.16), it is possible to appreciate something like a “columnar” structure for electrodes prepared through PVD: the particles appear well organized, and a quite compact structure is obtained; similar features have been previously found also for samples based on ruthenium oxide [20]. The Sol-Gel samples, on the contrary, appear characterized from a macro-porosity, which is particularly important for those prepared at 350 °C, with big and deep cracks, along the surface, that may host substrates in the electro-catalysis application. With reference to Sol-Gel samples, an investigation of more magnified images has been also tempted, but without obtaining interesting information because of the strong lateral differences along the surface; as a result, data have not been reported in this work of thesis.

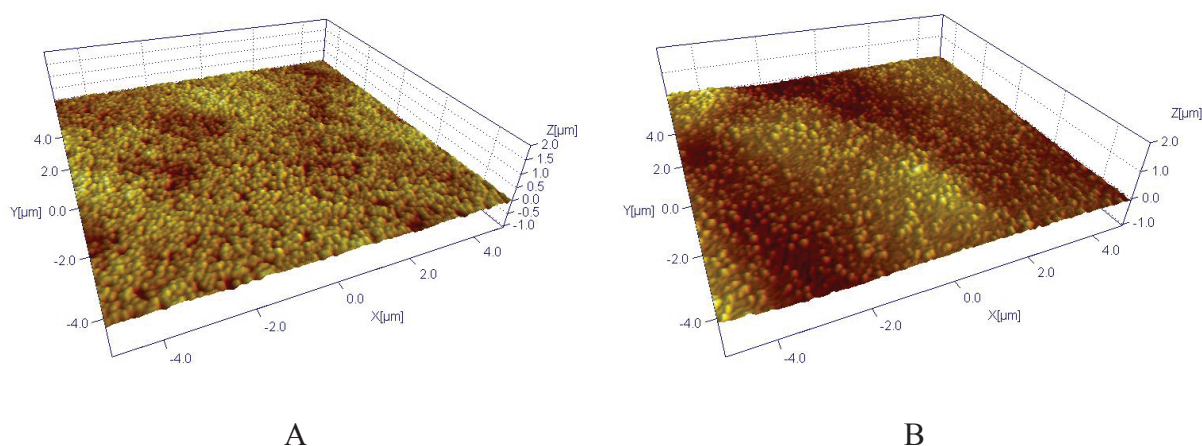
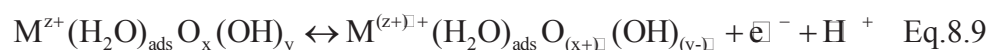


Fig.8.16. AFM images obtained for sputtered samples (A – prepared at 350 °C; B – prepared at 450 °C), by zooming to a total surface area of 100  $\mu\text{m}^2$ .

The preparation temperature plays a secondary effect, and its increase promotes the formation of a smoother surface in the case of Sol-Gel electrodes, while the effect is not appreciable for those prepared by sputtering, differences of roughness being linked to the uncertainty and to experimental errors connected with the microscopy approach. However, the surface of samples prepared at 350 °C is less compact and structured than that of samples synthesized at 450 °C: these material features are important for a better understanding of the electrochemical properties that will be treated in the following chapters.

## 8.6. Cyclic Voltammetry experiments for the estimation of the number of electroactive sites

As anticipated, the real surface of a catalyst, which works in a different phase with respect to the reagents, represents a fundamental aspect for the evaluation of its performances. Because of the characteristics and of the behavior of materials based on noble-metal oxides, the electrochemical technique of cyclic voltammetry may be used for gaining structural information. The most direct way for investigating the surface properties is to acquire the voltammetric curve in an aqueous system within a potential range where neither O<sub>2</sub> nor H<sub>2</sub> are evolved [21,22]. The charge obtained by integrating the voltammetric curves can be assumed to be proportional to the electrode surface area exposed to the solution. Because of the so-called “pseudo-capacitive” behavior of this family of oxide materials, it is possible to evaluate the contribution of the electro-active sites by considering only a portion of the voltammetric curves, and the latter must be collected under opportune conditions. Kodintsev *et al.* [23] characterized, by means of XPS and electrochemical techniques, electrodes of IrO<sub>2</sub> and RuO<sub>2</sub> prepared via thermal decomposition (at 400 °C) of chloride precursors. The O1s XPS signal was deconvoluted into three peaks, thus suggesting the presence of three different oxygen species on the oxide coating, which have been named as (i) oxide oxygen, (ii) hydroxide and (iii) adsorbed water. The authors also highlighted that the magnitude of contributions (ii) and (iii) decreased as XPS spectra relating to inner regions were recorded. This evidence suggested an electrode structure in which the adsorbed water molecules and hydroxyl anions were accumulated mainly inside of the outermost layers, as schematized by Equation 8.9.



The equilibrium is also defined as “injection-dejection” of H<sup>+</sup> because of the traffic of protons from the electrolyte to the electrode material, and vice versa, during the polarization.

So, when working in an sufficiently acidic environment, the voltammogram is constituted by different contributions, as schematized in Fig.8.17.

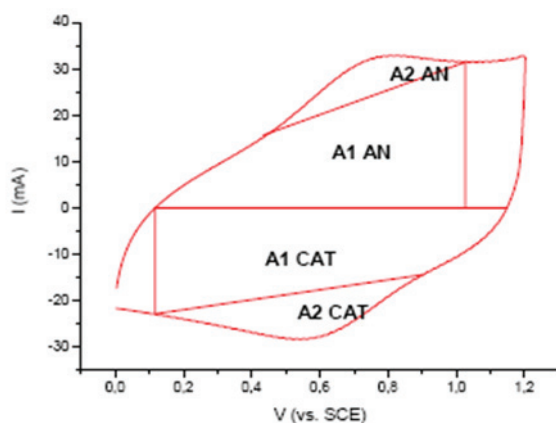


Fig.8.17. Example of a cyclic voltammetric curve collected for a DSA<sup>®</sup>-type material immersed in an inert electrolyte, having an acidic pH.

A1 AN and A1 CAT represent the pure capacitive contributions (anodic and cathodic, respectively) due to the double-layer charging, while A2 AN and A2 CAT relate to the “pseudo-capacitive” ones, associated with the oxidation of Ir<sup>III</sup> to Ir<sup>V</sup>, as well as to the reverse reaction. Fig.8.17 refers to the response of an ideal system, for which the faradaic contributions are perfectly resolved with respect to the capacitive background; in a real situation, considering a complex system in which a great number of non-equivalent catalytic sites exists, oxidative and reductive transitions take place over the whole range of potential, producing a very broad and extensive signal. The acquisition of CV curves from neutral environment are very useful for discriminating the purely capacitive behavior from that “pseudo-capacitive”, which can be attested only in acidic solutions.

By working in a neutral environment, it is possible to minimize the contribution due to redox sites, measuring only the effect of the double-layer capacity; then, by subtracting from the total charge (obtained by integrating the voltammetric curve) evaluated in acidic environment, the total charge measured in the neutral environment, it is possible to estimate a charge that is proportional to the number of electro-active sites involved in the redox process (Eq.8.10).

$$n = \frac{N_A Q_f}{\nu F} \quad \text{Eq.8.10}$$

In Eq.8.10,  $n$  is the number of electro-active sites,  $N_A$  is the Avogadro’s number,  $Q_f$  is the average faradic charge, at a particular scan rate,  $F$  is the Faraday’s constant (about 96500 C/mol), and  $\nu$  is the so-called “turn-over number” and represents the change in oxidation state of the studied substrate (its value is 2, in our case, since each iridium-site exchanges 2 electrons within the selected potential window).

This kind of approach was used, by working at different scan rates, estimating  $Q_f$  as an average of both anodic and cathodic charges (Eq.8.11) [24].



$$Q_f = \frac{(Q_{+,pH=0} + |Q_{-,pH=0}|)}{2} - \frac{(Q_{+,pH=7} + |Q_{-,pH=7}|)}{2} \quad \text{Eq.8.11}$$

Scan rates between 10 and 1000 mV/s (10, 25, 50, 100, 200, 300, 400, 500, 600, 700, 800, 900 and 1000 mV/s) were explored, because the imposition of different external constraints influences the kinetics of the redox processes of the iridium sites, and this point can give information about the nature of the involved electro-catalytic sites, as discussed later.

Tests were carried out in perchloric acid sufficiently concentrated (1M HClO<sub>4</sub>), and then in a solution based on the homologous salt (1M NaClO<sub>4</sub>): in this way, measurements have been obtained by working with the same ionic strength. When changing the electrolyte, it is important to pay attention to the dependence on pH of the electrochemical equilibria related to the solvent: in fact, as reported in the Pourbaix's diagram for the water molecule [25], and considering the Nernst equations for the reactions that produce oxygen and hydrogen (by oxidation and reduction of the water, respectively), it is necessary to modify the limits of the analyzed potential window, for ensuring that the measurement remains within the stability range of the solvent. In practice, the potentials have to be shifted of about 59 mV for each unit of pH variation (Eq.8.12).

$$E' = E - 0.059\Delta pH \quad \text{Eq.8.12}$$

In Eq.8.12,  $E'$  represents the new potential value, which decreases with an increase of the pH. An example of two voltammetric curves, collected in acidic and neutral environment, is shown in Fig.8.18.

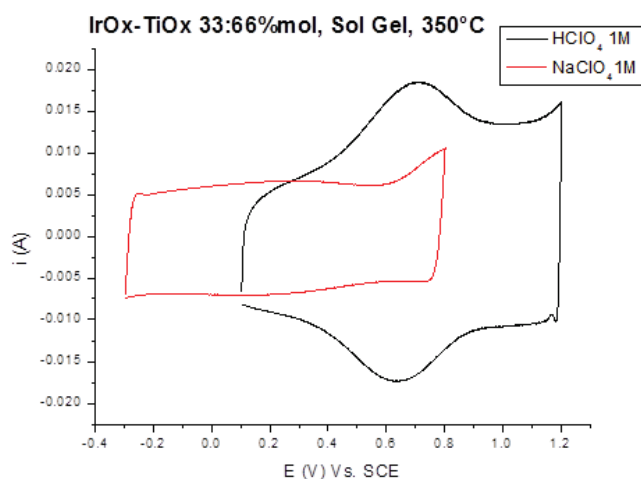


Fig.8.18. CVs collected at 100 mV/s for the IrO<sub>2</sub>-TiO<sub>2</sub> 1:2 % mol prepared by Sol-Gel at 350 °C, in acidic (pH≈0, black curve) and neutral environment (pH≈7, red curve).

The data, collected at different scan rates from 1M HClO<sub>4</sub> solution, and for all the analyzed samples, have been reported in Fig.8.19.

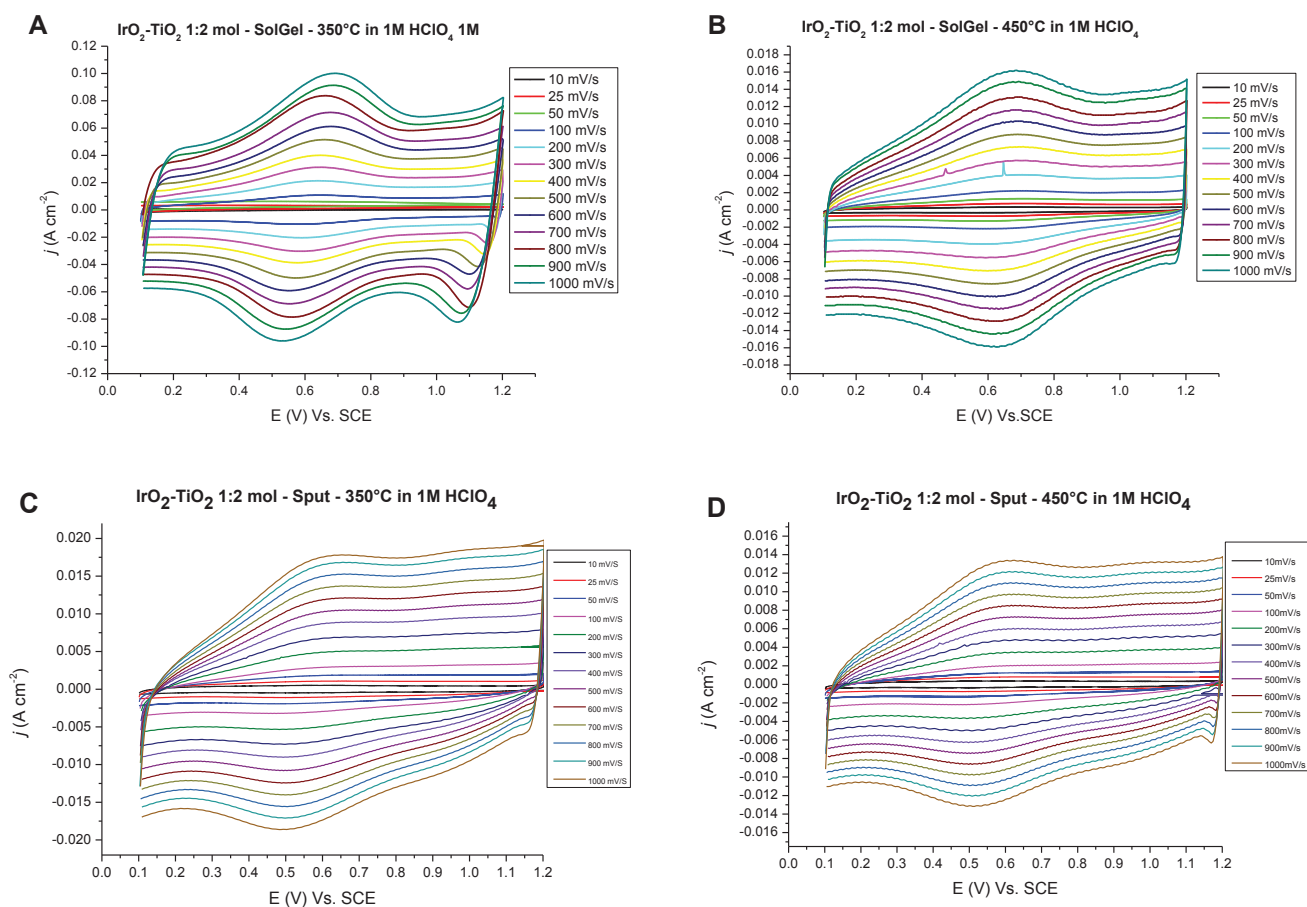


Fig.8.19. CVs recorded in 1M HClO<sub>4</sub>, at different scan rates, for the iridium-titanium oxide samples: (A) Sol-Gel 350 °C, (B) Sol-Gel 450 °C, (C) Sputtering 350 °C, (D) Sputtering 450 °C.

The shape of both anodic and cathodic peaks, characterized by a “tailing” of the current, is explainable through the multilayer model proposed by Laviron *et al.* in 1980 [26,27]; it has been shown that this behavior is equivalent to that of a system in which the electrons diffuse in the coating, and where different mass-transfer regimes take place depending on the rate of the electron exchange.

Results of measurements carried out in sodium perchlorate have been collected in Fig.8.20.

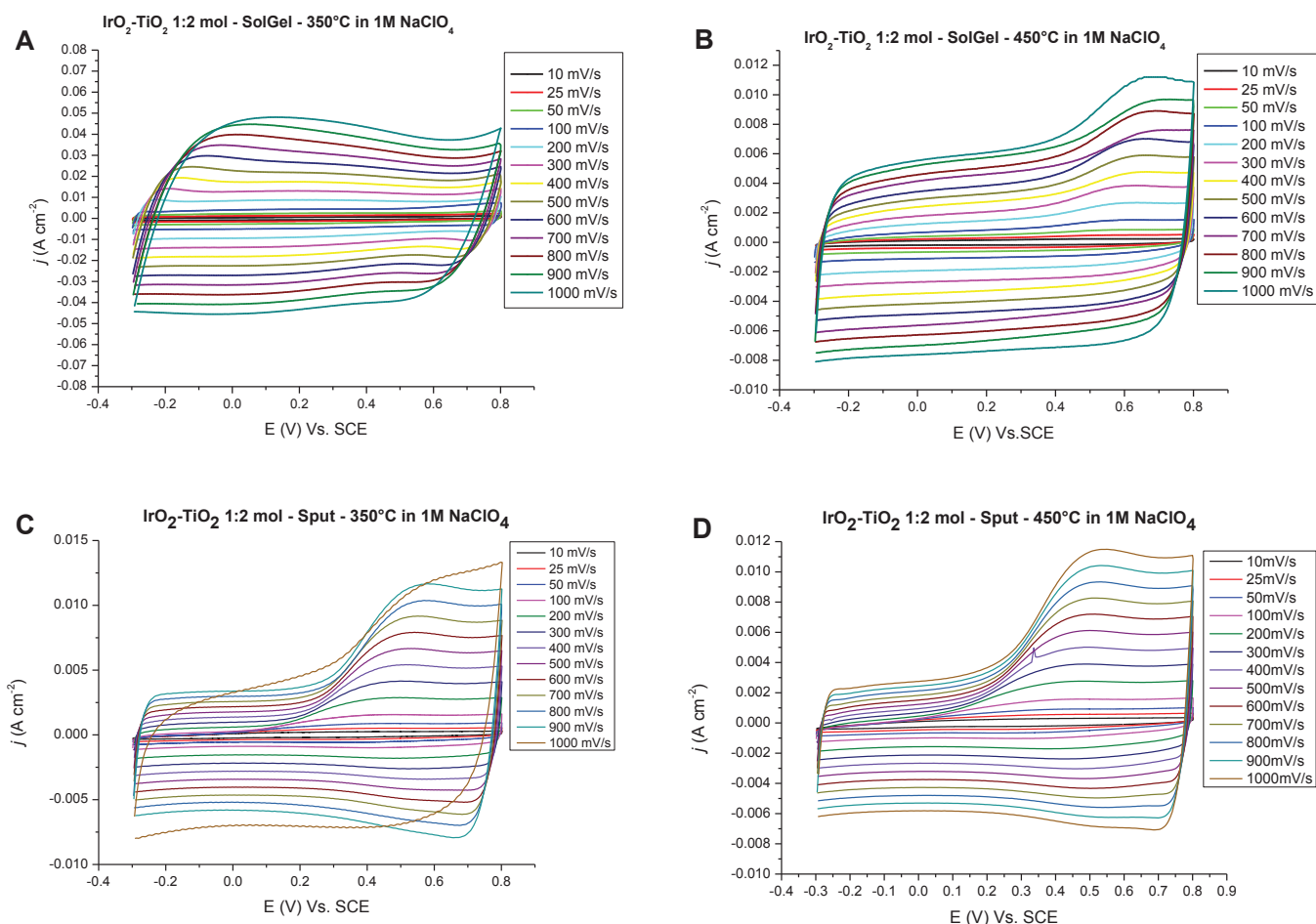


Fig.8.20. CVs recorded in 1M  $\text{NaClO}_4$ , at different scan rates, for the iridium-titanium oxide samples: (A) Sol-Gel 350 °C, (B) Sol-Gel 450 °C, (C) Sputtering 350 °C, (D) Sputtering 450 °C.

By observing the figures 8.19 and 8.20, the approach of subtracting the voltammetric areas, evaluated in two different environments, appears suitable for Sol-Gel samples, but quite tentative in the case of sputtered ones. In fact, voltammograms obtained from the neutral environment for sputtered electrodes appeared strongly asymmetric, with a broad anodic wave centered around 0.8 V vs. SCE that seems to be associated to an irreversible process. Because of this reason, only the cathodic portions of voltammograms were used for the evaluation on the number of electroactive sites, in the case of sputtered samples. The anomalous anodic signal, well visible only in the case of the sputtered specimens, may depend on the morphology and texture of the materials. A reorganization process and a re-distribution of a surface charge can start only when potential exceed a threshold value; in other words, an activation energy have to be supplied to the system for allowing this surface modification process. This kind of behavior probably exists also in acidic environment, but it cannot be appreciated due to the important faradaic contribution of the iridium sites; the latter, as previously mentioned, is manifested through a convolution of peaks over a wide interval of

potentials. Moreover, this aspect does not allow the identification of a unique baseline, in voltammograms collected for in acidic environment (Fig.8.20 C and D).

Observing the trend of the number of catalytic sites, plotted as a function of the scan rate (Fig.8.21), some interesting considerations can be drawn.

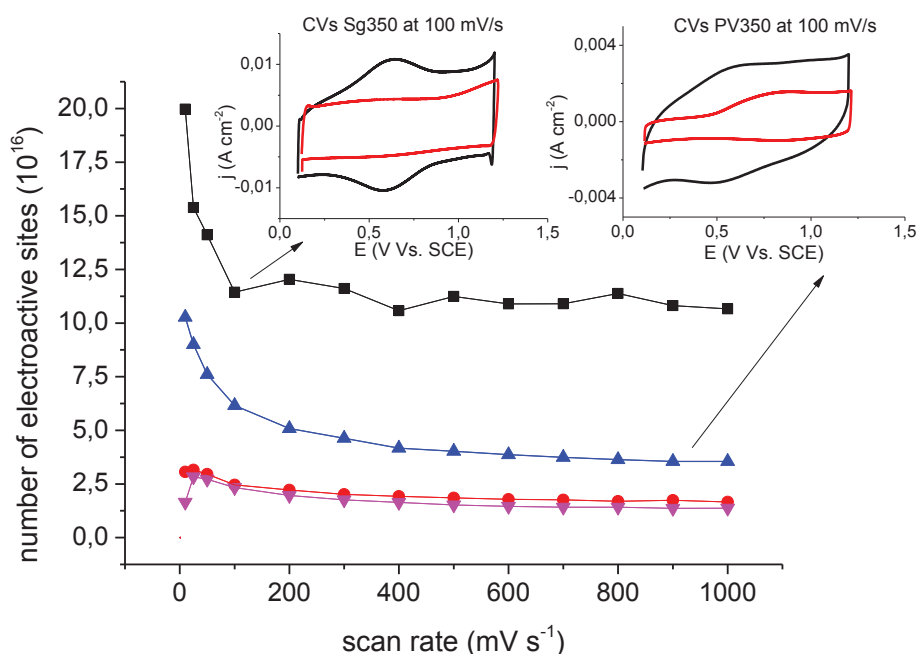


Fig.8.21. Scan-rate dependence of the number of electro-active sites, for all the analyzed samples: (■) SG350, (●) SG450, (▲) PV350, (▼) PV450. Inset graphs contain the comparison among cyclic voltammograms collected in acidic and neutral environment for SG350 and PV350 samples, at  $100 \text{ mV s}^{-1}$  (the potential window of the experiment done in neutral environment was shifted for facilitating comparison with the measure in acidic solution).

Samples prepared at  $350 \text{ }^\circ\text{C}$  are characterized by a steep decrease of the number of sites, when increasing the potential scan rate (indicated as  $r$ ). For the Sol-Gel samples, the number of electroactive sites per unit geometric area as well as the shape of its decay differ from that of other samples. A quite fast decrease is observed, up to an  $r$  value of about  $100 \text{ mV s}^{-1}$ , with a subsequent stabilization (above  $10^{17}$ ) and no further decrease (up to  $1 \text{ V s}^{-1}$ ). For the samples deposited through PVD, average values are still relatively high, but the rate of decrease when increasing  $r$  remains significant also above  $100\text{-}200 \text{ mV s}^{-1}$ . These differences may be tentatively accounted for by assuming a difference in pore size for the two films: a dominating macroporosity, in the case of the Sol-Gel samples, and a micro-meso porosity for the PVD ones. The two samples synthesized at  $450^\circ\text{C}$  exhibit a quite similar behavior, at this level of data elaboration. The number of electroactive sites per unit geometric area are close to  $10^{16}$  and charge-storage capacity is weakly affected by  $r$ . Within the frame of a general

increase of compactness, the temperature of synthesis apparently causes a clogging of microporosity.

To further discuss this aspect, related in turn to catalytic activity of the electrodes, it is worth reminding [28] that the number of dangling bonds at the surface of a rutile-structured oxide ranges between about 2 and  $7 \times 10^{14}$ ; accordingly, data in Fig. 8.21 indicate that a roughness factor ( $f_r$ ) as high as almost  $10^3$  is attained for the Sol-Gel sample synthesized at 350 °C. Even at higher scan rates (e.g.,  $r > 200 \text{ mV s}^{-1}$ )  $f_r$  remains at the level of  $10^2$ . The data in Tab.8.9, estimated through AFM, support this still qualitative expectation. These values, together with their important dependence on potential scan-rate, suggest that more than one monolayer, in the near-surface-region of electrode films, is involved in the charge-storage process; as an alternative, the “electrochemical” rugosity is high. On the other hand, the lower temperature in the Sol-Gel synthesis quite reasonably allows the formation of a more open surface texture, with a higher defectivity across the near-surface-region, and consequently a higher degree of hydration. This would favor a proton exchange via tunneling mechanisms (Grotthuss+tunneling).

Assuming a value of about  $10^{15}$  sites/cm<sup>2</sup>, for the average surface concentration of sites in a rutile-type structure, and normalizing the estimated number of active sites for the root mean square roughness ( $Sq$ , as reported in Tab.8.9), it is possible to estimate the number of “formal” monolayers involved in the proton-exchange process, as a function of electrode properties and of  $r$ , and, more in general, the percentage of the electrode surface that responds to  $r$  and to its change.

As shown in Fig. 8.22, the charge storage of the sol-gel electrode prepared at 350 °C is mainly due to its external surface, whose microporous component is lost within a narrow range of scan rates ( $r < 100 \text{ mV s}^{-1}$ ). The remaining fraction of the surface maintains its electroactivity irrespective of  $r$  ( $100 < r < 1000 \text{ mV s}^{-1}$ ). Owing to this characteristic, this specimen is expected to exhibit a high (electro)catalytic activity, e.g. toward reactions involving adsorbed intermediates, like ChIER and OER.

Concerning the material sputtered at 350 °C, more than one formal monolayer of sites contributes to the charge storage at very low  $r$  values. An increase of  $r$  is accompanied by a decrease of electroactive sites, from below a formal monolayer, down to about 0.5, coincident with the values attained by sol-gel prepared at 350 °C. Since the roughness is much lower than for the sol-gel electrode synthesized at 350 °C (Tab.8.9), the expected apparent catalytic activity, which is proportional to the product of roughness and effective site concentration, is larger for the latter.

With the exception of the sample sputtered at 350 °C at low  $r$ , the value of the normalized number of electroactive sites is always lower than unity, for all the samples: this outcome means that only a fraction of active sites is involved in the charging/discharging process. This is in agreement with the results obtained by L.D. Burke and collaborators, who worked with  $\text{RuO}_2$  electrodes that were characterized by means of CV and BET [29]. The columnar structure evidenced by AFM for PVD sample prepared at 350 °C, and related inter-particle surfaces, may provide the film texture with a significant degree of nano-porosity, somewhat hindering the proton transfer, when less hydrated zones are crossed. At sufficiently low  $r$  values, this component of the film surface remains accessible, otherwise not. Similar evidences have been previously obtained for PVD  $\text{RuO}_2$  [20]. Iridium sites, located in this portion of the film surface, are not expected to take part in the mentioned electrochemical reactions (see also: [30,31]).

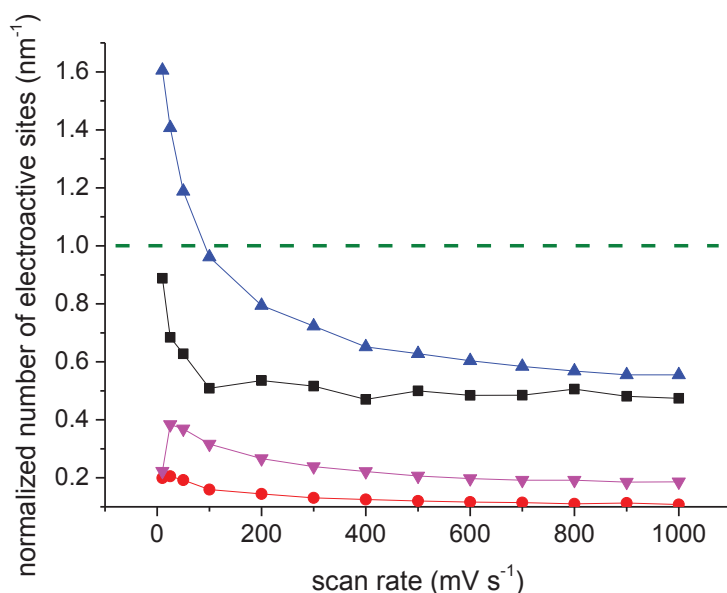


Fig.8.22. Number of electroactive sites, normalized for the roughness of samples and for the planar density of the metal centers in a rutile-type structure. (■) SG350, (●) SG450, (▲) PV350, (▼) PV450.

In order to attain further experimental evidences for the above analysis, the dependence of the cyclic voltammetric peak current on scan rate was studied. The outcomes obtained for sol-gel samples are shown in Fig.8.23.

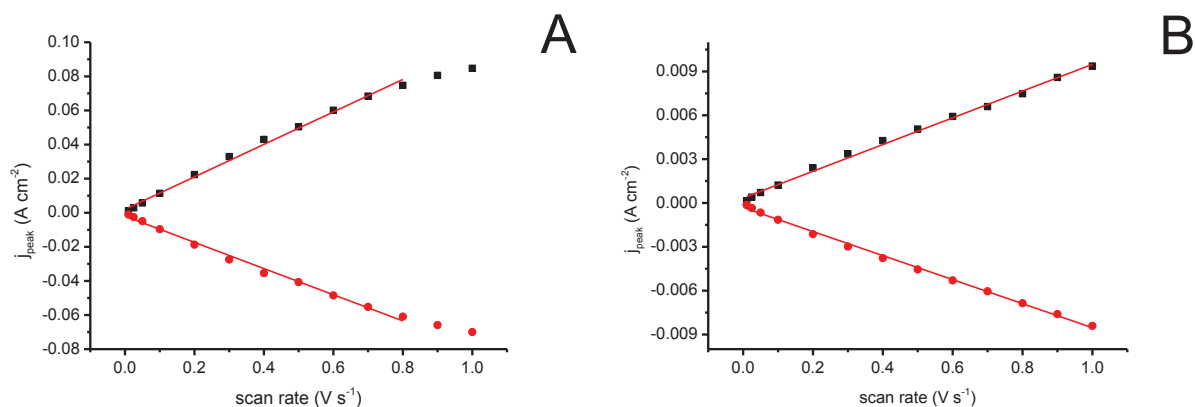


Fig.8.23. Dependence of the peak current on scan rate, for sol-gel samples prepared at (A) 350 °C, (B) 450 °C. Black dots refer to anodic peak currents, while the cathodic branch is represented by red ones.

The evaluation of peak currents was done by considering the current values measured in proximity of the peak potentials in acidic environment voltammograms (anodic and cathodic peaks fall at about 0.7 and 0.6 vs. SCE, respectively) and subtracting the corresponding values of current registered in neutral environment. Because of the asymmetric behavior of the CV curve in neutral environment, this procedure could not be carried out in the case of sputtered electrodes.

A good linearity of the peak current with respect to the first power of  $r$  was found, and both the anodic and cathodic branches showed a similar slope, denoting a process of protons exchange that involves the outer surface without any constriction of mass transfer; macro-roughness and macro-porosity are the main responsible for these results. A linearity in the plot  $i_p$  vs.  $r$  is commonly encountered and is typical of surface-modified electrodes, as explained *e.g.* by Bard and Faulkner [32]). Assuming that  $r$  is so high that appreciable diffusion-controlled phenomena are not occurring on the electrode surface, and that the electrochemical process considered is reversible, it is possible to consider the well-known equation (Eq.8.13) that correlates  $r$ ,  $i_p$  and the surface excess  $\Gamma$ , which in turn is proportional to the number of electroactive sites:

$$\frac{i_p}{r} = \frac{n^2 F^2}{4RT} \Gamma \quad \text{Eq.8.13}$$

Terms in Eq.8.13 have the usual meaning or have been already defined, and the peak current, in our case, has been already normalized to 1 cm<sup>2</sup> geometrical surface. By considering the slopes of linear trends showed in Fig.8.23, an estimation for the number of electroactive sites can be calculated. Owing to the fact that a single potential value has been considered in each branch (anodic and cathodic), a mono-electronic process has been hypothesized: in fact, only

when the analysis is carried out among the whole potential window, it is rightful to assume a change in the oxidation state of the iridium sites from Ir(III) to Ir(V), as done for the voltammetric charge based procedure, previously discussed. Average numbers of sites that amount to  $5.5 \times 10^{16}$  and  $5.5 \times 10^{15}$  were determined for sol-gel samples synthesized at 350 and 450 °C, respectively. Values are lower than those estimated with the integral method of voltammetric charges (Fig. 8.21, data points (■) and (●)), but such an outcome is quite reasonable since, in a wide range of potentials, electrochemical sites with a different chemical nature can be active. Of course, even if the nature of active sites is the same, the number of neighboring atoms and the number of chemical bonds with vicinal oxygen atoms can be different, especially when considering electroactive sites located on the surface, or in the so-called near-surface region.

Eventually, also an estimation of the double-layer capacity was attempted, basing on cyclic voltammograms collected in NaClO<sub>4</sub>. Two examples, which refer to the variation of anodic and cathodic charge as a function of scan rate, are shown in Fig.8.24. Double-layer capacities were estimated making reference to the average of anodic and cathodic voltammetric charge, normalized for the considered interval of potentials of 1.1 V (from -0.3 to 0.8 V vs. SCE). The practically constant value that is found for scan rates higher than 200 mV/s was chosen as representative for the double-layer capacity of electrodes.

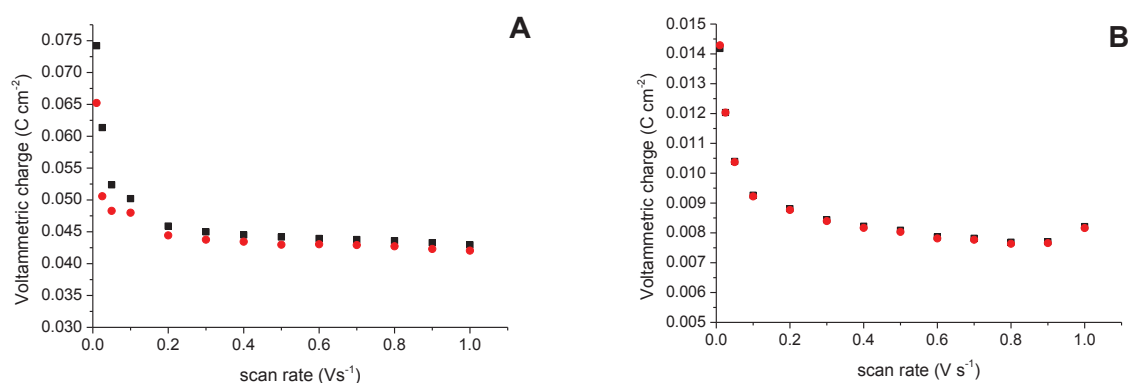


Fig.8.24. (■) Anodic and (●) Cathodic voltammetric charges evaluated through CV in neutral environment for (A) SG350 and (B) PV350 samples.

As shown in Tab.8.9, data are quite in accordance with those of surface extension measured by AFM (Tab.8.9). It's worth observing that values calculated for sputtered electrodes have been for sure overestimated, since the anodic contribution related to re-organization of the



surface (close to 0.8 V Vs. SCE) is comprised in the voltammetric area considered for the estimation

Sample	$C_{dl}$ (mF cm <sup>-2</sup> )
Sol-Gel 350°C	39.6
Sol-Gel 450 °C	7.47
Sputtering 350 °C	7.26
Sputtering 450 °C	6.77

Tab.8.9. Double-layer capacities, estimated from CV results collected in neutral environment.

## 8.7. ERD Analysis: evaluation of the amount of protons involved in the charging/dischargin process of iridium sites

The utilization of nuclear and ion-beam techniques does not represent a routinary analysis for the estimation of performances of the electrodes, but the approach has been anyway discussed in literature, in several cases [18,33,34], as it represents an important source of information for elucidating the behavior of the surfaces. For example, this family of techniques can be useful for examining the interaction between intermediates and the electrode surface, or, in other cases, for investigating more specific processes, such as the mass transport into the oxide matrix [35].

In the present work of thesis, a particular nuclear analysis, the Elastic Recoil Detection, has been exploited with the aim of verifying and validating the experimental results obtained by both AFM and CV in acidic environment. ERDA has been chosen to investigate the phenomenon of incorporation of protons, which, as discussed previously, is strictly related to the redox processes of the catalytic sites; this kind of investigation represents an alternative way for estimating the active surface of oxide-based electrodes. Since a large amount of hydrogen is usually found, especially on sol-gel samples, because of the incomplete pyrolysis of precursors, the isotope <sup>2</sup>D<sup>+</sup> was chosen as target for these experiments [9,18]. In addition, hydrogen can be also found because of the tendency of metal oxide based materials to adsorb atmospheric humidity, and the utilization of deuterons avoids any sort of experimental error or misunderstanding. Accordingly, a 1M solution of D<sub>2</sub>SO<sub>4</sub> in D<sub>2</sub>O was used to treat the electrodes by means of cyclic voltammetry.

Samples were cycled between 0.1 and 1.1 V vs. SCE several times (about 70-80 cycles), in order to guarantee a reproducible hydration of the material in the deuterium-rich environment; then, the dynamic measure was interrupted at 0.1 V (the less anodic potential) and this polarization potential maintained for 3600 s. In fact, protons (deuterons, in this case) are injected and captured by the electroactive surface of the electrode, when the catalytic metal sites get reduced. Theoretically, the amount of deuterons that remains “encaged” into the electrode material, after the prolonged polarization, should be proportional to the number of available electroactive sites. The outcomes of ERD analyses, carried out on all samples, have been reported in Fig.8.25.

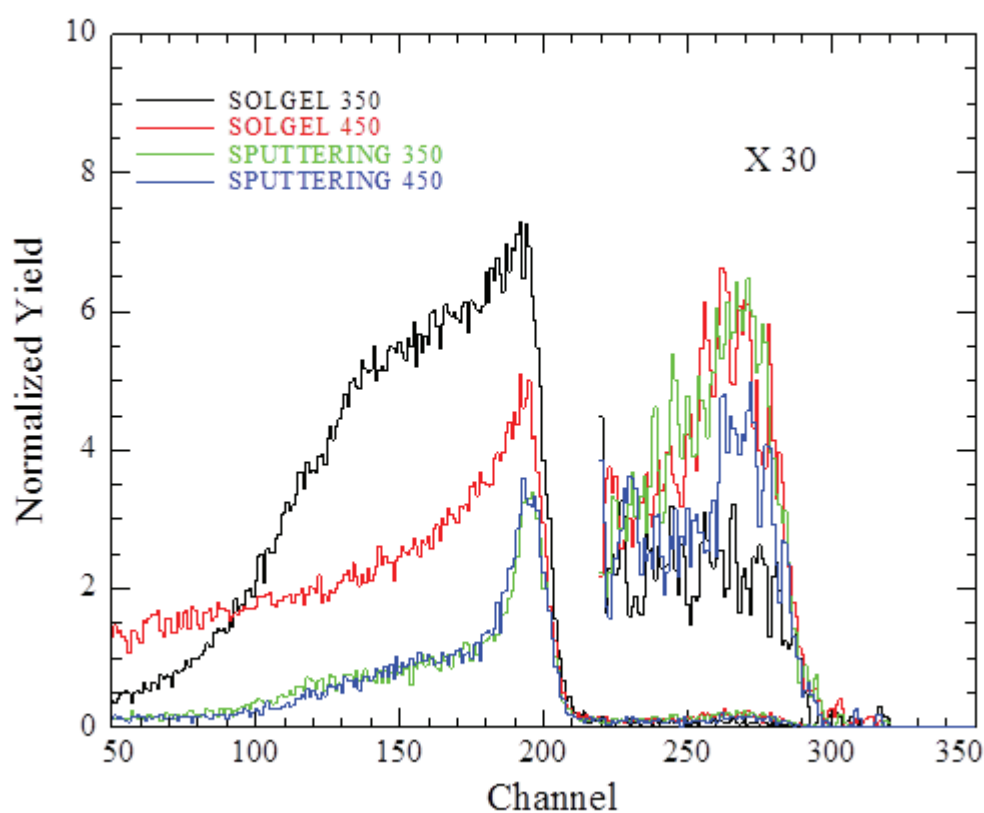


Fig.8.25. ERD analysis carried out on samples treated in  $D_2SO_4$  and  $D_2O$ . The signals related to deuterons are shown with a 30x magnification, because of their low intensity.

The signal related to deuterons can be found between channels 290 and 220 (from about 1.0 to 0.75 MeV, in the scale of energy) and, as it is possible to see, it is very less intense than that of protons (which is found between Ch. 210 and 50). In Tab.8.10, second column, the values of area experimentally evaluated have been summarized. The fitting procedure might produce a misleading interpretation of the outcomes, because of the weak intensities associated to deuteron signals, and it has to be carried out without losing the physical sense of

the phenomenon, especially for rough samples. Absolute cross-section, associated to  $D(^4\text{He}, D)^4\text{He}$  forward scattering, were calculated by Kellock *et al.* [36] and Kim *et al.* [37]. Anomalous results were obtained for the sample prepared by Sol-Gel at 350 °C: its character of electrode with a high electroactive surface does not seem to be confirmed, while this feature was well attested by means of CV. The preparative and subsequent ERDA characterization of this particular specimen was repeated several times but without any significant improvement in the obtained results: the small thickness, together with the presence of large pores, plausibly favors a creep of electrolyte solution, through the film, down to the interlayer; as a consequence, the formation of an insulating SiO<sub>2</sub> layer under the metal oxide-based coating may take place, causing the loss of electrical performance of the material. However, with the exception of this specimen, results obtained for the other three samples appear quite interesting: the third column in Tab.8.10 collects the values of deuterium amounts, expressed as atoms/cm<sup>2</sup>, while the fourth column includes those normalized for the average roughness index, as it was done for the CV results previously proposed.

Comparing quantities of deuterons entrapped on and into the film, with the trends reported in Fig.8.21, it is possible to see that all data are in good accordance (within the experimental error). The outcomes from this paragraph show that the sputtered material synthesized at 350 °C features the greatest extension, in terms of electroactive surface; a lower electroactive surface is presented by the homologous material prepared at 450 °C and by the Sol-Gel 450 °C, which are practically characterized by the same amount of deuterium encaged. Probably, the sputtered specimen prepared at 350 °C allows the exchange of a larger number of hydrogen/deuterium cations by virtue of its structure. Undoubtedly, it allows also the entrance of very small species within the nano-pores, and thus a great number of catalytic sites can be subjected to redox phenomena. Concerning the sol-gel electrode prepared at 450 °C, its surface is very rough, and the deuterium quantification is estimated with a lower precision, when compared with the cases of sputtered samples.

<b>Sample</b>	<b>A<sub>(D<sup>+</sup>)</sub></b>	<b>D<sup>+</sup> atoms (10<sup>15</sup>)</b>	<b>normalized D<sup>+</sup> atoms (10<sup>-3</sup>)</b>
<b>Sol-Gel 350 °C</b>	675	1.9	8.45
<b>Sol-Gel 450 °C</b>	1418	6.3	40.96
<b>Sput. 350 °C</b>	1253	4.2	65.63
<b>Sput. 450 °C</b>	985	2.7	36.58

Tab.8.10. Areas and normalized amounts of deuterium, measured for the different samples, after a prolonged (3600 seconds) polarization at 0.1 V vs. SCE in 1M D<sub>2</sub>SO<sub>4</sub> in D<sub>2</sub>O.

An example of how data have been treated is described in the following lines.

Fig.8.26 (A and B) shows RBS and ERDA data after the treatment in D<sub>2</sub>SO<sub>4</sub>, and the fitting of experimental results (red dots) is highlighted by the continuous line. RBS experiments, which were carried out in the same conditions mentioned in Par.8.4, were necessary for obtaining information about the effective planar densities, in terms of atoms/cm<sup>2</sup>; they allow the calculation of the absolute amounts of deuterium contained in the different oxide samples.

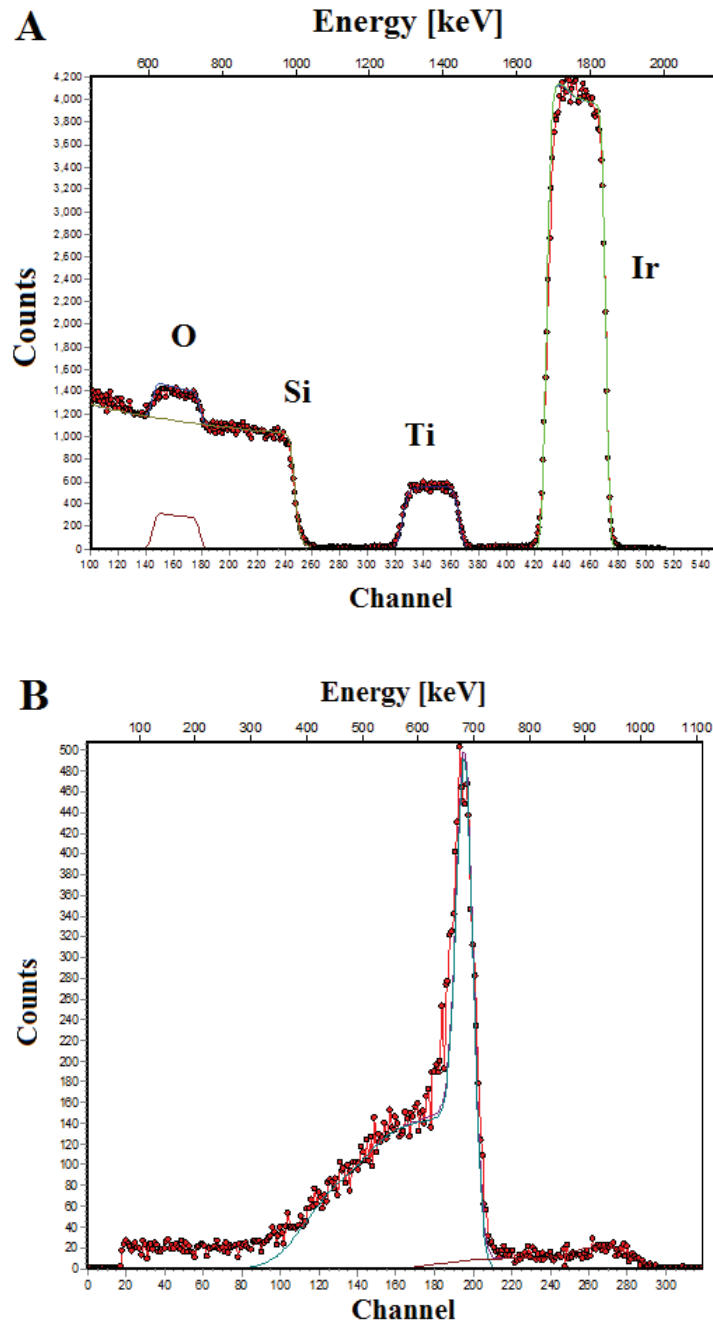


Fig.8.26. (A) RBS and (B) ERDA results, for the sputtered sample prepared at 450 °C and deposited on doped silicon, after a polarization treatment in deuterated environment.

The estimated amount of atoms, inside the different samples, has been collected in Tab.8.11: the relative abundance per each atom is written along a column, while the thickness per layer represents the total amount of atoms/cm<sup>2</sup>. Thus, by multiplying the thickness by the abundance of each atom, it is possible to estimate the absolute quantity of a given specie. In this case, the quantity associated to deuterium has been written in red, in Tab.8.11.

The right section of the table evidences the ratio Ir/Ti and, as it is easy to see, a quite constant value is obtained, confirming the high degree of homogeneity that can be obtained through a sputtering deposition.

<b>IrO<sub>x</sub>-TiO<sub>x</sub> 1:2 mol Sput. 450 °C</b>					
	<b>LAYER 1</b>	<b>LAYER 2</b>	<b>D Content estimated</b>	<b>Ir/Ti</b>	
<b>Thickness</b>	1.04E+18	6.19E+17		LAYER 1	LAYER 2
<b>Ir</b>	0.1110	0.1126	<b>2.7E+15</b>	0.61	0.66
<b>Ti</b>	0.1808	0.1712			
<b>O</b>	0.6834	0.6979			
<b>D</b>	0.0015	0.0018			
<b>H</b>	0.0233	0.0165			

Tab.8.11. Results of ERDA data fitting, for the sputtered sample prepared at 450 °C.

Of course, this whole procedure was repeated for each material studied.

## Bibliography

1. S. Pizzini, G. Buzzanca, C. Mari, L. Rossi, S. Torchio, *Mat. Res. Bull.* **7**, 449 (1972).
2. K.J. O'Leary, T.J. Navin, Abs. 257, *Chlorine Bicenten. Symp.*, Electrochem. Soc. Inc., Princeton, N.J., 174 (1974).
3. F. Hine, M. Yasuda, T. Yoshida, *J. Electrochem. Soc.* **124**, 500 (1977).
4. W.A. Gerrard, B.C.H. Steele, *Journ. of Applied Electrochem.* **8**, 417 (1978).
5. G. Novell-Leruth, G. Carchini, N. López, *The Journ. of Chem. Phys.* **138**, 194706 (2013).
6. U. Mizutami, *Hume-Rothery rules for structurally complex alloy phases* **1**, 1-6, CRC Press, Taylor and Francis group (2011).
7. E.F. Osborn, *J. Amer. Ceram. Soc.* **36**, 147 (1953).
8. Joint Committee on Powder Diffraction Standards; International Centre for Diffraction Data: Swarthmore, PA, 1988.
9. M. Guglielmi, P. Colombo, V. Rigato, G. Battaglin, A. Boscolo, A. De Battisti, *J. Electrochem. Soc.* **139**, 1655 (1993).
10. A. De Battisti, L. Nanni, G. Battaglin, Ch. Comninellis, *Oxide electrocatalysts. The case of RuO<sub>2</sub>-based film electrodes*, In *New Promising Electrochemical Systems for Rechargeable Batteries*, V. Barsukov and F. Beck (eds.), 197-211, Kluwer Academic Publishers (1996).
11. W.L. Bragg, *The Crystalline State*, G. Bell, London, 189 (1933).
12. Yu.E. Roginskaya, O.V. Morozova, *Electrochim. Acta* **40** (7), 817 (1995).
13. A.G. Shtukenberg, Yu O. Punin, Ol'ga V. Frank-Kamenetskaya, *Russ. Chem. Rev.* **75**, 1083 (2006).
14. B.E. Warren, J. Bisce, *J. of the Am. Ceramic Soc.* **21**(2), 49 (1938).
15. S. Andersson, B. Collén, U. Kuylenstierna, A. Magnéli, *Acta Chemica Scandinavica* **11**, 1641 (1957).
16. D. Grier, G. McCarthy, North Dakota State Univ., Fargo, North Dakota, *ICDD Grant-in-Aid* (1991).
17. United Steel Companies, Sheffield, England, UK, Private Communication.
18. A. De Battisti, G. Lodi, L. Nanni, G. Battaglin, A. Benedetti, *Can. J. Chem.* **75**, 1759 (1997).
19. E.P. Degarmo, J. Black, R.A. Kohser, *Materials and Processes in Manufacturing (9th ed.)*, Wiley, 223 (2003).

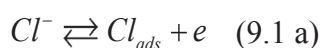
20. G. Battaglin, V. Rigato, S. Zandolin, A. Benedetti, S. Ferro, L. Nanni, A. De Battisti, *Chem. Mater.* **16**, 946 (2004).
21. L. Burke, O. Murphy, *J. electrochem. Soc.* **96**, 19 (1979).
22. D.V. Kokoulina, T.V. Ivanova, Y.I. Krasovitskaya, Z.I. Kudryavtseva, L.I. Krishtalik, *Elektrokhimiya* **13**, 1511 (1977).
23. I.M. Kodintsev, S. Trasatti, M. Rubel, A. Wieckowsky, N. Kauhler, *Langmuir* **8**, 283 (1992).
24. G. Battaglin, D. Rosestolato, S. Ferro, A. De Battisti, *Electrocatalysis* **4**, 358 (2013).
25. M. Pourbaix, N. de Zoubov, J. Van Muylder, *Atlas d'équilibres électrochimiques*, Paris, Gauthier-Villars Ed. (1963).
26. E. Laviron, *J. Electroanal. Chem.* **112**, 1 (1980).
27. E. Laviron, L. Roullier, C. Degrand, *J. Electroanal. Chem.* **112**, 11 (1980).
28. S. Levine, A.L. Smith, *Discuss. Faraday Soc.* **52**, 290 (1971).
29. L.D. Burke, O.J. Murphy, J.F. O'Neill, *J. Electroanal. Chem.* **81**, 391 (1977).
30. D. Galizzioli, F. Tantardini, S. Trasatti, *J. Appl. Electrochem.* **4**, 57 (1974).
31. W. O'Grady, C. Iwakura, J. Huang, E. Yeager, *Proc. Sym. Electrocatalysis, The Electrochemical Society*, N.J., USA, 286 (1974).
32. A.J. Bard, L.R. Faulkner, *Electrochemical Methods – Fundamentals and Applications*, J. Wiley & Sons, Inc. (1980).
33. G. Battaglin, A. De Battisti, A. Barbieri, A. Giatti, A. Marchi, *Surface Science* **251/252**, 73 (1991).
34. M.V. Reddy, A. Levasseur, *Journ. of Electroanal. Chem.* **639**, 27 (2010).
35. E. Sonder, J.R. Martinelli, R.A. Zuhr, R.A. Weeks, *Crystal Lattice Defects and Amorphous Mat.* **15**, 277 (1987).
36. A. Kellock, J. Baglin, *Nucl. Instr. Meth.* **B79**, 493 (1993).
37. C.S. Kim, S.K. Kim, H.D. Choi, *Nucl. Instr. Meth.* **B155**, 229 (1999).

## 9. Electrochemical Characterization: Investigation on the Chlorine Evolution Reaction (*ChlER*)

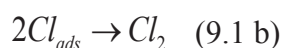
### 9.1. About the Chlorine Evolution Reaction: chronicle of the proposed mechanisms

The first study dealing with ruthenium dioxide, one of the most active components of the so-called *Dimensionally Stable Anodes* (DSAs) used in the chlor-alkali industry, was published in 1971 [1]. A necessary prerequisite for the understanding of this aspect is the detailed knowledge of the mechanism of the electrochemical reaction; in absence of this precious information, it is not possible to rationalize a specific electrode behavior, and any rationale improvement of its properties is hampered. In 1986, a quite interesting and thorough review on the state of the art on the kinetics of the chlorine evolution reaction on this kind of materials, including RuO<sub>2</sub>, RuO<sub>2</sub> + TiO<sub>2</sub>, Co<sub>3</sub>O<sub>4</sub> and NiCo<sub>2</sub>O<sub>4</sub>, was proposed by Trasatti [2], and the following paragraph reports a summary of his work, adding some considerations about works that were (or were not) considered by him. Because of the chemical similarities between ruthenium and iridium oxides, some information extracted from the literature concerning the former material appears useful also for the discussion of data on the latter. Moreover, iridium-oxide-based materials ensure a better degree of stability under strong anodic polarization, while ruthenium dioxide may form soluble or volatile compounds (RuO<sub>3</sub> and RuO<sub>4</sub>), and thus a better reproducibility of experimental results can be assured. The typical structure of electrode devices, used in kinetic studies, consists of a flat support (usually made of Titanium) coated with a thin (a few μm) layer of material, which has the morphology of a sintered powder; so, cracks, pores, both amorphous and crystalline domains are typical characteristics of such electrodes.

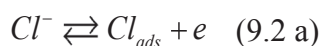
The first mechanism proposed for the chlorine evolution on ruthenium-oxide-based electrodes dates back to 1971 by Bianchi [3]; the anodic reaction proceeds via an electrochemical-chemical mechanism, known as a Volmer-Tafel sequence of steps. Actually, this proposal was not supported by any experimental evidences: the process was considered analogous to the electrochemical reduction of protons, for the hydrogen production, and owing to this similarity, the same model (the electrochemical extension of the Langmuir-Hinshelwood pathway proposed in heterogeneous catalysis) was taken into account:





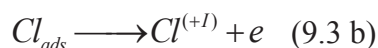


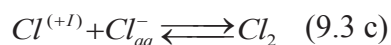
In 1972, an investigation based on a 13 %mol RuO<sub>2</sub> + 13 %mol IrO<sub>2</sub> + TiO<sub>2</sub> electrode (a composition close to that of industrial anodes) was published by Faita and Fiori; these authors reported that Tafel slopes decreased from 40 to 32 mV/decade as the NaCl concentration was increased from 1 to 4 mol/l [4]. However, data have probably been vitiated by the so-called *Losev's effect*: unusually low Tafel slopes can be attained as a result of a condition of supersaturation; actually, especially when working at high temperatures, a rise in the chlorine concentration nearby the electrode surface, when the electrode potential is increased, may lead to a sort of “supersaturation”, which can change the mass transfer regime and affect the  $E\text{-log}j$  dependence, resulting in an anomalously low slope for the polarization curve ( $b < 2.3RT/2F$ ) [5]. In addition, Faita and Fiori observed that the apparent reaction order at constant overpotential is variable, being almost zero at low overpotentials (which implies a fractional,  $<1$ , chemically significant reaction order at constant potential). Discussing their data, they proposed a mechanism (a Volmer-Heyrovsky sequence of steps), whose pattern is different from that previously proposed by Bianchi:



In 1973, Mortimer and Kuhn investigated coatings consisting of RuO<sub>2</sub> and IrO<sub>2</sub>, as well as RuO<sub>2</sub>-TiO<sub>2</sub> mixtures, studying the effects of different thicknesses and different calcination times during the Sol-Gel preparative, and those of different component ratios in the case of the mixtures [6]. On the whole, a conventionally linear Tafel behavior was not observed, but it was possible to extrapolate two regions: a curved section below 85 mV of overpotential, and a Tafel line (though not well identified) characterized by a slope between 95 and 108 mV/decade in the case of RuO<sub>2</sub> (120 mV/decade for IrO<sub>2</sub>), which varied with the chloride concentration and the temperature. A kinetic mechanism was not proposed, and the lack of a well-defined linear Tafel plot was explained in terms of semiconducting properties of films.

In 1975, Érenburg and coworkers focused their interest on the ruthenium-titanium mixed-oxide electrode (30-70 %mol); to account for the low Tafel slopes (30 mV/decade) recorded, they proposed a new mechanism [7,8], in which the rate-determining step consists of a barrier-less electrochemical oxidation of atomic chlorine:



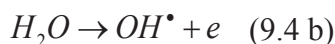
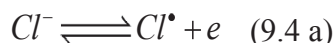


The Tafel slope of the anodic branch of the polarization curve is given by the relation  $b = 2.3RT / F(1 + \alpha)$ ; in the case of a barrierless discharging,  $\alpha=1$  and thus  $b=30$  mV/decade. When increasing the overpotential, Érenburg and coworkers saw that the barrierless process turned into a normal process, for which  $\alpha=0.5$  and  $b=40$  mV/decade. Thus, the polarization curves for those electrodes consisted of two parts, and the reaction orders with respect to  $Cl^-$  and  $Cl_2$  were the same for both portions, with the result that the value of the potential corresponding to their intersection did not depend on  $Cl_2$  partial pressure and  $Cl^-$  concentration. Following this consideration, Érenburg *et al.* suggested that the mechanism of the ChIER remains the same in both Tafel portions; consequently, a change in Tafel slope has to be correlated to variations in the transfer coefficient, and not to a replacement of the rate-determining step. In a subsequent paper [9], while working with electrodes based on pure ruthenium oxide, Érenburg and coworkers registered a unique Tafel slope of 40 mV/decade, and the aforementioned behavior of the mixed oxides was then attributed to the presence of two distinct kinds of surface sites, which differ in the strength of adsorption of the intermediates. Working with an excess of  $H_2SO_4$  (2 mol/l), in order to suppress the secondary effects due to changes in the structure of the double layer on the electrode and in the surface state (which may be induced by a change in chloride concentration), the reaction order with respect to chloride was estimated to be around 1 [10].

In 1977, Janssen *et al.* investigated the ChIER at  $RuO_2$ - $TiO_2$  30-70 %mol electrodes in solutions with a constant nominal chloride concentration ( $[Cl^-]=4$  M), made with NaCl and HCl in different ratios [11]. They measured Tafel slopes around 50-60 mV/decade, studying different parameters (solution composition, temperature, time of anodization, roughness, etc.), without recognizing any systematic correlation between them. Obtained data were in agreement with a Volmer-Heyrovsky mechanism of reaction (equations 9.2).

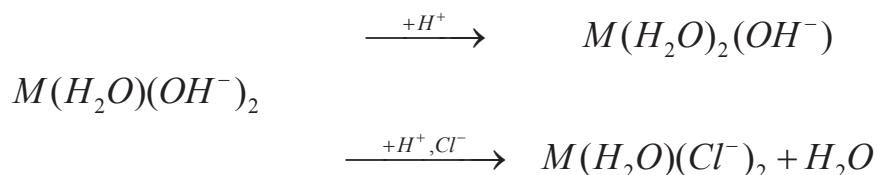
The ChIER at electrodes based on  $RuO_2$  and  $TiO_2$  mixtures, with different compositions, was later investigated also by Harrison and Denton (in 1978), who made use also of impedance measurements [12]. The estimated Tafel slopes were of 30 mV/decade for materials with a high content of noble metal oxide, increasing to 40 mV/decade when the ruthenium oxide content was less than 20% mol. The suggested mechanisms were those described by equations (9.1) and (9.3), respectively. Impedance measurements showed the presence of a single RC contribution, but at low  $RuO_2$  content the Nyquist diagrams became flatter, and this aspect was related to the porous structure of the system. Two years later, working with  $RuO_2$ - $TiO_2$  electrodes in different HCl/KCl solutions, and studying also the

chlorine reduction reaction, another mechanism was proposed [13], in order to justify a unitary reaction order with respect to chloride. The proposed mechanism is summarized by equations 9.4:



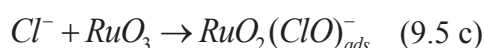
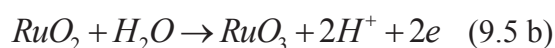
The above sequence of steps implies a less efficient production of chlorine, whose synthesis takes place through the preliminary formation of HOCl (subsequently, a chemical reaction with chlorides takes place, in acidic media); the authors suggest that HOCl can accumulate in the solution, depending on pH. The kinetics of the process was not investigated in more detail. However, they worked with solutions of NaCl/HCl at different ratios, where the strongly acidic pH does not allow an easy formation of HOCl (at least in terms of thermodynamic potentials), and thus their hypothesis does not seem plausible.

In the same year, two other papers appeared, one by Arikado *et al.* [14] and the other by Augustynski *et al.* [15], which added other interesting details to the complex data set discussed so far. They argued that not enough attention had been devoted to the properties of the oxide/solution interface. Arikado *et al.* determined the reaction order with respect to  $Cl^-$  from the slope of the  $\log j_0-E_{eq}$  relationship, which resulted to be 2.3. They also measured high values for the open-circuit potential, which have never been observed before and cannot be easily explained; the phenomenon was interpreted considering the replacement of a surface  $-OH$  species by  $-Cl$  species (surface specific adsorption), which gives rise to surface oxychloro-complexes. The observed enhancing effect of acidity, on the reaction rate, was related to a higher availability of specific Cl surface sites. The process of interaction between chloride and noble metal site can be schematized as follows:



During their investigations, carried out at  $RuO_2$  and  $RuO_2-TiO_2$  electrodes in 4M NaCl solutions, Augustynski *et al.* performed an XPS characterization of electrode surfaces, before and after the polarization tests [15]. On both materials, they detected the presence of surface defects having the structure of  $RuO_3$  (analogous to those found on ruthenium oxide powders), and two different chlorinated species: chloride ions and adsorbed atomic chlorine. As a matter of fact, the presence of chloride anions could be due to an incomplete pyrolysis of the salty

precursors. On the other hand, the relative concentration of  $Cl_{ads}$  and Ru indicated that the degree of surface coverage by chlorine intermediates was close to unity (thus suggesting a full coverage by adsorbed Cl species). This last outcome is in disagreement with the proposal of Érenburg *et al.* (equations 3), which implies  $\theta \ll 1$ . In addition, the above authors blamed the frequent recourse to an excess of  $SO_4^{2-}$  (adopted in order to suppress secondary effects of ionic distribution in the double layer) because of the tendency of that anion to adsorb on the electrode material, provoking modifications on the adsorption of chlorides. The mechanism suggested by Augustynski *et al.* is interesting because it requires a preliminary oxidation of the electrode surface (a typical step in the oxygen evolution reaction mechanism), which precedes the chloride oxidation:

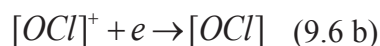


As above commented, the mechanistic scheme was proposed on the basis of XPS data only, without looking for any kinetic evidence.

Ex-situ investigations have been carried out also by Gorodetskii *et al.*, who studied  $RuO_2$ - $TiO_2$  electrodes, before and after polarization treatments (having a duration of 100 h) in 300 g/l NaCl solution, at pH=2 and 87°C, by means of Auger electron spectroscopy [16]. Their investigation pointed out that a large amount of chlorine was incorporated in the coating, while the surface layers appeared depleted of ruthenium (the final concentration was one half or less with respect to the initial one). In their work, Gorodetskii *et al.* confirmed the high coverages discussed by Augustynski *et al.* ( $\theta_{Cl}$  close to 1); moreover, they suggested that the incorporation of chlorine into the coating could modify drastically the properties of the electrocatalyst, allowing the chlorine evolution at high rates, notwithstanding the depletion of ruthenium.

The studies of Denton *et al.* and Augustynski *et al.* draw attention to the relevant role of the [ClO] specie in the ChIER mechanism; the involvement of the so-called “chloronium” species has been invoked also by Hepel *et al.* [17,18]. They carried out investigations on  $RuO_2$  single crystals, focusing on the (110) and (101) faces, and measuring, in both cases, a Tafel slope of 40 mV/decade; neither a reaction order nor a pH effect were reported. Moreover, using cyclic voltammetry in  $Cl_2$ -saturated chloride solutions (pH=0), they registered two cathodic waves having a diffusional nature, one centered around 0.8  $V_{SCE}$ , more pronounced for the (110) face, and the other centered around 0.2  $V_{SCE}$ , more pronounced

for the (101) face. According to the hypothesis of the authors, the former wave is due to the reduction of chloride species adsorbed on oxygen sites on face (110), but not on face (101), while the latter is related to the “normal” reduction of  $Cl_{ads}$  on ruthenium sites on face (101). The proposed mechanism is schematized by equations 9.6:



Actually, the above sequence of steps differs in several aspects from the outcomes of previous works, and a more detailed investigation would probably be necessary.

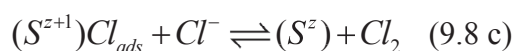
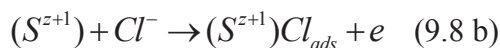
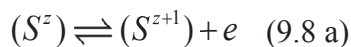
In 1979, Burke and O’Neill studied the chlorine evolution reaction on  $RuO_2$  anodes [19], proposing that the discharge of chloride ions takes place on oxidized surface sites ( $O_{ads}$  or, perhaps,  $RuO_3$ ). The obtained results, in terms of Tafel plots, were similar to those of Mortimer and Khun [6], where the linear region was very difficult to identify. Burke and O’Neill reported that the ChLER proceeds through the formation of  $HOCl/ClO^-$ , which is further decomposed in acidic solution and in the presence of chloride ions, producing gaseous chlorine; a mechanism of this type, somewhat similar to the Volmer-Heyrovsky scheme outlined by Jansen *et al.* [11], can be depicted as follows:



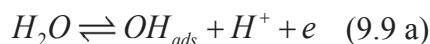
The reaction rate appears governed by the degree of coverage by adsorbed oxygen: in fact, the  $RuO_2$  anodes are very active also for the oxygen evolution, and they are also excellent catalysts for the oxidation of organic compounds, such as alcohols (above 1.0 V), even when a rupture of carbon-carbon bonds is required [20]; it seems unlikely for this latter reaction to occur easily in acidic solutions by means of a direct electron transfer, but it is likely that  $O_{ads}$  are decisive in this potential region. Moreover, by performing polarization tests and cyclic voltammetries with and without a vigorous stirring, the authors concluded that the  $Cl_2$  evolution proceeds involving only the external surface (as it was also suggested, one year later, by Mozota *et al.* [21], working with anodic iridium and ruthenium oxide-based rods of different thicknesses), while the  $O_2$  production implicates the whole catalytic mass.

In the same period, Tilak investigated the ChLER at  $RuO_2$ - $TiO_2$  electrodes, from 5 M NaCl solutions at 95°C, recording quite low Tafel slopes (28 mV/dec) and a stoichiometric number <1 [22]. As previously discussed, and in consideration of the experimental conditions adopted, the low values of Tafel slope could be due to the so-called *Losev effect* [5].

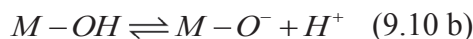
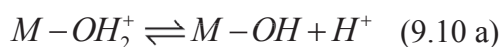
In 1981, Krishtalik reexamined his previous proposal of mechanism for the chlorine evolution, studying also the oxygen evolution reaction [23]. He concluded that the key factor, in the reaction rate, must be the redox behavior of surface sites. Such a statement represents an implicit form of the mechanism of Érenburg, which will be discussed later:



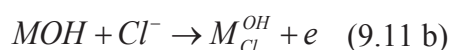
Érenburg *et al.* started talking about a retarding effect of  $H^+$  after noting a dependence of the reaction rate on pH and on the electrode potential [24]; obtained data were discussed on the basis of the following sequence of steps:



Their approach took explicitly into account the possible equilibria existing at the surface of oxide electrodes (on RTOEs – Ruthenium Titanium Oxides Electrodes – in particular) [24]:



In equations (9.10), M designates a surface metal site, belonging to the lattice of the metal oxide; when the pH is varied, the surface concentration of M-OH or  $MO^-$  species changes. Since those sites are likely to actually represent the surface active sites, an increase in pH may lead to an increase in the number of active sites and, consequently, to an acceleration of the chlorine evolution reaction [25]. However, to consider only the change in the number of active sites did not allow to adequately explain the experimental data: in particular, the reaction order with respect to  $H^+$  could not be higher than 1, and there was not a clear relation with the electrode potential. Since the experimental results showed a variation in  $R_{H^+}$  (reaction order with respect to  $H^+$ ) from  $\approx -0.5$  to  $\approx -2$ , the considered reaction scheme became as follows:



In view of that, the reaction rate can be written as:

$$i \sim a_{H^+}^{-2} a_{Cl^-} e^{(1+\alpha)E} e^{(1-\alpha)\phi^*} \quad \text{Eq. 9.12}$$

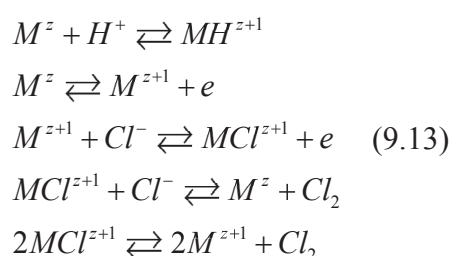
where  $\phi^*$  represents the electric potential on the reaction site, and  $\alpha$  is the anodic transfer coefficient. As shown, the pH and the electric potential on the site exert opposite effects.

All the considerations about the state of the surface active sites have been postulated without referring to the point of zero charge of RuO<sub>2</sub> (which varies from about 4.0 to 6.1, for oxide powders fired at temperatures from 300 to 700 °C) [26]; in case the reaction sites are positively charged, this may favor the adsorption of anions. Regarding IrO<sub>2</sub>, its *pzc* is < 2, in the pH region where the ChIER is studied.

The dependence of activity on pH was further investigated on pure RuO<sub>2</sub> single crystals, and on (110) and (230) faces in particular. The (230) face is more open than the (110), and has shown to be more active for the ChIER; a reaction order of -1 was estimated, with respect to the proton, at the (110) face, while no such dependence (R=0) was assessed for the (110) [27].

Tomcsányi *et al.* investigated RuO<sub>2</sub>-TiO<sub>2</sub> mixed-oxide electrodes of different compositions, by means of cyclic voltammetry and radiochemical techniques, working in 0.1M NaCl – 1M HClO<sub>4</sub> solutions [28]. The voltammetric behavior of an adsorbed intermediate was studied, and the experimental results showed that the electrooxidation of chloride, on this kind of electrode, proceeds through the steps of the Volmer-Heyrovsky mechanism.

Fernandez *et al.* [29,30,31] performed detailed studies on ruthenium-based materials prepared by spray pyrolysis on titanium wires starting from 0.16M Ru(NO)(OH)<sub>x</sub>(NO<sub>3</sub>)<sub>3-x</sub> precursors, using the polarization resistance method at conditions close to the equilibrium potential, and concluded that the Volmer-Tafel and Krishtalik-Érenburg mechanisms are both active:



They explored different chloride concentrations (from 0.5 to 4 M) and different pH (from 0 to 11), varying also the partial pressure of chlorine, from 0.2 to 1 atm. These experiments were carried out after the theoretical demonstration of the validity of Krishtalik-Érenburg mechanism [32] without any kinetic approximations.

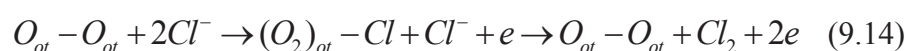
The experiments done using different spinels, like Co<sub>3</sub>O<sub>4</sub> and NiCo<sub>2</sub>O<sub>4</sub>, have always produced reaction orders with respect to H<sup>+</sup> smaller than 1: this evidence suggests that the

mechanism of ChLER at spinels is characterized by smaller degrees of freedom, with respect to that occurring on ruthenium oxide based electrodes. Since the  $pzc$  of  $Co_3O_4$  is about 7.5, at the operative pH of the ChLER the spinel surface should be positively charged, but no indications exist about the possibility to reach a saturation condition [33].

Da Silva *et al.* [34] investigated mixtures of  $RuO_2$  and  $Co_3O_4$  (mixed rutile/spinel oxides) for the ChLER from different chloride solutions, varying  $Cl^-$  and  $H^+$  concentrations. The reaction orders with respect to both species were determined, together with a constant Tafel slope of 33 mV/decade, for mixtures containing between 0 and 80% ruthenium oxide; a Tafel slope of 40 mV/decade was found at higher Ru contents. The experimental picture seems to confirm the mechanism originally proposed by Krishtalik (equations 9.8).

In 2006, Santana and De Faria [35] worked on  $Ru_{0.3}Ti_{0.6}Ce_{(0.1-x)}O_2-Nb_2O_5$  (with  $0 < x < 0.1$ ) studying both the OER and the ChLER and aiming to determine the reaction orders with respect to both, chloride and proton (measurements were carried out in 0.5-5M NaCl solution at  $pH < 2$ : different pH were obtained substituting NaCl with an equimolar amount of HCl). Tafel slopes of 30 and 40 mV/decade and a unitary reaction order with respect to  $Cl^-$  were in agreement with the mechanism proposed by Érenburg *et al.*, with an  $\alpha$  value close to 1, also in agreement with Kristhtalik literature works that talked about a ChLER as a quasi-barrierless reaction. The null reaction order, measured with respect to the proton, suggested a negligible effect of the surface structure of electrodes in the case of the ChLER, while a notable effect was found when studying the OER.

Modern developments in *ab initio* calculations (based on DFT) of electrochemical reactions [36,37,38] have paved the way to the study of the ChLER on  $RuO_2$  (110) at an atomic level, though using several approximations. With the utilization of an electro-thermodynamical approach [36], surface Pourbaix diagrams have been constructed, identifying the most stable structure of the catalyst surface as a function of pH and potential, and in equilibrium with  $Cl^-$ ,  $H^+$  and  $H_2O$ . This approach has been described in a review by Over [39], and the proposed mechanism for the ChLER was schematized as follows:



where  $O_{ot}$  represents under-coordinated surface oxygen atoms that are linked together. As can be seen, the Volmer-Tafel pathway is excluded when such a situation exists. However, when the under-coordinated ruthenium site is not blocked by the linkage between two  $O_{ot}$ , the chemical desorption mechanism can take place, as evidenced by Hansen in 2010 [40]. Obviously, these studies were carried out on pure ruthenium oxide, and the mechanism can change because of the addition of a valve-metal oxide; the availability of under-coordinated



ruthenium sites on the surface appears critical for the formation of the intermediate for pure RuO<sub>2</sub>, but may be irrelevant in the case of a mixture.

The whole experimental picture appears quite complex, and a systematic explanation of the reaction mechanism as a function of the electrode material used is not easy; difficulties essentially originate by the fact that all materials investigated differ for the preparation method (Sol-Gel, anodizing process, spray pyrolysis, etc.) and also the experimental conditions were different, at times. In addition, the utilization of very concentrated brines (4 M, near to the limit of saturation) can be justified making reference to the industrial production of chlorine in chlor-alkali plants, but such conditions do not appear appropriate for carrying out a kinetic study. In fact, in the presence of a so high ionic strength, assuming reasonable coordination numbers for both sodium and chloride ions, the organization of water molecules is forced by the presence of these ionic species, and the system cannot be considered from a correct thermodynamic point of view.

## **9.2. Polarization curves: Tafel slopes and Reaction Orders evaluation**

The chlorine evolution reaction was taken as a model for carrying out a systematic study of prepared samples. The importance of this electrochemical process in industry (especially in terms of development of electrode devices ), together with the confused experimental picture proposed in literature, have prompted toward a detailed study of that mechanism.

Before discussing the experimental data, it may be useful to recall a few theoretical notions about some basic concepts of electrode kinetics. The electrochemical kinetics can be considered similar to the conventional chemical catalysis, with the addition of the electrical variable. The current density,  $j$ , is proportional to the rate of the heterogeneous reaction,  $v$ , that takes place across the interface, through the Faraday's constant,  $F$ , and the number of exchanged electrons,  $n$ :

$$j = nFv \quad \text{Eq.9.15}$$

The well-known theory of Eyring-Evans-Polanyi, which refers to the kinetics of a chemical process (summarized in Eq. 9.16), can be also adapted for describing the electrochemical process taking place on an electrode surface (Eq. 9.17).

$$v = \kappa \frac{k_B T}{h} e^{-\frac{\Delta G^\ddagger}{RT}} \quad \text{Eq. 9.16}$$

$$v = \frac{i}{nF} = \kappa \frac{k_B T}{h} e^{-\frac{\Delta G^\ddagger}{RT}} e^{-\frac{\alpha_c F \Delta \Phi}{RT}} \quad \text{Eq. 9.17}$$

The equations derive from the steady-state theory, and the theoretical model was developed starting from basics of statistical thermodynamic [41,42]. Starting from this theoretical model, it is possible to write the equation that expresses the net speed of the electrochemical process on an electrode surface; this equation is one of the fundamental relationships of the electrochemical kinetics. It describes how the electrical current on an electrode depends on the electrode potential, considering that both a cathodic ( $\vec{i}$ ) and an anodic ( $\bar{i}$ ) reactions occur at the same electrode surface (Eq.9.18) [43].

$$i = \vec{i} - \bar{i} = i_0 \left\{ \exp\left[\frac{\bar{\alpha} n F \eta}{RT}\right] - \exp\left[-\frac{\vec{\alpha} n F \eta}{RT}\right] \right\} \quad \text{Eq.9.18}$$

where:

- $i$ : electrode current, normalized to the electrode surface, A m<sup>-2</sup>
- $\bar{i}$ : anodic electrode current density, A/m<sup>2</sup> (defined as  $i = I/A$ )
- $\vec{i}$ : cathodic electrode current density, A/m<sup>2</sup> (defined as  $i = I/A$ )
- $i_0$ : exchange current density, A/m<sup>2</sup>
- $E$ : electrode potential, V
- $E_{eq}$ : equilibrium potential, V
- $T$ : absolute temperature, K
- $n$ : number of electrons involved in the electrode reaction
- $F$ : Faraday constant
- $R$ : universal gas constant
- $\vec{\alpha}$ : so-called cathodic charge transfer coefficient, dimensionless
- $\bar{\alpha}$ : so-called anodic charge transfer coefficient, dimensionless
- $\eta$ : activation overpotential (defined as  $\eta = E - E_{eq}$ ).

$i_0$  is called *exchange current density* and represents the net current that passes through the electrode interface when the overpotential  $\eta$  is equal to zero. The above equation is valid when the studied process is controlled by the electron exchange phenomenon, and not by the mass transfer. Taking into account this aspect, the so-called Butler-Volmer equation can be written in a more general form (Eq. 9.19).

$$i = \vec{i} - \bar{i} = i_0 \left\{ \frac{C_o(0,t)}{C_o^*} \exp\left[\frac{\bar{\alpha} n F \eta}{RT}\right] - \frac{C_r(0,t)}{C_r^*} \exp\left[-\frac{\vec{\alpha} n F \eta}{RT}\right] \right\} \quad \text{Eq. 9.19}$$

where  $C_o$  and  $C_r$  refer to the concentration of the oxidized and reduced forms, respectively;  $C(0,t)$  represents the time-dependent concentration at the electrode surface, while  $C^*$  stands for the bulk concentration (which is formally constant). Eq. 9.18 is obtained from Eq. 9.19 by assuming that the concentration of the electroactive specie at the electrode surface is constant and equal to the bulk one, or, more generally, the concentration terms are constant and can be included in the exchange current value.

Taking into account the Eq. 9.18, the interesting forms of the Butler-Volmer equation, useful for obtaining mechanistic information, are the limiting cases, *i.e.*, the low overpotential region ( $\eta < 0.1\text{V}$ ) and the high overpotential region ( $\eta > 0.1\text{V}$ ) [44].

#### Low-overpotential region (“low field approximation”)

If the overpotential,  $\eta$ , is close to 0, it is possible to expand the Butler-Volmer equation using the Taylor-McLaurin series (Eq. 9.20), where the exponential terms are transformed in a sum of polynomials.

$$i = i_0 \left\{ 1 + \frac{\bar{\alpha}F\eta}{RT} + \dots - 1 + \frac{\bar{\alpha}F\eta}{RT} + \dots \right\} \quad \text{Eq. 9.20}$$

By stopping the two series to the first order, one obtains

$$i \approx i_0 \frac{(\bar{\alpha} + \bar{\alpha})F\eta}{RT} \approx i_0 \frac{nF\eta}{\nu RT} \quad \text{Eq. 9.21}$$

where  $n$  represents the number of steps in a mechanism in which the rate-determining one is repeated  $\nu$  times.

The equation degenerates to a linear function, where the slope  $\left( \frac{\delta i}{\delta \eta} \right)_{T,C}$  is proportional to the exchange current, as reported in Eq. 9.22.

$$\left( \frac{\delta i}{\delta \eta} \right)_{T,C} \approx \frac{i_0 n F}{\nu RT} \quad \text{Eq. 9.22}$$

#### High-overpotential region (“high field approximation”)

Let's consider again the Eq. 9.18: when the module of the overpotential is high enough, the contribution of one part of the electrochemical process can be neglected, and the net current corresponds only to the anodic or cathodic semi-reaction, respectively (Eq.9.23: in this example the cathodic contribution has been considered as negligible). This condition is

called *Tafel hypothesis* and, as shown in this paragraph, it can be used to obtain diagnostic parameters that help identifying the mechanism of the process considered.

$$i \approx i_0 \left\{ \exp \left[ \frac{\bar{\alpha} F \eta}{RT} \right] \right\} \quad \text{Eq. 9.23}$$

Considering the natural logarithms of both sides of equation 9.23, and rearranging the formula, it is possible to obtain the famous Tafel equation (written in 1905):

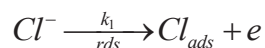
$$\eta = a + b \cdot \log i = \left( -\frac{2.303RT}{\bar{\alpha}F} \right) \log i_0 + \left( \frac{2.303RT}{\bar{\alpha}F} \right) \log i \quad \text{Eq. 9.24}$$

At first, the Tafel equation was proposed as an empirical equation relating the observed overpotentials to the current densities, for the hydrogen evolution reaction at mercury cathodes. It highlights the existence of a linear relationship between the overpotential and  $\log i$ , with a slope  $b$ , known as Tafel slope. The slope depends on the *transfer coefficient*,  $\alpha$ , which represents the fraction of the interfacial potential, at an electrode-solution interface, that lowers the free energy barrier for the electrochemical reaction of interest. The electroactive ions present in the interfacial region influence the interfacial potential, and an electrostatic work is done on the ion by a part of the interfacial electric field. What has been just discussed is the more general mathematical treatment, which refers to a multi-electron and multi-step electrochemical process; considering a single step reaction, with the exchange of only one electron, the Butler-Volmer equation can be simplified as follows:

$$i = \bar{i} - \vec{i} = i_0 \left\{ \exp \left[ \frac{(1-\beta)F\eta}{RT} \right] - \exp \left[ -\frac{\beta F\eta}{RT} \right] \right\} \quad \text{Eq. 9.25}$$

In that form, the cathodic and anodic transfer coefficients are substituted by  $\beta$  and  $(1-\beta)$ :  $\beta$  is called the *symmetry factor*, and its physical meaning is more intuitive than that of the transfer coefficient;  $\beta$  can vary between 0 and 1, and it is a measure of how the activated complex “resembles” to the reagent or to the product; it is called *symmetry factor* because usually (for common electrochemical reactions) it can be argued that a value of 0.5 corresponds to a symmetrical situation, in which the activated complex is placed exactly halfway between the reactant and the product. The symmetry factor is determined by the shape of the free-energy barrier, which the system must surpass along the reaction coordinate, as it is transformed from reactants to products [45]. The value of  $\beta$  also determines the degree of symmetry of the  $i/\eta$  plots, around the reversible potential. Furthermore, as it is possible to see in Eq. 9.24, the value of the intercept of the straight line is proportional to the exchange current density, theoretically providing a way to evaluate it, also under conditions of “high field” approximation.

The Tafel slope can be calculated for a hypothetical case, under certain assumptions. For example, let's consider the chlorine evolution reaction, under the assumption of quasi-equilibrium, and with the first step being rate-determining:



The rate of this step can be expressed as follows:

$$i_1 = Fk_1c_{Cl}(1-\theta)\exp(\beta EF / RT) \quad \text{Eq. 9.26}$$

This equation holds at high overpotentials, where the reverse reaction is negligible, and also the mass transport is ignored. Eq.9.26 depends on the symmetry factor, not to the transfer coefficient, because only a specific step is taken into account (not the whole process). Hypothesizing a very small partial coverage ( $\theta \ll 1 \rightarrow 1-\theta \approx 1$ ), the equation can be rewritten as follows:

$$i_1 = Fk_1c_{Cl} \exp(\beta EF / RT) \quad \text{Eq. 9.27}$$

For the overall reaction, one obtains:

$$i = nFk_1c_{Cl} \exp(\alpha_a EF / RT) = i_0 \exp(\alpha_a \eta F / RT) \quad \text{Eq. 9.28} \quad \text{with } i=2i_1 \text{ and } n=2$$

The exchange current density is proportional to the rate constant, to the concentration of reactant, and to the metal-solution potential difference at the reversible potential ( $E=E_{rev}+\eta$ ) (Eq. 9.29)

$$i_0 = Fk_1c_{Cl} \exp(\alpha_a E_{rev} F / RT) \quad \text{Eq. 9.29}$$

By taking the symmetry factor equal to 0.5, as said before, the Tafel slope becomes:

$$b = 2.3RT / \alpha_a F = 2.3RT / \beta F = 2(2.3RT / F) = 118mV \quad \text{at } 25^\circ C \quad \text{Eq. 9.30}$$

By using the same theoretical approach, and proceeding through more complicated cases (e.g., when the second step is assumed to be the rate-determining one, with the first one at quasi-equilibrium), it is possible to predict the Tafel slopes related to the mechanisms discussed in Par.9.1, as well-described in several book chapters [43,45].

The reaction order for an electrochemical process is expressed, as shown in Eq. 9.31, as the partial derivative of the current  $i$  (proportional to the process rate) with respect to the concentration  $c$  of a specie  $j$ , maintaining constant the temperature  $T$ , the pressure  $P$ , the potential  $E$  and the concentration,  $c_k$ , of the other species in solution (as well as the ionic strength).

$$\mathfrak{R}_i = \left( \frac{\partial \log i}{\partial \log c_j} \right)_{E,T,P,c_{k \neq j}} \quad \text{Eq. 9.31}$$

Another possibility is to refer to a reaction order taken at constant overpotential, but it is important to distinguish between them, since the reversible potential may change when the concentration of the reactant is modified, and thus also the overpotential can change, while the applied potential remains constant: because of this reason, the reaction orders estimated within this thesis work were determined according to the definition proposed in Eq. 9.31. To determine the concentration dependence, it is necessary to obtain a series of  $i/E$  plots and derive, from them, plots of  $\log i$  vs.  $\log c_j$  at a given potential; the slope of the line represents the reaction order at that particular potential  $E$ . The procedure can be applied to different regions of the polarization curves.

### **9.3. Preliminary tests for checking the electrochemical apparatus of measure**

Before studying the kinetics of the chlorine evolution reaction, a small number of preliminary tests were carried out on a selected sample ( $\text{IrO}_2\text{-TiO}_2$  1:2 mol, prepared by sol-gel at 350 °C). In particular, this initial investigation was focused on the oxygen evolution reaction (i.e., estimation of pertaining Tafel slope), since that process is well known in literature and should give irrefutable results on both iridium- and ruthenium-oxide-based materials [47,48,49], as well as on the possible effects of the anions of the supporting electrolyte (SE) present in solution. The specific adsorption of anions different from those interested by the reaction under study has to be avoided: sulfates seem to have a role in these terms, while the effects of perchlorates have been found to be unimportant [2].

The oxygen evolution reaction was studied under typical conditions, in a 1M  $\text{H}_2\text{SO}_4$  solution and at room temperature [50,51] using a Pt-mesh as CE and a common SCE as RE. The working electrode was pre-polarized at the highest potential value in order to enrich the solution in proximity of the electrode surface of dissolved oxygen; the steady-state polarization curve, corrected for the ohmic drop of the solution, is reported in Fig.9.1.

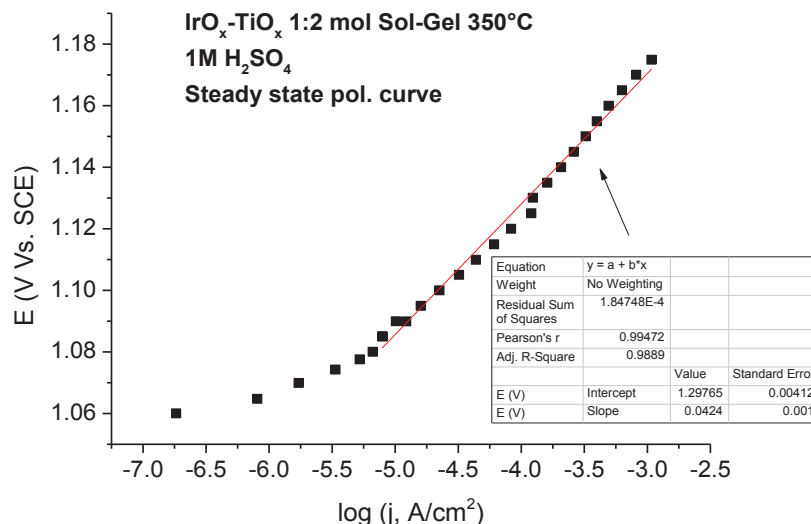


Fig.9.1. Steady-state polarization curve under oxygen evolution conditions in 1M H<sub>2</sub>SO<sub>4</sub> for the sol-gel 350 °C sample.

A good linearity with a slope of 40 mV/dec over 2.5 current decades has been found, suggesting a mechanism of oxygen evolution that proceeds via a Volmer-Heyrovsky pathway. The effect of the anion was then evaluated by registering a steady-state polarization curve under chlorine evolution conditions, working with a 1M solution of NaCl in which a strong acid (sulfuric or perchloric) has been added to obtain a concentration of 0.01M. As shown in Fig.9.2, no particular effects on the Tafel slope could be attested in the high overpotential region that is of interest for our studies.

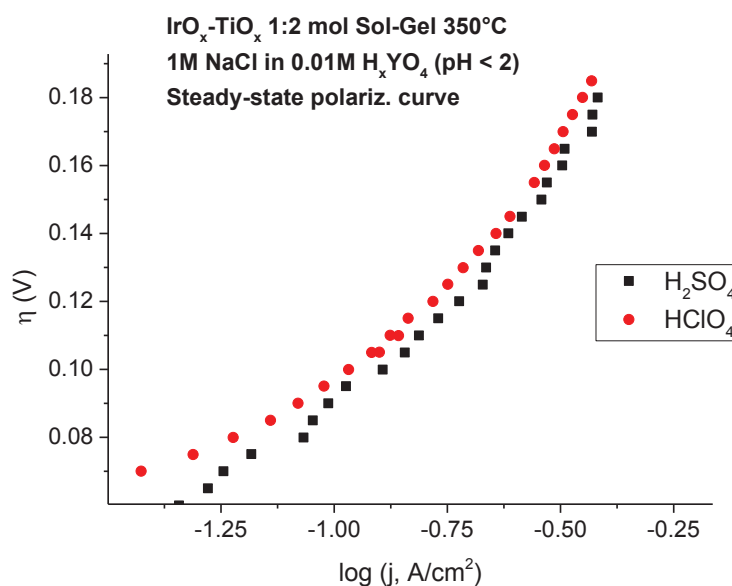


Fig.9.2. Steady-state polarization curves collected under ChIE conditions for Sol-Gel 350 °C sample: comparison between perchloric and sulfuric acids, used as supporting electrolyte for the correction of pH.

Differences in terms of pH are practically negligible, while the open circuit potentials differ of about 40 mV (1.10 V vs. SCE in the case of perchloric acid, 1.14 V vs. SCE when using sulfuric acid), probably because of possible effects of adsorption/coordination of the  $\text{SO}_4^{2-}$  anion on the electrode surface, which do not affect, however, on the behavior of the Tafel plot in term of slope, as seen also by Lodi *et al.* in 1978 [52]. For these reasons, the measuring system can be considered suitable to ensure the correct thermodynamic conditions necessary for the study of the kinetics of the electrochemical process, which is one of the objects of this research.

#### 9.4. Polarization curves collected at 25 °C

The polarization curves were collected, at first, at room temperature, varying the concentration of chlorides in solution, in order to obtain information about the reaction order of the main reagent. The concentrations of  $\text{Cl}^-$  explored were 0.05, 0.1, 0.5 and 1 mol/l, and a constant ionic strength was ensured at about 1 mol/l by adding specific amounts of sodium perchlorate. The pH of the system remained stable to 1.8, in the working electrode compartment, during all the time of testing, thanks to the utilization of 0.01 M  $\text{HClO}_4$ . All samples were pre-treated by cyclic voltammetry in 1M  $\text{HClO}_4$ , for reaching a reproducible level of hydration of the surface, and then under chlorine evolution reaction, by registering a “quasi-steady” polarization curve over a wide range of potential (from 1.50 to 1.05 V vs. SCE) for ensuring an activation of the material under the chosen experimental conditions. The polarization was started from the higher potential, by scanning the range with a scan rate of 0.5 mV/s. In addition, steady-state polarization curves were collected starting from the more anodic potential and decreasing it with a step of 5 mV, applying a step polarization time of 5 minutes (the required time to reach the steady state). The stability of the film was checked doing CVs in 1M  $\text{HClO}_4$  before and after each series of polarization tests. The data presented in this chapter are only related to the steady-state polarizations because they are of interest for the kinetic discussion about the chlorine evolution reaction.

As can be seen in Fig.9.3, a well-defined region of linearity cannot be identified, and this aspect will have important repercussions in the mathematical treatment proposed in this work of thesis. Of course, the uncompensated ohmic drop contribution of the solution was taken into account to correct the polarization curves; it was determined through *ad hoc* EIS experiments carried out at different potential values within the whole region explored.



For every sample, the reaction order with respect to chloride has been also evaluated, by choosing a value of potential that is located (as far as possible, for the reason just explained) in the “quasi-linear” Tafel region for all recorded curves. Tafel plots for the different specimens, collected point by point (steady-state conditions) for the different chloride concentrations, are reported below (Fig.9.3).

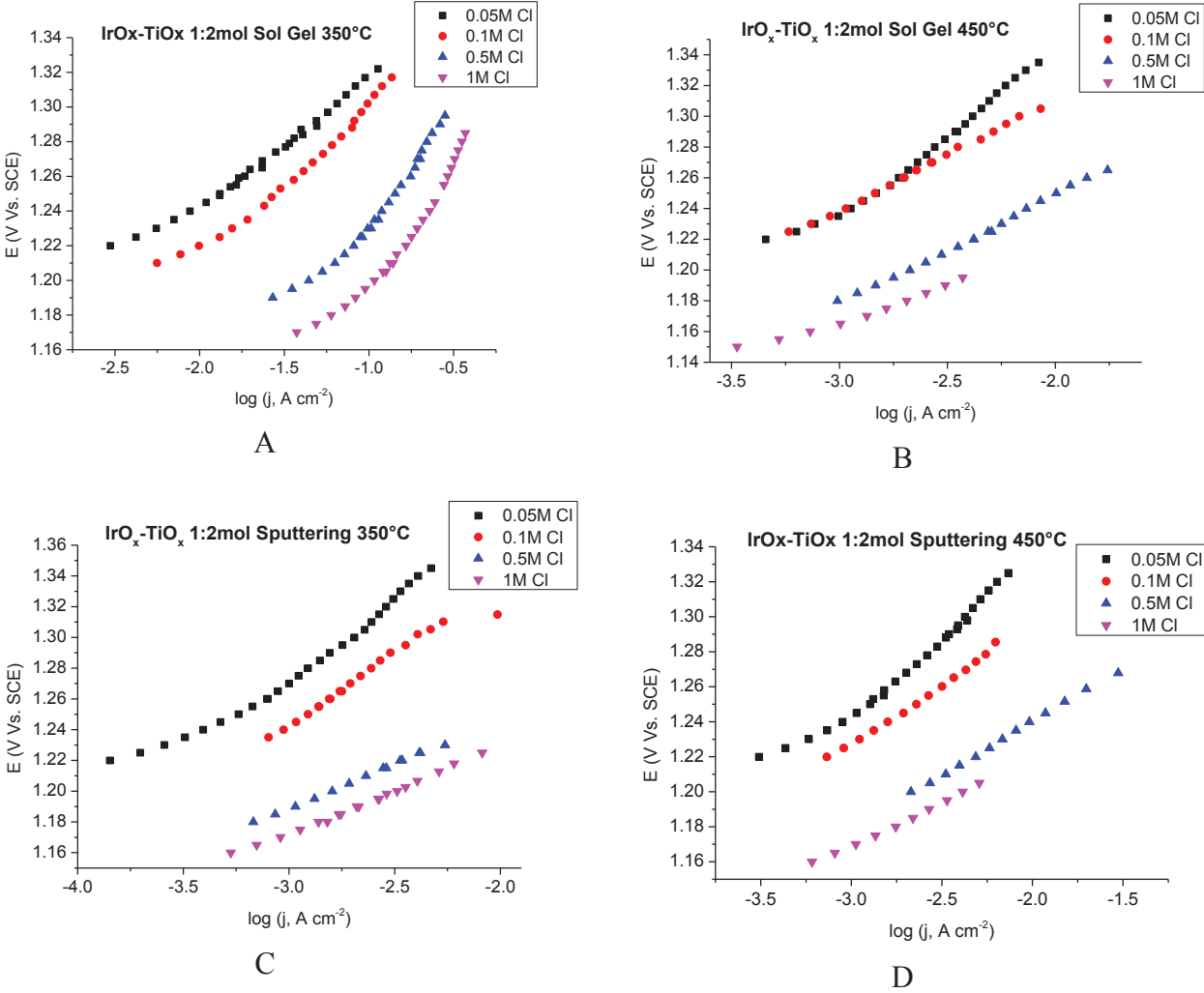


Fig.9.3. Tafel plots derived from steady-state polarization curves collected for Sol-Gel samples calcined at 350 (A) and 450 °C (B), as well as for sputtered samples prepared at 350 (C) and 450 °C (D).

The reaction order with respect to chloride was evaluated at 1.22, 1.24, 1.26 and 1.28 V vs. SCE: the first potential falls in the low-overpotential region, while the others in the high one; the average value was taken into account for the subsequent calculations (Fig.9.5). This approach is reasonable because also the values of current collected at 1.22 V appear reasonably free from any contribution due to the backward reaction of chlorine reduction: this evaluation was done by considering the whole Tafel plot, obtained from polarization curves collected under “quasi-steady” conditions, accomplished for activating each electrode

material. Two examples have been reported in Fig.9.4, where the data obtained with the lowest and the highest concentrations of chloride are compared, for the same sample.

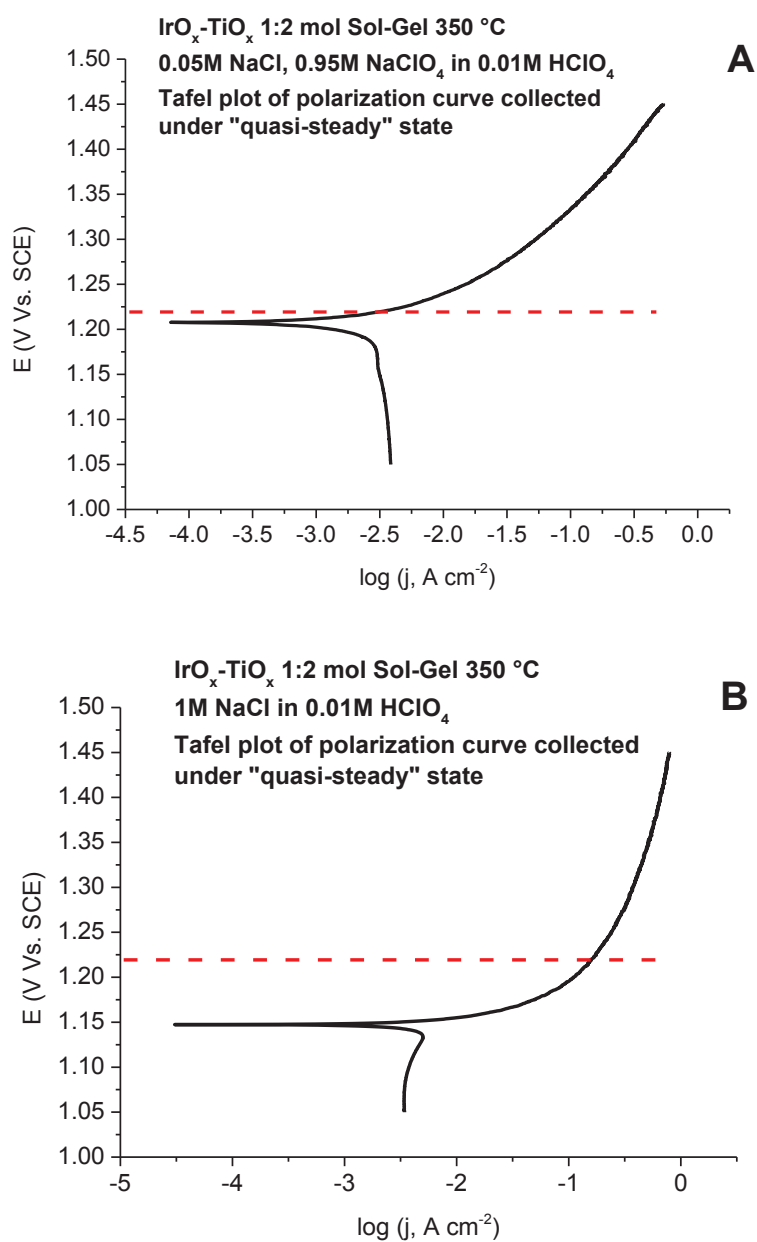


Fig.9.4. Tafel plots related to polarization curves collected under “quasi-steady” conditions for Sol-Gel samples calcined at 350 °C, working with a 0.05M (A) and a 1M (B) NaCl solutions; the red dash line points out the minimum potential assumed for evaluating the reaction order with respect to chloride.

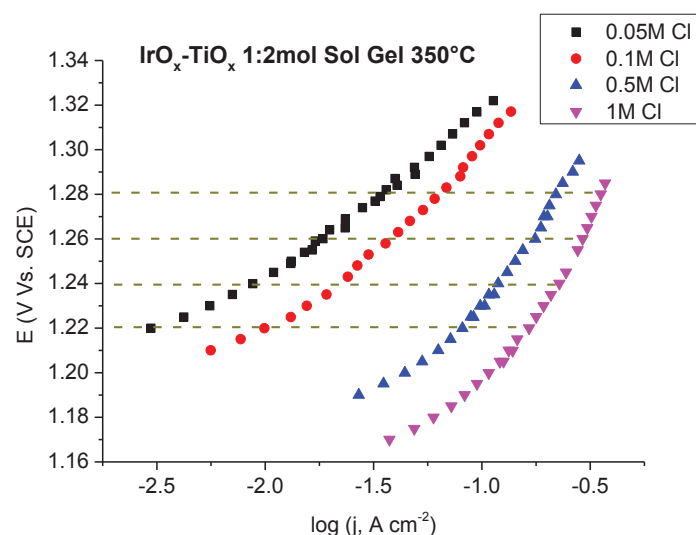


Fig.9.5. Tafel lines registered at different chloride concentrations for the Sol-Gel 350 °C sample. The dash lines indicate the four potential values taken into account for the estimation of  $RO_{Cl}$  (reaction order).

As it is possible to see by inspecting Tab.9.1, reaction order values are comprised between 1 and 2 (always less than two), and this aspect is in strong contradiction with the Volmer-Tafel and Volmer-Heyrovsky pathways; on the other hand, it is not even in perfect agreement with the hypotheses formulated by Krishtalik and Erenburg, previously discussed [23,24].

	<b>1.22 V<sub>SCE</sub></b>	<b>1.24 V<sub>SCE</sub></b>	<b>1.26 V<sub>SCE</sub></b>	<b>1.28 V<sub>SCE</sub></b>	<b>Average</b>
<b>Sol-Gel 350 °C</b>	1.30±0.06	1.05±0.03	0.93±0.03	0.77±0.01	<b>1.01±0.03</b>
<b>Sol-Gel 450 °C</b>	1.16±0.12	1.03±0.18	1.13±0.20	1.20±0.16	<b>1.13±0.17</b>
<b>Sputtering 350 °C</b>	1.27±0.06	1.24±0.05	1.28±0.08	1.41±0.12	<b>1.30±0.08</b>
<b>Sputtering 450 °C</b>	1.14±0.01	1.04±0.03	1.20±0.07	1.30±0.07	<b>1.17±0.05</b>

Tab.9.1. Reaction orders with respect to chloride for all the samples studied, estimated at different electrode potentials.

The reaction order with respect to the proton was also evaluated, taking into account two samples: one prepared by sol-gel and the other synthesized by sputtering. The low-field approximation was considered for these determinations, owing to the lack of linearity of Tafel plots; the cell assessment was the same described previously, maintaining also the same testing solution (1M NaCl in 0.01M HClO<sub>4</sub>, with a pH of about 1.8). The modification of concentration of protons was done by using a concentrated NaOH solution (about 30 g/l), which has been added drop by drop before each test: with this approach, the volume of the

solution where the working electrode is placed does not vary significantly and also the ionic strength remains constant. In fact, when adding NaOH, a neutralization reaction takes place:



Moreover, the low-field polarization does not modify appreciably the composition of the solution (causing *e.g.* a detectable depletion of chlorides); thus, all the experiments at different  $H^+$  concentrations can be carried out with the same initial solution. The low-field polarizations were carried out within an overpotential range of  $\pm 20$  mV around the equilibrium potential, with a scan rate of 0.1 mV/s, moving from the higher potential to the lower. Results are shown in Fig.9.6.

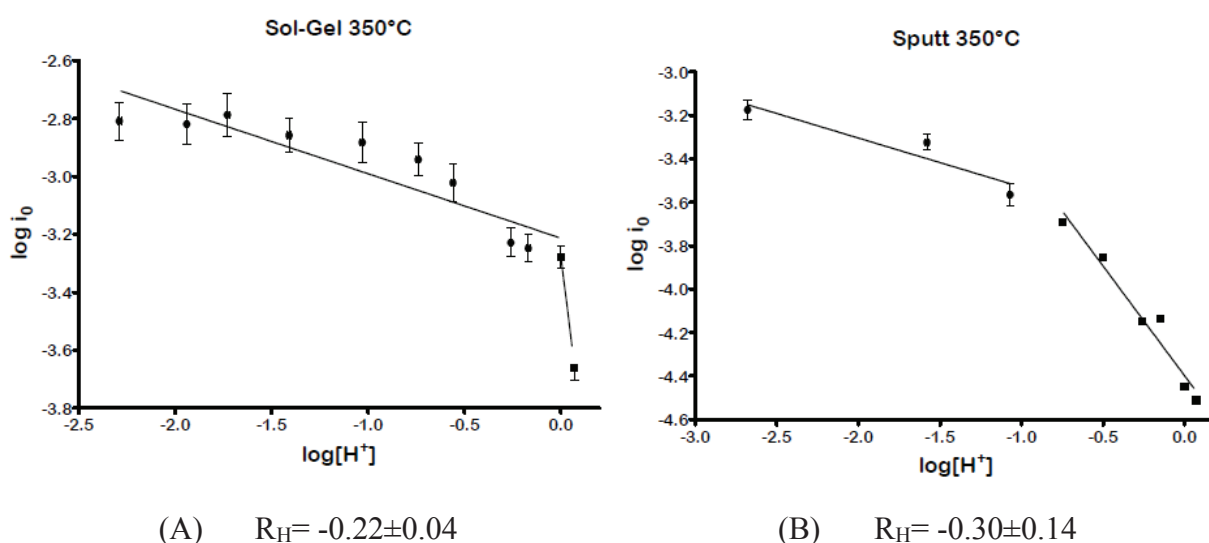


Fig.9.6. Reaction orders with respect to the proton, for Sol-Gel sample (A) and Sputtered one (B) calcined at 350 °C. The currents plotted are the exchange currents ( $\eta=0$ ) obtained by polarization tests carried out under low-field approximation. The slope value reported below each graph is the lower one, estimated considering the first part of the “curve”, where  $\log[H^+] < -1.0$ .

As reported in literature, in a paper by Érenburg [53], the rate of the chlorine evolution reaction increases with the pH. Other similar results were also obtained by Janssen [11,54], by Thomassen *et al.* [55] and Tamura and co-workers [14]; the first, in particular, has observed a high increase of the Tafel slope and a sharp decrease in the current when the pH became greater than 3. An unequivocal reason for these observations has not been proposed yet, but it might be related with screening effects in the double-layer or with something similar to a competition of two or more adsorption processes. Another anomalous outcome is represented by the abrupt decrease in the logarithm of the exchange current when  $\log[H^+]$  exceeds a particular value, which seems dependent on the nature of the material; an interesting aspect is that this value is ever comprised between  $0 < \text{pH} < 1$ .

As anticipated, the evaluation of the exchange current was carried out through the low-field approximation, in order to overcome the problem of non-linear Tafel plots; examples of collected curves are reported in Fig.9.7.

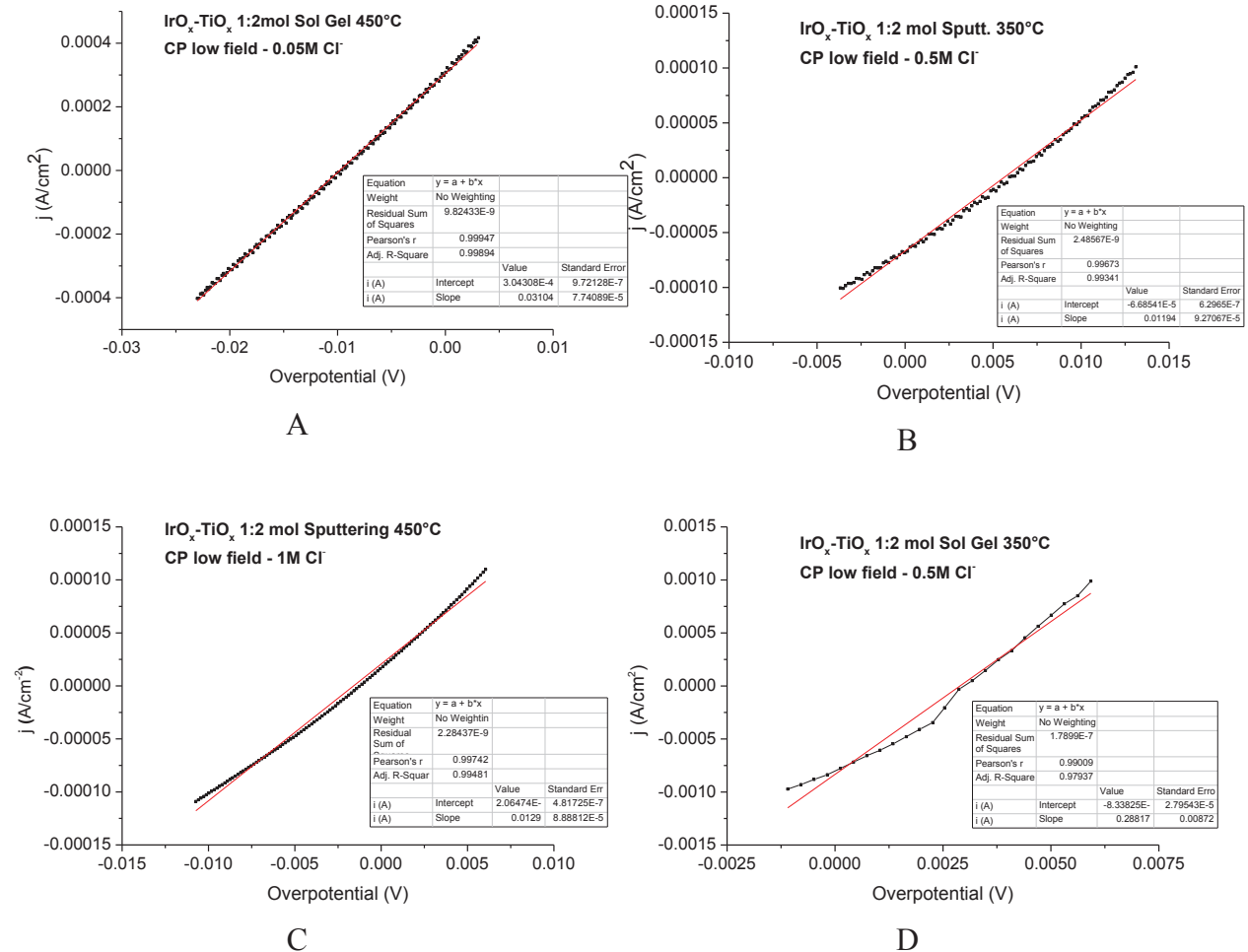


Fig.9.7. Examples of low-field polarization curves collected with different chloride concentrations, using different samples. It is worthy to note that the zero overpotential value never coincides with the condition of zero current: tests have been carried out using a continue polarization (even if conducted with a very low scan rate), which never allows the reaching of a perfect steady-state condition

The exchange current can be easily calculated from the slope of the straight line of the graph  $j$  vs.  $\eta$ . Obtained values have been collected in Tab.9.2. Let's consider the equation that expresses the exchange current:

$$i_0 = Fk_1c_{Cl} \exp(\alpha_a E_{rev} F / RT) \quad \text{Eq. 9.31}$$

Eq.9.31 shows that the exchange current depends both directly and indirectly from the concentration of chlorides, through the multiplicative factor  $c_{Cl}$  and through the  $E_{rev}$  in the exponential term. Moreover, the number of electroactive sites may influence the value of this

important parameter, and a comparison between different materials is possible only after a normalization. To do this, only the number of the sites most external has been taken into consideration: in fact, because of the dimensions of the chloride specie, it is plausible that only the outer electrocatalytic sites are effectively involved in the process. An estimation of the number of most external sites can be easily obtained by considering the values obtained during the cyclic voltammetric experiments discussed in Par.8.6, and referring to the number of electroactive sites calculated at the highest scan rate: in fact, because of the fast inversion on polarization direction, protons cannot diffuse in the deeper layers of material. Other approaches for obtaining a normalization can be obviously adopted, for example by considering the surface roughness [56] but this methodology involves the overall surface while, in the case of a mixed oxide, the part involved in the charging/discharging redox process is only a portion of it.

<b><math>j_0</math> (mA/cm<sup>2</sup>)</b>	<b>Chloride Concentration</b>			
<b>Sample</b>	<b>0.05M</b>	<b>0.1M</b>	<b>0.5M</b>	<b>1.00M</b>
<b>Sol-Gel 350 °C</b>	1.96	2.15	3.70	4.89
<b>Sol-Gel 450 °C</b>	0.40	0.28	0.25	0.30
<b>Sputt. 350 °C</b>	0.15	0.17	0.15	0.14
<b>Sputt. 450 °C</b>	0.45	0.26	0.24	0.17

Tab.9.2. Values of exchange current for the different samples, estimated at different chloride concentration. Data have been calculated with the low-field approximation.

The values of normalized exchange currents are collected in Tab.9.3.

<b><math>j_0/\#</math> electr. sites (mA/cm<sup>2</sup>)</b>	<b>Chloride Concentration</b>			
<b>Sample</b>	<b>0.05M</b>	<b>0.1M</b>	<b>0.5M</b>	<b>1.0M</b>
<b>Sol Gel 350 °C</b>	0.115	0.126	0.217	0.286
<b>Sol Gel 450 °C</b>	0.150	0.107	0.095	0.113
<b>Sputtering 350 °C</b>	0.031	0.036	0.032	0.028
<b>Sputtering 450 °C</b>	0.199	0.113	0.107	0.073

Tab.9.3. Values of exchange current, as reported in Tab.9.2, normalized by the number of electroactive sites involved in the electro-catalytic process.

The figures reported in Tab.9.3 can be related to a quantity proportional to the so-called “turnover number”:

$$n_{turnover} \propto \frac{i_0}{n_{electroactive\ sites}} \quad \text{Eq.9.32}$$

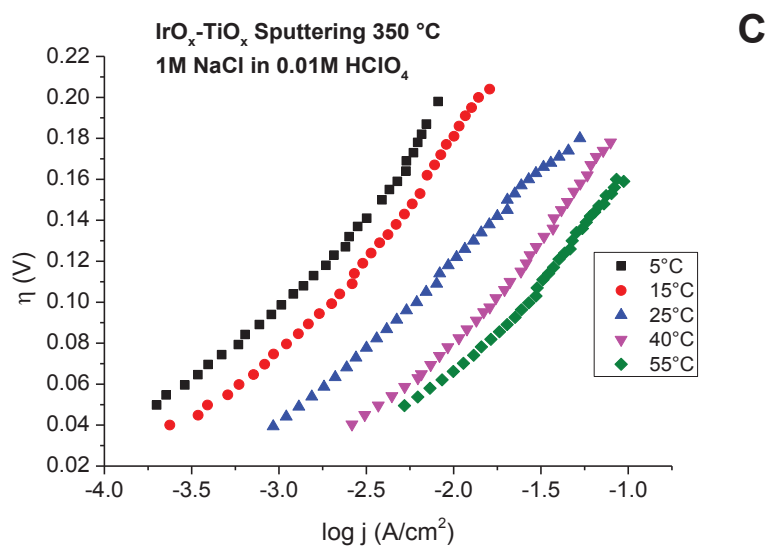
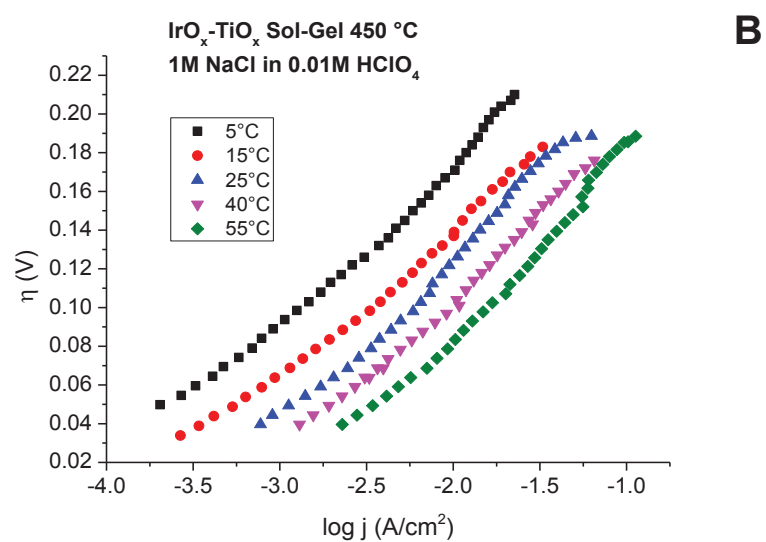
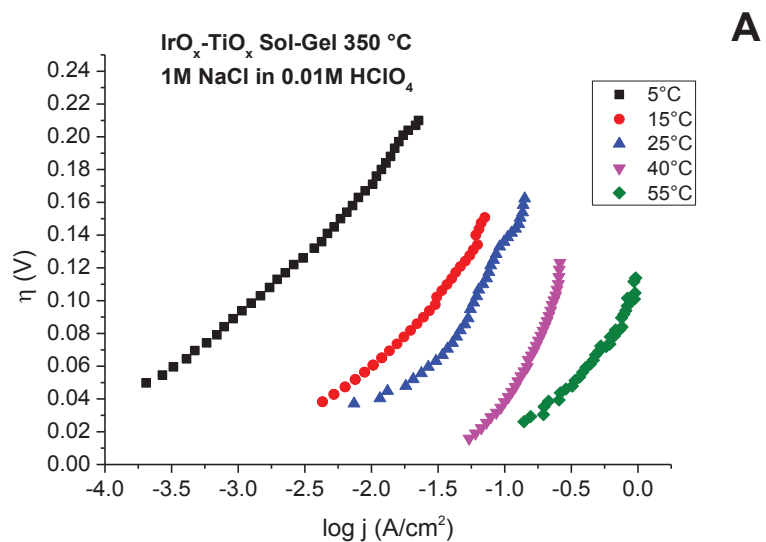
In the catalysis field, this quantity is defined as the number of moles of substrate that a mole of catalyst can convert before being deactivated; considering the parameter per unit of time, it is more correct to speak of “turnover frequency” [57]. This factor is very important for defining the performance of a catalyst and, in our case, it makes it possible to define a sort of ranking for the considered materials. Both the preparation technique and the calcination temperature appear to influence the characteristics of the different electrocatalysts, in the order shown below:

$$\text{Sol-Gel } 350\text{ }^\circ\text{C} > \text{Sol-Gel } 450\text{ }^\circ\text{C} > \text{Sputtering } 450\text{ }^\circ\text{C} \approx \text{Sputtering } 350\text{ }^\circ\text{C}$$

This trend has been verified for each chloride concentration considered, with the only exception of the 0.05M; however, it seems quite reasonable to exclude it, owing to the possible problems associated with the diffusion of the reagent from the bulk to the electrode surface.

## 9.5. Effect of the Temperature

Polarization curves at different temperatures were collected using the same cell equipment discussed for 25 °C tests. Actually, the cell compartments of WE and CE were equipped with interspaces that allow the recirculation of a glycol solution from a thermo-cryostat where the temperature can be set from about -30 to 120 °C; the RE semi-cell was maintained at room temperature (25 °C) in order to avoid shift of the reference potential during each test. Measurements were carried out at 5, 15, 25, 40 and 55 °C, for each electrode, and obtained curves are shown in Fig.9.8.





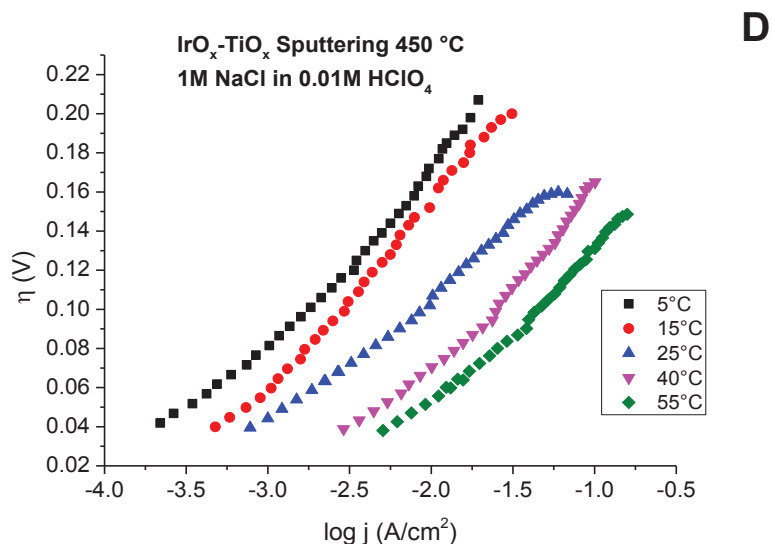


Fig.9.8. Polarization curves registered at five different temperatures, for the four coatings analyzed: (A) Sol Gel 350 °C, (B) Sol Gel 450 °C, (C) Sputtering 350 °C, (D) Sputtering 450 °C.

All points of the different curves have been collected under steady-state conditions, and corrected for the ohmic drop by means of impedance experiments; since also these experiments show a marked lack of linearity, the estimation of a Tafel slope is somewhat risky. Nevertheless, at a first approximation, it is possible to impose a linearization over at least 1-2 decades, over the overpotential range explored, and to extrapolate something related to a Tafel slope (as exemplified in Fig.9.9).

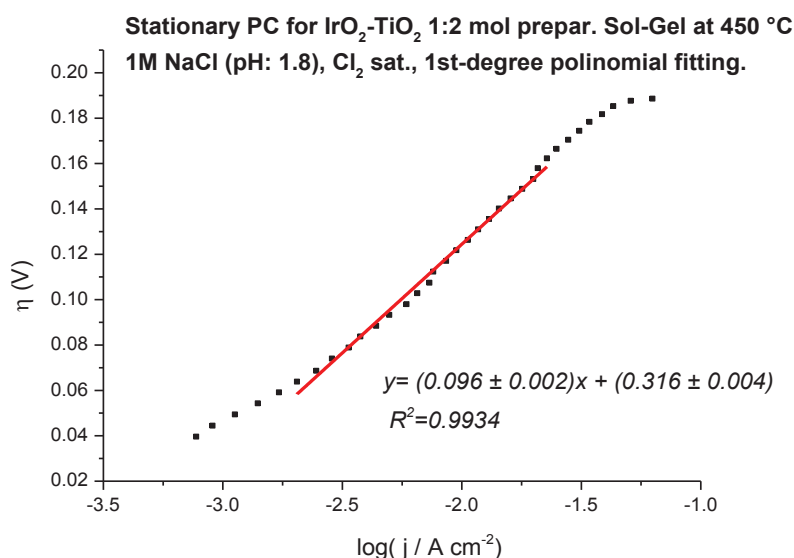


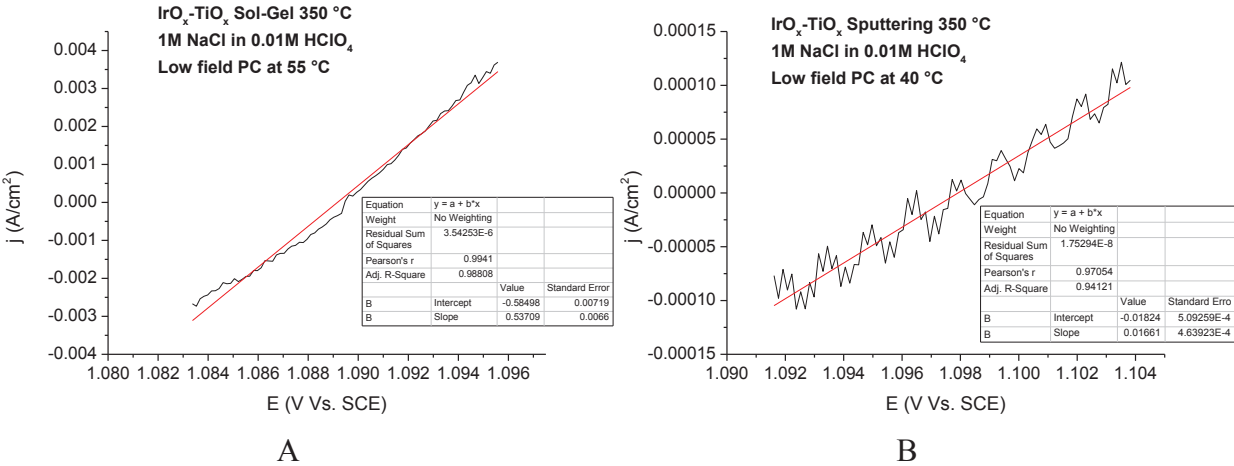
Fig.9.9. First degree polynomial fit for the stationary polarization curve registered at 25 °C for the sol-gel sample calcined at 450 °C.

Evaluated Tafel slopes have been collected in Tab.9.4: it is easy to see that values are always higher than those reported in literature, and this phenomenon is rather difficult to be explained. Moreover, because of the absence of a linear behavior, a variation in Tafel slope within  $\pm 20$  mV/dec, for the same sample at the different temperatures, can be found. Both the reaction orders as the Tafel slopes define an experimental framework difficult to interpret; the recourse to other techniques appears mandatory to make clear the collected information.

	<b>Tafel slopes (mV/dec) at the different Temperatures (°C)</b>				
<b>Samples</b>	<b>5</b>	<b>15</b>	<b>25</b>	<b>40</b>	<b>55</b>
<b>Sol-Gel 350 °C</b>	71	65	75	78	88
<b>Sol-Gel 450 °C</b>	71	65	96	78	88
<b>Sputtering 350 °C</b>	86	90	80	85	82
<b>Sputtering 450 °C</b>	69	98	68	68	68

Tab.9.4. Tafel slopes, at the different temperatures, estimated through a first order approximation fitting.

At the different temperatures, also the exchange currents were estimated, again by means of low-field measurements. Some examples are shown in Fig.9.10; the followed procedure and the subsequent calculation were the same adopted for the case of measurements at 25 °C.



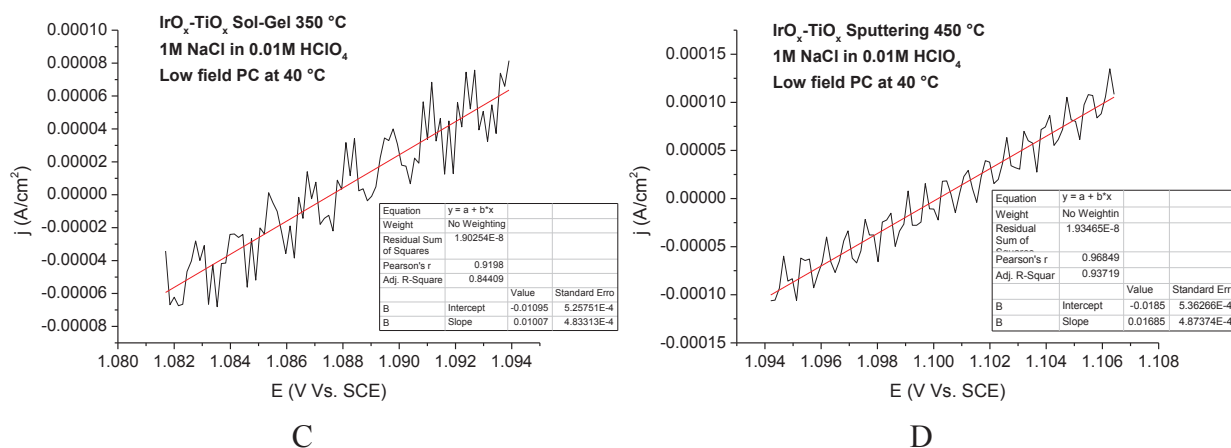


Fig.9.10. Examples of low-field polarization curves collected at different temperatures.

The values of exchange current density, estimated at the different temperatures, have been collected in Tab.9.5.

	<b>Exchange current densities <math>j_0</math> (mA/cm<sup>2</sup>) at different Temperatures (°C)</b>				
<b>Samples</b>	<b>5</b>	<b>15</b>	<b>25</b>	<b>40</b>	<b>55</b>
<b>Sol-Gel 350 °C</b>	2.78	5.45	7.50	6.88	7.59
<b>Sol-Gel 450 °C</b>	1.44E-2	3.55E-2	8.77E-2	0.14	0.31
<b>Sputtering 350 °C</b>	9.95E-3	2.49E-2	8.99E-2	0.22	0.43
<b>Sputtering 450 °C</b>	8.68E-3	3.30E-2	5.46E-2	0.23	0.28

Tab.9.5. Exchange current densities determined at different temperature for each sample in a 1M NaCl solution + 0.01M HClO<sub>4</sub>, Cl<sub>2</sub> saturated.

The small difference between the results obtained at 25 °C (4<sup>th</sup> column in Tab.9.4) and those obtained in previous tests, carried out at room temperature, is plausibly attributable to small changes in the surface roughness after the extended polarization tests, under chlorine evolution conditions; these changes were evidenced by means of cyclic voltammetric (CV) tests carried out in HClO<sub>4</sub> at 100 mV/s, before and after a polarization experiment: the CV approach can be used to check the state of the material, and only variations of voltammetric charge lower than 10% were accepted to consider the material as reusable.

With reference to the exchange currents and to currents recorded at higher potential values, Arrhenius plots were assembled in order to acquire information about the enthalpy of activation of the chlorine evolution reaction. In fact, it was possible to estimate the “apparent” enthalpy related with the formation of the activated complex, as treated by Conway [58], with the aim of extrapolating a parameter independent of the reagent concentration and from the

working temperature, which can thus measure the activity of the catalyst towards the studied electrochemical process.

The relationship between the “true” and the “experimentally determined” heat of activation, determined at constant overpotential, was originally studied by Temkin [59]; the rate constant  $k$  for the process of neutralization of an ion present at a given concentration can be expressed as follows:

$$k = \tau \frac{kT}{h} \exp\left[-\frac{\Delta G^{0\#}}{RT}\right] \exp\left[-\frac{\beta \Delta \phi_s^M zF}{RT}\right] \quad \text{Eq. 9.33}$$

The Gibbs free energy of activation ( $\Delta G^{0\#}$ ) can then be written as sum of the enthalpy ( $\Delta H^{0\#}$ ) and entropy ( $\Delta S^{0\#}$ ) of activation; analogously,  $\Delta \Phi_s^M$  can be expressed through the sum of the reversible potential ( $\Phi_{R,M}$ ), for the process concerned, and the overpotential ( $\eta$ ). Assuming, as a first approximation, an invariance of the activation entropy in the range of temperatures examined, by rewriting Eq. 9.33 and deriving the natural logarithm of  $k$  with respect to  $1/T$ , Eq. 9.34 can be obtained:

$$\frac{\partial(\ln k)}{\partial(1/T)} = -\frac{\Delta H^{0\#}}{R} + \frac{\beta}{R} \Delta H^0 = -\frac{1}{R} (\Delta H^{0\#} - \beta \Delta H^0) \quad \text{Eq. 9.34}$$

If double layer and coverage effects are independent of temperature, Eq.9.34 simplifies as follows:

$$\frac{\partial(\ln i_0)}{\partial(1/T)} = \left[ \frac{\partial(\ln k)}{\partial(1/T)} \right]_{\eta=0} = \Delta W^{0\#} = \Delta H^{0\#} - \beta \Delta H^0 \quad \text{Eq. 9.35}$$

$\Delta H^{0\#}$  can be determined from  $\Delta W^{0\#}$  only by accepting some assumptions, *e.g.* building up a non-thermodynamic calculation of  $\Delta H^0$  and knowing a number of other parameters, such as the heat of solvation of the reactant, the heat of sublimation, the ionization energy and the electrode work function. In order to obtain a comparison between the performances of the examined electrodes, the “apparent” heat of activation, evaluated at constant overpotential, represents a parameter sufficient to quantify the entity of the interaction between the electroactive site and the adsorbed intermediate.

The value of the apparent activation enthalpy can be estimated from the slope of the straight line in an Arrhenius plot [ $\ln(j)$  vs.  $1/T$ ]; for each specimen, the procedure was carried out at four different overpotentials (0, 75, 110, and 165 mV), and the value of  $\Delta W^{0\#}$  was obtained as an average. The desired outcome is then linked to the slope by a simple relation: slope =  $-\Delta W^{0\#}/R$ .

The activation energy in the case of a multi-step process is not only associated to *rds* through an Arrhenius relation, but also to the Gibbs free energies of quasi-equilibrium (or stationary)

processes that precede it, through a Van't Hoff equation. This contribution exists but is plausibly smaller than the real *rds* activation energy and can be omitted in most cases.

Figure 9.11 exemplifies the procedure for the sol-gel sample prepared at 450 °C, for the case  $\eta = 165$  mV. The values of  $\ln(j)$  plotted against  $1000/T$  must be processed at constant potential. During our investigation, the open circuit potential did not show to vary, from test to test, as a result of a temperature variation, and this can be probably related to some compensation phenomena that involve the electrode potential. Considering the Nernst equation:

$$E_{WE} = E_T^\circ + \frac{RT}{nF} \ln \frac{a_{Cl_2}}{a_{Cl^-}^2} \quad \text{Eq. 9.36}$$

$E_T^\circ$  depends on the temperature through a particular coefficient, and also the second term of the right part of the equation is T-dependent by means of a multiplicative term; a combination of effects on these terms, at different entities, can be the cause of the invariance of the open circuit potential: almost certainly, an increase in the  $\Delta G^0$  of the reaction is justified by a decrease of stability of the intermediate chlorine radical when increasing the temperature. Of course, also the input impedance of the instrument might result not sufficiently high, causing a low sensitivity in terms of potentiostatic measurements. In fact, a paper published by Faita *et al.* in 1967 [60] showed that the “absolute” standard potential of the  $Cl_2/Cl^-$  electrode decreases of about 30 mV when increasing the temperature from 25 to 50 °C; however, when the concentration of  $Cl_2$  and  $Cl^-$  is high enough, also the equilibrium that leads to trichloride ( $Cl_3^-$ ) formation can become important [61]:



The more the equilibrium is shifted toward the product side, the more the activity of chloride tends to decrease, with a consequent increase in the logarithmic term in Eq.9.36.

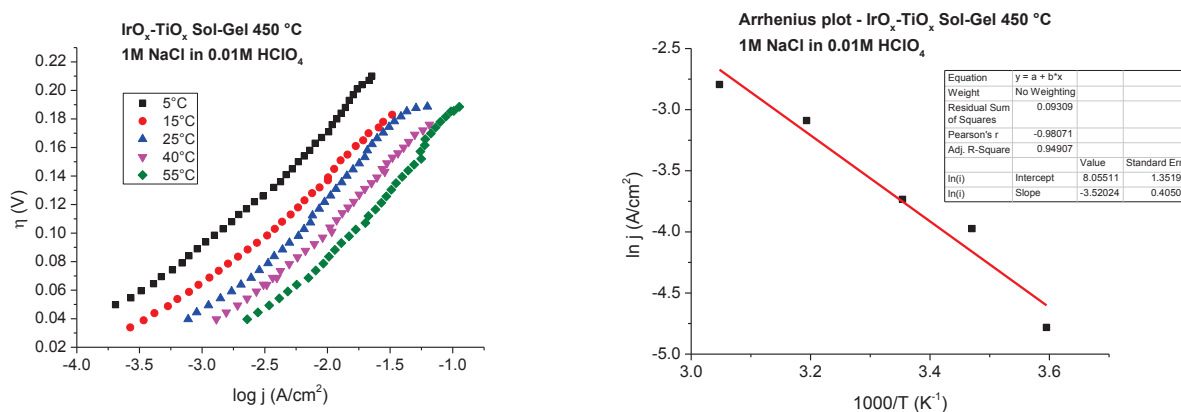


Fig.9.11. Ex. of Arrhenius plot, built for an overpotential of 165 mV, for Sol-Gel sample prepared at 450 °C.

The slope of the Arrhenius plot is proportional to the apparent activation energy of the rate determining step of the kinetic process, through the constant  $R$  ( $8.31 \text{ J mol}^{-1} \text{ K}^{-1}$ ):

$$\text{slope} = -\frac{\Delta W^{0\#}}{R} \quad \text{Eq.9.37}$$

Tab.9.6 collects the estimated values, calculated at the different overpotentials, as well as the average data.

<b>Samples</b>	<b><math>\Delta W^{0\#}</math> (kJ/mol) <math>\eta=0V</math></b>	<b><math>\Delta W^{0\#}</math> (kJ/mol) <math>\eta=75mV</math></b>	<b><math>\Delta W^{0\#}</math> (kJ/mol) <math>\eta=110mV</math></b>	<b><math>\Delta W^{0\#}</math> (kJ/mol) <math>\eta=165V</math></b>	<b><math>\Delta W^{0\#}</math> (kJ/mol) average</b>
<b>Sol-Gel 350 °C</b>	13.04	-	-	-	13.04
<b>Sol-Gel 450 °C</b>	45.03	38.80	35.31	29.96	34.69
<b>Sputtering 350 °C</b>	58.28	50.59	50.65	48.91	50.05
<b>Sputtering 450 °C</b>	53.53	52.34	51.83	53.97	52.71

Tab.9.6. Activation energies for the formation of the activated complex, calculated from Arrhenius plots obtained at different overpotentials.

Experimental data collected in Tab. 9.6 are quite in agreement with those reported by Iwakura and Tamura [14,62], which were calculated (by assuming either a square pyramid or a pentagonal bi-pyramidal structure for the activated complex, and using the crystal-field stabilization energy for the initial and transition states in the *rds*) as well as experimentally found, and are also compatible with the activation energies proposed by Trasatti for ruthenium-titanium oxide-based electrodes [63].

An anomalous response was attested for the Sol-Gel 350 °C sample, probably because of the formation of clathrate hydrates species, especially at low temperatures; in fact, this sample showed to be the most efficient catalyst, in terms of active surface, and the high quantity of gaseous chlorine produced may effectively lead to a situation of oversaturation in  $\text{Cl}_2$  in the solution volume immediately in contact with the electrode: by lowering the temperature to 5-10 °C, it is possible to form the so-called “clathrate hydrate (of chlorine)” ( $\text{Cl}_2 \times 8\text{H}_2\text{O}$ ), as demonstrated by the so-called “Faraday’s experience”. Moreover, in 1986, Bockris and Gochev [64] developed mathematical models to explain the effects of the

temperature on the symmetry factor, by examining double layer changes with temperature as well as kinetic effects; also small oscillations in Tafel slopes were attributed to these aspects. However, the considerations made by Bockris *et al.* were especially focused on the hydrogen evolution reaction, where the transport of the reactant is strongly conveyed by the molecules of the solvent, in aqueous systems.

Because of the above considerations, the low-field outcomes are, in our opinion, more reliable for the comparison between samples, at least when considering the Sol-Gel 350 °C sample.

## 9.6. Effect of the coverage on Tafel slopes and Reaction Orders

The experimental picture based on Tafel slopes and reaction orders appears difficult to interpret, in particular because of the lack of linearity in the Tafel graphs. The mathematical model proposed by Tilak and Conway in 1992 [65] was taken into consideration for trying to explain the overall set of results. In that paper, the analytical relations between Tafel slope ( $b$ ) and reaction order ( $\mathfrak{R}$ ) have been deduced by considering the two main types of mechanism: the Volmer-Tafel (V-T) and the Volmer-Heyrovsky (V-H) pathways, which are the most common models for explaining electrochemical reactions where only one intermediate specie is involved (*e.g.* H<sub>2</sub>, Cl<sub>2</sub>, etc.). According to the authors, there is often a discrepancy between experimentally measured kinetic parameters and theoretical values when considering heterogeneous processes where the adsorption of intermediates is involved: in particular, the quantity  $d \ln \theta / d \ln c$  deriving from the absorption isotherm is involved, where the fractional coverage of the reaction intermediate is related to the concentration of the reactant specie in the bulk (Cl<sup>-</sup> in our particular case). At first, a Langmuir-type adsorption can be considered for the mathematical development; however, when also the effects of lateral interactions have to be taken into account (when significant values of coverage are expected), a Frumkin isotherm model may be more reasonable. Starting from the fundamental equations of reaction order, net current of an electrochemical process and considering the coverage functions proposed by Langmuir and Frumkin, it is possible to deduce how the Tafel  $b$  can vary with the coverage (Eq.9.38).

$$b = \frac{d\Delta\phi}{d \ln i} = \frac{d\Delta\phi}{d \ln \theta} \times \frac{d \ln \theta}{d \ln i} = \mathfrak{R} \times \frac{d\Delta\phi}{d\theta} \times \frac{d \ln \theta}{d \ln i} \quad \text{Eq. 9.38}$$

In general, the surface coverage by the intermediate of the reaction changes with the electrode potential,  $\Delta\Phi$ .

The reaction order is also related to the coverage: in most cases, the current ( $i$ ) is determined not only by the reactant concentration ( $c$ ), but also by the coverage of an intermediate, which is related to  $c$  through an electrochemical adsorption isotherm:

$$\mathcal{R} = \left( \frac{\partial \ln i}{\partial \ln c} \right)_{E,T} = \left( \frac{\partial \ln i}{\partial \ln \theta} \right)_{E,T} \left( \frac{\partial \ln \theta}{\partial \ln c} \right)_{E,T} \quad \text{Eq. 9.39}$$

Let's consider a Langmuir-type adsorption, and the two above-cited mechanisms of reaction (i.e. the chemical- and the electrochemical-desorption pathways):

- Volmer-Tafel – reaction controlled by the recombination of intermediates, in the case of an adsorption isotherm of the Langmuir type:

$$b_{\text{apparent}} = \frac{b_{\text{theoretical}}}{1-\theta} \quad \text{Eq. 9.40}$$

$$\mathcal{R}_{\text{apparent}} = \mathcal{R}_{\text{theoretical}} \times (1-\theta) \quad \text{Eq. 9.41}$$

- Volmer-Heyrovsky – reaction controlled by the electrochemical desorption of the intermediate, in the case of an adsorption isotherm of the Langmuir type:

$$b_{\text{apparent}} = \frac{b_{\text{theoretical}}}{1-2\theta/3} \quad \text{Eq. 9.42}$$

$$\mathcal{R}_{\text{apparent}} = \mathcal{R}_{\text{theoretical}} \times (1-\theta/2) \quad \text{Eq. 9.43}$$

Looking at the above equations, it is easy to see that  $b_{\text{apparent}}$  (which is the experimentally determined) is always bigger than  $b_{\text{theoretical}}$ , while  $\mathcal{R}_{\text{apparent}}$  is always smaller than the theoretical value. Under these conditions, it's worth mentioning that a Tafel linearity can be found even if  $\theta \neq 0$ , provided that the coverage remains constant when varying the electrode potential; in general, a nonlinear Tafel plot is detected if the coverage is variable along the explored potential window.

The same approach can be used to describe a Frumkin-type adsorption, in which the interactions between intermediates are taken into account, and are expressed by the value of the parameter  $g$  ( $g < 0$  in case of attractive interactions,  $g > 0$  if they are of repulsive nature). In this case, the equations become more complicated; the connection between the reaction order and the coverage function changes as follows:



- Volmer Tafel – reaction controlled by the recombination of intermediates, in the case of an adsorption isotherm of the Frumkin type:

$$\mathfrak{R} = \left( \frac{\partial \ln i}{\partial \ln c_{Cl^-}} \right)_{E,T} = 2 \left\{ \frac{(1-\theta_{Cl^-})(1+g\theta_{Cl^-})}{1+g\theta_{Cl^-}(1-\theta_{Cl^-})} \right\} \quad \text{Eq. 9.44}$$

And for the Tafel slope,

$$b^{-1} = \left( \frac{\partial \ln i}{\partial E} \right)_T = \frac{2F}{RT} \left\{ \frac{1+g\theta_{Cl^-}(1-g\theta_{Cl^-})}{(1-\theta_{Cl^-})(1+g\theta_{Cl^-})} \right\}^{-1} \quad \text{Eq. 9.45}$$

- Volmer-Heyrovsky – reaction controlled by the electrochemical desorption of the intermediate, in the case of an adsorption isotherm of the Frumkin type:

$$\mathfrak{R}_{Cl^-} = \left( \frac{\partial \ln i}{\partial \ln c_{Cl^-}} \right)_{E,T} = 1 + (1-\theta_{Cl^-})(1+\beta g\theta_{Cl^-})/[1+g\theta_{Cl^-}(1-\theta_{Cl^-})] \quad \text{Eq. 9.46}$$

Correspondingly:

$$b^{-1} = \left( \frac{\partial \ln i}{\partial \eta} \right)_T = \frac{F}{RT} \{ \beta + (1-\theta_{Cl^-}) \times (1+\beta g\theta_{Cl^-})/[1+g\theta_{Cl^-}(1-\theta_{Cl^-})] \} \quad \text{Eq. 9.47}$$

Fig.9.12 shows the variation of the reaction order with both, the electrode potential (E) and the value of the interaction parameter (g), assuming a Volmer-Heyrovsky pathway.

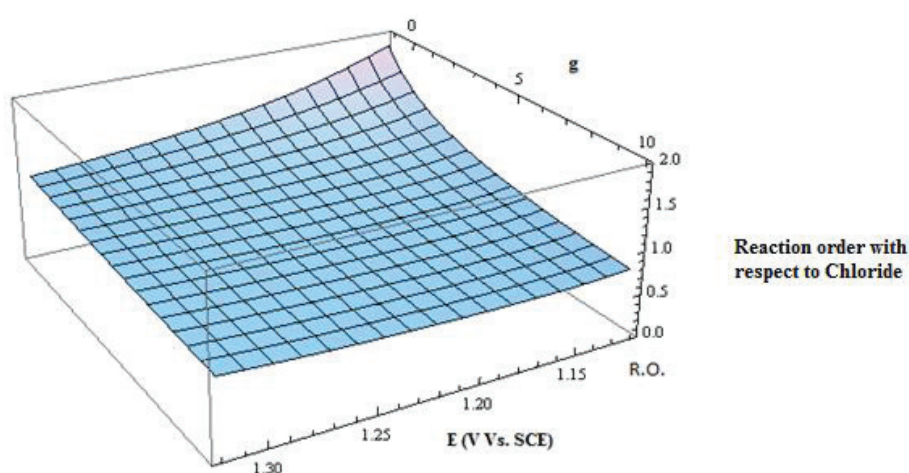


Fig.9.12. Reaction order function with respect to the potential E and the lateral interaction factor g, in the case of an electrochemical desorption as *rds*.

Conversely, the variation of the reaction order with  $g$  and the coverage is shown in Fig.9.13.

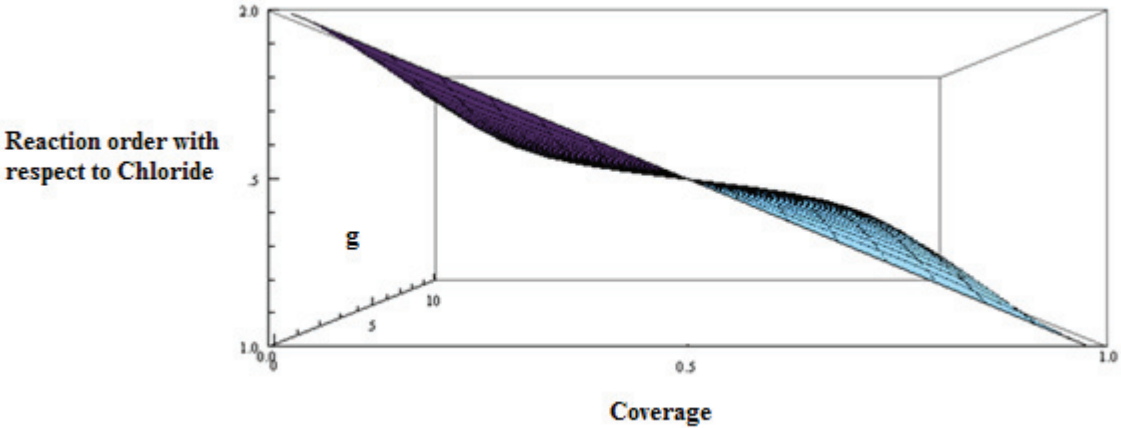


Fig.9.13. Reaction order function with respect to the intermediate coverage function and the lateral interaction factor  $g$ , in the case of an electrochemical desorption as *rds*.

The model was applied to polarization curves recorderd at 25 °C in 1M NaCl, for all the analyzed materials, and considering both mechanisms (V-T and V-H) as well as both isotherms (Langmuir and Frumkin). Tafel plots discussed in Par.9.5, collected at different temperature, were fitted using a 2<sup>nd</sup>-order polynomial function as exemplified in Fig.9.14.

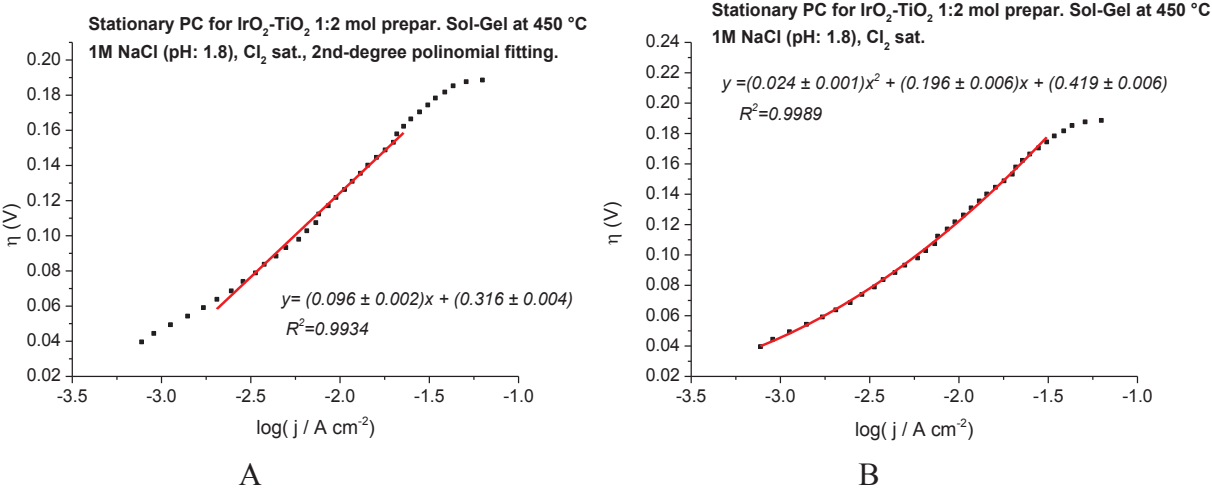


Fig.9.14. Fitting of a steady-state polarization curve by using a polynomial function either of the 1st order (A) or of the 2nd order (B). In the latter case, the agreement between experimental points and the fit function is better, and the interval of examined points can be extended also to the low-overpotential region.

Obviously, when using the second order polynomial, the Tafel slope cannot assume a constant value, but its variation can be described by a derivative function as follows::

$$b = \left( \frac{\partial E}{\partial \log i} \right)_{c,T} \quad \text{Eq.9.48}$$

Because of the reasons discussed above, the Tafel slope is a function of the coverage, while the coverage is a function of the potential; on the other hand, also the reaction order is a function of both, the coverage and the potential. In conclusion, a given mechanism can be verified by using the relationship resumed by Eq.9.49:

$$\mathcal{R}_{(E)} * b_{(E)} = f(\mathcal{G}_{(E)}) \quad \text{Eq.9.49}$$

Calculations were made considering both the chemical and the electrochemical desorption mechanisms, but a convergence was found only in the case of the Volmer-Heyrovsky pathway, which was thus confirmed as the active mechanism in our studied cases. This procedure represents a sort of mathematical test for discriminating between the two mechanisms considered. It can be schematized as follows:

- Assuming a particular mechanism of reaction and an adsorption model (at first approximation a Langmuir type, in our case), the product between the functions  $\mathcal{R}$  and  $b$  (which depend by the potential) origins a mathematical expression of the coverage (function of  $E$ ).
- The step just described was carried out considering four different potentials along the potential window scanned: 1.22, 1.24, 1.26 and 1.28 V Vs. SCE.
- The obtained coverage function was then compared with the one obtained by the first derivative of the polynomial fit of experimental Tafel plots (*e.g.*, the ones reported in Fig.9.14), and a convergence can be reached if the assumption of mechanism of reaction is correct.

In order to obtain the real coverage function, a recursive algorithm based on previous equations was applied; a first guess-value of coverage was estimated (the Langmuir isotherm was taken as guess-model), starting from the experimental values of  $\mathcal{R}_{Cl^-}$ , and a value for the lateral interaction factor,  $g$ , was eventually quantified. Then, the latter was used for calculating a new coverage function that, in turn, was used to obtain a more accurate value of  $g$ . By repeating this mathematical iteration several times, convergence between the coverage function, and the value of  $g$  can be obtained. The last step consisted in plotting the coverage functions obtained by considering the two different hypotheses. The whole iteration procedure was carried out using an algorithm written for the software Wolfram Mathematica<sup>®</sup> using equations described before. In Fig.9.15, the coverage functions, calculated by starting from experimental data, are proposed: the function based on Frumkin's isotherm is drawn in blue color, while that based on Langmuir is reported in violet.

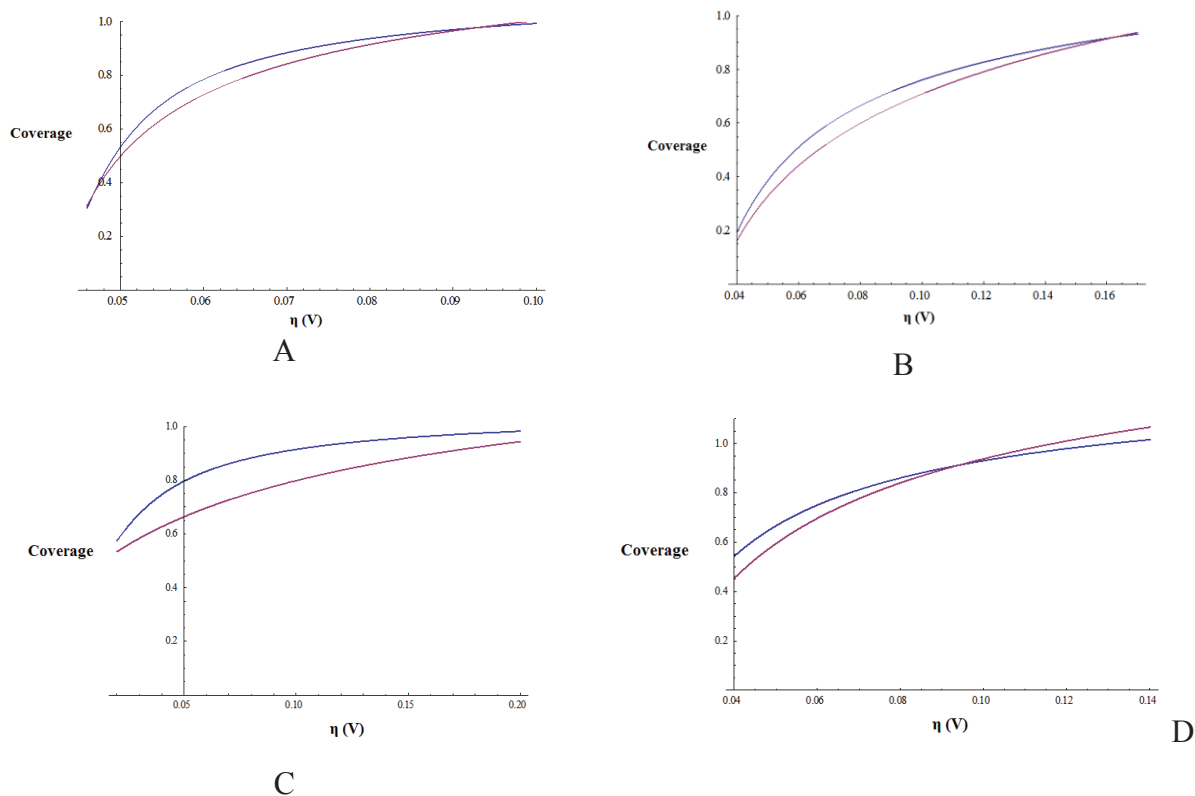


Fig.9.15. Coverage functions vs. overpotential, related to steady-state polarization curves collected in 1M NaCl solution (in HClO<sub>4</sub> 0.01M, pH= 1.8) at 25 °C for (A) Sol-Gel 350 °C, (B) Sol-Gel 450 °C, (C) Sputtering 350 °C and (D) Sputtering 450 °C samples.

The values of the parameter  $g$ , estimated by the above described recursive procedure, have been summarized in Tab.9.7.

	Sol-Gel 350 °C	Sol-Gel 450 °C	Sputtering 350 °C	Sputtering 450 °C
$g$	1.15	0.89	4.99	0.32

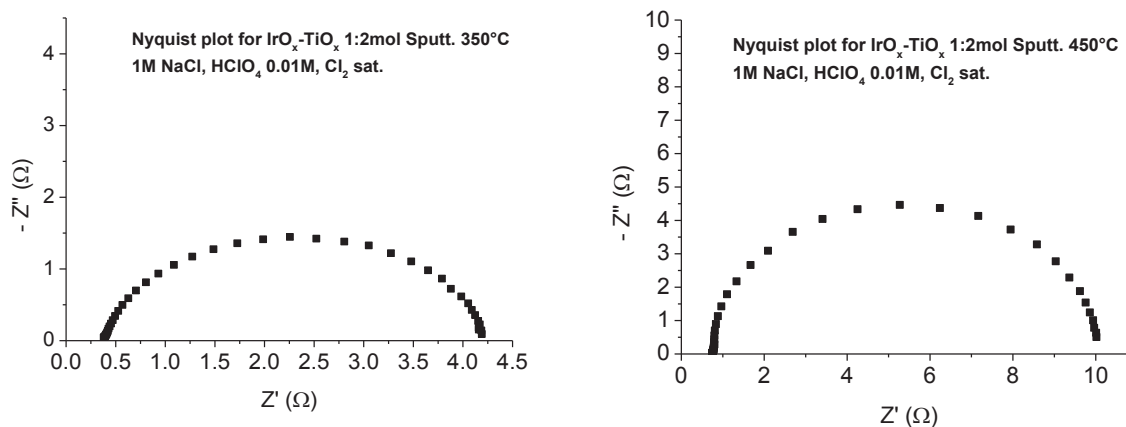
Tab.9.7. Lateral interaction parameter  $g$  calculated through the model proposed by Conway.

Generally speaking, the values of  $g$  are quite small, in agreement with the fact that only small differences can be appreciated between the Langmuir- and the Frumkin-based functions reported in Fig.9.15. Samples prepared at 350 °C seem to be characterized by strong interactions among the intermediates involved in the gas evolution reaction; another important consideration is that the value of coverage seems to increase quite fast: typically, when the overpotential is higher than 60-80 mV, the  $\theta$ -function remains practically constant and presents a high value, comprised between 0.8 and 1.0 (the surface saturation limit).

## 9.7. Impedance spectroscopy analysis on ChIER

The impedance spectroscopy was used for obtaining other useful information about the mechanism of ChIER. At first, all samples have been analyzed carrying out measurements on a wide range of potential, by working in solution 1 M in NaCl, 0.01 M in HClO<sub>4</sub>, and saturated with Cl<sub>2</sub>. The procedure adopted was the same applied for the steady-state polarization experiments: AC experiments were recorded after each polarization, when the conditions of the steady-state were guaranteed. All tests were performed in the frequency range from 10 kHz to 0.1 Hz, by applying a potential perturbation having an amplitude of  $\pm 5$  mV, and by exploring overpotentials from 220 mV to 40 mV, with steps of 5 mV; also, a treatment of pre-polarization (at the chosen overpotential, for 5 minutes) was applied. A residence time of 5 minutes at each potential was considered sufficient for guaranteeing the obtainment of the steady-state, and the impedance spectrum was subsequently collected without opening the circuit (in order to avoid extra-currents of closure, which would represent a noise). Moreover, every sample was pre-treated by carrying out 20 cycles of cyclic voltammetry (within 0.1 and 1.1 V vs. SCE, scan rate: 100mV/sec) in 1 M perchloric acid, in order to attain a reproducible hydration of samples. After each test, the status of the sample was checked again by cyclic voltammetry in perchloric acid. The distance between WE and Luggin capillary was set to about 2 mm, which was found to be the best compromise for obtaining good results (data not shown): every measure was tested using Kramers-Kronig relations, and acceptable results are obtained only by working with this distance [66,67].

Analyzing the different samples, two distinct situations were found, which are characterized by impedance responses that depend on the temperature of preparation rather than on the deposition method adopted. As shown in Fig.9.16, one time constant is visible for samples prepared at 450 °C, while two contributions not completely resolved appear in the case of films synthesized at 350 °C.



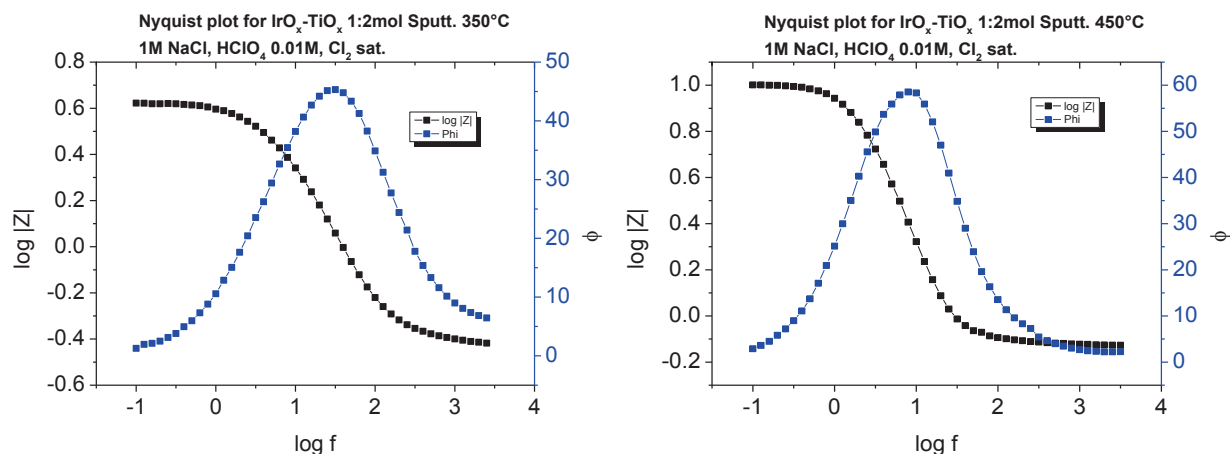


Fig.9.16. Impedance responses (Nyquist and Bode plots) for samples prepared at (A) 350 °C and (B) 450 °C.

The procedure of fitting was carried out applying the CNLS (Complex Non-Linear Least Square) method through the “Calculus-Modulus” algorithm; the choice of physically meaningful equivalent models has been done in agreement with the experimental results. In fact, especially when investigating the kinetics of an electrochemical process, the risk of introducing too many parameters exists. In order to avoid this misconception, the Fisher test was applied for evaluating if the addition of one parameter to the chosen equivalent circuit can lead to a significant statistic improvement in the fitting. Moreover, each fitting was considered acceptable if every parameters are associated to a percentage error less than 20%. The samples prepared at 450 °C have proven to be well modeled by using the simplest circuit (Fig.9.17), which comprises the resistance of the solution ( $R_s$ ) in series with a single RC mesh that involves the charge transfer resistance, related with the faradaic process of discharge of chloride ( $R_{ct}$ ), in parallel with the double layer capacity ( $C_{dl}$ ); the latter is typically expressed by a CPE (Constant Phase Element):

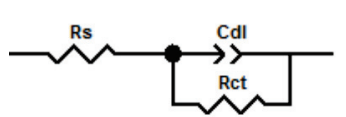


Fig.9.17. Randles circuit.

The above kind of circuit is known as Randles’ circuit [68].

A verification of the good fitting can be made by plotting the  $\log(1/R_{ct})$  vs.  $\eta$ , and comparing the trend with that of the corresponding  $\log j$ , determined step by step. The assessments for Sol-Gel and Sputtering samples prepared at 450 °C are reported in Fig.9.18.

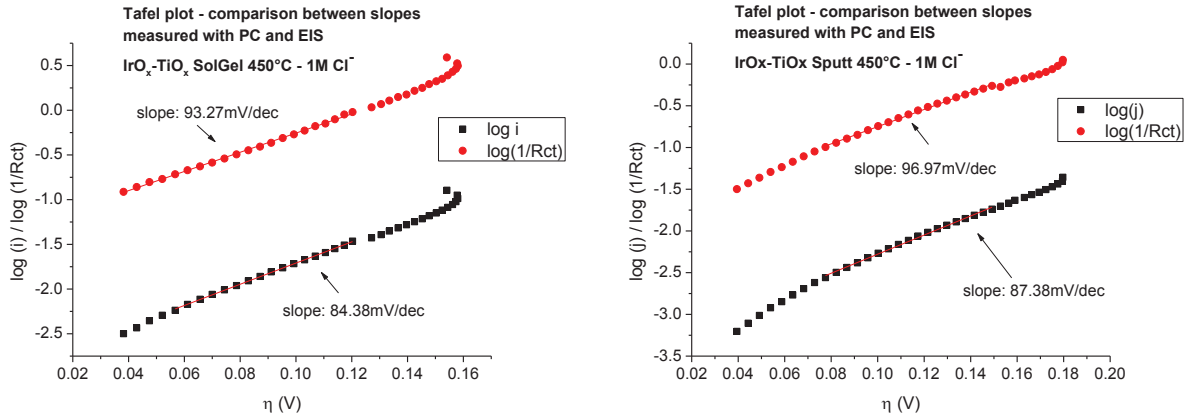


Fig.9.18. Tafel plots for 450 °C samples: current Vs inverse of the charge transfer resistance.

The agreement between the measured currents and the charge-transfer resistances determined through the fitting procedure is quite good, and confirms the validity of the chosen model.

The CPE (which is indicated as Q in the Boukamp equivalent circuit notation) has been used every times that a capacity was contemplated by the equivalent circuit: in fact, for solid electrodes, a frequency dispersion exists due to micro-roughness (due to pits, scratches, etc.), chemical inhomogeneity, as well as problems associated with the kinetics of adsorption of species [69, 70].

$$Z_{CPE} = \frac{1}{T(j\omega)^\phi} \quad \text{Eq.9.50}$$

Eq.9.50 shows the impedance associated to a Constant Phase Element ( $Z_{CPE}$ ), which is proportional to T (a parameter numerically equivalent to the capacity of the element, if  $\phi$  is equal to 1; it is not properly a capacity because its dimensions are  $F \text{ cm}^{-2} \text{ s}^{\phi-1}$ ) and to  $\phi$  (this parameter can vary from 0 to 1, where 1 represents the ideal situation where the CPE becomes a pure capacitor).

Brug's formula (Eq.9.51) was used to estimate the double layer capacity related to the respective CPE (see Fig.9.19) [71].

$$T = \bar{C}_{dl}^\phi \times \left[ \frac{1}{R_s} + \frac{1}{R_{ct}} \right]^{1-\phi} \quad \text{Eq.9.51}$$

The value determined by Eq.9.51 represents an average estimation of the double layer capacity, and the Brug's model is valid only when  $\phi$  is above 0.8-0.9 (this condition must be verified, at least within a portion of the explored potential window). The calculation was done for the samples prepared at 450 °C and obtained  $C_{dl}$  values have been reported in Tab.9.8.

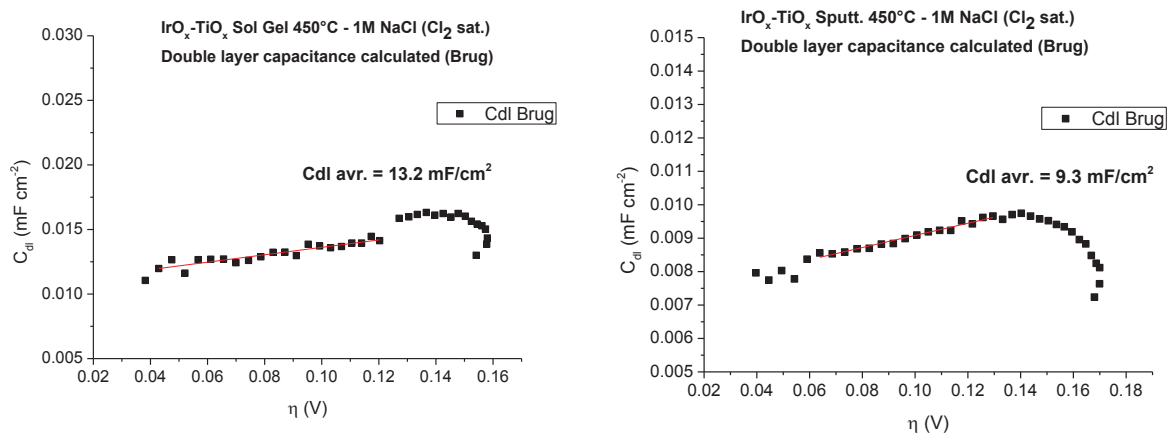


Fig.9.19. Double layer capacitance vs. overpotential, for the samples prepared at 450 °C.

Sample	C <sub>dl</sub> (Brug's model) (mF cm <sup>-2</sup> )
Sol Gel 450°C	13.2
Sputtering 450°C	9.3

Tab.9.8. Double layer capacitances evaluated through the Brug's model.

Both the figures reported in Tab.9.8 are an overestimation of the double-layer capacity of the catalyst coatings, owing to the fact that also the back side of the device (made of titanium) was exposed to the electrolyte during the test. However, this unknown contribution is the same for both samples, and a direct comparison can thus be done, observing that the Sol-Gel sample exposes a larger surface area, as also shown by the ex-situ analyses discussed in Chapter 8.

The study of samples prepared at 350 °C resulted to be more complex; two equivalent circuits were considered: one related to the porous electrode (Fig.9.20 A), while the other takes into account contributions due to adsorbed intermediates (Fig.9.20 B). In the former, the additional R<sub>1</sub>Q<sub>1</sub> mesh is placed in series with the R<sub>ct</sub>Q<sub>dl</sub>, while, in the latter, the two meshes are nested. Both circuits comprise the same number of elements, and it was mathematically demonstrated by Lasia [72] that the impedance response of a system that fits with one of them, can be fitted also with the other model, by using different values for the parameters but with a comparable statistical weight. Analyzing the data collected for samples prepared at 350 °C from 1 M NaCl solution, this problem was found, and requested a modification of experimental conditions.



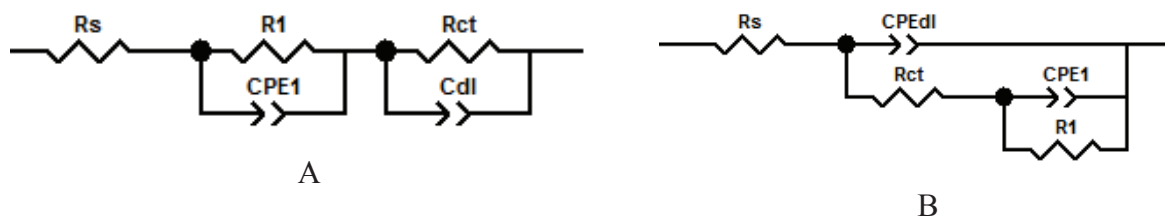


Fig.9.20. Equivalent circuit for the porous electrode (A) and for a system in which adsorbed intermediates are involved (B).

If the origin of the added mesh is due to porosity, the result should not vary when parameters like temperature or concentration of reagent in the solution are modified, because it represents a physical and geometric characteristic of the electrode; this is not true in the second case, where nested meshes are considered, because of the kinetic nature of  $R_1Q_1$ . Thus, the experimental conditions considered for the investigation of the two samples can be schematized as follows:

- NaCl 1M in HClO<sub>4</sub> 0.01M – 25 °C, Cl<sub>2</sub> sat. (E: 1.38 – 1.56 V Vs. SHE);
- NaCl 1M in HClO<sub>4</sub> 0.01M, Cl<sub>2</sub> sat. – 15 °C (E: 1.38 – 1.56 V Vs. SHE);
- HClO<sub>4</sub> 1M (0.34 – 1.24 V Vs. SHE);
- NaCl 0.5M in HClO<sub>4</sub> 0.01M, Cl<sub>2</sub> sat. – 25 °C (E: 1.364 – 1.544 V Vs. SHE).

Both the concentration of chloride and the temperature were varied under chlorine evolution conditions, and one test was carried out in HClO<sub>4</sub> by working with lower potentials, in the same conditions used for the determination of the electroactive sites by cyclic voltammetry.

It should be noted that fitting was tentatively tried also by using a combination (Fig.9.21) of the circuits previously reported in Fig.9.20, but no important improvement in the modeling could be found.

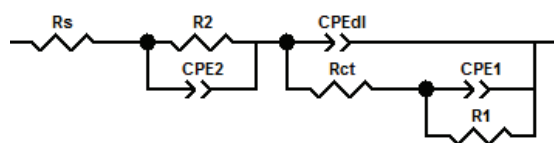


Fig.9.21. Equivalent circuit of a porous electrode, including an impedance contribution due to adsorbed species.

The complex circuit shown in Fig.9.21 was proposed by Cahan and Chen [73], and was also used by Lyons and Brandon, in relation with the study of the OER at passive metal electrodes [74]; as anticipated, it was not useful in our case.

An example of Nyquist and Bode plots collected under different experimental conditions, but at constant overpotential, for a sample prepared at 350 °C, is reported in Fig.9.22. In order to

allow the comparison between data collected under different experimental conditions, values of  $Z'$  were shifted by subtracting the solution resistance,  $R_s$ .

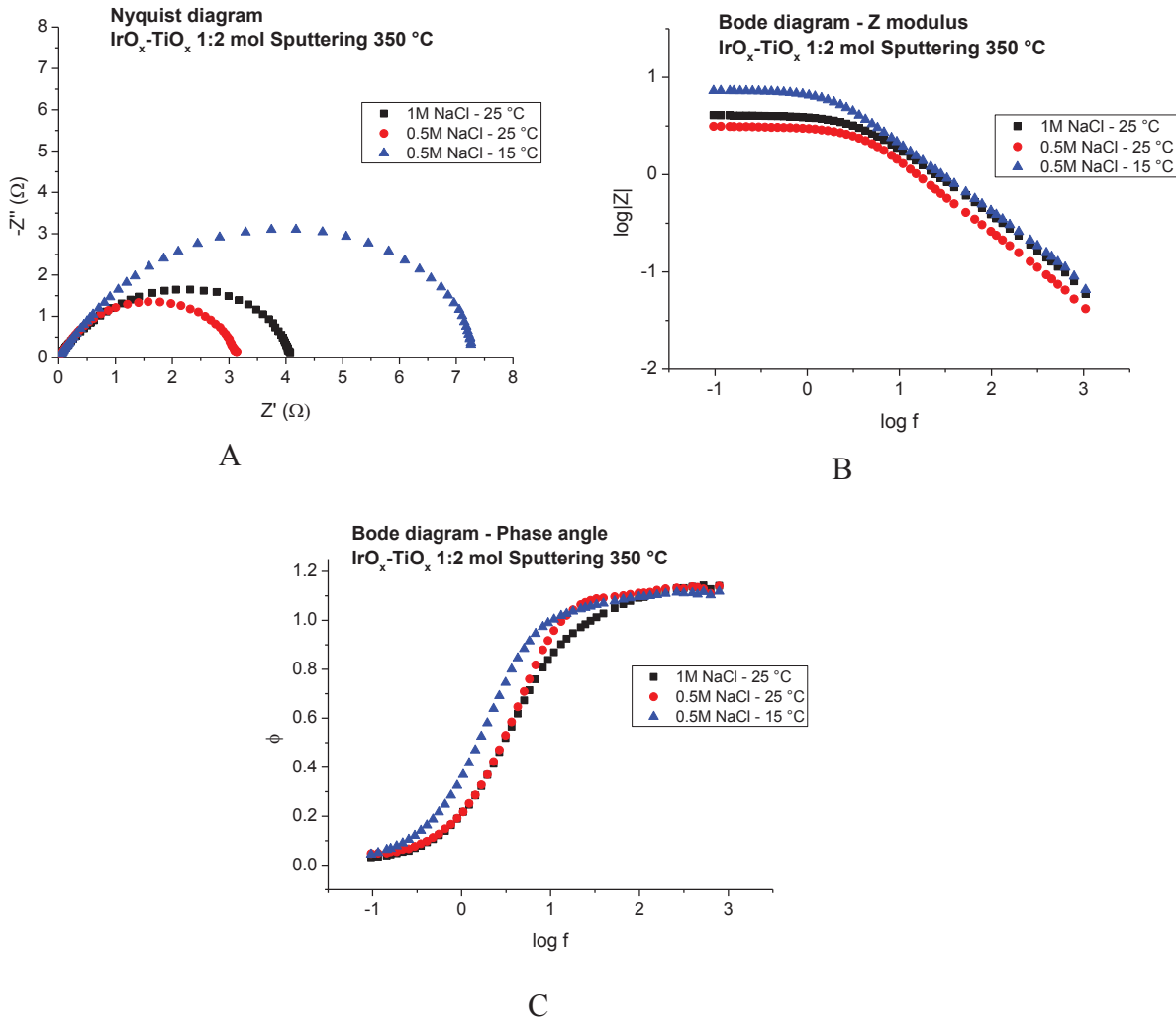


Fig.9.22. Nyquist (A) and Bode (B & C) diagrams, collected under different experimental conditions, for the sputtering sample prepared at 350 °C ( $\eta= 100$  mV).

For both specimens, a constant contribution at the higher frequencies is well visible, which does not seem to be related to a kinetic-controlled process, but rather attributable to a geometric characteristic of the sample. In fact, taking into consideration the models reported in Fig.9.20, the porous electrode model seems suitable to describe the behavior experimentally determined. A proof can be found by inspecting the graphs that can be obtained by plotting the logarithm of steady-state current ( $\log i$ ) and the logarithm of the inverse of the charge transfer resistance ( $\log R_{ct}^{-1}$ ), obtained by the fit, vs. the overpotential: if the slopes are similar, the model works well, and this was verified in all cases (Fig.9.23).

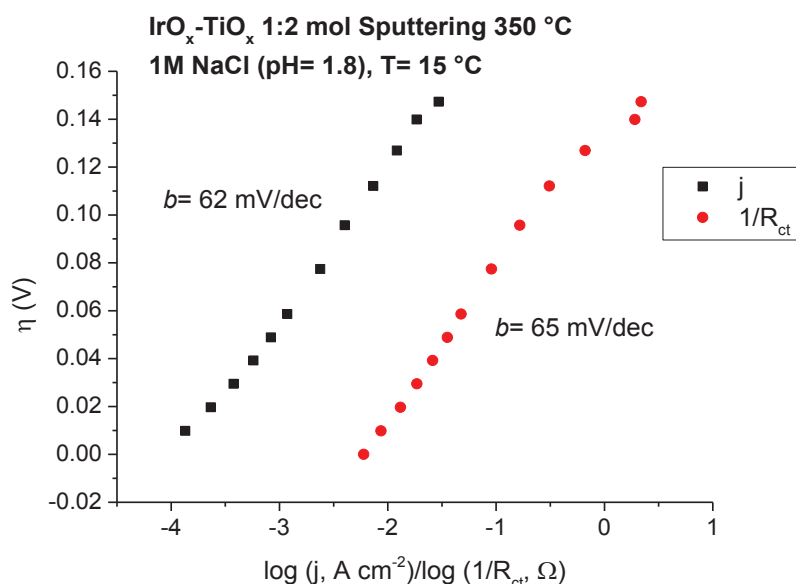


Fig.9.23. “Tafel plots” with current and using the  $R_{ct}$  evaluated through the equivalent circuit  $R_s(R_{ct}(R_1Q_1)Q_{dl})$  for sputtered sample prepared at 350 °C.

Small deviations can be found at high overpotential values, plausibly due to the important production of bubbles. An example of the results of a fitting procedure is reported in Tab.9.8.

By plotting  $R_{ct}$  and  $R_1$  against the overpotential, it is possible to appreciate that the second one is practically independent of the abscissa (picture A in Fig.9.24) and this behavior can be imputed to porosity, which characterizes materials prepared at the lowest temperature, as evidenced by the AFM and CV analyses discussed in Par.8.5 and 8.6, respectively.

The estimated pore resistances, at the different conditions of temperature and concentration examined, are comparable (picture B in Fig.9.24).

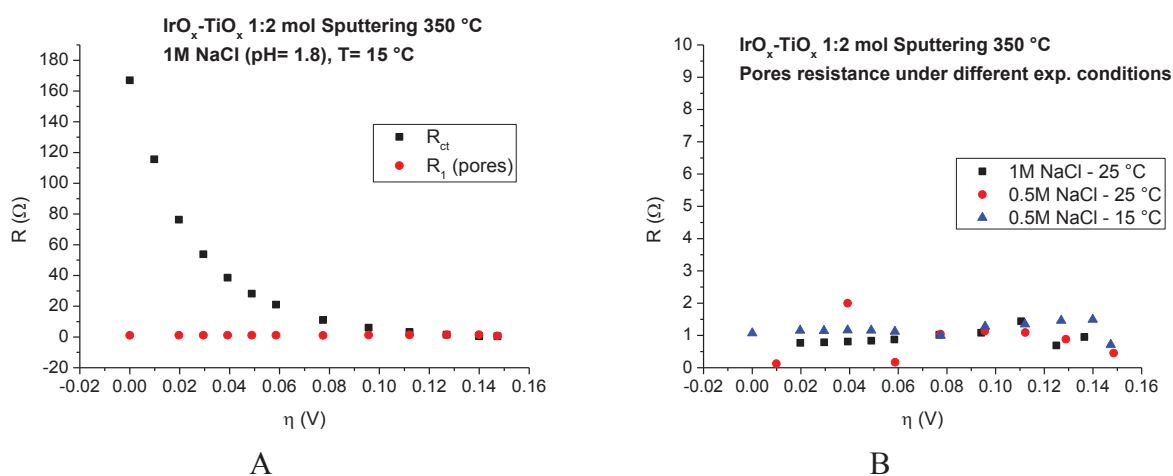


Fig.9.24. Sputtered sample prepared at 350 °C: (A)  $R_{ct}$  and  $R_1$  vs. overpotential; (B)  $R_1$  associated to porosity vs. overpotential, for all the explored conditions (under ChIER).

Similar results were obtained for the Sol-Gel sample prepared at 350 °C, even if small deviations have been attested owing to its high activity and very rough surface. That anomalous behavior, registered as a sort of noisy response, can be due to specific features of the material, as it will be discussed in subsequent sections.

Impedance tests carried out in perchloric acid 1 M showed a clear effect due to porosity: the equivalent circuit adopted was obviously different from that considered to fit the experiments under ChLER, and it is shown in Fig.9.25.

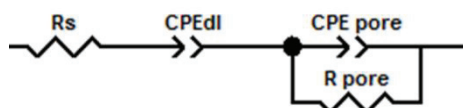


Fig.9.25. Equivalent circuit for fitting data from experiments in the absence of a faradaic process.

The explored potential range was the same used in CV (Par.8.6), from 0.1 to 1.1 V vs. SCE: in this range, the electrode material is characterized by a basic capacitive behavior; in this range, the electrode material is characterized by a basic capacitive behavior; a pseudo-capacitive contribution adds to the former, when the potential reaches 0.7 V Vs. SCE (a change in oxidation state of the electroactive sites takes place). Under these conditions, it is possible to determine both the pore resistance and the double-layer capacity (discussed later). The pore resistance determined for both samples is lower than those evaluated under ChLER, probably because of the different nature of the chemical species involved: the dimensions of proton, with respect to chloride, justify the smaller pore resistance measured, since their diffusion through the nano/micro-porosity of the coating is easier and characterized by a lower activation energy. To allow a comparison, data of pore resistance, determined in NaCl and HClO<sub>4</sub> solutions, have been collected in Tab.9.9.

<b>Sample</b>	<b>R<sub>pore</sub> (1M NaCl – 25 °C) (Ω)</b>	<b>R<sub>pore</sub> (1M HClO<sub>4</sub> – 25 °C) (Ω)</b>
<b>Sol Gel 350°C</b>	0.6	0.4
<b>Sputtering 350°C</b>	0.9	0.2

Tab.9.9. Pore resistances estimated in NaCl and HClO<sub>4</sub> solutions, for samples prepared at 350 °C.

The differences found may be due to different pore geometries, which can cause an anomalous mass transport of chemical species, inside and outside the cavities. Further investigations are necessary to solve this problem; Lasia [75] has treated exhaustively this topic, describing different models (semi-infinite pores, pores' shape, etc.) that lead to different

mathematic approximations able to solve the problem (De Levie model, Paasch's approximation); however, a so thorough investigation is beyond the scope of this thesis. Moreover, adopting the Brug's model, also the double-layer capacity was calculated (let's remind that the model works well only if  $\Phi$  (Eq.9.49) is larger than 0.8-0.9). Results have been summarized in Tab.9.10.

<b>Sample</b>	<b><math>C_{dl}</math> (Cl<sup>-</sup> 1M, 25 °C) (mF cm<sup>-2</sup>)</b>	<b><math>C_{dl}</math> (Cl<sup>-</sup> 0.5M, 25 °C) (mF cm<sup>-2</sup>)</b>	<b><math>C_{dl}</math> (Cl<sup>-</sup> 1M, 15 °C) (mF cm<sup>-2</sup>)</b>	<b><math>C_{dl}</math> (HClO<sub>4</sub>) (mF cm<sup>-2</sup>)</b>	<b><math>C_{dl}</math> average (mF cm<sup>-2</sup>)</b>
<b>Sol Gel 350°C</b>	-	-	-	53.9	<b>53.9</b>
<b>Sputtering 350°C</b>	7.9	10.3	8.0	9.7	<b>9.0</b>

Tab.9.10. Double-layer capacities evaluated under different conditions, for samples prepared at 350 °C.

The values of double-layer capacity were calculated using Eq.9.51, in the case of measurements under ChIER conditions, while the following simplified Brug's equation was adopted when the simpler circuit shown in Fig.9.25 was considered:

$$T = \bar{C}_{dl}^{\phi} (R_s)^{-(1-\phi)} \quad \text{Eq.9.52}$$

Only the potential values higher than 0.4 V vs. SCE were considered, because of the low conductivity of iridium oxide when the metal has an oxidation state of +3 (this is the main valence state in the region of potentials lower than 0.4 V); in fact, a low film conductivity can negatively affect the evaluation of the double-layer capacity. Fig.9.26 highlights the data that have been considered for the estimation of that material characteristic.

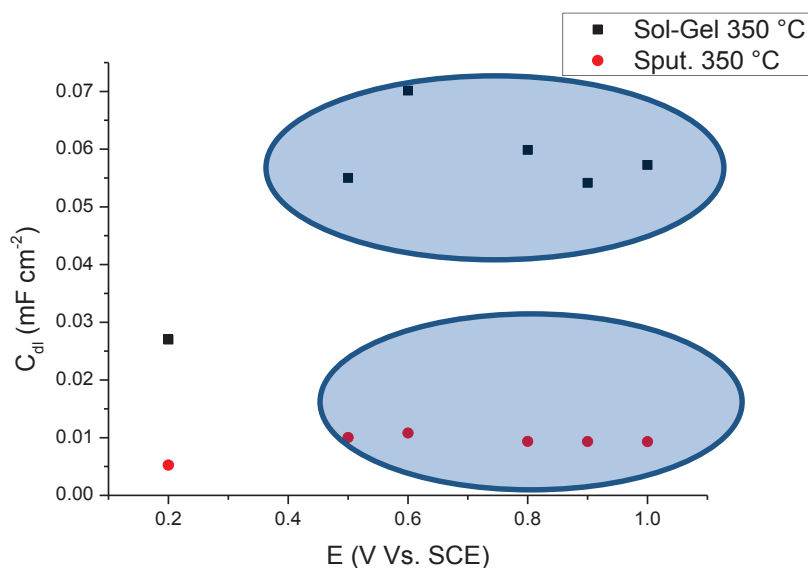


Fig.9.26. Double-layer capacity estimated in 1M  $\text{HClO}_4$  (potentials are lower than those required to allow the chlorine evolution reaction, in NaCl solution).

With reference to Fig.9.16, the flattened character of Nyquist impedance diagram was also noted by Denton *et al.* [13], who worked with  $\text{RuO}_2/\text{TiO}_2$  electrodes in KCl/HCl solutions with different compositions; they ascribed this characteristic to the film porosity, but without any sort of experimental demonstration. Also an Asiatic research group highlighted an analogous behavior, by working with Ru-La oxide-based materials [76] and they adopted the same model proposed in this paragraph, with the addition of a Warburg element in order to justify the presence of a flat portion of curve in the Nyquist diagram also at very low frequencies, which was attributed to the establishment of a diffusion controlled process.

Anomalous results, hard to interpret, were obtained also during this experimentation, in the case of samples prepared via Sol-Gel at 350 °C; the sample synthesis and related experiments were carried out several times, but reproducible responses were obtained. Concerning the impedance spectroscopy measurements, the fitting procedure resulted to be quite tricky: the equivalent circuit associated with the porous electrode works better with respect to the one comprising the effects of adsorbed intermediates (Fig.9.20), but errors associated to estimated parameters are higher than in the case of the homologous sputtered coating. This kind of strange behavior might be somehow related to the high catalytic performances of this material for the electro-synthesis of chlorine.

$\eta$ (V)	$\chi^2$	$SQ^*$	$R_s$	$R_s$ Err	$R_s$ Err%	$R_{ct}$	$R_{ct}$ Err	$R_{ct}$ Err%	$Q_{dl}$	$Q_{dl}$ T Err	$Q_{dl}$ T Err%	$Q_{dl}$ P	$Q_{dl}$ P Err	$Q_{dl}$ P Err%	$R_i$	$R_i$ Err	$R_i$ Err%	$Q_i$	$Q_i$ T Err	$Q_i$ T Err%	$Q_i$ P	$Q_i$ P Err	$Q_i$ P Err%
180	7.E-05	5.E-03	1.11	5.E-03	0.42	0.46	2.E-01	53.12	0.05	2.E-02	40.25	0.90	6.E-02	7.17	0.71	2.E-01	34.92	0.02	1.E-03	6.69	7.E-01	2.E-02	2.81
160	1.E-04	1.E-02	1.09	2.E-03	0.19	0.52	1.E-01	19.90	0.04	3.E-03	8.20	1.04	4.E-02	3.72	1.49	1.E-01	7.11	0.02	1.E-03	4.84	0.73	5.E-03	0.76
140	5.E-05	5.E-03	1.08	2.E-03	0.15	1.51	2.E-01	10.87	0.02	1.E-03	5.95	0.98	2.E-02	1.89	1.46	2.E-01	11.51	0.03	1.E-03	4.58	0.72	4.E-03	0.56
120	4.E-05	4.E-03	1.08	2.E-03	0.20	3.23	2.E-01	5.18	0.02	5.E-04	3.33	0.96	9.E-03	0.98	1.35	2.E-01	12.82	0.03	8.E-04	2.56	0.70	6.E-03	0.89
100	2.E-05	2.E-03	1.08	2.E-03	0.18	6.05	9.E-02	1.56	0.01	1.E-04	1.08	0.97	4.E-03	0.38	1.28	1.E-01	7.57	0.04	1.E-03	3.29	0.69	7.E-03	0.99
80	2.E-05	2.E-03	1.08	2.E-03	0.19	11.04	5.E-02	0.45	0.01	4.E-05	0.35	0.96	2.E-03	0.19	1.00	5.E-02	4.63	0.04	2.E-03	4.15	0.69	8.E-03	1.11
60	3.E-04	3.E-02	1.18	8.E-03	0.66	21.05	2.E-01	0.88	0.01	7.E-05	0.72	0.96	5.E-03	0.53	1.12	1.E-01	11.86	0.04	5.E-03	13.12	0.69	2.E-02	3.52
50	2.E-05	2.E-03	1.34	2.E-03	0.18	28.17	6.E-02	0.20	0.01	2.E-05	0.16	0.96	1.E-03	0.12	1.16	3.E-02	3.02	0.04	1.E-03	3.67	0.66	7.E-03	1.01
40	2.E-05	2.E-03	1.36	2.E-03	0.18	38.60	7.E-02	0.18	0.01	1.E-05	0.13	0.95	1.E-03	0.11	1.16	3.E-02	2.81	0.04	1.E-03	3.61	0.66	7.E-03	1.00
30	1.E-05	1.E-03	1.37	2.E-03	0.15	53.86	8.E-02	0.15	0.01	1.E-05	0.10	0.95	8.E-04	0.09	1.14	3.E-02	2.24	0.04	1.E-03	3.07	0.66	6.E-03	0.85
20	2.E-05	2.E-03	1.37	2.E-03	0.16	76.34	1.E-01	0.17	0.01	9.E-06	0.10	0.95	8.E-04	0.08	1.15	3.E-02	2.22	0.04	1.E-03	3.15	0.66	6.E-03	0.88
10	3.E-04	3.E-02	1.30	1.E-02	0.77	115.60	9.E+01	80.59	0.10	1.E-02	9.99	0.50	2.E-02	3.28	85.08	3.E+00	3.15	0.01	1.E-04	1.24	1.01	6.E-03	0.62
0	1.E-05	1.E-03	1.39	2.E-03	0.13	167.00	3.E-01	0.20	0.01	7.E-06	0.07	0.95	6.E-04	0.06	1.07	2.E-02	1.61	0.04	1.E-03	2.66	0.68	5.E-03	0.73

Tab.9.8. Fitting results relative to test of Sputtered/450 °C sample carried out in 1M NaCl solution (pH: 1.8) at 15 °C. Data collected when  $\eta=180$  mV where excluded because of the high percentage errors associated to parameters; this is probably due to noise disturb provoked by gas bubbles evolution. However, this point is of little interest because of deviations verified and associated to Losev effect [5]. In the case evidenced in green, the high error associated to the charge transfer resistance was not considered because of the noise at low frequencies verified during the test.

\* SQ stands for Sum of Squares.

## Bibliography

1. S. Trasatti, G. Buzzanca, *J. Electroanal. Chem.* **29**, App.1 (1971).
2. S. Trasatti, *Electrochim. Acta* **32**, 369 (1987).
3. G. Bianchi, *J. Appl. Electrochem.* **1**, 231 (1971).
4. G. Faita, G. Fiori, *J. Appl. Electrochem.* **2**, 31 (1972).
5. V.V. Losev, *Elektrokhimiya* **17**, 733 (1981).
6. A.T. Kuhn, C.J. Mortimer, *J. Electrochem. Soc.* **120**, 231 (1973).
7. R.G. Érenburg, L.I. Krishtalik, I.P. Yaroshevskaya, *Élektrokhimiya*, **11**, 1072 (1975).
8. R.G. Érenburg, L.I. Krishtalik, I.P. Yaroshevskaya, *Élektrokhimiya*, **11**, 1076 (1975).
9. R.G. Érenburg, L.I. Krishtalik, I.P. Yaroshevskaya, *Élektrokhimiya*, **11**, 1236 (1975).
10. R.G. Érenburg, L.I. Krishtalik, I.P. Yaroshevskaya, *Élektrokhimiya*, **11**, 1068 (1975).
11. L.J.J. Janssen, L.M.C. Starmans, J.G. Visser, E. Barandrecht, *Electrochim. Acta* **22**, 1093 (1977).
12. I.R. Burrows, D.A. Denton, J.A. Harrison, *Electrochim. Acta* **23**, 493 (1978).
13. D.A. Denton, J.A. Harrison, R.I. Knowles, *Electrochim. Acta* **24**, 521 (1979).
14. T. Arikado, C. Iwakura, H. Tamura, *Electrochim. Acta* **23**, 9 (1978).
15. J. Augustynski, L. Balsenc, J. Hinden, *J. Electrochem. Soc.* **125**, 1983 (1978).
16. V.V. Gorodetskii, P.N. Zorin, M.M. Pecherskii, V.B. Busse-Machukas, V.L. Kubasov, Y.Y. Tomashpol'skii, *Elektrokhimiya* **17**, 79 (1980).
17. T. Hepel, H. Pollak, W.E. O'Grady, *J. Electroanal. Chem.* **188**, 281 (1985).
18. T. Hepel, H. Pollak, W.E. O'Grady, *J. Electrochem. Soc.* **133**, 69 (1986).
19. L.D. Burke, J.F. O'Neill, *J. Electroanal. Chem.* **101**, 341 (1979).
20. L.D. Burke, O.J. Murphy, *J. Electroanal. Chem.* **101**, 351 (1979).
21. J. Mozota, M. Vukovic, B.E. Conway, *J. Electroanal. Chem.* **114**, 153 (1980).
22. B.V. Tilak, *J. Electrochem. Soc.* **126**, 1343 (1979).
23. L.I. Krishtalik, *Electrochim. Acta* **26**, 329 (1981).
24. R.G. Érenburg, L.I. Krishtalik, N.P. Rogozhina, *Elektrokhimiya* **20**, 1183 (1984).
25. R.G. Érenburg, *Elektrokhimiya* **20**, 1602 (1984).
26. S. Ardizzone, S. Trasatti, *Advances in Colloid and Interface Science* **64**, 173 (1996).
27. V. Consonni, S. Trasatti, F. Pollak, W.E. O'Grady, *J. Electroanal. Chem.* **228**, 393 (1987).
28. L. Tomesànyi, A. De Battisti, G. Hirschberg, K. Varga, J. Liszi, *Electrochim. Acta* **44**, 2463 (1999).



29. J.L. Fernandez, M.R.G. de Chialvo, A.C. Chialvo, *Electrochim. Acta* **47**, 1129 (Part I) (2002).
30. J.L. Fernandez, M.R.G. de Chialvo, A.C. Chialvo, *Electrochim. Acta* **47**, 1137 (Part II) (2002).
31. J.L. Fernandez, M.R.G. de Chialvo, A.C. Chialvo, *Electrochim. Acta* **47**, 1145 (Part III) (2002).
32. J.L. Fernandez, M.R. Gennero de Chialvo, A.C. Chialvo, *Electrochem. Communications* **2**, 630 (2000).
33. C. Pirovano, S. Trasatti, *J. Electroanal. Chem.* **180**, 171 (1984).
34. L.M. Da Silva, J. F.C. Boodts, L.A. De Faria, *J. Braz. Chem. Soc.* **14** (3), 388 (2003).
35. M.H.P. Santana, L.A. De Faria, *Electrochim. Acta* **51**, 3578 (2006).
36. J.K. Nørskov, J. Rossmeisl, A. Logadottir, L. Lindqvist, J.R. Kitching, T. Bligaard, H. Jonsson, *J. Phys. Chem. B* **108**, 17886 (2004).
37. J.S. Filhol, M. Neurock, *Angewandte Chemie Int. Ed.* **45**, 402 (2006).
38. K. Jacobi, Y. Wang, G. Ertl, *J. Phys. Chem. B* **110**, 6115 (2006).
39. H. Over, *Electrochim. Acta* **93**, 314 (2013).
40. H.A. Hansen, I.C. Man, F. Studt, F. Abild-Pedersen, T. Bligaard, J. Rossmeisl, *J. Phys. Chem.* **12**, 283 (2010).
41. M.G. Evans, M Polanyi, *Trans. Faraday Soc.* **31**, 875 (1935).
42. H. Eyring, *J. Chem. Phys.* **3**, 107 (1935).
43. A. Bard and L. Faulkner, *Electrochemical Methods. Fundamentals and Applications*, 2nd edition, John Wiley and Sons, Inc. (2001).
44. J.O'M. Bockris, A.K.N.Reddy, and M. Gamboa-Aldeco, *Modern Electrochemistry 2A. Fundamentals of Electrodicts*, Second Edition, Kluwer Academic/Plenum Publishers, 1083, (2000).
45. E. Gileadi, *Electrode kinetics*, VCH Publishers, Inc. (1993).
46. B.E. Conway, T.C. Liu, *Ber. Bunsenges. Phys. Chem.* **91**, 461 (1987).
47. L.A. da Silva, V.A. Alves, M.A.P. da Silva, S. Trasatti, J.F.C. Boots, *Can. J. Chem.* **75**, 1483 (1997).
48. L.M. da Silva, J.F.C. Boots, L.A. de Faria, *Electrochimica Acta* **46**, 1369 (2000).
49. J.M. Hu, J.Q. Zhang, C.N. Cao, *Int. Journ. of Hydrogen Energy* **29**, 791 (2004).
50. M.H. Miles, E.A. Klaus, B.P. Gunn, J.R. Locker, W.E. Serafin, *Electrochim. Acta* **23**(6), 521 (1978).

51. L.D. Burke, O.J. Murphy, J.F. O'Neill, S. Venkatesan, *J. Chem. Soc., Faraday Trans. 1* **73**, 1659 (1977).
52. G. Lodi, E. Sivieri, A. De Battisti, S. Trasatti, *J. Appl. Electrochem.* **8**, 135 (1978).
53. R.G. Érenburg in *Dvionoi Sloi I Adsorbztiyana Tverdykh Elektrodakh* **6**, 382, Tartus. Gos. Univ. (1981).
54. L.J.J. Janssen, in *Modern Chlor-Alkali Technology* (Edited by Jackson) **2**, 271, Ellis Horwood, Chichester (1983).
55. M. Thomassen, C. Karlsen, B Børresen, R. Tunold, *Electrochim. Acta* **51**, 2909 (2006).
56. S. Trasatti, *Electrodes of Conductive Metallic Oxides, Part B* **10**, 591-599, Elsevier Scientific Publishing Company (1981).
57. J. Hagen, *Industrial Electrocatalysis: A Practical Approach*, Weinheim, Germany, Wiley-VCH (2006).
58. B.E. Conway, *Theory and Principles of Electrode Processes- Modern Concept in Chemistry*, The Ronald Press Company Ed., New York.
59. M.I. Temkin, *Zh. Fiz. Chim.* **22**, 1081 (1948).
60. G. Faita, P. Longhi, T. Mussini, *J. Electrochem. Soc.* **114**(4), 340 (1967).
61. M. S. Sherril, E. F. IZard, *J. Am. Chem. Soc.* **53**, 1667 (1931).
62. M. Inai, C. Iwakura, H. Tamura, *Electrochim. Acta* **24**, 993 (1979).
63. S. Trasatti, *Electrodes of Conductive Metallic Oxides, Part B* **10**, 576-577, Elsevier Scientific Publishing Company (1981).
64. J.O'M. Bockris, A. Gochev, *J. Electroanal. Chem.* **214**, 655 (1986).
65. B.V. Tilak, B.E. Conway, *Electrochim. Acta* **37**(1), 51 (1992).
66. H.A. Kramers, *Phys. Zeit.* **30**, 52 (1929); R. de L. Kronig, *J. Opt. Soc. Am.* **12**, 547 (1926).
67. J.R. Macdonald, *Impedance Spectroscopy Emphasizing Solid Materials and Systems*, Wiley, New York (1987).
68. J.E.B. Randles, *Discussions on the Faraday Soc.* **1**, 11 (1947).
69. R.C. Salvarezza, A.J. Arvia, *Modern Aspects of Electrochemistry* **30**, R.E. White, B.E. Conway and J. O'M. Bockris, Eds., Plenum..
70. T. Pajkossy, *J. Electroan. Chem.* **364**, 111 (1994).
71. G.J. Brug, A.L.G. Van den Eeden, M. Sluyters-Rehbach, J.H. Sluyers, *J. Electroanal. Chem.* **176**, 275 (1984).
72. A. Lasia, *Electrochemical Impedance Spectroscopy and its Applications*, Springer, XI, 367 (2014).
73. B.D. Cahan, C.T. Chen, *Journal of Electrochemical Society* **129**, 700 (1982).

74. M.E.G. Lyons, M.P. Brandon, *Journal of Electroanalytical Chemistry* **631**, 62 (2009).
75. A. Lasia, Electrochemical Impedance Spectroscopy and its applications, *Modern Aspects of Electrochemistry*, B.E. Conway, J. Bockris, R.E. White, Edts., Kluwer Academic/Plenum Publishers, New York, **32**, 143 (1999).
76. L. Ping, L. Quinfeng, X. Likun, X. Lili, S. Hongging, *Acta Chimica Sinica* **70**(10), 1166 (2012).

## 10. Effects of Chlorine Evolution on materials

### 10.1. XRD investigation – evaluation of phase modifications

The samples prepared on titanium supports and subjected to strong chlorine evolution were investigated through XRD spectroscopy in order to compare their response to that obtained from as-prepared specimens. Any modification of crystalline phases and, in general, of the texture of the matrix can be ascribed to effects due to the electrochemical gas evolution. It's worth remembering that the ChLER is not responsible for damages on the coating, while the very small percentage of oxygen evolution causes electrode modifications and/or deterioration. Unfortunately, the OER contribution cannot be totally avoided, from both thermodynamic and kinetic reasons, and the amorphous and crystalline portions of the electrode can provide different responses to the polarization stimulus. Fig.10.1 shows a comparison of diffractograms obtained before and after the execution of the electrochemical tests described in Chapter 9.

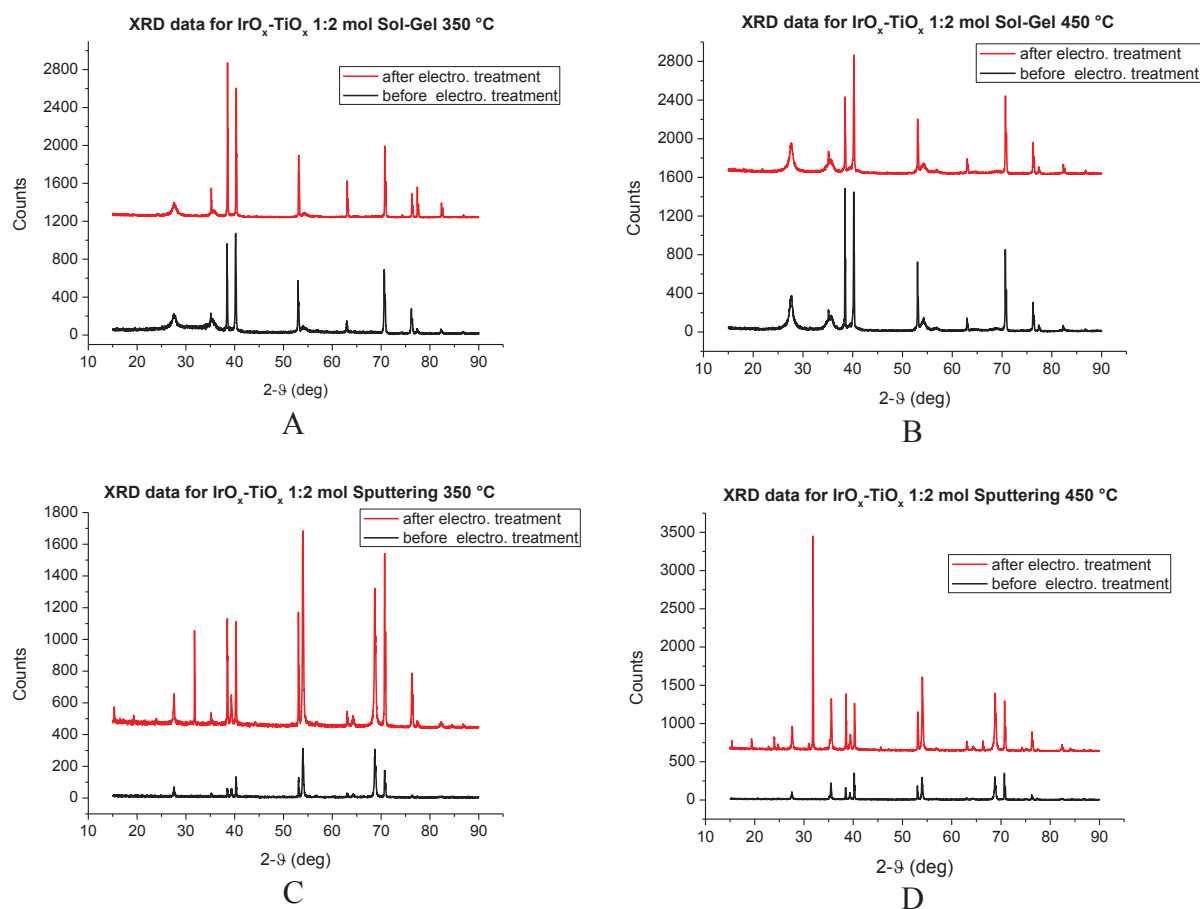


Fig.10.1. Comparison between diffractograms before (black line) and after (red line) the possible stress suffered under ChLER, for all samples: (A) Sol-Gel 350 °C, (B) Sol-Gel 450 °C, (C) Sputtering 350 °C, (D) Sputtering 450 °C.

In general, no modification in the nature of crystalline phases can be attested, and the relative intensities between peaks remain practically constants, thus suggesting that a selective erosion/dissolution of material does not take place. With reference to the sputtered electrodes, the absolute value of counts increased, after the ChIER investigation; even an augmentation of the intensity of signals pertaining to the metal support is attested, possibly indicating that a thinner coating is exposed to the X-radiation. On the other hand, a negligible modification of signals associated to the iridium and titanium oxide phases has been observed in the case of sol-gel samples, and only an increase of titanium peaks from the metal support is evidenced. The prolonged treatment of polarization seems to cause a partial dissolution of the coating, in the case of sputtered samples, with a preferential attack toward the amorphous phase, which appears as the more sensitive and reactive portion of the device. In the case of sol-gel samples, the situation appears more complicated, since the crystalline phase does not seem to suffer any dissolution (actually, a small decrease can be observed in the case of the electrode calcined at 350 °C). Because of the high roughness, and of the consequent presence of a wide macro-porosity, a coating dissolution can occur preferentially in channels and pores, and a decrease of the average thickness of the system is more prone to experimental uncertainty, if compared to the case of the sputtered electrodes.

## **10.2. RBS and XPS experiments: findings from the ChIER**

A combined ex-situ investigation has been carried out by means of two surface (and near-surface) non-destructive techniques, aiming to confirm the hypotheses emerged after the electrochemical investigation on the kinetics of the chlorine evolution reaction. Owing to the different nature of samples studied, the experiments will be discussed separately.

### RBS tests

Very thin coatings were deposited on silicon-doped supports, exactly as it was done in the case of ERD analyses discussed in Par.8.7: a light support and a low thickness film (about 0.2  $\mu\text{m}$ ) are necessary conditions in order to analyze atoms characterized by a low mass (chlorine, in this particular case). An initial conditioning of samples has been carried out, by recording 50 voltammetric cycles at 100 mV/s in a 1M solution of  $\text{HClO}_4$ , from 0.1 to 1.1 V Vs. SCE, and then by polarizing each specimen in 1M NaCl at a current density of 1000  $\text{A m}^{-2}$  for 1h. The RBS analyses were performed using the same conditions of the tests previously discussed (Par.8.4), before and after chlorine evolution process.

An example of obtained results is shown in Fig.10.2.

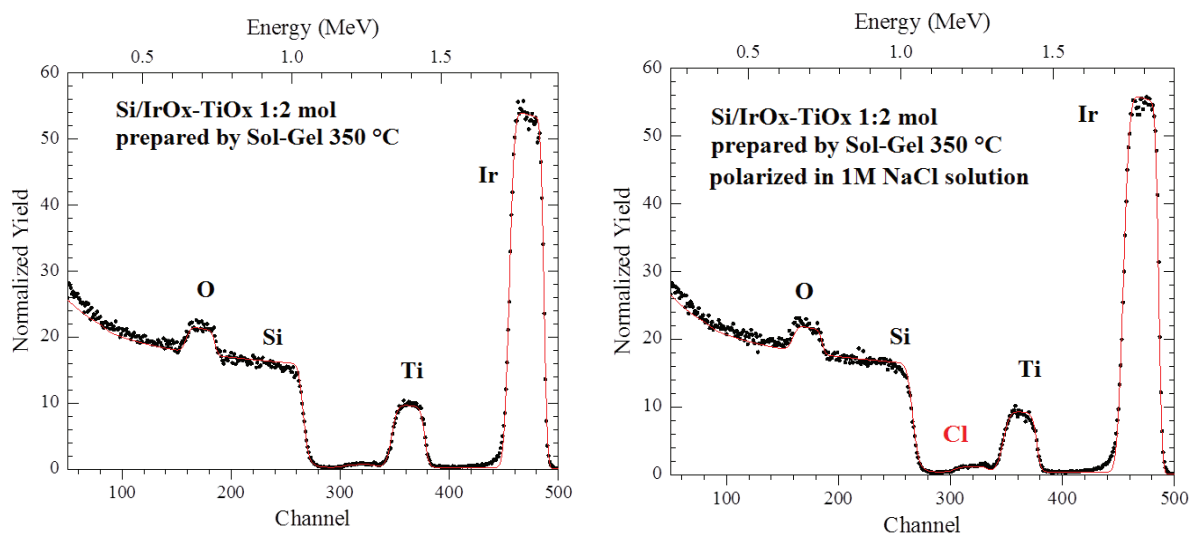


Fig.10.2. RBS spectra for the  $\text{IrO}_x\text{-TiO}_x$  1:2 mol prepared by Sol-Gel at 350 °C on silica supports, before and after a strong polarization under chlorine evolution conditions.

The signal pertaining to chlorine appears between channels 300 and 340, well resolved with respect to Ti. In the case of sol-gel samples, an increase in chlorine content is well visible: an important amount of Cl remains strongly linked to the material, after the polarization; the Cl concentration, after the ChLER, is approximately doubled. In particular,  $\text{Cl}_{0.05} \rightarrow \text{Cl}_{0.10}$  for the sol-gel sample prepared at 350 °C and  $\text{Cl}_{0.00} \rightarrow \text{Cl}_{0.07}$  for that prepared at 450 °C. Of course, the electrode calcined at the lower temperature may contain a larger amount of residual chlorine, just after the preparation, because of an incomplete pyrolysis of precursors. Moreover, owing to the signal profiles, which extend also in the low energies region, a presence of Cl also in the bulk of films (at a depth of several nanometers) is suggested, especially for the sample prepared at 350 °C. The sputtered samples prepared at 350 and 450 °C have shown a nonspecific intensification in the background signal between channels 300 and 340, which indicates that a given amount of chlorine is present, but a precise quantification is not possible. Because of the lack of cracks and macro-porosity, in these samples, the adsorbed chlorine plausibly remains on the surface, and may easily leave the surface thank to the vacuum conditions of the RBS chamber. This phenomenon does not apply in the case of Sol-Gel coatings, where cracks and macro-porosity are present along the surface, and they may block the chlorine adsorbed inside them, by means of different interactions. It should be underlined that the Rutherford spectroscopy detects the chlorine adsorbed on surface pores as “bulk chlorine”, because the beam loses energy by interacting with the material present in peaks and crests. Accordingly, the data discussed within this

chapter are not in disagreement with the results previously proposed. Actually, the present outcomes can provide important indications for the study of the kinetics of the ChIER, especially because they highlight the presence of high amounts of chlorine on the surface during the process, thus corroborating the application of the mathematical model proposed by Conway for an electrochemical process that involves adsorbed intermediates. Additionally, these evidences confirm the results of previous researches, as discussed e.g. by Augunstynskii *et al.* [1] and Gorodetskii *et al.* [2], who found large amounts of chlorine on the surface by using XPS and Augèr spectroscopies, respectively. Moreover, by working with electrodes based on ruthenium and titanium oxides, Gorodetskii detected a layer of adsorbed chlorine as a consequence of an electrolysis under chlorine evolution conditions; the coverage of intermediates was so high to completely mask ruthenium and titanium contained in the coating; these metals became visible from the Augèr spectroscopy only after a strong etching of the surface. These two papers have the only limitation of the absence of electrochemical data related to the kinetics of the ChIER. Since the investigated materials may significantly differ from the others discussed in the literature, because of issues related to the preparation method (which was not as reproducible as today), to look for a correlation with kinetics details obtained by others is not advisable.

#### XPS preliminary tests

Samples of 1  $\mu\text{m}$  thickness, deposited on electro-polished titanium supports, have been investigated. The approach adopted has been the same of the RBS analyses previously discussed: four samples were polarized under strong chlorine evolution conditions; experimentally, a galvanostatic polarization was carried out in a 1M solution of NaCl (pH: 1.8), applying a current density of 1000 A/m<sup>2</sup> for 3600 s and by working at room temperature. Then, a comparison between “as-prepared” and treated samples has been done by means of the spectroscopic technique.

Two examples of gathered spectra are proposed in Fig.10.3: they relate to IrO<sub>x</sub>-TiO<sub>x</sub> 1:2 mol samples prepared by sputtering at 350 °C.

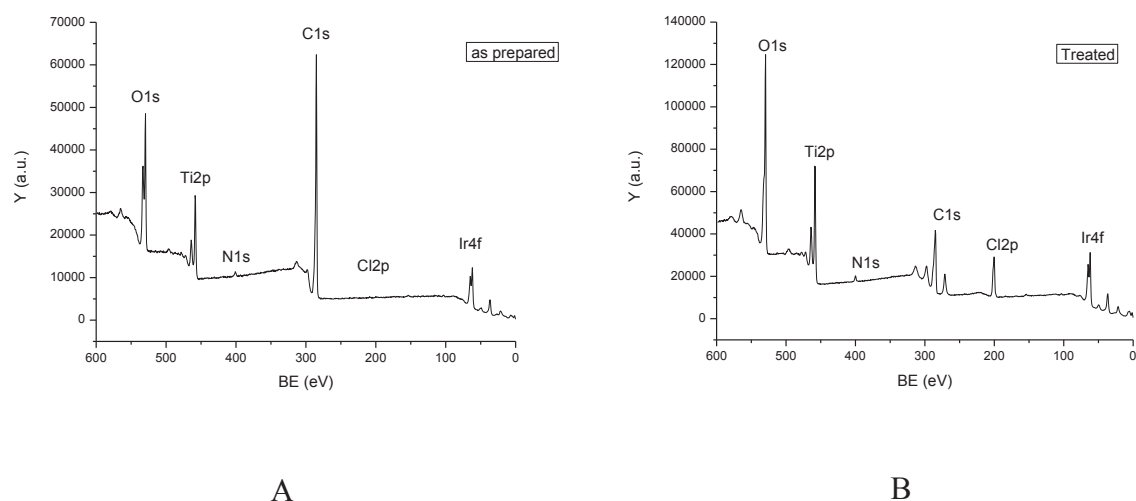


Fig.10.3. XPS results for specimens (A) as prepared, and (B) polarized under Chlorine evolution conditions; samples have been synthesized by sputtering at 350 °C. The Cl 2p signal has a binding energy of about 200 eV.

A fitting procedure was applied to the relevant photoelectron peaks, using the INDAGO software; obtained results have been collected in Tab.10.1.

<b>Conc. % at.</b>	<b>Ti 2p</b>	<b>O 1s</b>	<b>C 1s</b>	<b>N 1s</b>	<b>Ir 4f</b>	<b>Cl 2p</b>
<b>Solgel 350 As prep.</b>	16.7	62.0	12.7	0.1	5.9	<b>2.6</b>
<b>Solgel 350 Treated</b>	13.9	44.8	29.3	5.2	3.9	<b>2.9</b>
<b>Solgel 450 As prep.</b>	18.5	59.1	16.3	0.0	5.4	<b>0.6</b>
<b>Solgel 450 Treated</b>	19.9	60.6	10.9	0.0	7.7	<b>0.8</b>
<b>Sputt 350 As prep.</b>	5.2	24.5	67.9	0.9	1.4	<b>0.0</b>
<b>Sputt 350 Treated</b>	10.5	38.6	38.3	1.5	2.7	<b>8.4</b>
<b>Sputt 450 As prep.</b>	10.2	36.0	49.2	0.7	3.6	<b>0.2</b>
<b>Sputt 450 Treated</b>	14.4	47.6	29.8	0.2	5.0	<b>3.0</b>

Tab.10.1. Summary of preliminary XPS results on Ti-supported coatings treated under chlorine evolution conditions.



Some interesting information can be obtained by inspecting the obtained results; it's worth remembering that this technique, unlike the RBS, is a actual surface technique, the analyzed sample thickness being between 10 and 80 Å (depending on the photoelectrons take-off angle, with respect to the normal to the sample surface). Considerations can be resumed as follows:

- Films tend to adsorb both water and CO<sub>2</sub> (especially those synthesized by sputtering). The reactivity of surfaces seems to be related to the nature of the preparative method.
- Only the sputtered samples (especially that prepared at 350 °C) seem to “encage” an appreciable amount of chlorine; also the sample synthesized at 450 °C shows an 3% increase in chlorine.

The presence of water and carbon dioxide, both adsorbed on the surface, can shield the surface by X-rays, hiding the signals of iridium and titanium, and thus explaining the anomalous estimations of Ir/Ti ratios. Moreover, the XPS technique requires more extreme vacuum conditions, with respect to RBS, and the area hit by the source beam is very localized, interesting (as already anticipated) only the actual surface region (on the contrary, RBS can analyze a thickness of several nanometers).

At a first analysis, the information provided by XPS seem to be in contradiction with those provided by RBS; however, in consideration of the aforementioned reasons, XPS data have to be considered as only preliminary, and further investigation is necessary for obtaining more conclusive information, possibly regarding also the nature of the adsorbed intermediate (whether it is present as anion, or as radical, etc.). This can be done by choosing ad hoc samples, with particular features, and selecting specific experimental conditions for the conditioning treatments of polarization.

### **10.3. Service-life evaluation: accelerated tests on electrode devices**

A description of possible processes that may lead to DSA<sup>®</sup> deactivation has been deeply discussed by Martelli *et al.* [3], who classified mechanisms into five large classes:

1. Support passivation;
2. Coating dissolution;
3. Coating detachment;
4. Mechanical damages;
5. Mixed mechanisms.

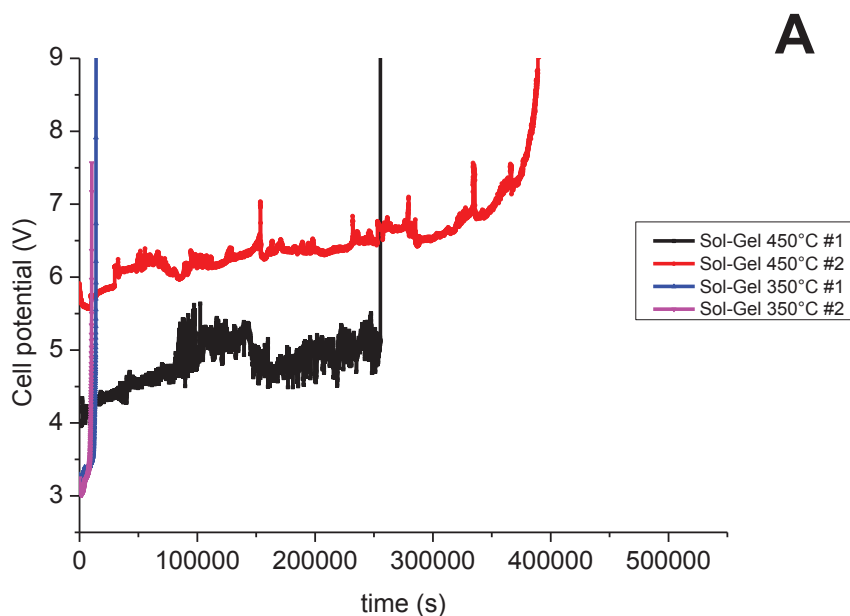
Experiments for service-life evaluation have been carried out in milder conditions with respect to those reported in industrial protocols [see *e.g.* 4]. An analysis of different coatings

has shown that mixtures based on IrO<sub>2</sub> and Ta<sub>2</sub>O<sub>5</sub> are the best coatings for OER in terms of anodic efficiency and stability; anyway, tests described in this section, on IrO<sub>2</sub>-TiO<sub>2</sub> films, have been carried out for extrapolating general information rather than for real application purposes. As already known, the long-term performance of a DSA<sup>®</sup> is determined by the properties of the active coating, the interlayer(s) and the presence of a suitable metal support (generally Ti). The latter two subjects are much less popular, as they affect electrode service-life rather than catalytic activity, even though secondary influences of the interlayer and support on the catalytic activity cannot be ruled out in principle (the case of strong catalyst-support interaction). Mentions to these parts of the electrode are more frequent in patent literature, rather than in fundamental works [5,6,7,8,9].

In the present case, the support was not subjected to any particular treatment, and also the interlayer has not been inserted: by operating in this way, it is possible to extract interesting information about behavior of the coating, in terms of reactivity and permeability with respect to the electrolyte.

Experiments were carried out on *ex-novo* electrodes, which have been previously hydrated by performing a number of CVs in 1M HClO<sub>4</sub> at 100 mV/s. Tests have been performed on different electrodes of the same type, and the average value of service-life time has been taken into consideration in the discussion.

An example of results is reported in Fig.10.4 ((A) sol-gel samples, and (B) sputtered specimens).



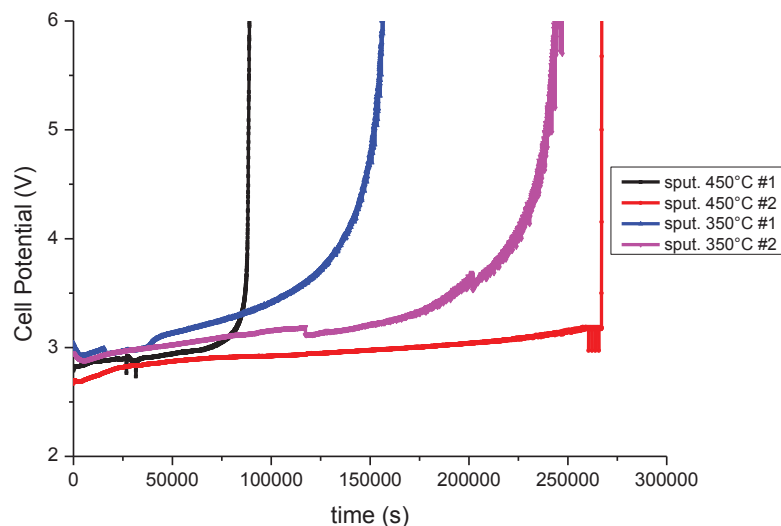


Fig.10.4. Service life experiments carried out in 15% H<sub>2</sub>SO<sub>4</sub> solution at  $j$ : 10 kA/m<sup>2</sup> and T: 60 °C for (A) sol-gel and (B) sputtered electrodes. Each graph reports two curves, related to 2 different samples for each preparation method and calcination temperatures, which are indicated with #1 and #2, respectively.

Tab.10.2 summarizes the average service-life times estimated for each sample.

Sample	Service life (h)
Sol-Gel 350 °C	3.1
Sol-Gel 450 °C	173
Sputtering 350 °C	99
Sputtering 450 °C	99

Tab.10.2. Average service-life times for the different samples.

As expected, the time of life of the Sol-Gel sample prepared at 350 °C is the lowest one, while its homologous calcined at 450 °C seems to be the most longevous. The sputtered samples show intermediate characteristics, with an average life of about 100 hours. Because of the nature of our samples, the main reasons for deactivation seem to be those proposed by Jovanović *et al.*, and by Arikado *et al.*, on papers published in 1992 and 1977, respectively [10,11]:

- An oxidation of electrocatalytic oxide in the film, which can form soluble species and dissolve in the electrolyte.
- A passivation of the Ti support (formation of an insulating TiO<sub>2</sub> layer) at the substrate/film interface, as a result of electrolyte permeation through the coating, and

reactivity of the support towards oxidizing agents such as chlorine and, especially, oxygen.

Of course, a main discriminating factor, between a deactivation pathway and the other, is represented by the coating morphology [12]. A paper published by Panić *et al.* [13], who have worked on the influence of the aging time of (40% RuO<sub>2</sub> + 60% TiO<sub>2</sub>)/Ti anodes prepared by sol-gel, evidenced that the dominant effect is represented by the film dissolution under chlorine evolution conditions. It is quite reasonable to consider that ruthenium can access to higher oxidation states (+6 and +8), thus leading to the formation of soluble compounds. However, when the main component is represented by iridium oxide, it is well known that the stability is augmented.

Data collected suggested that the porosity, and so the passivation of the titanium support, is the most likely cause of death for the electrodes. The macro-porosity, well visible on 350 °C Sol-Gel specimen, allows an easier permeation of the electrolyte, compared to the case of the sample calcined at 450 °C (which is more compact). Referring to the sputtered samples, the situation appears a bit different: it is sensible to think that the “columnar” structures, seen by AFM, are responsible for electrolyte diffusion toward the support. Owing to the dimensions of pores, this is a slow but inevitable process, especially during a prolonged polarization, when the morphology of the surface can undergo local modifications. A possible confirmation for this hypothetical explanation comes from the lack of any particular treatment of the metal support on which the coating is prepared, as well as from the lack of an interlayer, as cited before.

Sol-Gel deposits (when considering a constant thickness) can guarantee a good insulation of the support only when prepared at the highest calcination temperature, since roughness and macro-porosity are minimized; in the case of sputtered electrodes, the temperature seems not to have important consequences: the columnar growth of the coatings originates a huge number of nano-channels, in which the solution can flow and diffuse.

## 11. Summary on Discussions, and Conclusions

The ultimate goal of this work of thesis would be the identification of a correlation between the proposed results, if possible.

The performed studies on the oxide phases have provided some interesting information about the crystallization behavior of each component: the temperature of 350 °C seems to be a threshold value for the activation of the crystallization process, when working on non-metal supports (amorphous silica, in our case). When the coating is synthesized on a metal support, on which crystallization nuclei are present, an order for the final system is favored, as confirmed by the detection of intense and well-defined XRD signals. Analyzing different molar compositions for the mixture, it was shown that a high concentration of iridium oxide favors the growth of crystalline phases, with respect to samples richer in titanium oxide, in which amorphous or nano-crystalline domains are dominant. Moreover, the presence of iridium oxide, at a sufficient molar abundance (>20%), is guarantee for a greater extension of crystalline fraction (and, in general, for a higher average crystallite size), and it forces the growth of the titanium oxide crystals, stabilizing the rutile form also for the latter, which otherwise would crystallize under anatase form in the studied experimental conditions. By maintaining constant the oxide mixture composition, no important effects of the pyrolysis temperature could be appreciated on the trend of crystallite dimensions; it should also be noticed that their variations can occur in different ways, along different lattice planes. The formation of a substitutional solid solution has been verified over the whole interval of molar compositions; its presence is always accompanied by the presence of separate domains of the two oxides. Observing the measured values of cell volume, the conditions for a certain degree of microstructural metastability can be assumed, due to the fact that the titanium oxide component tends to crystallize with a lattice structure that is smaller than the nominal equilibrium one. The addition of iridium oxide is the cause for an important increase of cell parameters, which amounts to more than 2 Å when the mixture composition is approaching pure IrO<sub>2</sub>. The solid solution itself is expected to be metastable, and the experiments carried out through the synchrotron light have shown that by increasing the temperature over 650 °C, the oxide phases tend to segregate into separate domains.

The morphological and structural analyses, coupled with the electrochemical ones, have provided interesting information with regard to the specific properties of materials. The nature of the preparation method seems to affect the stoichiometry in oxygen of deposited films: the sol-gel technique seems to favor a ratio of 1:2.4 between the metal cation (Ir or Ti) and

oxygen, while reactive sputtering allows a better control on the oxidation state. Furthermore, also the crystallinity degree is influenced, and a more extended amorphous phase, with smaller crystallites, is favored in the case of sputtered samples. Considering that a significant amount of valve-metal oxide (which is usually a semi-conductor) is used for preparing industrial electrodes, a control on the stoichiometry of deposits may strongly influence their electrical (conductivity) and mechanical properties.

Owing to a good packing of columnar structures, PVD originates more compact films, with respect to sol-gel, and this limits the real electroactive surface, while probably guaranteeing a longer service life. The sol-gel samples are characterized by a larger number of electroactive sites, due to the existence of macro-roughness and macro-porosity, both well visible by AFM analysis. The correlation among CV, AFM and ERD analysis demonstrated that, in general, only the external surface is involved in the charging/discharging processes but, in the case of the sputtered sample prepared at 350 °C, both the method and the deposition temperature are the causes for a widespread “nano-porosity”, which allows the diffusion of protons, under a constrained mass-transport regime, that involves also the near-surface region. The deposition temperature affects the compactness of the materials: its increase causes a decrease of roughness indexes, especially for the sol-gel samples, while sputtered samples remain practically unaffected, with only a decrease in the porosity degree, as evidenced by trends relating to the number of electroactive sites. In the case of sol-gel samples prepared, heating at the temperature of 450 °C triggers the diffusion of titanium species through the bulk of the material and surface-segregation of titanium oxide domains. Some extent of Ti diffusion from interlayer and/or the Ti support itself, could also contribute to this phenomenon. Valve-metal segregation been also been observed in similar materials [14].

Polarization experiments, carried out for investigating the kinetics of the chlorine evolution reaction, have evidenced a lack of linearity in the high-field region of Tafel plots, for all samples; also, average Tafel slopes were higher than 60 mV/dec (estimations obtained by fitting data with a first order polynomial function).

The phenomenological background is further complicated by the choice of the electrolyte composition, as a number of works in literature have been performed in concentrated brine solutions (4 M in NaCl) and high temperatures (around 60-80 °C). In solutions with so high ionic strengths, assuming solvation numbers of 6 for both Na<sup>+</sup> and Cl<sup>-</sup> [15], the number of “free” moles of solvent is negligible and both, thermodynamics and kinetics of such systems becomes more and more complex.

Although substantially not commented, non-linearity in Tafel plots was also observed by other research groups: Kuhn *et al.* [16], Burke *et al.* [17] and by Érenburg *et al.* [18]; in the latter case, Tafel slopes around 40 mV/dec were observed. As far as electrochemical reaction order with respect to Cl<sup>-</sup> is concerned, a nearly unitary reaction order with respect to chloride was found, in good accordance with literature papers (see Par.9.1). This value is not compatible with the proposed mechanisms (with the exception of the Krishtalik one). More in detail, the mechanism proposed by Érenburg and Krishtalik [19,20], assumes a Cl(+1) species as adsorbed intermediate, possibly an oxochloride complex (see also: [21,22]). However, looking at the Pourbaix diagrams, its formation under the explored conditions is also quite improbable.

The observed inhibitory effect of the protons, on the rate of the ChlER, probably arises from modifications on the properties of the surface, and it demonstrates that the discharge of the chloride anion takes place on a strongly oxidized surface, where the interaction between sites and intermediates can take place only via surface-oxygen atoms. In fact, the inflection observed between  $-1,0 < \log[H^+] < 0,0$  (which depends on the preparation method) is in agreement with the approximated value of *pzc* (point of zero charge) proposed by Ardizzone *et al.* for the case of iridium-oxide powders [23]. The destabilization of the reaction intermediates, which causes a decrease of the reaction rate, does not seem to be related to aspects of surface charge (since a net positive charge on the electrode surface should attract the chloride anions), but rather to the inability of electroactive sites to coordinate the chlorine radicals through oxygen bond {Ir-O-Cl}, because of the presence of an excess of H<sup>+</sup> linked to oxygen atoms.

In view of the above outlined complexity of the experimental evidence, it has been decided to apply the mathematical model proposed by Tilak and Conway in the early 90s [24] to our results, thus attempting to explain curved Tafel plots, high slopes, as well as reaction orders with respect to chloride comprised between 1 and 2. Following this approach, we concluded that the reaction proceeds via a Volmer-Heyrovsky pathway, which involves high coverage values for the reaction intermediate. The Langmuir adsorption model has proved to be sufficient to describe the state of the adsorbed intermediate, and no significant improvements have been obtained by introducing the lateral interaction parameter that characterizes the Frumkin isotherm. Estimated coverage values were around 0.8, in the Tafel region, and they proved to be characterized by small variations, sufficient to produce non-linearity in the Tafel plots. The impedance spectroscopy analysis did not supply additional useful information on the behavior of adsorbed intermediates, plausibly because of the small variation of coverage as a function of overpotential, in the Tafel region: it is worth

remembering that the so-called “pseudo”-capacity related to reaction intermediates is proportional to  $\partial \mathcal{G} / d\eta$  and, if this term is not large enough, the contribution of the mesh due to the adsorbed intermediates degenerates into a single resistance of adsorption/desorption, not visible on both Nyquist and Bode’s plots. In fact, the faradaic contribution of the electrochemical discharge of chloride is visible in each case, and a second contribution is visible only for samples prepared at 350 °C. The latter contribution, which can be assessed at the highest frequencies, is due to a geometrical factor that is characteristic of electrodes prepared at the lowest calcination temperature, and it was discriminated by varying parameters such as temperature and reactant concentration, which have no effects on geometric and physical features of analyzed samples.

As regards the intrinsic activity of electrocatalytic sites, toward the chlorine evolution reaction, both the conventional exchange currents and the enthalpies of activation were evaluated, for all samples. It has been possible to estimate the “apparent” enthalpy of activation related to the formation of the activated complex, as treated by Conway [25], and this procedure was attempted in order to extrapolate a parameter, independent of the reagent concentration and of the working temperature, able to measure the activity of the catalyst towards the electrochemical process of interest. By observing the values of exchange current, normalized by the number of the most external electroactive sites, the most active material resulted to be the sol-gel sample prepared at 350 °C, followed by all the others, which are characterized by values very close to each other. It should be remembered that this normalization approach provides a real turnover number, for each examined material, which can be directly compared with the activation energies. Considering the apparent enthalpies of activation, obtained from Arrhenius plots, the ranking of specimens appears quite in accordance with the above one, as reported below (materials are listed in order of activity):

$$\text{Sol-Gel } 350 \text{ }^\circ\text{C} > \text{Sol-Gel } 450 \text{ }^\circ\text{C} > \text{Sputtering } 450 \text{ }^\circ\text{C} \approx \text{Sputtering } 350 \text{ }^\circ\text{C}$$

The order of magnitude of the activation enthalpies may appear high, but it is reasonable if we consider that the interactions between Ir sites and chlorine intermediates are mediated by oxygen atoms; in this regard, a study of gaseous oxychlorides of iridium has been proposed by Bell *et al.* [26], and their outcomes are in accordance with values gathered in our laboratory.

The evaluation of the turnover number, through a normalization of the exchange currents, has been confirmed to be a valid approach for building up a sort of ranking among electrocatalysts. The performances of electrodes prepared by sol-gel are higher than those of sputtered samples, but further work is necessary for improving the reactivity of



electrocatalytic sites. Another interesting aspect, which it is worth noting, is that the temperature of preparation has a small effect on the chemical nature of the iridium centers, in the case of sputtered samples. Certainly, this result is due to the different characteristics of the two synthetic approaches: the reactive sputtering produces a more compact film, in which the degrees of freedom of atoms are limited with respect to a preparation that starts from a gel precursor; the coordination and the bond strength of iridium atoms, with their surrounding chemical environment, obviously influence the charge density on metal center, and its reactivity towards reagents and reaction intermediates; in these terms, materials prepared via sputtering appear to be disadvantaged. The most active phase of iridium-based electrocatalysts seems to be the amorphous one, as witnessed by the XRD results attained after strong polarizations under ChIER conditions: as a general outcome, the dissolution/corrosion of coatings involves only the non-crystalline portion. This aspect is a further confirmation to the fact that electroactive sites characterized by a greater number of “dangling” bonds are more active towards an interaction with chloride anions.

A still pending issue of this work of thesis is represented by the sample prepared via sol-gel at 350 °C, because of its strange behavior under certain conditions. In fact, when looking at Tafel plots associated with polarization curves collected at different temperatures, a parallelism cannot be found and this has hindered the estimation of  $\Delta H^\ddagger$  in the high-field region. In fact, the calculation was carried out only by taking measurements around the reversible potential. Probably, the high electroactivity of this specimen toward the studied reaction, together with the physical characteristics of its surface, are the causes of the cited evidences. All proofs have been attempted several times, working with different specimens, and observing a good reproducibility, and this suggests that the cited behavior is caused by particular features of the coating, which are not still completely clarified.

Tests of service-life have shown that the control of morphological characteristics represents one of the most important tasks for obtaining a durable device: aspects related to both macro- and “meso-/nano-” porosities are remarkable during polarization treatments. Under these terms, the calcination temperature strongly affects the durability of sol-gel coatings, while appears to have minimal effects on sputtered samples, for which the nature of the preparative plays the main role.

Eventually, a detailed electrochemical study of samples prepared by sputtering, and a comparison of performances with traditional sol-gel coatings, is currently in progress in our laboratories, in order to better understand the characteristics of electrodes prepared by means of this relatively unconventional synthetic approach. In any case, the results highlighted in this work of thesis have underlined some promising features, such as the elemental deposition

control and possibility to obtain smooth surfaces, which in turn influence the electrical, mechanical and electrocatalytic properties.

## Bibliography

1. J. Augunstynskii, L. Balsenc, J. Hinden, *J. Electrochem. Soc.* **125**(7), 1093 (1978).
2. V.V. Gorodetskii, P.N. Zorin, M.M. Pecherskii, V.B. Busse Machukas, V.L. Kubasov, Y.Y. Tomashpol'skii, *Elektrokhimiya* **17**, 79 (1981).
3. G.N. Martelli, R. Ornelas, G. Faita, *Electrochim. Acta* **39**, 1551 (1994).
4. A. Calderara, F. Sala, F. Timpano, WO 2012101141 A1 (2012).
5. H.J. Jansen, A. Mackor *EP 0538955 B1*, (1998).
6. A. Pellegrini, *EP 0183100 B1* (1990).
7. F. Cardarelli, P. Taxil, A. Savall, Ch. Comninellis, G. Manoli, O. Leclerc, *J. Appl. Electrochem.* **28**, 245 (1998).
8. F. Gestermann, H.D. Pinter, G. Speer, P. Fabian, R. Scannel, *US 7211177 B2* (2007).
9. P. Rossi, *US 8083921 B2* (2011).
10. V.M. Jovanović, A. Dekanski, P. Despotov, B. Nikolić, R.T. Atanasoski, *J. Electroanal. Chem.* **339**, 147 (1992).
11. T. Arikado, C. Iwakura, H. Tamura, *Electrochim. Acta* **22**, 513 (1977).
12. V. Panić, A. Dekanski, S. Milonjić, R. Atanasoski, B. Nikolić, *J. Serb. Chem. Soc.* **65**, 649 (2000).
13. V. Panić, A. Dekanski, S. Milonjić, R. Atanasoski, B. Nikolić, *Electrochim. Acta* **46**, 415 (2000).
14. G. Battaglin, V. Rigato, S. Zandolin, A. Benedetti, S. Ferro, L. Nanni, A. De Battisti, *Chem. Mater.* **16**, 946 (2004).
15. H. Ohtaki, T. Radnai, *Chem. Rev.* **93**, 1157 (1993).
16. A.T. Kuhn, C.J. Mortimer, *J. Electrochem. Soc.* **120**, 231 (1973).
17. L.D. Burke, J.F. O'Neill, *J. Electroanal. Chem.* **101**, 341 (1979).
18. R.G. Érenburg, L.I. Krishtalik, I.P. Yaroshevskaya, *Elektrokhimiya* **11**(7), 1068 (1975).
19. R.G. Érenburg, L.I. Krishtalik, I.P. Yaroshevskaya, *Élektrokhimiya*, **11**, 1072 (1975).
20. R.G. Érenburg, L.I. Krishtalik, I.P. Yaroshevskaya, *Élektrokhimiya*, **11**, 1076 (1975).
21. D.A. Denton, J.A. Harrison, R.I. Knowles, *Electrochim. Acta* **24**, 521 (1979).
22. R.G. Érenburg, L.I. Krishtalik, N.P. Rogozhina, *Elektrokhimiya* **20**, 1183 (1984).
23. S. Ardizzone, S. Trasatti, *Advances in Colloid and Interfaces Science* **64**, 173 (1996).
24. B.V. Tilak, B.E. Conway, *Electrochim. Acta* **37**(1), 51 (1992).

25. B.E. Conway, in *Theory and Principles of Electrode Processes*, pp. 106-109, Ronald Press Company (New York) (1965).
26. W.E. Bell, M. Tagami, *J. Phys. Chem.* **70**, 640 (1966).

## Acknowledgments

Pursuing PhD degree was one of the most amazing and intense period of my life; it was a period characterized by very intense emotions and good sensations but, sometimes, by bad times where frustration dominated... but I think this is the price necessary to pay: a success is made of a great number of failures.

With sincerity and kindness, I'd like to thank:

My family: my father Dorian, my mother Milena, my sister Mara and her husband Gabriele, my young nephew Jacopo and my girlfriend Elena, who are my constant points of reference in my life.

Prof. Achille De Battisti, Professor of Electrochemistry at the University of Ferrara, my Master and my tutor during this period of thesis. His support and direction along all three years of work were fundamental to encourage me to do a research work of quality. His wisdom and suggestions have contributed to an important growth of myself.

Dr. Sergio Ferro, research assistant at the University of Ferrara. I think he is one of the best scientist and person who I've ever met. He taught me fundamental things for being a good researcher.

Prof. Giancarlo Battaglin, Professor at the University of Venezia. A person characterized by high scientific culture and great human qualities; this work of thesis couldn't be done without his support.

Prof. Andrzej Lasia, Professor at the University of Sherbrooke (CN). He introduced me to the complex topic of electrochemical impedance spectroscopy. He believed in me and provided me a great number of scientific stimuli.

Prof. Alvise Benedetti and Prof. Pietro Riello, Professors at the University of Venezia, for their precious suggestions about the discussion of XRD data and for the experimentation carried out at ELETTRA center in Trieste.

Dr. Rossano Amadelli, research assistant at CNR. His scientific and moral support helped me for overcoming obstacles during PhD period.

Dr. Christian Urgeghe and Dr. Marianna Bricese, DeNora industries, for supplying titanium supports and SEM experimentation.

Dr. Piero Schiavuta and Dr. Veronica Vascotto, VenetoNanoTech, for AFM analysis.

Dr. Laura Meda and the Physical Chemistry department of Istituto ENI Donegani for XPS analysis.

Dr. Stefano Neodo, Dr. Luca Mattarozzi, Dr. Martina Donatoni and Dr. Mirco Natali, great colleagues and friends who helped me every time I found a problem with great friendliness and affection.

My best friend Paolo, and his family: Roberto, Laura and Elena, who are for me a second family. I will always carry you in my heart.

All colleagues that I've met all over the world during congresses, summer schools and stages: Dr. Aleksandar Cvetkovski, Dr. Pablo Arevalo Moscoso, Dr. Bozena Losiewicz, Dr. Agnieszka Smolka, Dr. Magdalena Szklarska, Dr. Carlos Martizez Huitle, Dr. Przemyslaw Kwolek, Dr. Yaser Khani, Dr. Federico Bella, Dr. Francesco Di Franco, Prof. Monica Santamaria, Dr. Eleonora Ussano, Dr. Alessandra Campana, Dr. Alessandro Boni, Dr. Nicola Dalle Carbonare, ...

All my friends and musicians who shared with me their personality and their emotions... and who have signed my life... Love you: Andrea Duò, Stefano Pavan, Leonardo Marin, Damiano Mantovani, Matteo Bellan, Federico Mancin, Alan Biasin, Thomas Beccari, Francesco Bovolenta, Mauro Catellani, Simone Coppiello, Aligi Pasqualetto, Alessandro Vaccaro, Michele Ambrosi, Luca Barbini, Stefania Grimaldi, Tiziana De Poli, Massimo Furlan, Mauro Bonaldo, Ivo Pieretto, Elisa Gallio, Benedetta Frezzato, Fabio Crepaldi, Nico Viviani, Andrea Biolcati, Paolo e Andrea Prencisvalle, Federico Ronconi, Matteo Toso, Lorenzo Pieragnoli, Andrea Bondi, Luca Cappelli, Francesco Bondi, Romina Fabbri, Francesco Costa, Alberto Pozzati, Marco Guarnieri, Luca Stoppa, ...

Beside, I would like to thank all the people I forgot to mention.

Davide